MULTI-SCALE MODELLING OF PRISTINE AND TRANSITION METAL DOPED SPINEL $LiMn_2O_4$ CATHODE MATERIALS

A thesis presented

By

HLUNGWANI DONALD

To

The Department of Physics

In fulfillment of the requirements for the degree of

Doctor of Philosophy

In the subject of

Physics

Faculty of Science and Agriculture

School of Physical and Mineral Sciences

University of Limpopo (Turfloop campus)

South Africa

Supervisor: Prof. R.S. Ledwaba

Co-supervisor: Prof. P.E. Ngoepe

2024

Declaration

I declare that the thesis hereby submitted to the University of Limpopo for the degree of Doctor of Philosophy has not been previously submitted by me for a degree at this or any other university, that it is my work both in design and execution and that all materials contained herein have been duly acknowledged.

Mr D. Hlungwani

Signature: 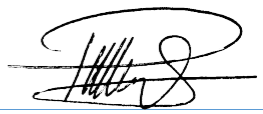

[redacted] [redacted] Date 03/09/2024

Dedication

I dedicate this work affectionately to the following:

Florah Chabangu

Freddy Hlungwani

Evah Hlungwani

Bongani Hlungwani

Swiringene Nkuna

Nkateko Hlungwani

Tinyiko Hlungwani

Dzunisani Hlungwani

Acknowledgements

First and foremost, I would like to thank God for His mercy and grace. I am where I am today because of him. I would like to express my sincere gratitude to my supervisors, Prof. R.S. Ledwaba and Prof. P.E. Ngoepe, for affording me the opportunity to work on this riveting and cutting-edge research project and also for their continual support and exposure to different research techniques. I am thankful for their guidance, patience, and inspiration throughout this research project. They patiently taught me essential research techniques, which enabled me to successfully carry out this project. I also thank my family for their support, love, and understanding. I would also like to thank our research group, Materials Modelling Center (MMC), for research tools and support. I also thank Dr. K.W. Phoshoko and Dr. K. Kgatwane for their technical support. I would also like to thank the university, particularly the physics department, for allowing me to register for my Master's degree. I would also like to extend my sincere gratitude to NRF for its financial support.

Abstract

Lithium-manganese-oxide with a spinel structure has attracted enormous attention as a future cathode material for lithium-ion batteries. $LiMn_2O_4$ is affordable due to the abundance of manganese in South Africa (80% of the world reserves) and provides high-rate capability. However, its commercialization is currently hindered by structural instabilities linked to its Mn^{3+} component. During cycling, the increasing amount of Mn^{3+} (≥ 50%) onsets the Jahn-Teller effect, which destabilizes the spinel structure, leading to a loss of capacity.

Hence, in this work, there emanates a need to introduce Ni and Co as dopants to reduce the concentration of Mn^{3+} and also stabilize the transition metal and oxygen bond in the structure. To incorporate this effectively, the Buckingham potentials for the interactions that arise from doping $LiMn_2O_4$ with Co and Ni were derived using a technique inspired by machine learning methods. The Buckingham potential parameters were derived with guidance from potential energy surfaces from electronic structure calculations. The potential reduced the fitted structure properties and elastic constant to an acceptable percentage difference of less than 7.1%. The potentials were utilized to investigate the microstructural changes and Li^+ transport properties of $LiMn_2O_4$ influenced by the introduction of Co and Ni on the Mn^{3+} sites in the structure. The developed potentials were able to determine the thermodynamic properties aligned with experimental observations such as melting point and the crucial high-temperature behaviour of $LiCo_2O_4$ and $LiNi_2O_4$ in the test of their veracity. The melting point of $LiNi_2O_4$ was found to be lower than that of $LiCo_2O_4$, which could be attributed to the observed lower melting point of Ni when compared to that of Co.

Moreover, the potentials were further employed to perform simulated synthesis of $LiCo_2O_4$ and $LiNi_2O_4$ nanospherical structures. X-ray diffraction (XRD) patterns and atomic structure snapshots showed the dominance of the LiM_2O_4 (M=Co, Ni) co-existing with the M_3O_4 and Li_2MO_3 high-temperature impurity phases, which is in line with the findings of Mouhib and co-workers. Moreover, the average bond distances of the Co-O (~1.92 Å) and Ni-O (~1.91 Å) interactions were found to be smaller than that of the Mn-O (~1.923 Å) interaction, in line with the experimental values. Therefore, the M-O (M=Co, Ni) bond will be stronger than the Mn-O bond, which will improve the

structural stability of $LiMn_2O_4$. Since a shorter bond length will result in higher electron affinity between M-O (M=Co, Ni) as compared to Mn-O.

The subsequent step was to employ the derived interatomic potentials to define the interactions within the Co- and Ni-doped $LiMn_2O_4$ spinel. Monitoring of the impact of these dopants demonstrated that the introduction of Co and Ni in $LiMn_2O_4$ did not compromise the cubic spinel structure. Therefore, in line with our findings in $LiCo_2O_4$ and $LiNi_2O_4$ spinel systems, the bond length between the dopants (Co and Ni) and oxygen (< 1.923 Å) was also found to be shorter than the bond length of manganese and oxygen (~1.923 Å). This also supports the view that the partial substitution of manganese with Co and/or with Ni could result in improved structural stability, which will improve capacity retention. Furthermore, Co and Ni were only observed in the 16d octahedral sites and were not found in the 8a tetrahedral sites on the microstructure, unlike in the case of pure $LiMn_2O_4$ phases, where some Mn atoms migrate into the tetrahedral sites. Therefore, Co and Ni do not disrupt Li transport in the 8a tetrahedral sites, which affects capacity retention and rate capabilities. Furthermore, one extremely crucial aspect is the impact of the dopants on the ionic diffusion of the spinel material. When comparing the effects of the two dopants, Ni was found to improve the diffusion of lithium ions in the spinel structure compared to Co. Since, the Ni-doped $LiMn_2O_4$ spinel structure (1.6×10^{-12} m^2/s) was found to have a higher value for diffusion coefficient at 300 K as compared to the Co-doped $LiMn_2O_4$ spinel structure (0.61×10^{-12} m^2/s). Moreover, the ionic conductivity of Li also demonstrated the same behaviour, Ni-doped $LiMn_2O_4$ spinel nanomaterial was found to have a value of 0.94×10^{-6} S cm^{-1}, while the Co-doped $LiMn_2O_4$ spinel nanomaterial had a value of 0.23×10^{-6} S cm^{-1}.

The ultimate exploration in this work was the morphological impact on the ionic diffusion and conductivity of the $LiNi_2O_4$ spinel cathode material. This sparked particular interest in further exploration since the Ni-dopant demonstrated enhanced diffusivity. As such, the role of pore size in $LiNi_2O_4$ nanoporous structures on transport properties (i.e., ionic diffusion) and microstructural changes was probed. Increasing the pore size was found to also increase the surface area and the diffusion of lithium ions in the structure. The surface areas of the 0.30, 0.21, and 0.15 nm nanoporous materials were found to be 22.16, 15.50, and 12.05 $Å^2$, respectively. The same was

also noted in the calculated ionic conductivities of Li^+, which were found to be ~2.34 x $10^{-8,}$ ~7.86 x 10^{-8}, and ~1.50 x 10^{-7} S/cm for the nanoporous structures with pore diameters of 0.15, 0.21, and 0.30 nm, respectively. Therefore, a nanoporous spinel structure could enhance rate capabilities, and fast charge and discharge rates could be achieved.

The overall stability of Li-Mn-O can be enhanced by the partial substitution of Mn with Co and Ni. Additionally, the transport of Li^+ ions is not disrupted by Co and Ni at dopant concentrations of ≤ 0.02. Moreover, Ni was found to have superior influence over the migration of Li^+ ions in the structure. Therefore, the charge and discharge processes can be enhanced by single-doping $LiMn_2O_4$ spinel with Ni. The rate of charge and discharge can also be further enhanced by the design of nanoporous materials with larger pore diameters (≥ 0.21 nm), which are crucial for large-scale high-energy and high-power density applications.

Table of Contents

List of Tables

List of Figures

List of Abbreviations

Abbreviation	Definition
XRD	X-ray Diffraction
LMOs	Layered Metal Oxides
LIBs	Lithium-ion Batteries
HEVs	Hybrid Electric Vehicles
EVs	Electric Vehicles
MD	Molecular Dynamics
PEDs	Portable Electronic Devices
KMF	Kalahari Manganese Field
BIF	Banded Iron Formations
TMOs	Transition Metal Oxides
Li-Mn-O	Lithium Manganese Oxide
A&R	Amorphization and Recrystallization
PES	Potential Energy Surface
DFT	Density Functional Theory
IAPs	Interatomic Potentials
TM	Transition Metal
RDF	Radial Distribution Function
FHI-Aims	Fritz Haber Institute Ab initio molecular simulations
GULP	General Utility Lattice Program
LDA	Local Density Approximation
GGA	Generalized Gradient Approximation
PBE	Perdew-Burke-Ernzerhof
PW91	Perdew-Wang
PAW	Projector-Augmented Wave
NAO	Numeric Atom-Centered Orbital
VASP	Vienna Ab initio Simulation Package
NVE	Microcanonical ensemble
NVT	Canonical ensemble
ASE	Atomic Simulation Environment
MSD	Mean Square Displacement

List of Symbols

Symbol	Definition
r	Separation distance between two atoms
Q	Ionic charge
e	Electronic charge
v	Voltage
P	Pressure
T	Temperature
ε	Permittivity of electrolyte
K_B	Boltzmann constant
D	Diffusion coefficients
m	Mass
$\ddot{\boldsymbol{r}}$	Acceleration
ρ	Density

List of Constants

Charge of electron	$e = 1.6\ x\ 10^{-19}\ C$
1eV	$1.6\ x\ 10^{-19}\ J$
Atmospheric Pressure	$P_{atm} = 1.05\ x\ 10^{5} nm^{-2}$
Universal gas constant	$R = 8.31\ J\ K^{-1} mol^{-1}$
Planck's constant	$h = 6.63\ x\ 10^{-34}\ J.s$
Boltzmann gas constant	$K = 1.38\ x\ 10^{-23}\ Jmol^{-1}$

CHAPTER 1

Introduction and Background

Lithium-manganese-oxide, which crystallizes into a spinel structure, has been receiving growing interest as one of the affordable and high-voltage positive electrode materials for lithium-ion batteries (LIBs). This material consists of three-dimensional diffusion channels that facilitate the facile movement of Li^+, resulting in high-rate capabilities required in hybrid electric vehicles (HEVs) and electric vehicles (EVs) [1, 2]. Moreover, $LiMn_2O_4$ spinel has an environmentally acceptable impact and satisfactory thermal stability, which cements its suitability for large-scale applications (smart grids, HEVs, and EVs) [3, 4]. However, this material deteriorates during the charge/discharge cycles, resulting in a significant loss of capacity, which has detoured its commercial usage [5, 6]. The exponential technological growth and the need to sufficiently support electric vehicles call for the development of cost-effective, safe, durable, and energy-dense positive electrode materials to enhance the current performance of the leading lithium-ion batteries. To date, the positive electrode material is one of the most expensive components in lithium-ion batteries and among the impediments regarding the battery's energy density. As such, insights that will guide the improvement of $LiMn_2O_4$ are of paramount importance. Additionally, the reinforcement of the performance of LIBs will also aid significantly in solving the energy crisis by providing adequate energy storage systems. The abundance of manganese in parts of South Africa makes manganese-based electrode materials like $LiMn_2O_4$ attractive [7, 8].

The dominance of lithium-ion batteries in portable electronics is largely due to significant research efforts delegated to finding new materials and understanding their behaviour and how they relate to battery performance [9]. A deeper insight into the link between material structure and its properties is pivotal to the improvement of materials. Cation doping has been reported as one of the most effective methods for tuning material properties. Hence, it can be instrumental in enhancing the performance of promising lithium-ion battery cathode materials [10, 11, 12]. Particularly, the performance of $LiMn_2O_4$ spinel, which is plagued by capacity fading. To date, little is known about the effect of cation doping on $LiMn_2O_4$ spinel at the microscale. Such

studies are currently viable through molecular dynamics (MD) simulations, which are based on interatomic potentials (IP). MD methods are significant in predicting and unravelling material properties. The scarcity of accurate IPs has been a bottleneck for microscale simulations. The availability of accurate IPs is proportional to the impact and veracity of these methods in the science community.

1.1 The performance and advances of the current leading rechargeable batteries

LIBs have been the most preferred secondary battery since their commercialization in 1991 due to their high power and high energy densities as compared to other rechargeable batteries. They have been well received in portable electronic devices (PEDs), a market characterised by exponential growth [13]. The growing need to move away from the traditional generation of electricity that results in global warming has seen lithium-ion batteries gain traction in the storage of energy garnered from renewable energy sources [14]. As such, they are playing an important role in solving unprecedented climate change. Moreover, they also support revolutionary electric vehicles (EVs) or hybrid electric vehicles (HEVs) [15]. The main components that make up a lithium-ion battery are the positive electrode (cathode), the negative electrode (anode), and the electrolyte.

1.1.1 Structure and operation of a lithium-ion battery

In a lithium-ion battery, during a discharge process (PED plugged in), Li^+ ions migrate from the negative electrode (anode) into the positive electrode (cathode) due to a potential difference between the two electrodes. The two electrodes dipped into an electrolyte are separated from each other by a porous membrane. Subsequently, during a charge process, lithium ions move from the cathode into the anode. Electrons move through the external circuit in the direction of Li^+ ions in both processes. Lithium ions move through the porous membrane in the electrolyte from the cathode into the anode [16, 17, 18]. The operation and the significant components of this rechargeable battery are captured in Figure 1.1.

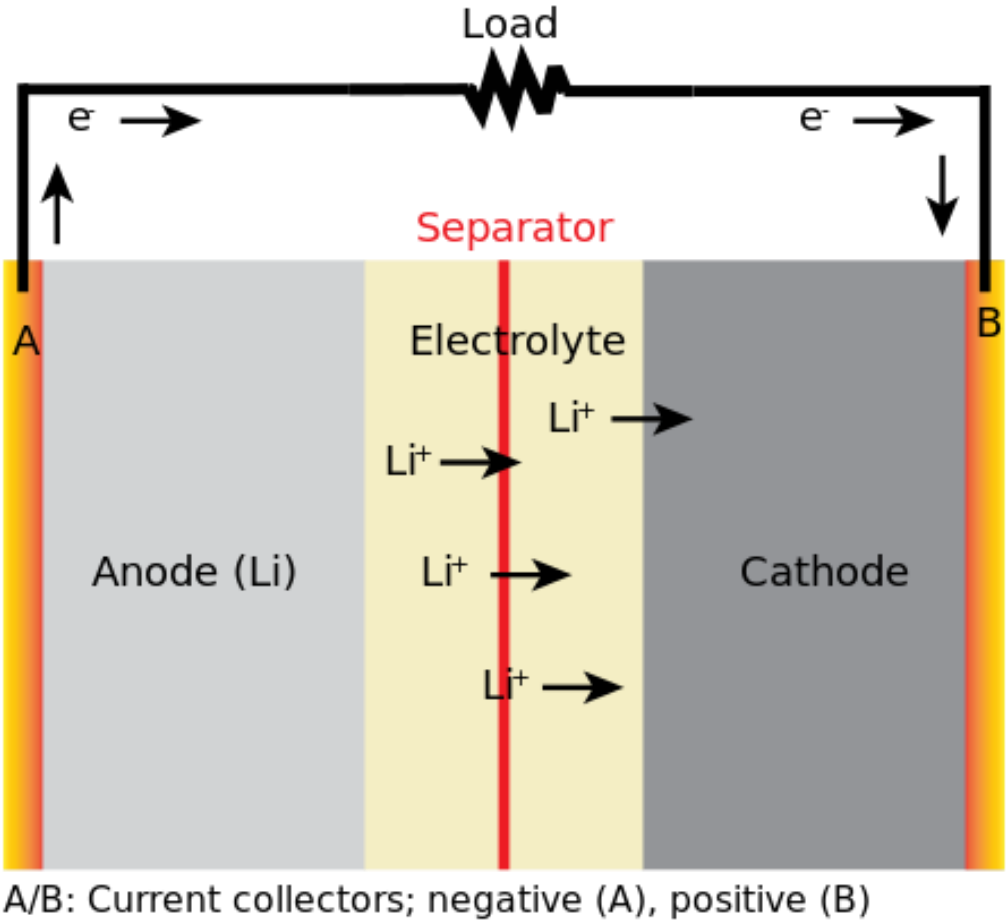

Figure 1.1: Illustration of the structure and operation of a lithium-ion battery. Lithium ions are moving from the anode (negative electrode) into the cathode (positive electrode) through the separator (porous membrane) during a discharge process. Electrons are moving in the same direction through the external circuit.

1.1.2 Applications

Figure 1.2 shows the wide application areas of LIBs. They are dominant in portable electronic devices (PEDs), and their usage is growing exponentially. Furthermore, their usage and demand are also increasing in the storage of the fluctuating energy generated from renewable sources [19, 20, 21]. Moreover, they are also a source of power for HEVs and EVs. However, for full support of HEVs and EVs, the current performance of lithium-ion batteries requires improvement. Economically viable lithium-ion battery operational materials will be instrumental in powering HEVs and EVs on a large scale.

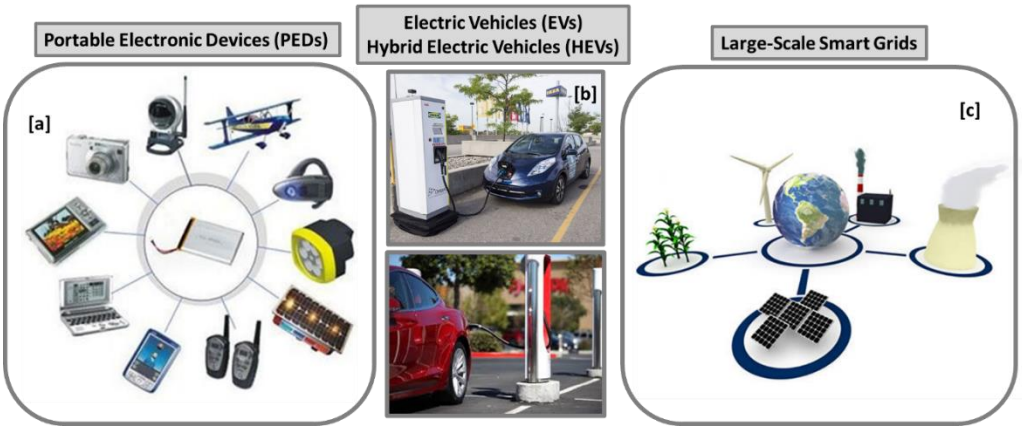

Figure 1.2: Broad applications of lithium-ion batteries. (a) Application in portable electronic devices [22], (b) hybrid electric vehicles (HEVs) [23] and electric vehicles (EVs), and (c) Smart grids [24].

1.2 Literature review

The heightening demand for environmentally benign, durable, and affordable high-power density and high-energy density energy storage systems calls for urgent improvement of the current battery systems. The positive electrode material is currently reported as the most expensive component in a lithium-ion battery [25, 26]. Manganese is affordable and less toxic than cobalt, hence, manganese-rich positive electrode materials are crucial to the realisation of economically viable lithium-ion battery systems [27]. This is due to the abundance of manganese, particularly in South Africa. The richest manganese deposits are hosted in the Kalahari Manganese Field (KMF), situated in the Northern Cape province of South Africa. The site hosts about 77% of manganese metal in banded iron formation (BIF) deposits when compared to land-based manganese deposits around the world [28, 29, 30]. Moreover, manganese is found to be extremely abundant, and when compared to other abundant elements in the earth's crust, it ranks 12th. Transition-metal-based cathode materials for lithium-ion batteries given considerable research attention are $LiFePO_4$, $LiNiO_2$, $LiCoO_2$, $LiMnO_2$, and $LiMn_2O_4$ [31, 32, 33, 34, 35].

1.2.1 Layered metal oxides

Layered metal oxides (LMOs) have been cathode materials of choice for lithium-ion batteries since their commercialization by Sony in the 1990s [19, 36, 37]. LMOs can yield theoretical capacities greater than 270 $mAhg^{-1}$ and operate at voltages greater

than 3.7 V [38, 39]. The exponentially growing energy needs have triggered a great deal of research interest in lithium-ion batteries. Investigations of the properties and performance of TMOs are vital to the design of high-energy positive electrode materials to meet the ever-growing energy demands [40].

$LiNiO_2$ is among the most studied high-capacity cathode materials, with a reversible capacity greater than 200 mAh/g. However, despite its cost-effective factor and alluring capacity, its full commercialization is deterred by its inferior cyclic performance. Several anisotropic phase changes have been observed at high charge or discharge cycles, leading to a significant loss of capacity. Additionally, $LiNiO_2$ possesses safety concerns linked to the release of oxygen [41, 42, 43].

The majority of commercial lithium-ion batteries utilize $LiCoO_2$ as a positive electrode material due to its high discharge voltage, superior cyclic performance, and heightened theoretical capacity of over 200 mAh/g. However, the material is expensive, its capacity deteriorates during prolonged cycling, and it is thermally unstable, hence, it falls short of supporting electric vehicles (EVs) or hybrid electric vehicles (HEVs) [44, 45]. Li_2MnO_3 has also been extensively investigated as a prospective Li-ion battery cathode material. It can yield high capacities of ~250 mAh/g when used in the 2 V and 4 V voltage ranges. However, upon cycling, Li_2MnO_3 transforms into a structure like that of cubic spinel, which results in performance attenuation. The layered-to-spinel transformation is attributed to the loss of oxygen in the structure during Li^+ extraction, which precludes its full utilisation [46, 47, 48, 49].

1.2.2 Drawbacks of spinel-type lithium-metal-oxides (LMOs)

The paucity and toxicity of cobalt call for the replacement of the commonly utilized positive electrode for lithium-ion batteries, layered Li_xCoO_2 [50, 51, 52]. Lithium-manganese-oxide (Li-Mn-O) electrode materials with a spinel-type structure are currently gaining significant attention as a prospective replacement for Li_xCoO_2. Li-Mn-O spinel cathode materials are economically feasible as compared to Li-Co-O layered cathode materials on account of the abundance of manganese [28, 29, 30]. Moreover, Li-Mn-O electrodes provide well-accepted voltages and energy densities. Additionally, Li-Mn-O spinel is environmentally benign and possesses acceptable thermal stability, which is a significant requirement for large-scale applications (HEVs, EVs, and smart grids). Three-dimensional diffusion pathways of the Li-Mn-O spinel offer fast charging

and discharging rates. However, at high operating voltages and elevated temperatures, $LiMn_2O_4$ spinel loses capacity as a result of manganese dissolution. This has been the main reason for the delayed commercialization of Li-Mn-O spinel [53, 54, 55, 56, 57].

1.2.3 Synthesis methods

1.2.3.1 Experimental synthesis methods for spinel LMOs

Lithium-manganese-oxide spinel is largely prepared using a solid-state reaction synthesis method. This method yields decent results, and due to its scalability, it has been widely adopted in industries. In a solid-state reaction, a given solid material is decomposed with heat to yield a new solid and a gas. The resulting particles are generally non-uniform and less crystalline. However, for more homogeneous particles with an evenly distributed composition, additional heat treatment is required [58, 59, 60]. Alternatives to solid-state synthesis are sol-gel, co-precipitation, spray-pyrolysis, and the combustion synthesis method. Sol-gel yields atomically homogeneous products with improved crystallinity after a few calcination steps and at lower temperatures. However, this synthesis route requires a significant amount of precursor [61, 62, 63]. Another method for producing more crystalline $LiMn_2O_4$ spinel is the co-precipitation synthesis route. The process is not complicated, and it consumes less energy. However, the equipment for this synthesis route is expensive, and it doesn't offer much control over particle size and distribution [64, 65]. A method that offers control of particle size at a shorter reaction time is the spray-pyrolysis synthesis method. The method yields uniform spherical nanoparticles at a lower cost. However, its deposition rate is unsatisfactory, and finding the optimal temperature for powder growth is quite a challenge [66, 67]. Last but not least is the combustion synthesis route, which yields products with the smallest particle sizes with few calcination stages. Moreover, combustion synthesis is a relatively inexpensive, simple, and versatile high-temperature approach. The only challenge is particle agglomeration [68, 69, 70].

1.2.3.2 Simulated synthesis methods

The simulated amorphization and recrystallization technique (A&R) [71] is one of the vital techniques in large-scale computer simulations. Capturing significant material behaviour and properties that evolve during synthesis has been difficult to model computationally until the establishment of A&R. Various and essential structural features linked to the behaviour and properties of materials emerge during synthesis. Computational methods that give access to such physical and chemical processes are crucial to the engineering of novel, valuable materials. The simulated A&R technique makes it possible to model such significant features, resulting in simulated models that are comparable to materials synthesised with traditional experimental methods. Moreover, models representing electrode materials of various morphologies can be modelled using the A&R approach. Consequently, valuable insights can be shed on the development of durable, high-power, and high-energy electrode materials.

Lee and co-workers have successfully studied and characterised the chemistry of defects in layered $LiNi_{1/3}Co_{1/3}Mn_{1/3}O_2$ using MD simulations based on empirical potentials. Moreover, they also shared insights on the mechanism of intrinsic antisite defects in the $LiNi_{1/3}Co_{1/3}Mn_{1/3}O_2$ layered structure. Their findings were in line with experiments [72]. Dean et al. used the A&R approach to generate undoped and Ti-doped CeO_2 nanostructured models. The introduction of Ti in the CeO_2 structure was found to change its morphology from polyhedral to spherical, and the whole mechanism was delineated through detailed atomic-level snapshots [73]. A model of Li-MnO_2 rich in microstructural features such as point defects, vacancy defects, and microtwinning was generated in a study by Maphanga et al. using large-scale atomistic simulations. The model was comparable to experiments through X-ray diffraction (XRD) patterns and atomic-level structural snapshots [74]. Moreover, Ledwaba and co-workers employed the amorphization and recrystallization technique to characterise the phase transition of the Li-Mn-O nanoparticulate electrode associated with capacity fading and further model its discharge process [75].

1.2.4 Cation doping of lithiated-transition-metal oxides

Several reports advocate for the substitution of the Mn^{3+} in the Mn_2O_4 octahedron of $LiMn_2O_4$ spinel with divalent or trivalent cations as a solution for preventing this

material from deteriorating during charging or discharging [76, 77, 78]. The decay of $LiMn_2O_4$ at high temperatures and at deep charge/discharge voltages is associated with the following: (a) uneven distribution of Li^+ in $[Mn_2O_4]$, (b) surface disproportionation reaction of manganese ($2Mn^{3+} = Mn^{2+} + Mn^{4+}$), and the Jahn-Teller distortion due to the high-spin Mn^{3+}. This results in the loss of manganese in the electrolyte and lattice instability. Partial substitution of Mn^{3+} with other cations such as Co, Zr, Ni, Mg, etc. lowers the amount of manganese in the structure. A cation that results in a stronger M-O (M=Co, Ni, Zr, Mg, etc.) bond than the Mn-O bond imparts better structural stability. Xiong et al. reported that an average manganese valence of ≥ 3.6 is required to restore the capacity of the materials during cycling [79].

The partial substitution of manganese with Co and Ni has been largely recommended for retaining the electrochemical performance of $LiMn_{2-x}M_xO_4$ (M=Co, Ni) [80, 81, 82]. Wei et al. found that the average valence of manganese in $LiMn_{2-x}Ni_xO_4$ increases with nickel content. Moreover, some Ni ions occupy the 8a sites when the concentration of Ni reaches 20% of manganese (i.e., $x \geq 0.4$) [83]. Nickel-doped Li-Mn-O (LiNiMnO) nanosheets were prepared by Zhang and co-workers. Improved cyclic performance was observed as compared to the un-doped counterpart. The LiNiMnO nanosheets retained 81% of their practical capacity (i.e., 113.27 $mAhg^{-1}$) on their 500^{th} cycle [84]. The substitution of manganese by cobalt (Co) has also been predominantly investigated to lessen the deterioration of Li-Mn-O spinel during cycling. The solid-state reaction route was employed to prepare a Co-doped Li-Mn-O spinel with enhanced electrochemical performance. In 20 cycles, the capacity of $LiMn_{2-x}Co_xO_4$ ($0 \leq x \leq 0.5$) only dropped by 1% and less, while the un-doped counterpart lost about 28% of its capacity [85].

Furthermore, the importance of partial substitution was also cemented by the replacement of a small amount of nickel in layered $LiNiO_2$ with Co and Mn to form $LiNi_{0.6}Co_{0.2}Mn_{0.2}O_2$, in which deep cycling stability was achieved, which is in contrast to the un-doped structure [86]. This evidences the capability of cation doping in affecting the performance and properties of a number of cathode materials. In manganese-rich positive electrode materials suffering capacity decay, such as $LiMn_2O_4$, doping with a trivalent cation could reduce the amount of Mn^{3+} that causes manganese dissolution due to Jahn-Teller distortion and the disproportional reaction of manganese ($2Mn^{3+} \rightarrow Mn^{2+} + Mn^{4+}$). An appropriate substitution of a certain amount

of Mn^{3+} by the same amount of a trivalent cation could ensure structural stability and superior cycling performance. Moreover, the capacity attenuation could also be lessened [87, 88, 89].

1.2.5 Nanosized electrodes in lithium-ion batteries

LIBs have been extensively remarkably successful in the market for PEDs but are yet to make an impact in large-scale applications such as electric vehicles (EVs) or hybrid electric vehicles (HEVs) [18, 16, 90]. They are falling short in the latter market due to high costs and inferior energy and power density. The electrochemical performance of the electrode materials could be significantly enhanced by taking advantage of the appealing properties of nanomaterials. The short diffusion path and high electrolyte/electrode contact area of nanostructured electrode materials can improve the rate capability and power density of the battery. Moreover, the cyclic performance could also be improved as a result of the enhanced ability of nanostructured electrodes to deal with strain during a charge or discharge process [91, 92, 93]. Hence, the engineering of novel nanosized positive electrode materials coupled with cation doping can effectively better the electrochemical performance of LIBs.

A layered $LiNi_{1-x}M_xO_2$ (M = transition metal) positive electrode composed of nanosized primary particles yielded higher-rate capabilities than its bulk counterpart [94]. In a study by Kim and co-workers, bulk and nanostructured Li_2MnO_3 and $LiNi_{0.5}Mn_{0.3}Co_{0.2}O_2$ electrodes were generated and compared using a high-energy ball mining approach. The nanostructured electrodes displayed superior discharge capacitance and structural stability when compared to their bulk counterparts [95]. The glycine-nitrate process was employed to synthesise a nanosized $LiMn_2O_4$ spinel made up of primary particles of 10 nm. The nanostructured spinel electrodes could yield capacity > 57 $mAhg^{-1}$ at a 2.44 mA cm^{-2} (10 C) discharge rate, showing their high-rate capabilities [96]. As such, nanotechnology will be instrumental in accelerating the advancements of lithium-ion batteries to meet the growing energy needs.

1.2.6 Derivation of Interatomic potentials for classical simulations

Methods that determine the potential energy surface (PES) from the Kohn-Sham theory of electron density (Density Functional Theory) are improving in terms of accuracy and simulation time [97, 98]. However, compared to large-scale atomistic

simulations, these methods are still limited in handling systems containing more than thousands of atoms for longer simulation times (~nanoseconds) [99, 100, 101]. Atomistic simulations such as molecular dynamics (MD) rely on interatomic potentials (IAPs) to determine the energy of interaction [102, 103, 104, 105, 106]. IAPs are an approximation of the electronic potential energy as given by Schrodinger's equation, and they depend on the atomic coordinates. Moreover, IAPs scale linearly with the number of particles and, hence, allow studies of the microstructure of complex systems. The behaviour of all matter can be indirectly or directly inferred from the interaction of atoms through atomic forces. Therefore, properties such as temperature, hardness, and pressure, which are linked to the interatomic forces, can be explored through MD simulations at the microscale. Furthermore, IAPs allow for investigation of the movement of Li^+ ions in battery materials and the essential structural peculiarities such as vacant lattice sites, occupied interstitial sites, interconnections of crystal grains in polycrystalline materials, stacking faults, etc., which are the essential matrix for lithium-ion battery performance [107, 108, 109].

IAPs are usually expressed as an expansion of a set of functions that depends on atomic positions. The functions also contain parameters that uniquely describe the interaction in question and are attained by fitting to structure information (elastic constants, bulk modulus, shear modulus, poisson's ratio, etc.). The data could be elastic constants that are related to the interatomic forces. The potential functions are designed to capture interactions such as the coulombic interaction emanating from charged ions, the Van der Waals interaction, which is due to instantaneous dipole moments, and Pauli's Exclusion Principle. IAPs are essential for the exploration of microstructural changes underpinned by the interactions of thousands of atoms, which impact electrochemical performance. The IAP function utilized in this study is discussed in detail in chapter 2. The accuracy of large-scale atomistic simulation hinges on the underlying IAP function. Hence, a substantial amount of attention has been directed towards attaining accurate interatomic potentials through nesting, designing new functions, or machine learning [110, 111].

1.2.7 Structural description of lithium-transition-metal-oxide ($LiTM_2O_4$) spinel

The promising cathode material for lithium-ion batteries, LiM_2O_4 (M=Mn, Co, Ni), crystallises into a spinel-type structure with a space group of Fd-3m. The cubic

$LiMn_2O_4$ consists of oxygen atoms in an ordered cubic-close arrangement, in which lithium atoms are situated at the 8a tetrahedral sites and the transition metal (TM) atoms are situated at the 16d octahedral sites, as illustrated in Figure 1.3 [112, 113, 114]. The cubic-closed, packed array of oxygen atoms provides the three-dimensional channels that allow the insertion and extraction of lithium ions.

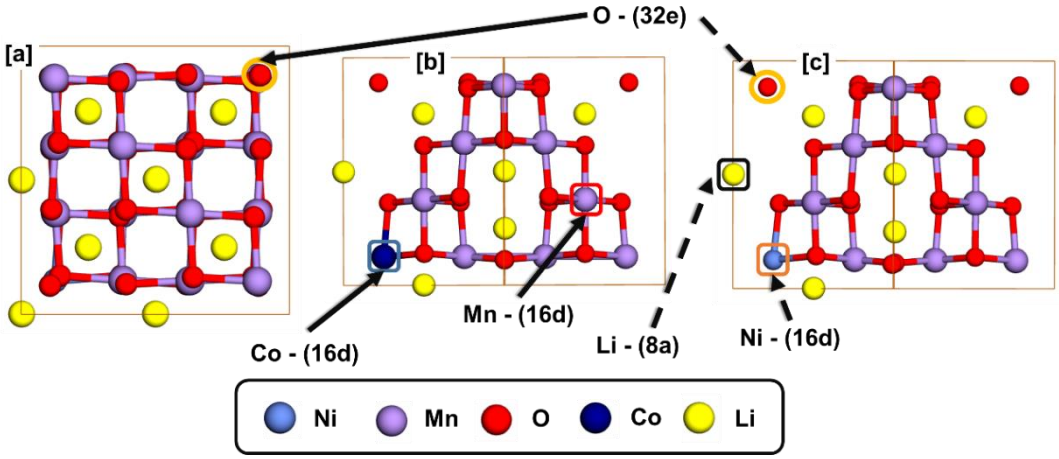

Figure 1.3: (a) Co- and (b) Ni-doped Li-Mn-O spinel conventional unit cells. Manganese (cyan), cobalt (dark blue), nickel (royal blue) atoms are situated at the 16d octahedral site, lithium atoms (yellow) are occupying the 8a site and oxygen atoms (red) are occupying the 32e sites.

Table 1.1: Structural properties of spinel $LiTM_2O_4$ (TM=Mn, Co and Ni).

Property	**$LiMn_2O_4$**	**$LiCo_2O_4$** [115]	**$LiNi_2O_4$** [116]
Lattice parameter(Å)	a=8.24 [117, 118]	a=8.05	a=8.04
Crystal lattice ($Å^3$)	cubic	cubic	Cubic
Space group	Fd-3m [119]	Fd-3m	Fd-3m

1.3 Intentions of the study

$LiMn_2O_4$ spinel is currently attracting sizable interest as a viable replacement for the toxic and expensive layered $LiCoO_2$ cathode material for lithium-ion batteries [120, 121]. $LiMn_2O_4$ spinel has a three-dimensional crystal structure that facilitates the easy movement of lithium ions. Moreover, it provides high cycling voltages, is

environmentally benign, possesses acceptable thermal stability, and is affordable due to the abundance of manganese [122, 123]. Hence, it is deemed one of the most promising positive electrode materials for improving the performance of LIBs, as required for application in revolutionary EVs or HEVs and to match the exponential technological advancement [124, 125, 126, 127]. However, $LiMn_2O_4$ spinel exhibits poor cycle performance, especially at deep discharge states and at elevated temperatures due to irreversible structural changes. The changes are attributed to Mn dissolution due to the disproportionation reaction [128], phase transformation [129], and lattice instability [130] associated with the Mn^{3+} Jahn-Teller ion. A significant amount of Mn^{3+} disproportionates into Mn^{4+} and Mn^{2+} ($2Mn^{3+} -> Mn^{4+} + Mn^{2+}$), wherein the Mn^{2+} ions at the surface dissolve in organic electrolytes, resulting in poor capacity retention [131, 132]. Moreover, a concentration of Mn^{3+} that is ≥ 50% leads to the onset of the Jahn-Teller distortion, which results in a cubic to tetragonal phase transformation. The phase change leads to a large volume change, which compromises the Li-Mn-O spinel structure [133, 134, 135].

First-principles studies have shown that the substitution of a small percentage of manganese in $LiMn_2O_4$ with cations such as Co, Ni, Al, etc. has a positive impact on the cyclic performance of this material [136, 137, 138]. Improved cyclic performance can be achieved by increasing the average valence of manganese in the structure to at least 3.5. This was found to lessen the number of the high-spin Jahn-Teller active Mn^{3+} ions in the structure [139, 140]. However, the effect of cation doping has been largely explored through density functional theory and traditional experimental studies. Investigations of intricate physical and chemical phenomena taking place at the microscale, stemming from interactions of a large number of atoms (> 1 000) at a practical cost, are currently possible through molecular dynamics (MD) methods [102, 103, 104]. Particularly transport properties and reversible and irreversible microstructural changes, which significantly affect electrochemical performance. The rate capabilities of a battery are largely influenced by the ionic conductivity and morphology of the electrode material [141]. High-rate capabilities are crucial for energy storage applications in electric vehicles and smart grids. Although the partial substitution of Mn with Ni, Co, Zr, etc. improves the stability and capacity retention of $LiMn_2O_4$, there's little to no information on how the doping affects the transport properties (i.e., diffusion, ionic conductivity, etc.) of the material. Such investigations

can be easily realised with MD simulations when compared to traditional experiments and first-principles approaches. However, a bottleneck to such MD studies is currently the lack of accurate interatomic potentials, particularly for interactions that arise from doping Li-Mn-O spinel with Ni and Co.

In this study, an approach inspired by machine learning techniques and the GULP code is employed to develop accurate interatomic potentials that arise from doping $LiMn_2O_4$ spinel with Co and Ni [142, 143]. $LiCo_2O_4$ and $LiNi_2O_4$ microstructures will be generated with MD simulations as a test for the derived interatomic potentials (Co-Co, Co-Li, Co-O, Ni-Ni, Ni-Li, and Ni-O). The microstructure will be analysed to provide insights into the structural stability of the material, which will be utilized to infer its durability and safety. Moreover, it will also shed light on the TMO_6 (M=Co, Ni) octahedron in comparison to the MnO_6 octahedron and, as such, provide guidance on the doping of $LiMn_2O_4$ with Co and Ni. Furthermore, the derived potentials will be utilized to elucidate the impact of the partial substitution of Mn with Co and Ni on the transport of Li^+ in $LiMn_2O_4$, which is currently not clear in literature. The transport of Li^+ in the structure impacts the cyclability and rate-capability, which are important requirements for large-scale applications (smart grids, electric vehicles, etc.). Additionally, the impact of the doping on the microstructure of $LiMn_2O_4$ will also be explored to provide knowledge of the stability of the material.

The study utilizes both first principles and classical mechanics methods. The derivation of the interatomic potential involves a method inspired by machine learning (ML) techniques and the General Lattice Utility Program (GULP) [142, 143]. The method was chosen since the lack of accurate interatomic potentials (forcefields) is actually exacerbated by the ambiguous derivation process, which is often defined as art rather than science. The process for finding parameters of an interatomic potential function to obtain a description of the interactions in a material involves fine-tuning the starting parameters until they yield structure properties (elastic constants, shear modulus, poisson's ratio, bulk modulus, etc.) that are comparable to the fitted structure properties. However, the potential parameters that are initially supplied have a significant influence on the finally refined parameters. Therefore, the initial potential parameters should at least constitute some sort of relationship with the physical or chemical characteristics of the interaction to be described. Therefore, the ML-inspired approach is used to find initial potential parameters that are linked to the behaviour of

the interaction to be described from a potential energy surface computed from the DFT electron density. Finally, the preliminary potential parameters are refined with the GULP code in spinel systems. This method facilitates the development of accurate interatomic potentials that incorporate a DFT level of accuracy to a certain degree.

Furthermore, the well-researched atomistic simulation technique, simulated amorphization and recrystallization (A&R), will be used to simulate the microstructure of $LiCo_2O_4$ and $LiNi_2O_4$ to test the derived interatomic potentials [71]. The A&R technique is essential for generating structures with myriad microstructural features that affect electrochemical performance and are also noted in experiments. As such, the method is crucial for probing microstructural changes and their impact on electrochemical performance. Moreover, the A&R technique will also be employed to generate Co- and Ni-doped $LiMn_2O_4$ nanostructures, which will be utilized to investigate the impact of doping on Li^+ transport. Moreover, the resulting nanostructures will be characterised and analysed through radial distribution functions (RDFs), atomic-level structural snapshots, and x-ray diffraction (XRD) patterns. Furthermore, the synthesized spinel nanostructures will be compared to theoretical models for validation. The impact of doping the spinel $LiMn_2O_4$ structure with Co and Ni on electrochemical properties and structural integrity will be examined to aid in the design of safe, affordable, high-energy, and high-power positive electrode materials. The developed Ni-Ni, Ni-Li, and Ni-O Buckingham potentials will be further tested by generating nanoporous structures of $LiNi_2O_4$ to probe the impact of pore size on electrochemical performance.

1.4 Hypothesis

The study aims to provide insights that will improve the performance of $LiMn_2O_4$ spinel, which suffers structural degradation due to lattice instabilities largely caused by the Jahn-Teller distortion and the disproportionation reactions of Mn^{3+} [89, 144, 145]. The structural instabilities can be lessened by decreasing the number of Mn^{3+} ions in the $LiMn_2O_4$ spinel structure and strengthening the mean transition metal (TM)-oxygen (O) bond length. This can be achieved by substituting a small amount of Mn^{3+} ions with cations, which will increase the mean valence of manganese in the structure. As such, cations such as Co^{3+} and Ni^{3+} can increase the mean valence of manganese in the material and strengthen the TMO_6 framework due to their smaller ionic radius of 0.55 Å and 0.53 Å, respectively, compared to the ionic radius of 0.645 Å of Mn^{3+} [146, 147].

Moreover, the bond energies of Co-O and Ni-O are higher than the bond energy of the Mn-O interaction [148, 112]. Moreover, the introduction of Co and/or Ni in the spinel structure may also influence the transport of Li^+ in the structure, since a more stable TMO_6 framework will provide more room for migration of these ions in the structure. Therefore, the $LiMn_2O_4$ can be stabilized with the partial substitution of Ni and/or Co, which will curb the structural degradation during cycling and hence improve its cyclic performance.

1.5 Outline of the study

Chapter 1 captures the current state of LIBs, their advantages, hindrances, and solutions to the outlined problems. Additionally, the structural properties of the spinel systems investigated in this work have also been detailed in this chapter. In chapter 2, the methods used to perform this study are briefly discussed. The theory and the importance of these methods are concisely captured. In chapter 3, we discuss the development of Buckingham interatomic potentials for the potentials emanating from the partial substitution of Mn with Ni in $LiMn_2O_4$. The development process and the results of testing the Buckingham interatomic potentials have been fully discussed. The developed potentials were further tested through large-scale simulations of $LiNi_2O_4$ and $LiCo_2O_4$ to provide insights on the doping of $LiMn_2O_4$ spinel with Co and Ni, this is discussed in chapter 4. The effect of doping $LiMn_2O_4$ spinel with Co and Ni at the microscale is detailed in chapter 5. In chapter 6, the developed Ni-Ni, Ni-Li, and Ni-O have also been tested on the simulation of the nanoporous $LiNi_2O_4$ spinel structure. The chapter discusses the effect of nanostructuring on the transport properties of the $LiNi_2O_4$ spinel material. Chapter 7 provides a brief discussion of all the findings of this work. The formulated solutions and recommendations are also discussed.

CHAPTER 2

Research Methodology

The chapter details all the methods utilized to carry out the current study. The study employs the Fritz Haber Institute ab initio molecular simulations (FHI-aims) code [149] based on Density Functional Theory (DFT) to model the potential energy surface of Co-O, Co-Co, Co-Li, Co-Mn, Ni-O, Ni-Ni, Ni-Li, Ni-Mn, and Ni-Co interactions. The latter potential surfaces, coupled with chosen first-principles calculated elastic properties, will be fitted using the General Utility Lattice Program (GULP) [142] to derive the required empirical interatomic potentials. The derived interatomic potentials will be used to carry out atomistic molecular dynamics (MD) [150] simulations. Moreover, Co, Ni, Cr, and Zr doped $LiMn_2O_4$ nanoarchitectures will be generated using the MD simulated amorphization and recrystallization technique [71].

2.1 Density functional theory (DFT)

Density functional theory (DFT) is a quantum mechanics-based theory that is significantly used in studies of organic and inorganic materials owing to its low computational cost and accuracy in finding the solution of Schrödinger's equation [151, 152]. DFT gives the approximate solution of the chief quantum mechanics equation, Schrödinger's equation. Kohn and Hohenberg formulated the many-body approximate solution of Schrödinger's equation based on two theorems [153]. The first theorem postulates that the properties of a system at its lowest energy state are uniquely defined by a three-dimensional (*x, y, z*) electronic density. As such, the complicated physical interaction between electrons can be deduced from this electronic density. The second theory indicates that the correct electronic density minimizes the entire energy of the systems based on an unknown functional, the exchange-correlation energy functional [153]. As such, the accuracy of the results significantly depends on the approximation method of the exchange-correlation energy functional. Moreover, the whole energy of a system can be linked to the Kohn and Hohenberg single-electron density $n(\boldsymbol{r})$ represented by single-electron wave functions $\psi_i(\boldsymbol{r})$, which can be written as:

$$E[\{\psi_i\}] = E_{known}[\{\psi_i\}] + E_{XC}[\{\psi_i\}], \quad (2.1)$$

The $E_{known}[\{\psi_i\}]$ represents the known energy contribution and $E_{XC}[\{\psi_i\}]$ is the contribution due to the unknown functional. The known energy contributions can be expounded mathematically as:

$$E_{known}[\{\psi_i\}] = \frac{h^2}{m}\sum_i \int \psi_i^* \nabla^2 \psi_i d^3\boldsymbol{r}_i +$$

$$\int V(\boldsymbol{r}_i) n(\boldsymbol{r}_i) d^3\boldsymbol{r} + \frac{e^2}{2}\iint \frac{n(\boldsymbol{r}_i) n(\boldsymbol{r}_j)}{|\boldsymbol{r}_i - \boldsymbol{r}_j|} d^3\boldsymbol{r}_i d^3\boldsymbol{r}_j. \quad (2.2)$$

The $E_{known}[\{\psi_i\}]$ energy is equal to the electronic energies, the Coulomb interaction describing the nuclei and electronic interaction, the Coulombic interactions between, and the Coulombic nuclei-nuclei interactions, respectively, as indicated on the right side of equation 2.2. Kohn and Sham demonstrated that the use of single-electron wave functions can simplify the daunting task of finding the true electronic density through exchange-correlation approximation methods. The Kohn-Sham equations thus take the form:

$$\left[\frac{h^2}{m}\nabla^2 + \mathrm{V}(\boldsymbol{r}_i) + V_H(\boldsymbol{r}_{ij}) + V_{XC}(\boldsymbol{r}_i)\right]\psi_i = \varepsilon_i \psi_i(\boldsymbol{r}_i). \quad (2.3)$$

The $\mathrm{V}(\boldsymbol{r}_i)$ potential is due to the nuclei and electron interaction, $V_H(\boldsymbol{r}_{ij})$ is due to the Coulombic repulsive interaction between the electrons, and $V_{XC}(\boldsymbol{r}_i)$ defines the exchange-correlation, and is subtle defined as:

$$V_{XC}(\boldsymbol{r}_i) = \frac{\delta E_{XC}(\boldsymbol{r}_i)}{\delta n(\boldsymbol{r}_i)}, \quad (2.4)$$

where, δ represents the functional derivative [153]. The DFT approach is computationally feasible. The DFT solution revolves around probing the electronic density as a function of the three spatial coordinates rather than exactly solving Schrodinger's equation, which requires iterating the whole Hilbert space to find the appropriate wave function. It has made significant inroads spanning different areas, exploring the electronic structure of systems to predict their properties.

2.1.1 The approximation methods of the exchange-correlation functional

The postulation of Hohenberg, Kohn, and Sham showed that the minimum energy corresponding to the true electronic ground state depends on the exchange-correlation functional. As such, the solution of the Kohn-Sham equations requires a description of the exchange-correlation functional, which is unknown in its true form. However, if one can regard the electronic density as the same as the density of a uniform gas, the exchange-correlation functional of such a density can be defined exactly. At any given point in space, in such a scenario, the electron density is the same $\{n(\boldsymbol{r}) = constant\}$. As such, the Kohn-Sham equations can now be solved, wherein the exchange-correlation potential is set as one of a uniform electron gas in this manner:

$$V_{XC}(\boldsymbol{r}_i) = V_{XC}^{electron\ gas}[n(\boldsymbol{r}_i)] \tag{2.5}$$

This exchange-correlation functional approximation method uses the locality of the electron density of a gas. It exploits its uniformity, and it is therefore called the Local Density Approximation (LDA) [154, 155]. At last, the approximate solution to the Schrodinger equation is realized, however, in the absence of the exact exchange-correlation functional. The quest to find the exchange-correlation functional that is close to the exact functional has rendered this area one of the most important active areas of research. Consequently, different exchange-correlation functionals have been developed, one popular functional after LDA is the generalized gradient approximation (GGA). This functional incorporates a bit of information about the previous density compared to the local density for a more precise definition of the exchange-correlation functional. This may suggest that GGA yields more accurate results than the LDA functional. However, tragically, the complexity brought about by the different ways in which the gradient can be updated results in a number of GGA functionals. The Perdew-Burke-Ernzerhof (PBE) and the Perdew-Wang (PW91) functionals are widely adopted GGA functionals [156, 157]. The choice of a functional relies on the type of property, calculation, or material under study.

2.1.2 Plane-wave pseudopotential method

2.1.2.1 Plane-wave basis set

The electronic function of a periodic solid can be written as the product of the periodic part of the cell and the wavelike part, as stated by the Bloch's theorem [158],

$$\varphi_i(\boldsymbol{r}) = \mathrm{e}^{\mathrm{i}\mathbf{K}.\boldsymbol{r}} f_i(\boldsymbol{r}). \tag{2.6}$$

The periodic part of the cell can be written as follows,

$$f_i(\boldsymbol{r}) = \sum_{\boldsymbol{G}} c_{k,\boldsymbol{G}} \mathrm{e}^{i\mathbf{G}.\boldsymbol{r}}, \tag{2.7}$$

wherein, the wave function is represented by a set of discrete plane waves. Moreover, the wave vectors are the reciprocal lattice vectors $\boldsymbol{G}$ of the crystal. The reciprocal lattice vector is defined as $\boldsymbol{G} = \frac{2\pi m}{l}$, where l defines the lattice vector. Therefore, the electronic wave function may be written as a summation of plane waves,

$$\varphi_i(\boldsymbol{r}) = \sum_{G} c_{i,\boldsymbol{K}+\boldsymbol{G}} \mathrm{e}^{i(\boldsymbol{K}+\boldsymbol{G}).\boldsymbol{r}}. \tag{2.8}$$

In principle, the representation of the electronic function in this manner requires an infinite number of plane waves. However, the plane waves with higher kinetic energy $(\hbar^2/2m)|\boldsymbol{K}+\boldsymbol{G}|^2$ for the coefficients $C_{i,\boldsymbol{K}+\boldsymbol{G}}$ are less important than those possessing low kinetic energy. This then provides a way to only include the plane waves with less kinetic energy based on some cutoff energy. The introduction of cutoff energy to the discrete plane waves representing the electronic wave functions yields a defined basis set. However, the shortening of the plane-wave basis set at a given cutoff energy will yield spurious total energy, wherein increasing the cutoff energy could lessen the error. Another setback of this approach is that the tally of basis states is not continuous with the cutoff energy. A denser k-point set can be employed to remedy this problem, and if the problem persists, a better solution is to opt for a pseudopotential approximation.

2.1.2.2 Pseudopotentials

The representation of the electronic function with a set of discrete plane waves, as stated by Bloch's theorem [158], fails in cases where the tightly bound centre orbitals and the speedy oscillations of the waves that describe the valence electrons in the centre region are to be captured, as it requires a large number of plane waves. As

such, an all-electron calculation with a huge plane-wave basis set would require a massive amount of computational time. The electronic wave functions can be written using fewer plane waves. It is well known that core electrons have little to no effect on most physical properties of materials compared to valence electrons. The valence electrons have a greater effect on most material properties. As such, the pseudopotential approach exploits this by disregarding the contribution of the core electrons and replacing it with a spurious pseudopotential that is projected onto a set of pseudo-wave functions instead of the true valence wave functions [159, 160]. Figure 2.1 illustrates the all-electron and the pseudo-electron wave functions and their respective potentials. In the area where the core electrons reside, the wave function of the valence electrons oscillates rapidly. This ensures the orthogonality between the valence wave functions and the core wave functions, as required by the exclusion principle. The construction of the pseudopotential guarantees that the movement of the scattering properties or the change in phase is the same for those ions and the electrons at the centre of the wave functions of the valence electrons. The pseudopotential is generally defined as,

$$V_{NL} = \sum_{lm} |lm > V_l < lm|, \tag{2.9}$$

where $|lm >$ defines the spherical harmonics and the pseudopotential for the angular momentum (l) is given by V_l.

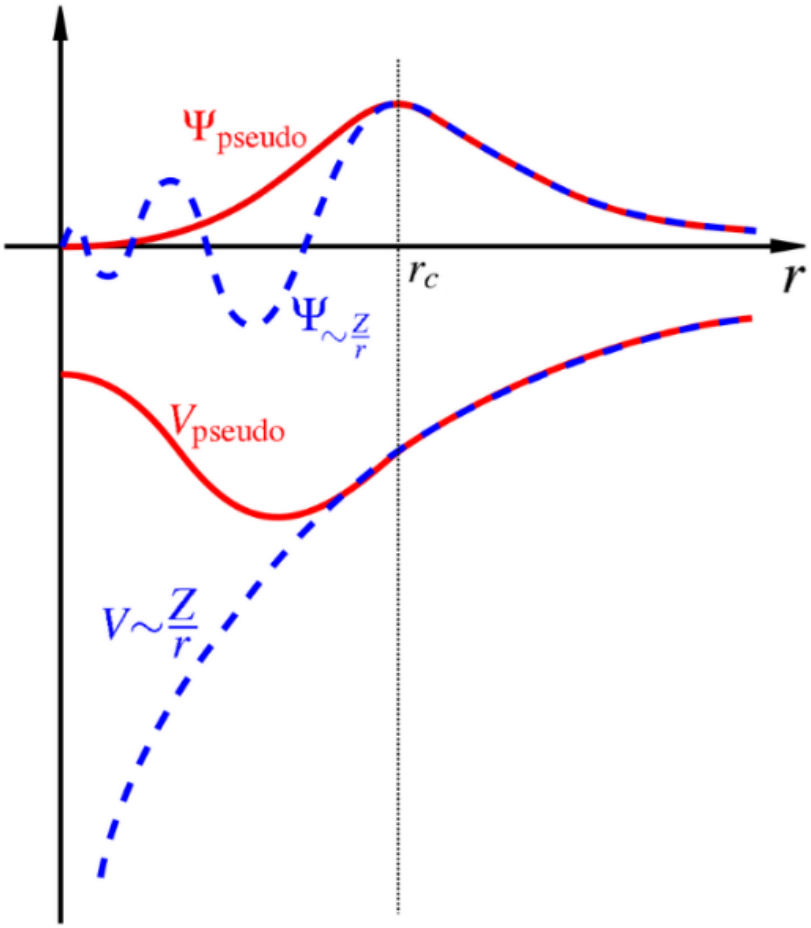

Figure 2.1: The wavefunction due to the real potential (blue) and the pseudopotential (red). The Coulomb and pseudopotential wavefunctions are equal at a given cut-off radius r_c [161].

2.1.2.2.1. Norm-conserving pseudopotentials

In a norm-conserving pseudopotential, the pseudo-wave functions and their respective potentials are constructed such that they are similar to the actual valence wave functions outside some core radius, r_c. However, inside this radius r_c, the wave function of the pseudoelectron is found to be different from the true wave function per the norm-conserving construction. This is required so that the desired accurate exchange-correlation energy can be obtained. Local and non-local pseudopotentials capable of correcting even superior-order energy reliance of the scattering are called ab initio or nom-conserving. Moreover, they are efficient in defining the scattering linked to a variety of ionic environments [162, 163].

2.1.3 DFT based simulation codes employed in the study

2.1.3.1 Fritz Haber Institute ab initio molecular simulations (FHI-aims)

The FHI-aims code is a software package for simulating the behaviour and properties of various molecules and materials, largely used by the computational chemistry and physics communities [149]. It is predominantly based on the DFT of Kohn-Sham equations and perturbation theory [164, 165, 166]. The code utilizes the all-electron true potential with numeric atom-centered basis functions in order to achieve a high-level electronic structure description. A significant number of atoms can be handled by the program to yield very reasonable accuracy at a reasonable computational cost. FHI-aims was developed at Duke University, TU Munich, USTC Hefei, Aalto University, the University of Luxembourg, TU Graz, Cardiff University, etc. The FHI-aims code makes use of numeric atom-centered orbital (NAO) basis functions, which allow for the generation of optimized basis sets that yield high accuracy. O (N) scaling with system size for large systems is achieved by strictly separating different spatial regions from one another [167, 168, 169]. FHI-aims is one of the ab initio codes that can predict the properties of unknown materials in the absence of any clues or input from experiments. It is generally used to calculate material structure, mechanical, magnetic, optical, and numerous other intricate properties. In this work, it is used to calculate the potential energy surface of the interactions that arise from doping Li-Mn-O spinel with Co and Ni to guide the development of the interatomic potentials of these interactions.

2.1.3.2 Vienna Ab initio Simulation Package (VASP)

The Vienna Ab initio Simulation Package (VASP) is a quantum chemistry code largely based on DFT. The VASP code yields an approximation of the many-body Schrodinger's equation as outlined by Walter Kohn and Lu Jeu Sham [166]. Moreover, the electronic density is represented by plane wave basis functions, and pseudopotential functions such as the Projector-Augmented-Wave (PAW) method, norm-conserving, or ultrasoft are used. The code is primarily utilized in material science, metallurgy, etc. to calculate the electronic structure and properties of various organic and inorganic materials [170, 171, 172]. In this work, we are going to use it to

compute the mechanical properties (elastic constants, bulk modulus, and young's modulus) required for fitting interatomic potentials with the GULP code [142].

2.2 Molecular dynamics

Molecular dynamics (MD) simulation methods are based on statistical mechanics aimed at calculating the equilibrium and dynamic properties of a large-scale system. MD simulation allows for a detailed atomic snapshot of the system's microstate at a given time and space. The atomic dynamics can elucidate the thermally accessible states of the system. As such, the dynamics of molecules are essential in determining the behaviour and properties of materials. The basic idea of MD is to determine the spatial trajectory of a system under the influence of a given force field using Newton's equation of motion [173, 174]. The classical equations of motion for a simple atomic system can be expanded as follows:

$$m_i \ddot{\boldsymbol{r}}_i = f_i, \tag{2.10}$$

$$f_i = -\frac{\partial}{\partial r_i} \boldsymbol{U}. \tag{2.11}$$

where m denotes the mass of the atoms and $\boldsymbol{r}_i$ denotes the three spatial coordinates of each atom. The forces acting on the atoms are determined by the potential energy $\mathcal{U}(\boldsymbol{r}^N)$, where $\boldsymbol{r}^N$ is the whole set of 3N atomic coordinates. The results of molecular dynamics simulations are as good as the underlying force fields, especially the mechanical description of the structure. An optimal initial configuration corresponding to a minimum potential energy surface guided by experiments is encouraged to start an MD simulation. The velocity of the species is set to a value that ensures that their kinetic energy E_k is in line with the target temperature T. Following the equipartition theorem for each $\frac{k_B T}{2}$ normal mode, at thermal equilibrium. We can then write:

$$\sum_{i,a} m \boldsymbol{v}_{i,a}^2 = (N_F k_B T)/2, \tag{2.12}$$

wherein the degrees of freedom in the system are given as N_F.

2.2.1 The potential model

The potential model offers a description of the energy of the system at a given point and time based on the atomic coordinates of the atomic species with respect to their atomic positions. The interatomic or intermolecular potentials are defined by a set of mathematical functions, in which appropriate input parameters are obtained by fitting the mathematical functions to significant experimentally generated lattice properties, such as lattice constants. Such an approximation of the atomic or molecular potential as implemented in molecular dynamics or Monte Carlo simulations overcomes the system size constraint faced by quantum mechanics-based electronic structure methods. A trajectory of a system comprising a vast number of atoms can be successfully followed with a molecular dynamics simulation, wherein numerical methods are employed to compute the system's properties.

2.2.2 Born model of ionic solids

In classical simulation, a crystal is seen as composed of formally charged ionic spheres exhibiting infinite atomic arrangement. This is known as the Born model of ionic solids, therefore, such a crystal can be described by the potential model. The interatomic or intermolecular potential between the interacting atoms or molecules can be expressed as a function of their atomic positions. The long-range energy of two interacting ionic spheres, regarded as point charges, is given by:

$$U_{ij} = \frac{1}{4\pi\varepsilon}\frac{q_i q_j}{\boldsymbol{r}ij} + \phi(\boldsymbol{r}_{ij}), \tag{2.13}$$

where U_{ij} gives the contribution due to interacting between two ionic spheres and $\phi(\boldsymbol{r}_{ij})$ denotes the short-range interaction. Moreover, ε represent the permittivity of the vacuum, q_i and q_j representing the point charges denoting the ionic spheres, and the separation distance as $\boldsymbol{r}_{ij}$. The accuracy of the results depends on the short-range interaction since the electrostatic energy is predefined [175, 176].

2.2.2.1 Buckingham potential

The Buckingham potential is a mathematical formulation by Richard Buckingham that describes the potential felt by two interacting atoms outside their bond length. The potential function describes the Van der Waals energy and captures the Pauli

Exclusion Principle. Richard Buckingham used an exponential function to represent the repulsion, which becomes stronger for values of r (the distance between the interacting atoms) that are less than the bond length. The Buckingham potential is expressed as:

$$V(r) = Ae^{-Br} - \frac{\lambda}{r^6}, \tag{2.14}$$

wherein Ae^{-Br} denotes the nuclear-nuclear repulsion and the $-\frac{\lambda}{r^6}$ represents the attraction. This contributes to the representation of the bond length of the interacting atoms [177]. The Buckingham potential is widely adopted in many large-scale atomistic simulations, in which comparable results to experiments were obtained. However, this potential fails at describing interactions that take place near-zero separation, since the exponential part of the Buckingham potential extends to a finite value as r approaches zero, while the attraction term extends to infinity. MD simulation codes such as DL_POLY [178] that make use of this potential function can detect this condition when it occurs and automatically inhibit its un-physical nature at atomic separation values r that are near zero. Another potential function that is widely adopted in Monte Carlo or MD simulations is the Lennard-Jones potential [179, 180], commonly written as:

$$V(r) = 4\epsilon\left[\left(\frac{\sigma}{r}\right)^{12} - \left(\frac{\sigma}{r}\right)^{6}\right], \tag{2.15}$$

or as expressed as:

$$V(r) = \frac{A}{r^{12}} - \frac{B}{r^6}, \tag{2.16}$$

where, ϵ describes the strength of the bond between the two atoms, and σ is the value of r at which V is zero. The London dispersion forces are estimated by the $-\frac{B}{r^6}$ term and the nuclei-nuclei repulsion is described by the $\frac{A}{r^{12}}$ term, wherein the values of A and B are based on the atoms under study and are obtained by fitting to experimental data.

2.2.3 Statistical ensembles

The intricate systems of statistical mechanics possess a wide range of properties that depend on the state of the system at a given time. These states are equally probable

and represent a copy of the system at a certain time with properties based on the constraints imposed on the system. The copies of the systems are called ensembles, and they are required before one can invoke the probability function. In a statistical ensemble, thermodynamic properties such as energy, temperature, and pressure can be controlled to obtain a specific simulation environment. In this work, we employ the micro-canonical and the canonical ensembles. A micro-canonical ensemble is viewed as having isolated systems that possess the same energy, wherein the energy of each system in the ensemble lies within E and $E + \Delta E$. This ensemble is characterized by constant particles (N), volume (V) and energy (E). The trajectory of the micro-canonical ensemble can be viewed as an exchange between the potential energy and the kinetic energy, but the total energy is not changed. It follows the conservation of energy. However, there exists the canonical ensemble, which can be viewed as a system in contact with a heat bath such that different microstates can have different energies. This ensemble is characterized by a constant number of particles (N), volume (V) and temperature (T) [181, 182].

2.2.4 Amorphization and recrystallization (A&R) technique

The amorphization and recrystallization technique [71] is a MD synthesis technique used to introduce complex structural features that are observed in materials from experiments to simulated models. The amorphization process is the onset of the technique, in which the system is heated in a statistical micro-canonical ensemble to yield an amorphous (unstable) structure characterized by a loss of long-range atomic ordering. Following the latter process is the recrystallization process, which is carried out in a canonical ensemble. As the energy is allowed to change in this ensemble, the atoms in the system occupy atomic positions, which yield low energy configurations, resulting in a polycrystalline or crystalline structure. The simulated amorphization and recrystallization technique has been widely used due to its capability to generate complex structures from which a number of properties can be obtained. The technique afforded researchers a chance to simulate structures containing features that are observed experimentally. Consequently, the generated structures are instrumental to insightful findings. Essential microstructural features evolve as the simulated recrystallization process proceeds. The technique can capture microstructural peculiarities such as grain boundaries, point defects, dislocations, etc. Such structural

features are deemed essential as they affect the performance of various materials in different application areas [183, 75, 74, 184].

2.2.5 Simulation codes based on force fields

2.2.5.1 DL_POLY

DL_POLY is a large-scale atomistic MD simulation code capable of running segments of its code on a wide range of high-performance parallel computers due to its built-in parallel algorithms. The code can simulate systems containing a smaller number of atoms to systems with millions of atoms. The simulated amorphization and recrystallization technique will be employed to generate pristine and doped spinel Li-Mn-O nanostructures required for structural analysis in this work [178]. Moreover, the technique has been successfully and extensively used [183, 75, 74, 184].

The General Utility Lattice Program (GULP) is a force field-based method widely used to fit interatomic potentials, fitting to energy surfaces, and empirical data. It has been extended to solving condensed phase problems for systems with various boundary conditions [142]. The code focuses on lattice dynamics to provide analytical solutions with various force fields based on the shell model of ionic solids. In the current work, it will be utilized in fitting empirical interatomic potentials of Co, Ni, Cr, and Zr to be incorporated into spinel $LiMn_2O_4$.

2.3 Analytical procedure

2.3.1 Crystallographic defects

The regular, ordered arrangement of atoms in a crystal does not extend perfectly through the crystal in real materials. Hence, materials comprise significant deformations, some arising during cooling as a function of temperature or high-energy radiation, resulting in imperfect crystals. This leads to materials showing distinctive behavioural patterns due to these imperfections. Various material properties (mechanical, optical, and electric properties) are affected differently by different types of defects [185, 186]. The crystal deformation or imperfection can occur on the surface, on a lattice point, or along the lines of the crystal, and they are respectively called surface, point, and line defects. Crystal defects such as vacancy, substitution, and interstitial defects fall under the category of point defects. Point defects heavily affect

the conductivity of electricity and heat in materials. The effect also varies from one material type to another. In semiconductors, substitutional defects are the major influencers of electronic conductivity. In electrode materials, vacancy defects are appreciated due to their contribution to providing extra intercalation sites. Moreover, the mechanical properties of different materials can be fine-tuned through crystallographic defects [187, 188, 189, 190].

2.3.1.1 Surface defects

Materials are formed by a variety of crystal grains with different orientations joined together by grain boundaries. The joined crystal grains, oriented differently, form a polycrystalline material, as shown in figure 2.2. Moreover, atoms in a single crystal exhibit long-range atomic ordering that extends through the crystal [191, 192]. Grain boundaries are surface defects, and they can discontinue the motion of line defects. They can control the mechanical properties of materials, particularly metals. In a case where two crystals possessing different orientations are joined by a grain boundary, the grain boundary is called a high-angle boundary, and when their orientation is similar but not the same, the grain boundary is called a low-angle boundary [193, 194].

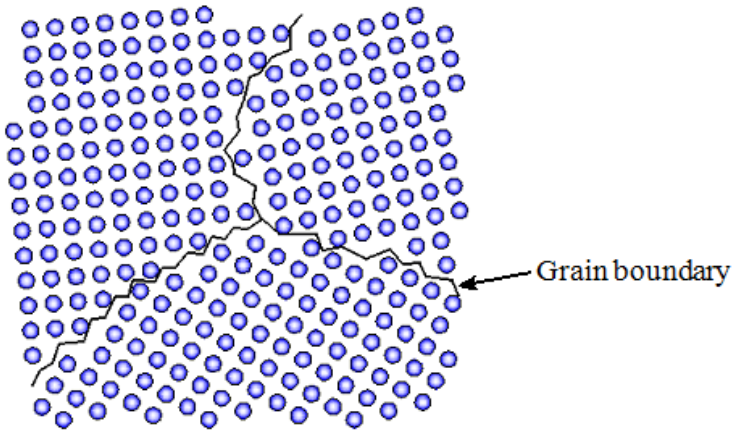

Figure 2.2: Demonstration of a crystal comprising of grain boundary surface defect [195].

2.3.1.2 Point defects

The disruption of the regular lattice arrangement by displacement of atoms from their lattice positions into interstitial positions or a mere absence of an atom on a lattice site falls under the category of point defects. The disruption of the lattice arrangement by

the absence of an atom or atoms in a lattice site is called a vacancy defect, which results in a misalignment in the atomic position of the surrounding atoms. The vacancy defect can form during plastic formation or other processes that alter the shape of a crystal and also during crystallization from a molten substance [196, 197]. Furthermore, the displacement of an atom from its lattice position into sites that are normally unoccupied forms an interstitial lattice point defect. Interstitial point defects generally occur in small concentrations and can be as a result of added impurity (foreign atom) or one of the atoms (self-interstitial) occupying an interstitial site. Moreover, the defect that forms when an atom occupies a position normally occupied by a different atom is called substitution. Other point defects also include the Frenkel and Schottky defects. A Frenkel defect occurs when an ion moves from its normal lattice position into an interstitial site, resulting in a vacancy and an interstitial point defect (vacancy-interstitial), as illustrated in figure 2.3. A Schottky defect occurs in a material consisting of ionic bonds, where a cation and an anion are missing from their lattice positions to maintain charge neutrality. A similar situation is shown in figure 2.4, where a lattice is strained due to a cation or anion vacancy.

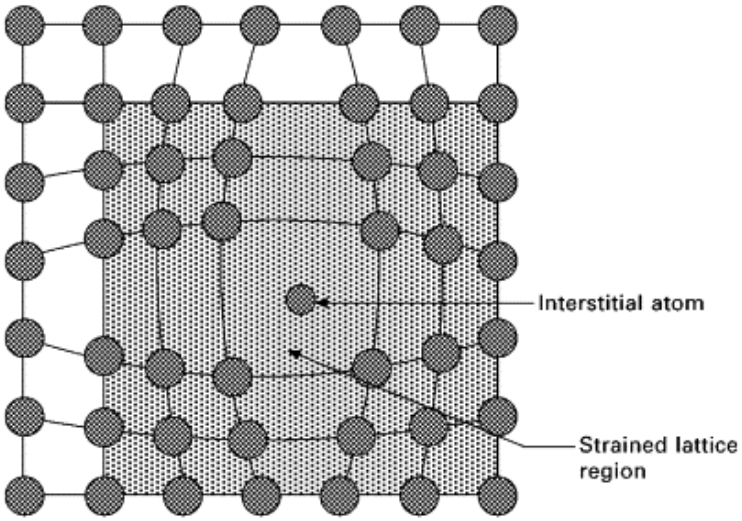

Figure 2.3: A schematic illustration of an interstitial point defect and the lattice strain caused [186].

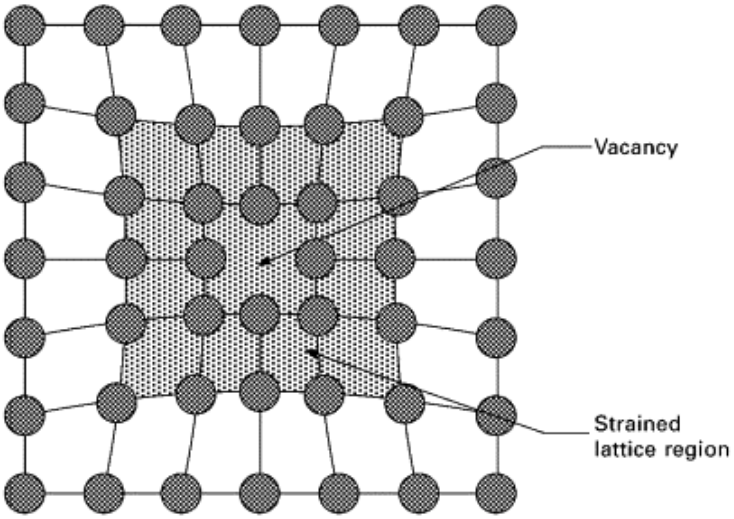

Figure 2.4: An illustration of a vacancy point defect resulting in a high strain region denoted by the shaded area [186].

2.3.1.3 Line defects

Dislocations are line defects that significantly exist in metals, causing irregularities within the crystal structure. They move when stress is applied to the material, and their motion then allows for slip-plastic deformation to take place. The two types of dislocations are edge and screw dislocations. Dislocations significantly affect the mechanical properties of materials, for example, ductility and deformations. A significant amount of dislocations in a metal increases the interaction between dislocations, which yields high-strength and hard metal [198]. In a line defect, a perfect atomic arrangement is disturbed along a given lattice plane in the crystal. These types of lattice disturbances are called line defects since they can be described in terms of their width and length. They can be formed during plastic forming and also during crystallization. Strong metals consist of a significant number of line defects, and low-strength metals contain a lower concentration of line defects [199, 200].

2.3.2 Radial distribution functions (RDFs)

Radial distribution functions (RDFs) are used to characterize the internal structure of a material. They describe the probability of locating an atom at a given atomic separation r away from a marked point (reference) in a crystal. Liquids, solids, and gases exhibit different RDF graphs. Hence, the phase of a material can be determined from the detailed distribution of atoms in the material given by RDF graphs. Moreover,

the bond length of the atoms contained in the system can be deduced from the first peak of the RDF graph. The first RDF peak denotes the nearest neighbour distance of the atomic interaction in question.

The average density of a liquid at any point is the same. It is called bulk density since it is the same in the entire system. Consequently, in such a system, the density at a reference point uniquely defines the density of the entire system, and hence, the coordination number is given as:

$$n_{ij}(\boldsymbol{r}) = 4\pi\rho \int_{r\,min}^{r\,max} \boldsymbol{r}^2 G(\boldsymbol{r}) d\boldsymbol{r}, \tag{2.17}$$

wherein the density of the system is given as the number of atoms N contained per volume V, $\rho = \frac{N}{V}$ and $n_{ij}(\boldsymbol{r})$ as the probability of finding an atom at a separation distance r away from a marked atom [201, 202].

2.3.3 X-ray diffraction pattern

X-ray diffraction (XRD) patterns are a great analytical tool to characterize the structure and phase of materials. Information, such as crystal lattice parameters, can be obtained from XRD patterns. The diffraction angles and their respective intensities capture significant information required to characterize materials. Materials with high long-range atomic ordering exhibit clear XRD diffraction peaks [203, 204]. Crystals of sizes that are less than or about 100 nm depict broad XRD peaks, as explained by the Sherrer [205] equation given as:

$$\langle L \rangle = \frac{K\lambda}{\beta cos\theta}, \tag{2.18}$$

where the wavelength of the incident x-ray is λ, the dimension of the particle is $< L >$ in the direction perpendicular to the reflecting plane, and the peak width is β. The reflection angle is given by θ and K is a constant given by $2\sqrt{\frac{(ln2)}{\pi}}$. A database of XRD patterns exists in which the XRD patterns of the unknown materials to be characterized are compared. Moreover, the crystallinity and the presence of structural defects can be inferred from XRD patterns.

CHAPTER 3

Derivation and Validation of Buckingham Interatomic Potentials From A First-Principles Starting Point With The General Utility Lattice Program (GULP)

3.1 Introduction

In this chapter, interatomic potentials for interactions that emerge from doping $LiMn_2O_4$ spinel with Co and Ni are derived and validated. The potentials will be used to monitor the impact that doping $LiMn_2O_4$ with Co and Ni has on the microstructure and transport properties of spinel. An approach inspired by machine learning methods will be used to derive the interatomic potentials. The approach involves learning from interatomic interactions that are influenced by interactions that are based on electronic density. The learning is done using a curve-fitting function from the SciPy library called curve_fit [143]. Subsequently, the learned information will be transferred to classical interactions using the classical dynamics code for fitting interatomic potentials, the General Utility Lattice Program (GULP).

Interatomic potentials are among the fundamental inputs for molecular dynamics (MD) simulations. The interactions of atoms, behaviour, and properties of materials are governed by interatomic forces, which are calculated from interatomic potentials. The description of classical potential energy surfaces with parameterized mathematical functions has been a widely adopted approach in MD simulations. The parameters of the parameterized interatomic potential function are derived from experimental data for the description of different atomic interactions. The process of finding these potential parameters that reproduce a given set of experimental data for a certain interaction is generally called fitting and is quite challenging. However, it is well known that in the fitting process, the initial potential parameters have an impact on the final potential parameters. The general rule of thumb has been to make a sensible guess of the initial parameters, predominantly based on past experiences. Therefore, a physical starting point is a crucial requirement for the derivation of accurate interatomic potentials.

Classical interatomic potentials will be crucial for enabling studies of thermodynamic properties, microstructure, and transport properties such as diffusion at a practical computational cost. Such studies are crucial as they give a detailed picture of how the material will perform and serve as a guideline for the development of durable, affordable, and robust high-energy and high-power positive electrode materials for the leading lithium-ion batteries.

3.2 Methodology

The first step for derivation of the interatomic potentials is to calculate potential energy surfaces with the Fritz Haber Institute ab initio molecular simulations (FHI-aims) program [149]. The potential energy surface contains information about interatomic interactions based on the DFT electron density, which is retrieved with the curve_fit function [143]. The potential energy surfaces are calculated with the Density Functional Theory (DFT) code. The curve_fit function yields preliminary Buckingham potential parameters containing information for isolated interatomic interactions that are based on electron density (DFT). Finally, the preliminary interatomic interactions are refined with GULP in spinel systems ($LiCo_2O_4$, $LiMn_{1.875}Co_{0.125}O_4$, $LiMn_{1.875}Ni_{0.125}O_4$, and $LiCo_{1.875}Ni_{0.125}O_4$) [142]. The final potentials also include information about interatomic interaction in a spinel environment. The Co-Co, Co-Li, and Co-O interactions were derived in $LiCo_2O_4$ spinel, and the Ni-Ni, Ni-Li, Ni-O, and Ni-Mn interactions were derived in Ni-doped $LiMn_2O_4$ ($LiMn_{1.875}Ni_{0.125}O_4$). Furthermore, the potentials for the Co-Ni and Mn-Co interactions were derived from $LiCo_{1.875}Ni_{0.125}O_4$ and $LiMn_{1.875}Co_{0.125}O_4$, respectively.

3.2.1 FHI-aims

The potential energy of the interactions at different atomic separation distances between 0.8 and 9 Å was calculated with the Atomic Simulation Environment (ASE) FHI-aims calculator, which is a Python module for running and manipulating the FHI-aims code. The FHI-aims calculation was considered to have converged to a physical system when the difference between the previous total energy and the current total energy of the self-consistency cycle is less than or equal to 10^{-6} eV [149]. Furthermore, the change in the eigenvalue sum between the earlier and present self-consistency cycles is less or equal to 10^{-3} eV, and the difference in atomic forces between the previous and current self-consistency cycles is <= 10^{-4} eV/Å. The atomic_zora scalar

relativistic treatment was sufficient to compute the potential energy of the atomic interactions (Co-O, Co-Co, Co-Li, Co-Mn, Ni-O, Ni-Ni, Ni-Li, and Ni-Mn). Moreover, the Gaussian broadening function with a width of 0.3 Å was used to accurately determine the Femi level of these interactions.

3.2.2 Machine Learning Approach: SciPy curve_fit function

The SciPy curve_fit function was used to fit the Buckingham potential function to the calculated DFT potential energy surfaces [143]. This process yields Buckingham potential parameters, which reproduce the potential energy surfaces. The curve_fit function optimizes the initial guessed parameters using a machine learning technique to find the best fit to a data set. Important parameters of the curve_fit function are the model function to fit (the Buckingham potential function in this case) to a data set, the starting parameters of the model function, and the data set (the DFT potential energy surfaces in this case).

3.2.3 General Utility Program (GULP)

The curve_fit function yields Buckingham potential parameters containing the unique characteristics of each one of these interactions. However, the potential energies are not calculated in a spinel environment, to capture this, the GULP program was utilized to refine the preliminary potential function parameters [142]. The GULP program is widely used for deriving empirical forcefields from energy surfaces and empirical data or data from first-principles calculations. The derivation process was carried out under ambient conditions. The fitting process entails the minimization of the sum of squares function given below:

$$F = \sum_{i=1}^{N_{obs}} w_i (f_i^{obs} - f_i^{calc}) \quad (3.1)$$

where f_i^{obs} represents empirical data and f_i^{calc}denotes the calculated data compared through the weighting factor w_i. Moreover, the total number of fitted properties is given by N_{obs}. Furthermore, the interatomic potentials fitted in this work make use of the Li-Li, Li-O, Mn-O, Mn-Mn, and O-O interatomic potentials fitted elsewhere [74].

3.2.4 Vienna Ab initio Simulation Package (VASP)

The fitting data supplied to the GULP code, referred to as experimental data in this study, was calculated from the Vienna Ab initio Simulation Package (VASP) [170, 171, 206]. The VASP code employs boundary conditions and replaces the nucleus and core electrons with an approximate potential that is fixed. A cutoff energy of 750 eV was sufficient to sample the number of plane waves required to make up electronic wavefunctions for the calculations. The conjugate gradient method was selected for determining how atoms are updated and moved by setting IBRION = 2. Moreover, the generalized gradient approximation (GGA) was selected as the exchange-correlation functional [156], and the projector-augmented wave (PAW) was the pseudopotential selected [207]. Furthermore, to sample the Brillouin zone, a 4x4x4 Monkhorst pack k-mesh was chosen.

3.3 Results

3.3.1 Potential Energy Surface (PES)

In this section, the potential energy surfaces of the interatomic interactions emanating from replacing a small amount of manganese with cobalt or nickel in a lithium-manganese-oxide spinel are discussed. A potential energy surface (PES) gives the potential energy of a system of two or more interacting atoms as a function of one or several parameters such as atomic positions, angles, etc. A PES that is described in terms of the distance between atomic nuclei is generally called a potential energy curve. Potential energy surfaces provide insights into the reaction pathways and molecular geometry of a given system. Therefore, from a PES, it can be deduced that at larger atomic separations, the attractive forces between the two interacting atoms are zero. At smaller values of r, the repulsive force is dominant and results in energy increase following the Pauli's Exclusion Principle. A point in the PES where neither the attractive nor the repulsive force is dominant is called the minimum point, and it represents the equilibrium bond length of the interaction.

Figure 3.1 (a-h) shows the potential energy curve of the interactions arising from doping $LiMn_2O_4$ spinel with Co and Ni. The potential energy curves were considered for the separation distances between 0.8 Å and 9 Å. Furthermore, each point was 0.49 Å apart from a consecutive point in the atomic separation range of 0.8 Å and 9 Å to

obtain an optimal fit to the potential energy surfaces (to avoid overfitting and underfitting). The energy of interactions at smaller separations is increasing rapidly in the potential energy curves for all the interactions following Pauli's exclusion principle. At large atomic separations, the energy of interaction is close to zero for all the interactions. The Co-O interaction possesses more substantial attractive characteristics than the Co-Co, Co-Li, and Co-Mn interactions. Furthermore, the Ni-O interaction also has greater attractive characteristics than the Ni-Ni, Ni-Li, and Ni-Mn interactions. Therefore, all the essential, unique characteristics of these interactions are captured by the PES interactions.

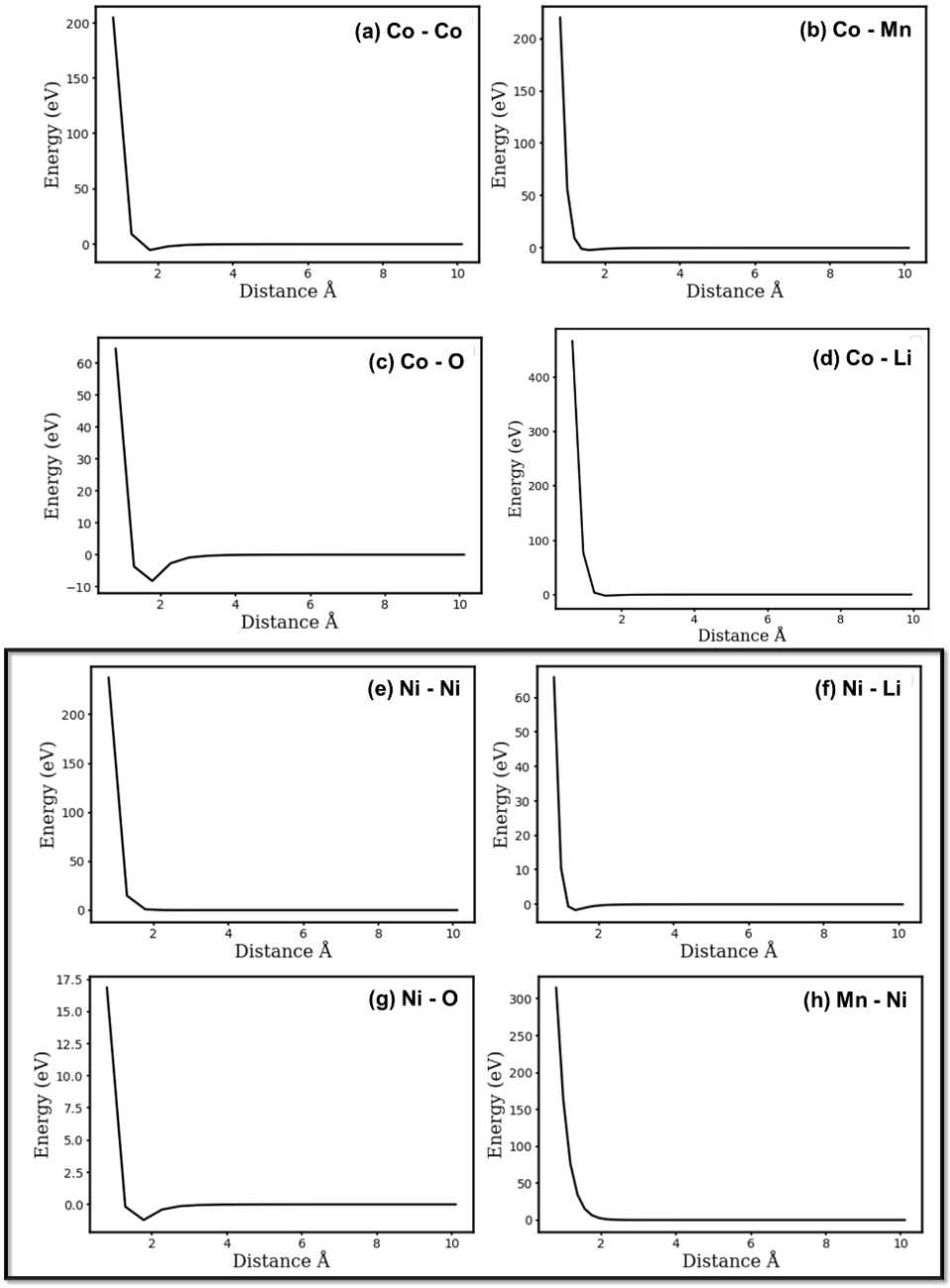

Figure 3.1: Potential energy surfaces (a-h) of the interactions originating from doping $LiMn_2O_4$ spinel with cobalt (Co) and nickel (Ni) calculated with the DFT code FHI-aims [139].

3.3.2 Fitting the Buckingham potential function to the potential energy curves

The potential energy surfaces illustrated in figure 3.2 are fitted to the Buckingham potential energy function through curve fitting. The Buckingham potential function gives an approximation of the energy of interaction for atoms that are not directly bonded. It takes the interatomic separation and the constants A, ρ, and C. The A and

ρ parameters describe the repulsive part and C constitute the attractive part of the potential energy. The constants of the Buckingham potential function are unique for different interactions and are derived from empirical or computational data.

Figure 3.2. shows a plot of potential energy curves fitted to a Buckingham potential function for the interactions emanating from substituting a small amount of manganese in $LiMn_2O_4$ spinel with Co and Ni. The curve_fit function of the SciPy library was utilized to fit the Buckingham function to the potential energy surface data [143]. Curve fitting entails optimizing the set of parameters of a function that describes the behaviour of the data in question so that the function can correctly predict an output value for a given input. The main aim is to obtain a model that does not overfit or underfit the given set of data. As illustrated in figure 3.2, the Buckingham potential function has been fitted successfully to the potential energy curves. The interactions of Ni-O and Co-O show more attractive behaviour at the equilibrium bond distance than interactions such as Co-Co and Ni-Ni. These differences are incorporated into the fitted Buckingham potential functions illustrated in table 3.1. As such, the potentials include a description of the physical and chemical attributes of the interactions. The determined Buckingham parameters will be further fine-tuned in the GULP environment to capture the behaviour of the Co-Co, Co-O, and Co-Mn interactions in the Li-Mn-Co-O spinel [142].

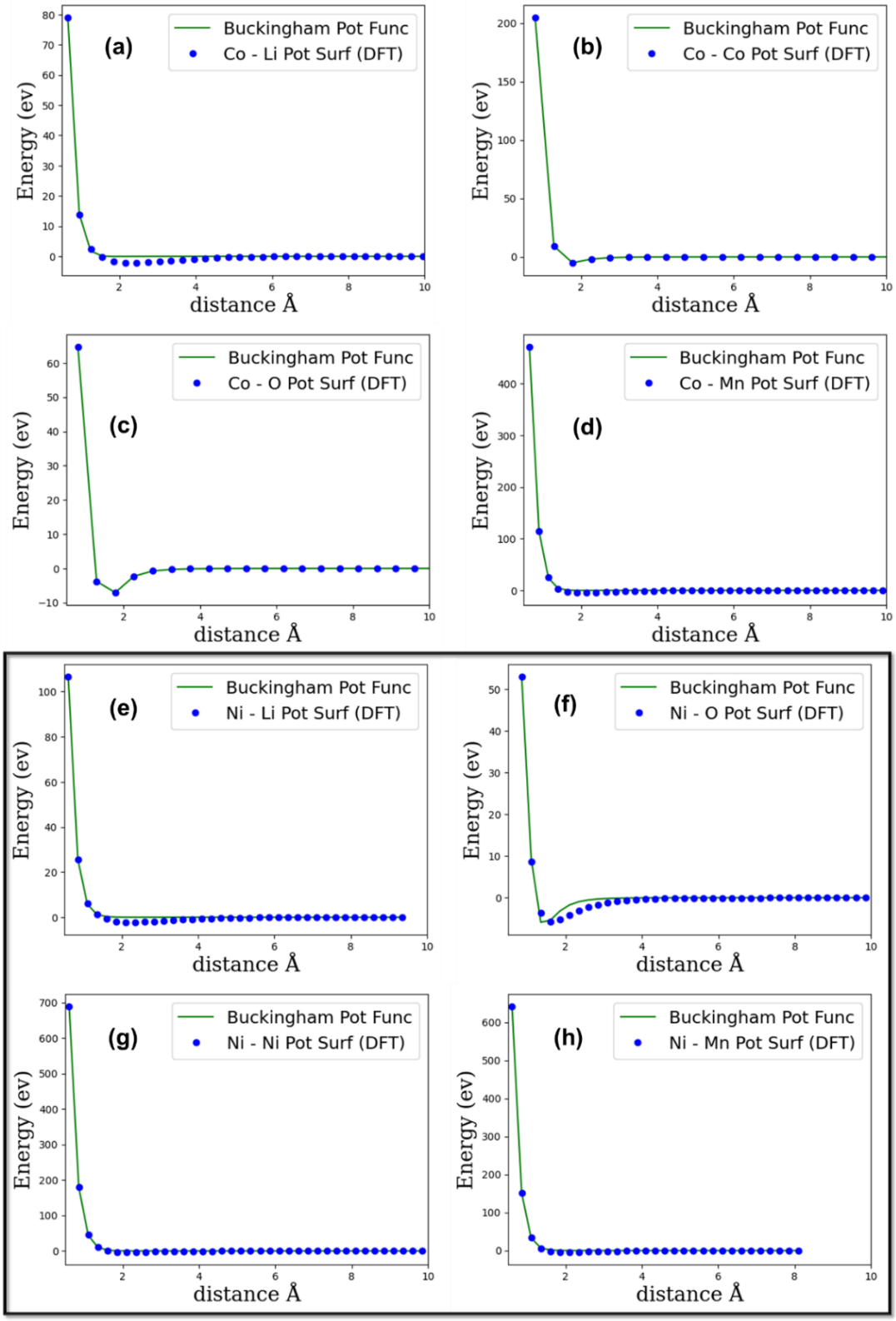

Figure 3.2: Buckingham potential functions (a-h) fitted to DFT potential energy surfaces using the curve_fit functions based on machine learning for the interatomic interactions emanating from doping Li-Mn-O spinel with Co and Ni.

Table 3.1: Preliminary Buckingham potential parameters (A, ρ, and C) for the interactions emerging from doping Li-Mn-O spinel with Co and Ni determined from DFT potential surfaces by the python curve_fit function of the open source SciPy library. The potentials in this table will be further refined with the GULP code to generate functional potential parameters [142].

Interactions	$\boldsymbol{A}\ (\boldsymbol{eV})$	$\boldsymbol{\rho}(\text{Å})$	$\boldsymbol{C}(\boldsymbol{eV}\text{Å}^{-\boldsymbol{6}})$
Co-Co	48021.956	0.162	36.672
Co-O	197015.503	0.166	399.998
Co-Li	17265.034	0.148	10.158
Co-Mn	120663.933	0.144	64.581
Ni-Ni	24314.539	0.176	5.329
Ni-Li	30436.320	0.166	59.990
Ni-O	79183.977	0.128	22.809
Mn-Ni	13891.161	0.234	36.672
Co-Mn	31071.223	0.165	10.002

3.3.3 Structure properties.

The Buckingham potential parameters in table 3.1, derived from potential energy curves determined with the curve_fit function, will be further refined with the GULP program. The GULP program derives potential parameters from empirical data or computational data. In this section, the Buckingham potential parameters in table 3.1 will be refined with the GULP program from computational data, wherein the computational data is structure properties (elastic constants, bulk modulus, and shear modulus) calculated with the VASP code [170, 171, 206] for the structures $LiMn_{1.875}Ni_{0.125}O_4$, $LiCo_2O_4$, $LiMn_{1.875}Co_{0.125}O_4$, and $LiMn_2O_4$. Elastic properties are chosen due to their strong correlation to the atomic forces of solid materials [142]. The mechanical stability and elasticity of solids can be characterized by elastic constants. Moreover, elastic properties govern how materials react to external forces, and as such, they allow inferences on the durability of materials. The strength of a material can be inferred from the bulk modulus (B), shear modulus (G), Young's modulus (E), and Poisson's ration (ν). The interatomic relations are captured by the elastic

constants. Hence, valuable insights about atomic bonding and the stability of the structure can be derived from the elastic constants [208].

The VASP calculations were performed with a strain of 0.003. All the spinel structures ($LiCo_2O_4$, $LiMn_2O_4$, $LiMn_{1.875}Co_{0.125}O_4$, and $LiCo_{1.875}Ni_{0.125}O_4$) are mechanically stable, as suggested by the elastic constants in table 3.2, which are inferred by following equation 3.1. The equation describes the stability conditions for crystals with cubic symmetry [209, 210].

$$C_{44} > 0, C_{11} - C_{12} > 0, and\ C_{11} + 2C_{12} > 0 \qquad (3.2)$$

The elastic constants for all these structures are listed in table 3.2. The C_{ij} elastic constants can only be determined experimentally from single-crystal samples, however, the bulk modulus and shear modulus can be obtained from polycrystalline materials. This limits the availability of the C_{ij} elastic constant for comparison between experimental and computational studies. The bulk modulus of $LiMn_2O_4$ in this study was found to be 138.52 GPa, which is not far from the 119.00 GPa determined experimentally in a study by Lin and co-workers [211]. Moreover, an experimental bulk modulus value of 134.00 GPa for $LiCo_2O_4$ was also obtained, which is comparable to the 145.52 GPa calculated in this work [212]. The C_{44} is positive for all the structures. Furthermore, C_{11} is greater than C_{12} in all the cases, as such $C_{11} - C_{12} > 0$ is true for all the structures. For example, C_{11} is 222.585 GPa and C_{12} is 104.944 GPa. Therefore, $C_{11} - C_{12}$ is 117.641 GPa, which is greater than zero for $LiCo_2O_4$. The C_{11} and C_{12} elastic constant values for all the structures are positive, hence, the $C_{11} + 2C_{12} > 0$ mechanical stability criterion for cubic symmetry structures is also satisfied for all the structures in table 3.2.

Table 3.2: Elastic properties of $LiCo_2O_4$, $LiMn_2O_4$, $LiMn_{1.875}Co_{0.125}O_4$, and $LiCo_{1.875}Ni_{0.125}O_4$ calculated with DFT. The C_{ij} elastic constants (C_{11}, C_{12}, and C_{44}) and moduli (the Bulk modulus B, and Shear modulus G) are shown. The structure properties in this table are used to refined the preliminary Buckingham interatomic potential with the GULP code listed in table 3.2 [142].

Compound	C_{11} (GPa)	C_{12} (GPa)	C_{44} (GPa)	B (GPa)	G (GPa)
$LiCo_2O_4$	222.585	104.944	82.350	145.518	71.520
$LiMn_2O_4$	210.500	102.530	95.550	138.520	76.010
$LiMn_{1.875}Co_{0.125}O_4$	209.040	97.840	85.120	134.580	71.200
$LiCo_{1.875}Ni_{0.125}O_4$	212.477	111.564	81.599	144.200	65.002

3.3.4 Fine-tuning the Buckingham interatomic potential parameters determined with the curve_fit function with the GULP program.

The Buckingham potential function parameters in table 3.4 were derived successfully with the GULP program, version 1.3 [142]. The input of the program for the fitting process was the structure properties (elastic constants, bulk modulus, and shear modulus) and the potential parameters in table 3.1. The process involves finding the minimum of the sum of squares function, which compares the given set of structure properties to the structure properties calculated from the potential parameters (currently derived potential parameters) [142]. The potential parameters were derived using the relax fit approach, in which properties are obtained from a structure with minimized atomic forces. Furthermore, the structure is optimized at every point, wherein the experimental structure properties and the calculated structure properties are compared. The fit was performed at a temperature of 300 K and a pressure of 0.00 GPa. Partial atomic charges were employed to describe the non-covalent electrostatics of the interactions. The partial atomic charges and atomic masses of Ni, Co, O, and Mn in $LiMn_{1.875}Ni_{0.125}O_4$, $LiCo_2O_4$, and $LiMn_{1.875}Co_{0.125}O_4$ are shown in table 3.3, calculated in accordance with the study by Maphanga et al. [74].

Table 3.3: Partial atomic charge of Co, Mn, and O in Li-Mn-O spinel and their atomic masses utilized in this study in generating interatomic potentials and performing MD simulations.

Ion	Partial Atomic Charges	Atomic Mass (u)
Co	1.922	58.930
Mn	1.922	54.938
Ni	1.922	58.693
O	-1.098	15.999
Li	0.548	6.941

The preliminary Buckingham interatomic potentials in table 3.1 obtained through curve fitting have been successfully refined with GULP. The final refined potentials are illustrated in table 3.4 [142]. The Buckingham interatomic potentials for the Co-Co, Co-Li, and Co-O interactions were derived from the $LiCo_2O_4$ spinel. The results of the structural properties are shown in table 3.5. The structure properties calculated from the derived potentials are compared to the fitted structure properties, referred to as experimental. The fitted $LiCo_2O_4$ lattice parameters and cell volume are reproduced within a percentage difference of less than 0.2%. Moreover, the calculated elastic properties were found to compare well to the fitted elastic properties, as evidenced by the obtained percentage difference of less than 5.0%. The percentage difference between the calculated and fitted bulk modulus was found to be 3.0%. The Buckingham potentials for the Co-Mn interaction were fitted in a Co-doped Li-Mn-O ($LiMn_{1.875}Co_{0.125}O_4$) spinel structure. Table 3.6 shows the structural and electronic properties results for the derivation of the Buckingham interatomic potential parameters for the Co-Mn interaction in $LiMn_{1.875}Co_{0.125}O_4$ spinel. The lattice parameter of the fitted structure compared well to the lattice parameter of the structure deduced from the derived Buckingham interatomic potentials, with a percentage difference of < 0.7%. Moreover, the cell volume of the $LiCo_2O_4$ spinel structure determined from the derived potentials was found to be 541.981 $Å^3$, which does not vary much from the cell volume of the fitted structure of 552.980 $Å^3$. A percentage difference of less than 2.0% was obtained, which indicates a good comparison between the calculated and fitted cell volumes. Furthermore, the calculated and fitted elastic constants are also in good agreement, which is evidenced by a percentage

difference of less than 3.3%. The calculated bulk modulus of 134.58 GPa does not veer much from the fitted bulk modulus of 132.740 GPa. The percentage difference was found to be less than 1.4%, which indicates a good comparison.

Table 3.4: The final derived Buckingham potentials for the interactions that arise from doping $LiMn_2O_4$ spinel with Co and Ni. The potentials were derived from the $LiCo_2O_4$, $LiMn_{1.875}Co_{0.125}O_4$, and $LiMn_{1.875}Ni_{0.125}O_4$ spinel structures.

Interactions	$A\ (eV)$	ρ(Å)	$C(eV\text{Å}^{-6})$
Co – Co	48021.956	0.162	63.937
Co – O	68670.662	0.166	21.732
Co – Li	17210.534	0.148	10.158
Co – Mn	120663.933	0.256	1695.250
Ni – Li	30451.195	0.166	9.335
Ni – O	84002.097	0.169	49.086
Ni – Mn	610056.862	0.234	3378.044
Co – Ni	31071.223	0.165	54.294

Table 3.5: Comparison of the VASP (fitted) and GULP (calculated) structure properties (C_{ij} elastic constants and Bulk modulus (B)) of $LiCo_2O_4$ under temperature of 300K and pressure of 0.00 GPa. The fitting of the Co-Co, Co-Li, and Co-O interactions.

Properties	Experimental	Calculated	Percentage difference
α(Å)	8.129	8.123	0.074
Volume (Å^3)	537.127	536.063	0.198
C_{11} (*GPa*)	222.585	229.713	3.152
C_{12} (*GPa*)	104.944	110.176	4.864
C_{44} (*GPa*)	82.350	85.279	3.495
B (*GPa*)	145.518	150.021	3.047

Table 3.6: Comparison of the VASP (fitted) and GULP (calculated) structure properties (C_{ij} elastic constants and Bulk modulus (B)) of $LiMn_{1.875}Co_{0.125}O_4$ under temperature of 300K and pressure of 0.00 GPa. The fitting of the Co - Mn interaction.

Properties	Experimental	Calculated	Percentage difference
α(Å)	8.153	8.208	0.670
Volume (Å^3)	541.981	552.980	2.009
C_{11} (*GPa*)	209.040	211.364	1.1057
C_{12} (*GPa*)	97.840	94.682	3.281
C_{44} (*GPa*)	85.120	84.215	1.069
B (*GPa*)	134.580	132.740	1.377

The Ni-Ni, Ni-Li, Ni-O, and Ni-Mn interatomic potentials have been successfully derived in the Ni-doped $LiMn_2O_4$ ($LiMn_{1.875}Ni_{0.125}O_4$) spinel structure. The fitted and calculated structure properties are compared in table 3.7. The computed and experimental cell volumes and cell parameters are within a percentage difference of < 0.5%. Moreover, the fitted elastic constants and bulk modulus are within a percentage difference of less than 6.7% with the fitted elastic constant and bulk modulus. The results for the derivation of the Buckingham interatomic potentials for the Co-Ni interaction are illustrated in table 3.8. The cell parameters of the structure determined from the derived Buckingham interatomic potentials were found to be 8.121 Å, which is not far off from the fitted lattice parameter of 8.126 Å. The calculated cell volume was found to be comparable to the experimental cell volume, as evidenced by a percentage difference of < 0.2%. The fitted and calculated elastic constants and bulk modulus are also in good agreement, as shown by a percentage difference of less than 7.1%.

Table 3.7: Comparison of VASP (fitted) and GULP (calculated) structure properties (C_{ij} elastic constants and Bulk modulus (B)) of $LiMn_{1.875}Ni_{0.125}O_4$ under temperature of 300K and pressure of 0.00 GPa. The fitting of the Ni-Ni, Ni-Li, Ni-O, and Mn-Ni interactions.

Properties	Experimental	Calculated	Percentage difference
α(Å)	8. 1552	8.167	0.141
Volume ($Å^3$)	542.380	544.682	0.423
C_{11} (*GPa*)	214.540	223.853	4.249
C_{12} (*GPa*)	96.460	103.118	6.672
C_{44} (*GPa*)	86.430	88.996	2.924
B (*GPa*)	135.820	141.255	3.923

Table 3.8: Comparison VASP (fitted) and GULP (calculated) structure properties (C_{ij} elastic constants and Bulk modulus (B)) of $LiCo_{1.875}Ni_{0.125}O_4$ under temperature of 300K and pressure of 0.00 GPa. The fitting of the Ni – Ni, Ni – Li, Ni – O, and Mn - Ni interactions.

Properties	Experimental	Calculated	Percentage difference
α(Å)	8.126	8.121	0.057
Volume ($Å^3$)	536.496	535.576	0.172
C_{11} (*GPa*)	21.250	22.819	7.130
C_{12} (*GPa*)	11.156	11.152	0.039
C_{44} (*GPa*)	8.160	8.657	5.912
B (*GPa*)	14.421	15.041	4.207

3.3.5 Application of the derived-interatomic potentials in molecular dynamics simulations.

The derived Co-Co, Co-Li, and Co-O Buckingham interatomic potentials listed in table 3.4 have been used to study the behaviour of a 7000-atom $LiCo_2O_4$ spinel structure at various temperatures with molecular dynamics simulations, as illustrated in figure 3.3. The atomic-level structure images show that the crystalline structure of $LiCo_2O_4$ is intact even at a temperature of 1800 K. The atomic vibrations of atoms about their lattice positions are increasing with increasing temperature, as generally anticipated. Since the increase in temperature raises the kinetic energy of the system. This, then, increases the vibration of atoms about their lattice positions. Therefore, the Co-Co, Co-Li, and Co-O Buckingham interatomic potentials were able to capture this phenomenon. Furthermore, the crystalline-to-amorphous phase transition is observed at a temperature of ~1900 K. Moreover, the structure was found to be completely in an amorphous state at a temperature of 2000 K. Figure 3.4 shows a graph of total energy vs. temperature, which reveals the effect of increasing temperature on the total energy of the system. The crystalline-to-amorphous phase change is also found to take place at a temperature of ~1900 K in Figure 3.4. The increase in temperature from this point (~1900 K) only increases the entire energy of the system, which is used to change the phase of the structure from crystalline to amorphous. The temperature of the system remains constant until the structure is completely amorphous.

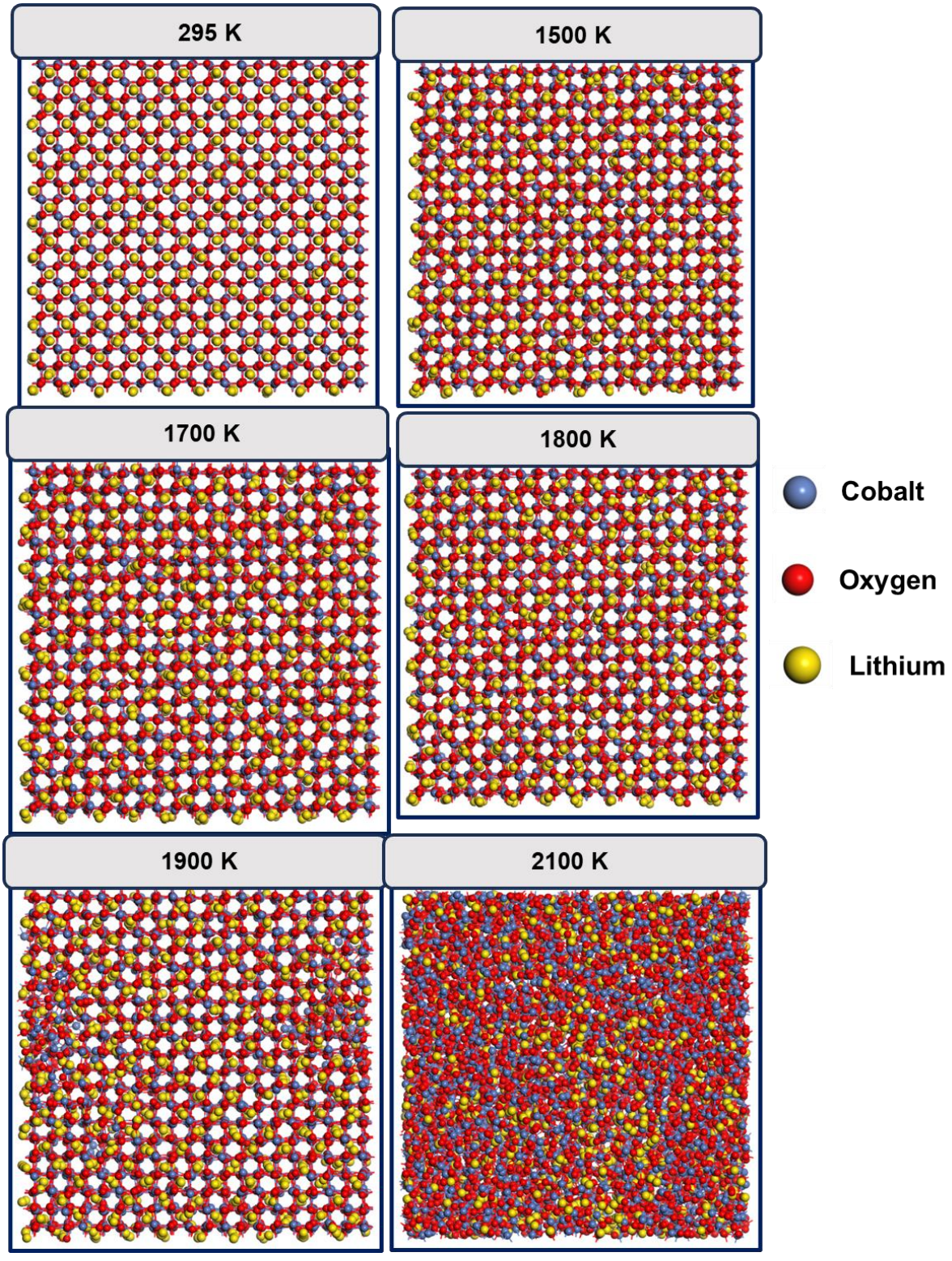

Figure 3.3: Atomic-level structure images of $LiCo_2O_4$ spinel illustrate the effect of increasing temperature on the phase of this material.

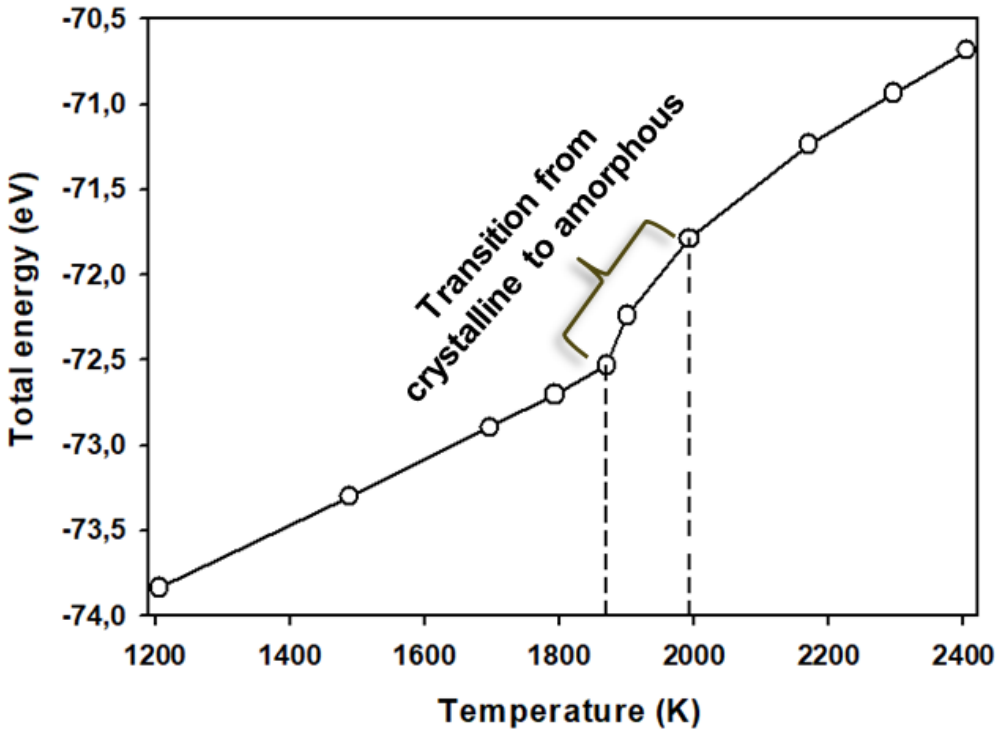

Figure 3.4: Illustration of the melting point of $LiCo_2O_4$ spinel captured by the total energy plotted against temperature.

The Buckingham interatomic potentials for the Ni-Ni, Ni-Li, and Ni-O interactions were also used to simulate the behaviour of $LiNi_2O_4$ spinel as a function of temperature with molecular dynamics (MD) simulations. The MD simulations are used to investigate the ability of the derived potentials to simulate the behaviour of LiN_2O_4 at various temperatures, which is essential for the investigation of temperature-dependent properties. In figure 3.5, the vibration of atoms about their lattice positions is seen to increase with temperature. The increase in temperature of the systems increases the kinetic energy of the atoms. The derived Ni-Ni, Ni-Li, and Ni-O interatomic potentials were able to simulate this, as is generally expected. The crystalline-to-amorphous phase transition takes place at a temperature of ~1800 K for the $LiNi_2O_4$ spinel structure. Furthermore, the total energy vs. temperature plot also shows that the structure transitions to amorphous at a temperature of ~1800 K, as illustrated in figure 3.6.

The radial distribution functions (RDFs) in figures 3.7 and 3.8 detail the distribution of atoms in $LiCo_2O_4$ and $LiNi_2O_4$ spinel. The crystalline-to-amorphous phase change is indicated by the broadening of RDF peaks as the temperature is heightened. For

$LiCo_2O_4$, at a temperature of 2000 K, the probability of finding an atom with respect to a refence atom in any position between the separation distance of 3.5 Å and 10 Å is greater than zero. Therefore, the structure is in an amorphous phase at this temperature. Similarly, for $LiNi_2O_4$, g(r) values that are greater than zero are observed at a temperature of 1900 K in the atomic distances that are between 3.5 Å and 10 Å. This suggests that $LiNi_2O_4$ is entirely amorphous at a temperature of 1900 K.

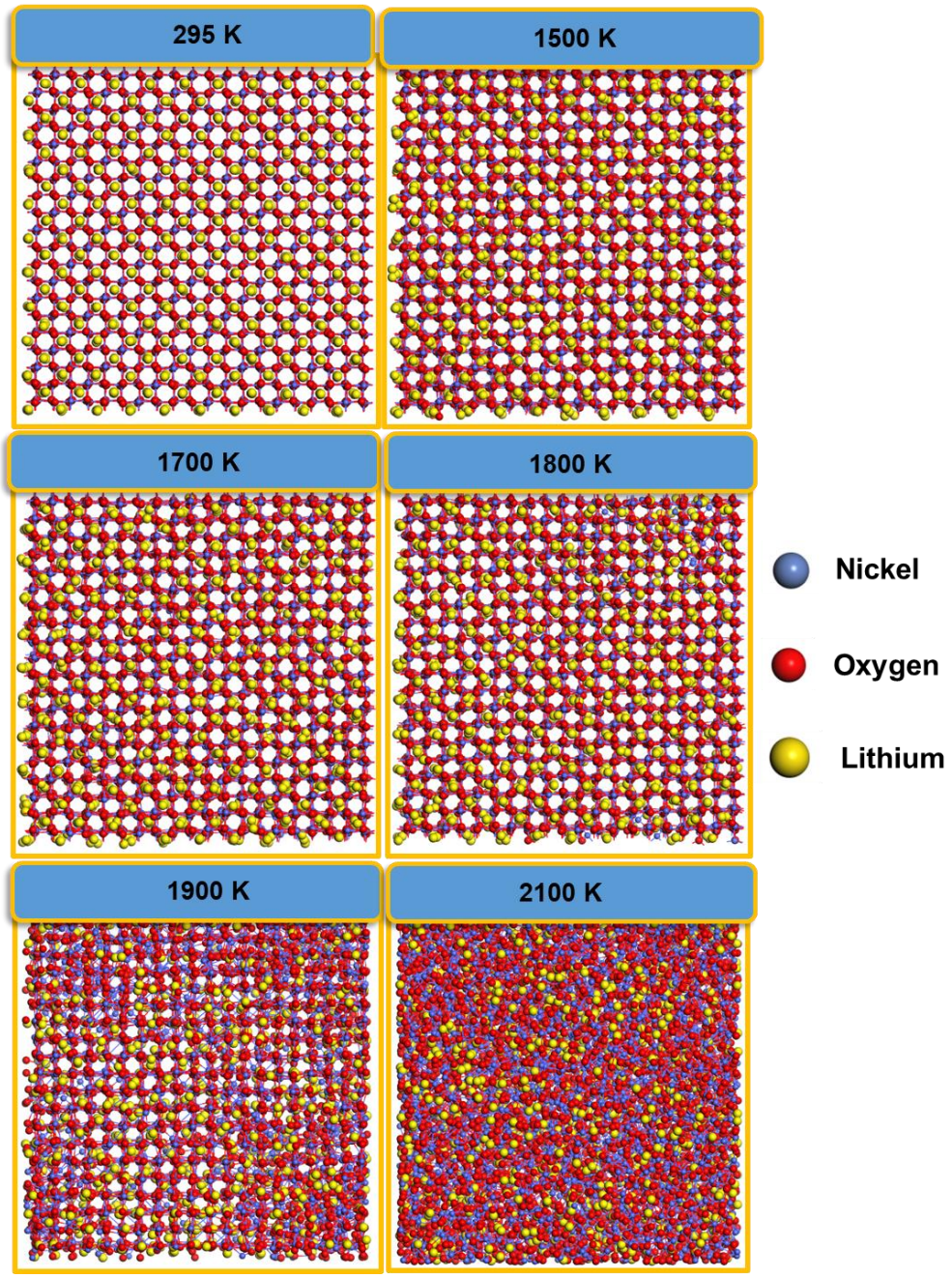

Figure 3.4: Atomic structure images of $LiNi_2O_4$ demonstrate the impact of increasing temperature on the material.

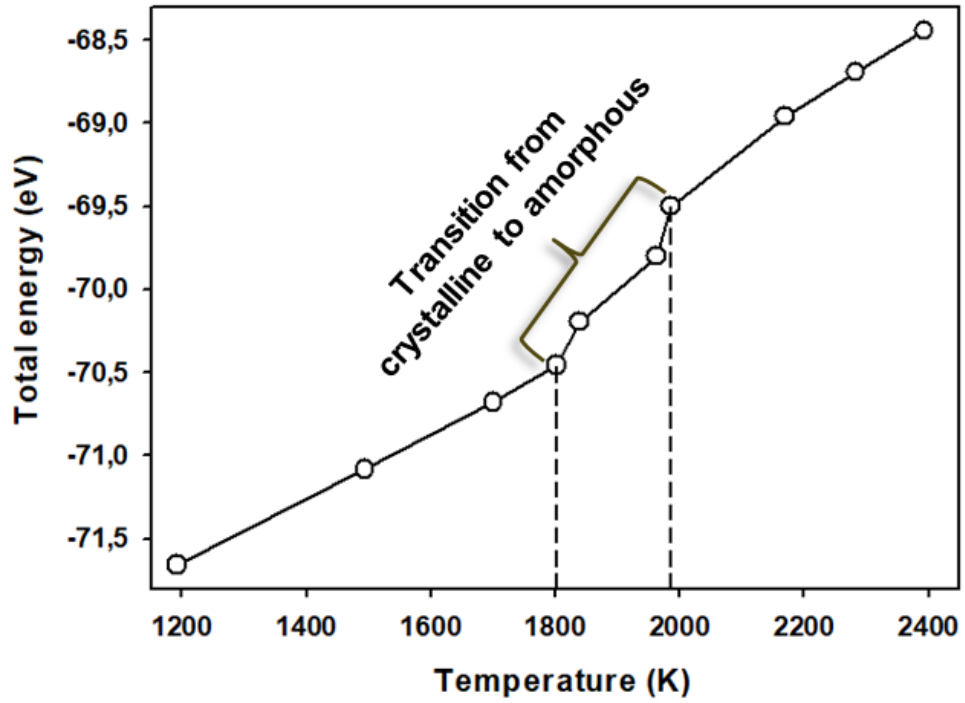

Figure 3.5: The total energy and temperature graph of $LiNi_2O_4$ spinel shows the melting point of this material.

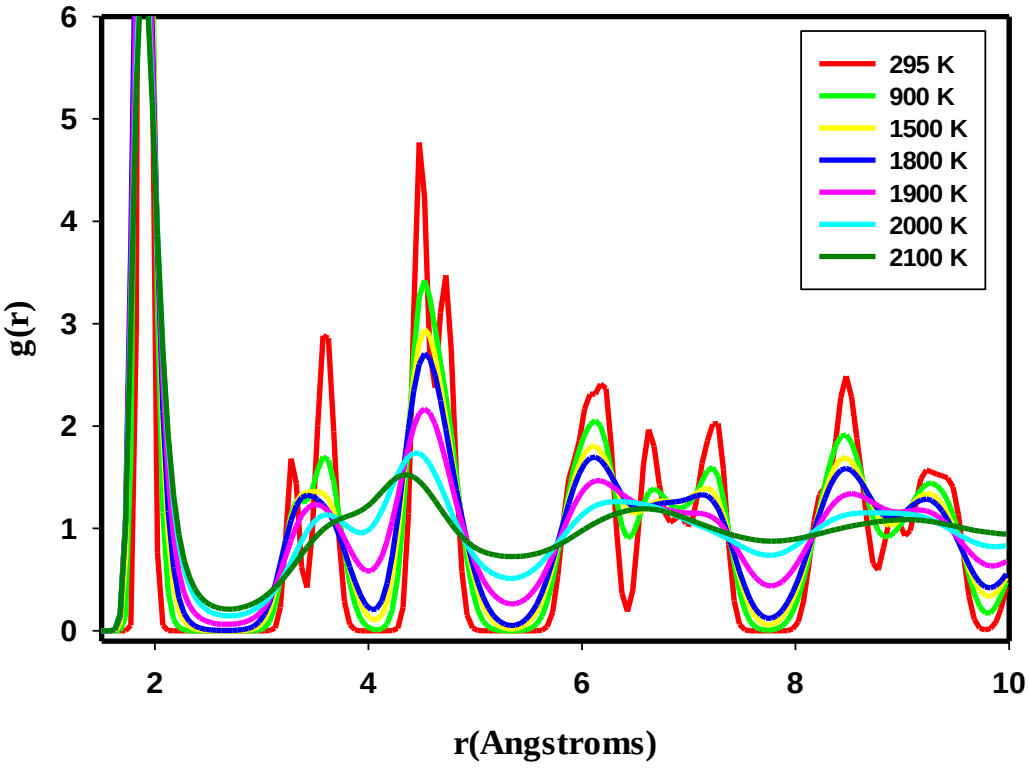

Figure 3.6: RDF graph of the Co-O interaction in $LiCo_2O_4$ spinel showing the effect of temperature increase in these structures.

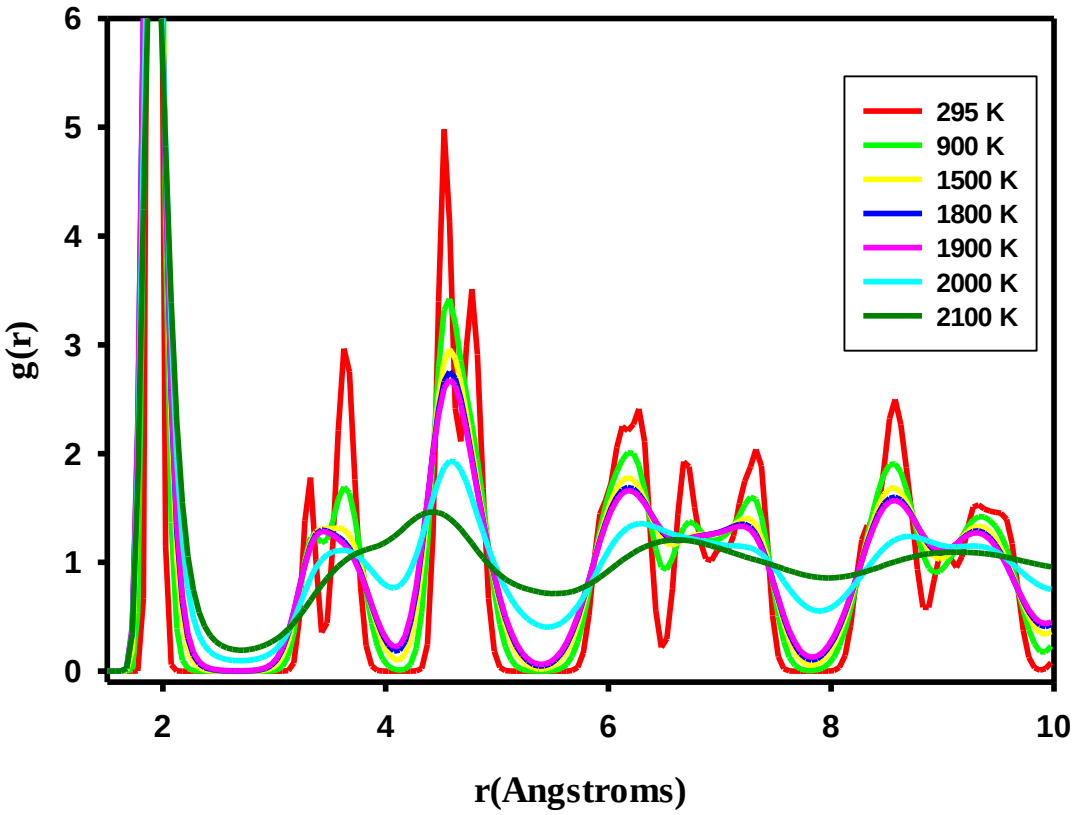

Figure 3.7: RDF graph of the Ni-O interaction in $LiNi_2O_4$ spinel showing the impact of temperature on the distribution of Ni and O atoms in the structure.

3.4 Discussion

In this chapter, the derivation of the Buckingham interatomic potentials for the Co-Co, Co-Li, Co-O, Co-Ni, Mn-Co, Mn-Ni, Ni-Li, Ni-Ni, and Ni-O interactions is discussed. The study is prompted by the scarcity of accurate interatomic potentials for interactions that emanate from doping $LiMn_2O_4$ spinel with Co and Ni. In DFT studies, it has been shown that the stability of $LiMn_2O_4$ can be improved with cation doping, particularly doping with Ni and Co due to their comparable ionic radius to that of manganese [213, 214, 215, 216]. However, there is a need to evaluate the structural changes that occur after the substitution of Co and/or Ni in the $LiMn_2O_4$ spinel and how they affect electrochemical performance. Moreover, due to a lack of information on the influence of the introduction of Ni and Co on the transport properties of Li^+ in $LiMn_2O_4$, such as diffusion and conductivity.

The method for deriving the potential Buckingham parameters in this study involved calculating potential energy surfaces with DFT. The information from the potential energy surfaces was interpolated to the Buckingham potential function parameters

with the SciPy function curve_fit [143]. Furthermore, the potential parameters are then refined in spinel systems with the GULP code [142]. The approach facilitates the incorporation of interatomic interactions influenced by the DFT electron density. This yields interatomic potentials that are capable of simulating myriad and complex interactions in cathode materials during battery operation.

The potential energy surfaces for the interactions that originate from doping $LiMn_2O_4$ spinel with Co and/or Ni were calculated successfully with the FHI-aims DFT code [149]. The various characteristics of the interactions were captured by the DFT potential energy surfaces. The potential energy surface plot of Co-O and Ni-O interactions showed a bigger well at equilibrium (where the repulsive and attractive forces are balanced) compared to the other interactions. The Mn-Ni, Ni-Li, Ni-Ni, Co-Li, Co-Mn, and Co-Co interactions showed more repulsive behaviour evidenced by a lack of a pronounced well at the equilibrium of attractive and repulsive forces of interactions. This is in line with the fact that a bond between a cation and an anion is stronger than the bond between two cations. The calculated potential energy surfaces from DFT electron density contained this information.

The information contained by the potential energy surface was successfully interpolated into a Buckingham potential function with the curve_fit function. The Buckingham interatomic potential functions plotted with the interpolated parameters from potential energy surfaces are compared to the potential energy surface plot. For the M-O (M=Co, Ni) interaction, the deep well denoting a strong electron affinity is also reproduced. The Buckingham potential function plot of the Mn-Ni, Ni-Li, Ni-Ni, Co-Li, Co-Mn, and Co-Co interactions also assimilates the repulsive behaviour of these interactions.

The potential parameters for all the interactions we further refined with the GULP code in spinel systems ($LiCo_2O_4$, $LiMn_{1.875}Ni_{0.125}O_4$, $LiMn_{1.875}Co_{0.125}O_4$, and $LiCo_{1.875}Ni_{0.125}O_4$) since they will be applied in similar systems. The process requires structure properties (elastic constant, bulk modulus, and shear modulus) and potential parameters to refine. The structure properties were successfully calculated with the VASP code. Elastic constants are quite a challenge to calculate experimentally since they are determined from single-crystal samples. This limits the availability of experimental data to compare with computational studies. The bulk modulus of

$LiMn_2O_4$ was found to be 138.52 GPa, which is comparable to the value of 119.00 GPa determined by Lin et al. [211]. For the $LiCo_2O_4$ spinel structure, a bulk modulus of 145.52 GPa was obtained, which is not far from the value of 134.00 GPa calculated by Dang [212]. For the doped spinel structures, there was nothing to compare with in experiments. Furthermore, the elastic properties of all the structures were used to check their mechanical stability using the stability criteria for structures with cubic symmetry [209, 210]. All the structures were found to meet the stability conditions. Hence, they are mechanically stable. Therefore, they can be used as input structures in refining the preliminary Buckingham potential function parameters.

Finally, the preliminary potentials were successfully refined in spinel structures with the GULP code [142]. The Buckingham potential parameters for Co-Co, Co-Li, and Co-O interactions were refined successfully in $LiCo_2O_4$ spinel. The fitted structure properties compare to a percentage difference of less than 5% with the structure properties calculated from the final potentials. Moreover, the potentials for the Co-Mn interaction were fine-tuned in Co-doped $LiMn_2O_4$ spinel ($LiMn_{1.875}Co_{0.125}O_4$) structure. The percentage difference between the fitted and calculated structure properties was found to be ≤ 3.3%. Furthermore, the Ni-doped spinel structure was used to adjust the Ni-Ni, Ni-Li, Ni-O, and Ni-Mn in a Ni-doped Li-Mn-O Buckingham interatomic potentials. A percentage difference of less than 6.7% was obtained between the calculated and fitted structure properties. The Buckingham interatomic potentials for the Co-Ni interaction were also refined in Ni-doped $LiCo_2O_4$ spinel ($LiMn_{1.875}Co_{0.125}O_4$). The properties calculated from the derived potentials deviate slightly from the fitted structure properties. A percentage difference of less than 7.1% was observed for this structure. Therefore, the Buckingham potentials were all refined successfully since the fitted and calculated structure properties were in good agreement with a percentage not exceeding 7.1%. A percentage difference of less than 7% is a good comparison for the derivation of interatomic potentials. Hence, the derived potentials can be used to monitor the impact of substituting Co and Ni on $LiMn_2O_4$ on its microstructure and transport properties.

The derived potentials were further utilized to monitor the impact of temperature on the lattice of $LiCo_2O_4$ and $LiNi_2O_4$ with molecular dynamics simulations. The lattice structure was found to distort with increasing temperature for the two structures ($LiCo_2O_4$ and $LiNi_2O_4$). The vibrations of atoms about their lattice positions were found

to also increase with temperature. This is attributed to the fact that the temperature of the system increases the kinetic energy of the atoms. This behaviour was generally expected. This is deduced from the atomic-level structure images. The state of atoms in the spinel structures was examined through RDF graphs. The $LiCo_2O_4$ and $LiNi_2O_4$ were found to have the crystalline-to-amorphous phase transition at a temperature of ~1900 K and ~1800 K, which is in line with the atomic snapshots and RDF graphs. The total energy vs. temperature plot also reveals that the $LiNi_2O_4$ spinel structure has the lowest melting temperature when compared to the melting temperature of $LiCo_2O_4$. This is in line with the fact that Ni has a smaller melting point when compared to Co [217, 218].

CHAPTER 4

Simulated Amorphization and Recrystallization of LiM_2O_4 (M=Co, Ni) and Co- or Ni-doped $LiMn_2O_4$ spinel

4.1 Introduction

The interatomic potentials developed in chapter 3 for the Co-Co, Co-Li, Co-O, Ni-Ni, Ni-Li, and Ni-O interactions have been employed to perform the simulated synthesis (A&R) of LiM_2O_4 spinel (M=Co, Ni) [71]. The A&R-simulated structures will provide insight on the microstructure of these spinel systems, which will guide the doping of $LiMn_2O_4$ with Co and/or Ni. The investigation is motivated by the shortage of knowledge of microstructural features and how they relate to electrochemical performance. Moreover, the study also serves as validation for the Buckingham interatomic potentials developed in chapter 3. The simulated amorphization and recrystallization will be utilized to generate LiM_2O_4 (M=Co, Ni) spinel nanospherical structures [71]. The simulated synthesis technique is essential for introducing myriad structural features that influence battery performance and are also observed in experiments. Thi et al. used simulated amorphization and recrystallization to generate an 8 nm MnO_2 nanostructure comprising a host of microstructural features such as dislocations, vacancy defects, etc. [219]. LiM_2O_4 (M=Co, Ni) amorphous structure is generated under the NVE ensemble. The amorphous state is confirmed by atomic-level snapshots and RDF graphs. Subsequently, the structures are recrystallized under the NVT ensemble. The recrystallized structure is characterized by atomic snapshots, RDF, and X-ray diffraction patterns. The formed phases are compared to theoretical phases and compared to XRD's of the respective phases from experiments. Moreover, the distribution of atoms in the generated spinel nanostructures will be measured by RDFs.

4.2 Method

The amorphisation and recrystallisation technique generated the LiM2O4 (M=Co, Ni) nanostructures successfully. The simulated synthesis was performed with the DL-_POLY code [220] using the interatomic potentials developed in chapter 3. Moreover,

the Li-Li, Li-O, Mn-O, Mn-Mn, and O-O were derived elsewhere [74]. The simulated amorphization was carried out under the microcanonical (NVE) ensemble. In this ensemble, the system is not allowed to share energy and particles with its surroundings. Moreover, the simulated recrystallization is carried out under the NVT ensemble. A conventional LiM_2O_4 (M=Ni, and Co) unit cell structurally optimized by the METADISE code [221] was cleaved into a nanospherical spinel structure containing 26700 atoms as illustrated in figure 4.1. The 26700-atom LiM_2O_4 (M=Ni, Co) nanosphere was used as an input structure for the simulated synthesis. The A&R MD technique was performed with the DL_POLY code, wherein a time per step of 0.0005 ps for 1 000 000 steps, equilibration of 5 000, 1d-2 Ewald precision, and a cutoff radius of 10 Å were employed.

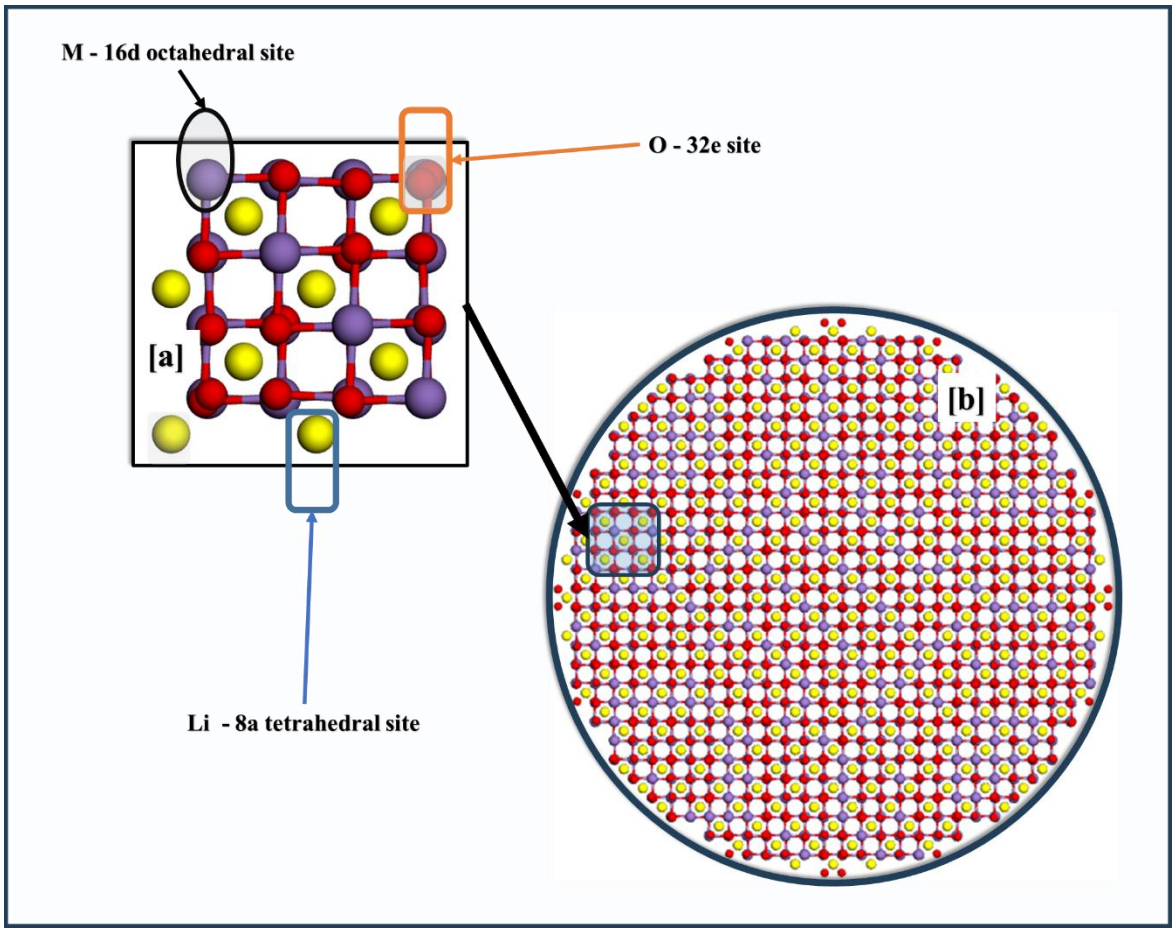

Figure 4.1: The generation of (b) a spinel nanosphere from (a) a conventional spinel unit cell as a required input for the simulated synthesis (A&R). The LiM_2O_4 (M=Co, Ni) spinel is composed of lithium atoms (yellow) in 8a tetrahedral sites, cobalt or nickel atoms in 16d octahedral sites, and oxygen atoms (red) in 32e sites.

4.3 Simulated synthesis of $LiCo_2O_4$ spinel

4.3.1 Simulated Amorphization of $LiCo_2O_4$

In this segment, the simulated amorphization of $LiCo_2O_4$ spinel structure is discussed. The process starts with a crystalline nanosphere comprising 28007 atoms, as illustrated in figure 4.2 (a). The $LiCo_2O_4$ spinel structure was gradually heated up under the microcanonical ensemble. Figure 4.3 illustrates the loss of long-range atomic ordering as evidenced by the broadening of RDF peaks with increasing temperature. The change from crystalline to amorphous was noted at a temperature of ~1900 K. However, the $LiCo_2O_4$ spinel structure was found to be totally amorphous at ~2000 K, as illustrated in figure 4.2 (b). Moreover, the structural snapshot of $LiCo_2O_4$ spinel in figures 4.2 (b) and (c) shows poor or irregular atomic arrangement.

Figure 4.3 shows the RDF graph of the Co-O interaction in $LiCo_2O_4$ spinel at a temperature of 2000 K. A sharp long peak is observed at ~1.89 Å, which denotes a first neighbour distance characterizing the Co-O bond and is responsible for the short-range atomic ordering. A cobalt atom is at least ~1.89 Å atoms apart from an oxygen atom in the amorphous $LiCo_2O_4$ spinel structure. The lack of clear atomic arrangement in the amorphous structure is described by the three broad RDF peaks located at the separation distances of 4.23 Å, 6.57 Å, and 9.07 Å. The broad RDF peaks are associated with a low probability of finding atoms at defined atomic separations. Therefore, the $LiCo_2O_4$ spinel structure at 2000 K exhibits poor long-range atomic ordering.

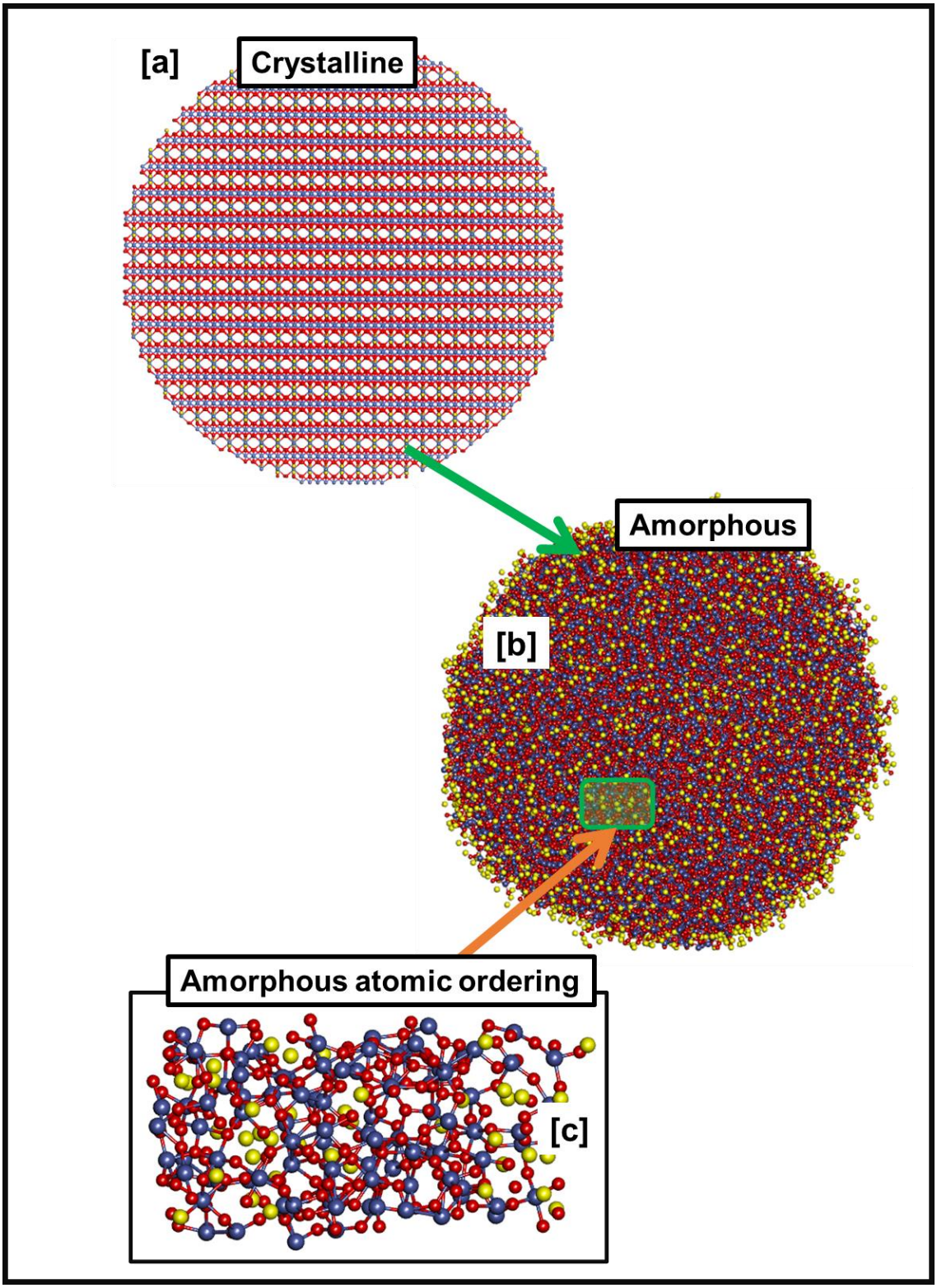

Figure 4.2: (a) A crystalline $LiCo_2O_4$ spinel nanosphere consisting of 28007 atoms gradually heated into (b) an amorphous $LiCo_2O_4$ spinel structure. (c) A small portion of the amorphous $LiCo_2O_4$ spinel structure illustrates the atomic arrangement in the structure.

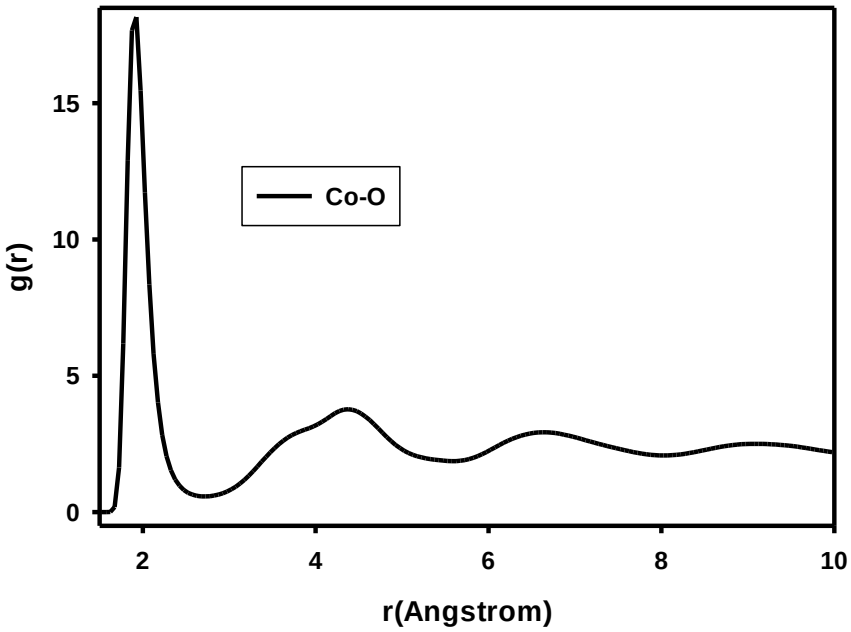

Figure 4.3: Illustration of the RDF graph of the Co-O interaction in $LiCo_2O_4$ spinel.

4.3.2 Simulated Recrystallization of $LiCo_2O_4$

4.3.2.1 Structural Characterization of Recrystallized $LiCo_2O_4$ nanosphere.

The 28007-atom $LiCo_2O_4$ amorphous nanosphere shown in figure 4.2 (b) has been successfully recrystallized and cooled to a temperature of 5 K. Figure 4.4 (a) shows the recrystallized $LiCo_2O_4$ nanosphere, wherein patterns of Li, Co, and O can be noted from the structure, illustrating successful recrystallization. Furthermore, the patterns are pointing in different directions, suggesting that the nanomaterial recrystallized into a polycrystalline structure. A few layers have been cleaved from the $LiCo_2O_4$ nanosphere for examination of recrystallization within the structure, as shown in Figure 4.4 (b). Patterns of Li, Co, and O can be observed in the sliced portion of the polycrystalline $LiCo_2O_4$ spinel nanosphere. The state of the recrystallized $LiCo_2O_4$ spinel structure is also examined with an RDF plot of the Co-O interaction. Figure 4.5 shows the RDF graph of a $LiCo_2O_4$ spinel nanosphere recrystallized at 1900 K and cooled to a temperature of 5 K. The first neighbour distance is observed at ~1.92 Å, which is comparable to the value of the Co-O average bond length in the range between 1.88 Å - 1.92 Å obtained by Jalem et al. [222]. The Co-O average bond distance is the average value for the Mn^{4+} and Mn^{3+} ions. The first neigbhor distance

is followed by two sharp peaks evidencing the presence of long-range atomic ordering in the polycrystalline $LiCo_2O_4$ spinel structure.

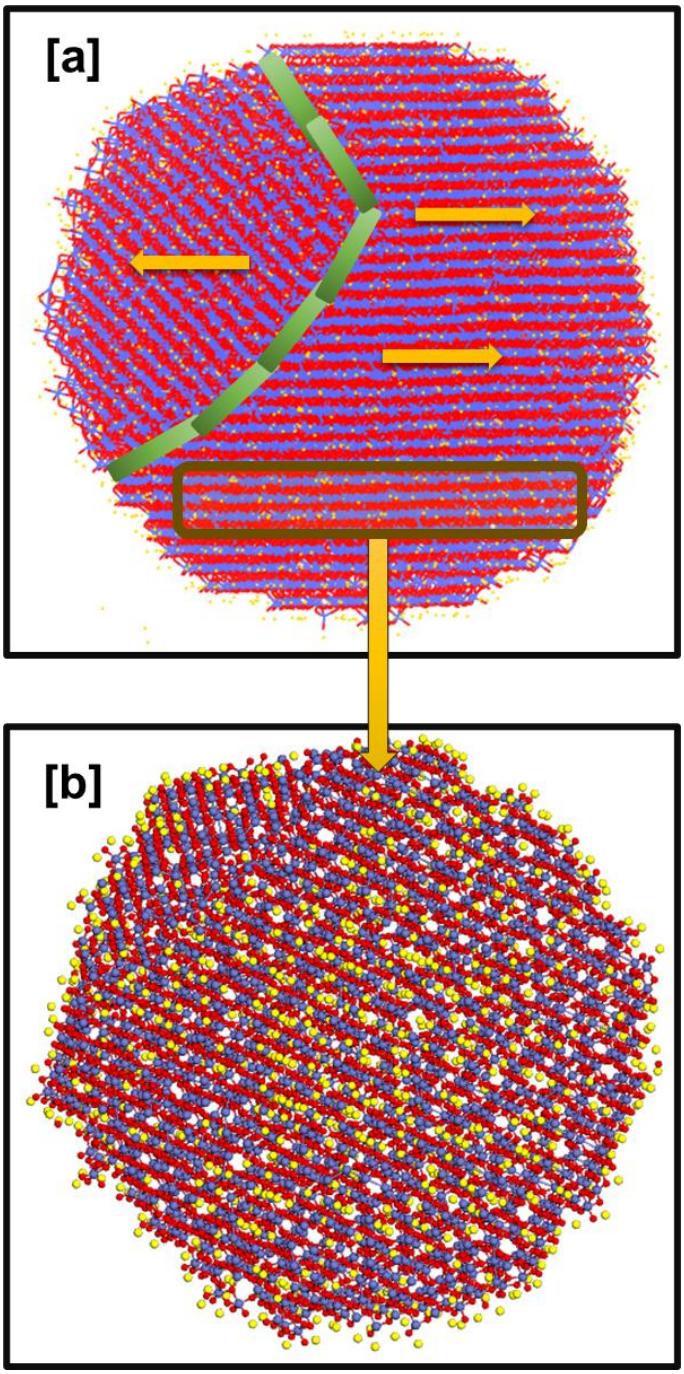

Figure 4.4: (a) $LiCo_2O_4$ spinel nanosphere recrystallized at a temperature of 1900 K showing patterns of Li, Co, and O atoms. (b) A few layers of Li, Co, and O atoms were cleaved from the $LiCo_2O_4$ nanosphere to capture the state of the structure inside.

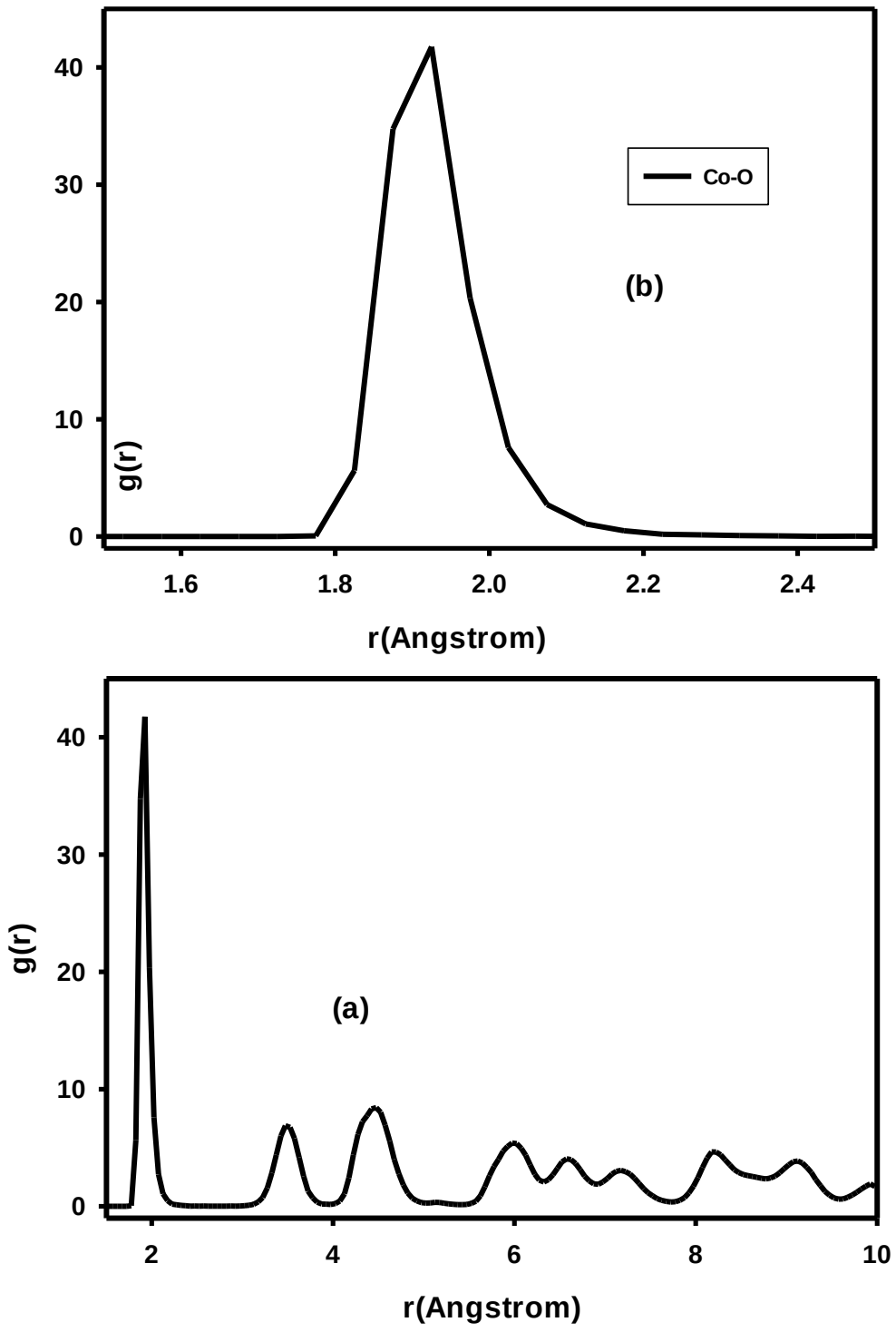

Figure 4.5: (a) RDF of $LiCo_2O_4$ spinel recrystallized at a temperature of 1900 K and cooled to ta temperature of 5 K. (b) The first neighbour peaks in is also magnified.

The recrystallized $LiCo_2O_4$ spinel structure has been characterized at the atomic level, as illustrated in figures 4.6 and 4.7. A portion containing a few layers of Li, Co, and O has been extracted from the recrystallized nanosphere, as shown in figure 4.6 (a).

Lithium, cobalt, and oxygen atoms are occupying lattice positions. This demonstrates the successful recrystallization of the $LiCo_2O_4$ spinel nanosphere. A few cobalt atoms are occupying the 8a tetrahedral sites, where they are surrounded by four oxygen atoms. This suggests the formation of the Co_3O_4 spinel phase, which has been reported to form during the synthesis of $LiCo_2O_4$ spinel at high temperatures [223, 224]. However, the extracted portion of the A&R simulated spinel structure shows a significant number of lithium atoms in the 16c octahedral sites, which are bonded to six oxygen atoms, forming a CoO6 octahedral framework. Figure 4.6 (b) shows a spinel phase captured from the extracted portion in Figure 4.6 (a). Oxygen atoms can be observed in the 32e lattice sites, and cobalt atoms are noted in the 16d octahedral sites. Lithium atoms are noted in the 16c octahedral sites instead of the 8a tetrahedral sites, due to the high-temperature Co_3O_4 impurity phase. The Co^{2+} in the tetrahedral sites precipitates the hoping of Li^+ ions into the 16c octahedral sites [224, 225]. Furthermore, the captured spinel phase is validated by a theoretical $LiCo_2O_4$ spinel model shown in figure 4.6 (c), showing the Li, Mn, and O atoms occupying the 16c octahedral, 16d octahedral, and 32e sites, respectively.

Figure 4.7 illustrates the $LiCo_2O_4$ spinel phase in the A&R-simulated structure in a layer view. The portion was extracted from the structure in figure 4.4 (a). Figure 4.7 (b) shows a spinel phase, in which a layer that is characterized by a lithium atom that is followed by three cobalt atoms is in between two layers of oxygen atoms. The layer pattern is comparable to a theoretical layer pattern of the spinel phase shown in Figure 4.7 (c). Moreover, another layer-view of atoms has been captured in Figure 4.7 (d), where a layer of alternating Li and Co atoms is in between two oxygen layers. The pattern is comparable to the theoretical model of a layer-view pattern of spinel shown in Figure 4.7 (e). Furthermore, the Co_3O_4 spinel phase is also observed in the recrystallized $LiCo_2O_4$ spinel structure. In experiments, it has been found that the Co_3O_4 impurity phase occurs in the spinel structure at elevated temperatures [224]. Figure 4.8 (a) illustrates the presence of the Co_3O_4 spinel phase in the structure, which has been further magnified in Figure 4.8 (b) and compared to a theoretical Co_3O_4 model in Figure 4.8 (c).

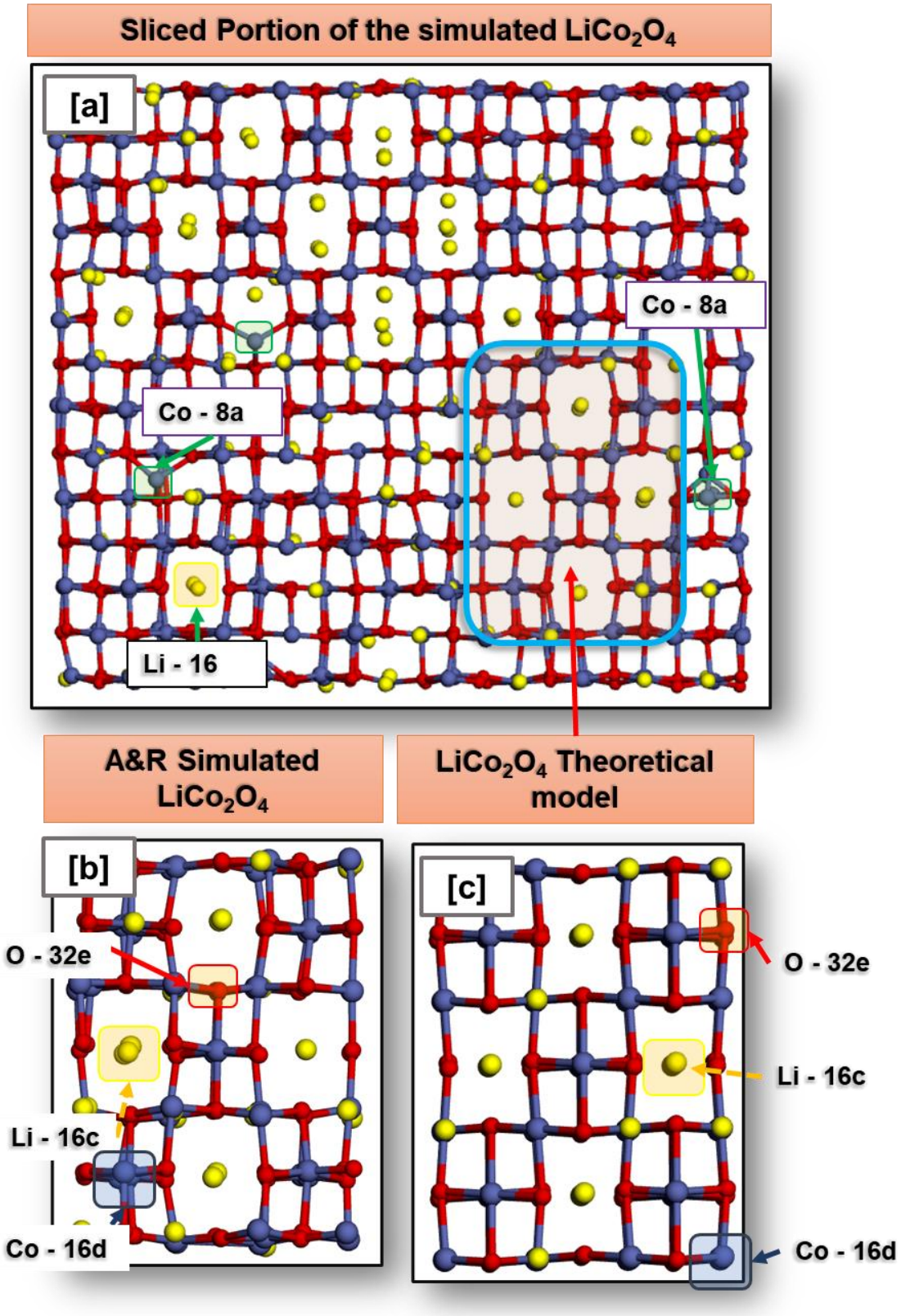

Figure 4.6: Demonstration of (b) a $LiCo_2O_4$ spinel phase in a slice portion of the A&R-simulated spinel nanosphere. The simulated spinel phase is validated by (c) theoretical spinel model.

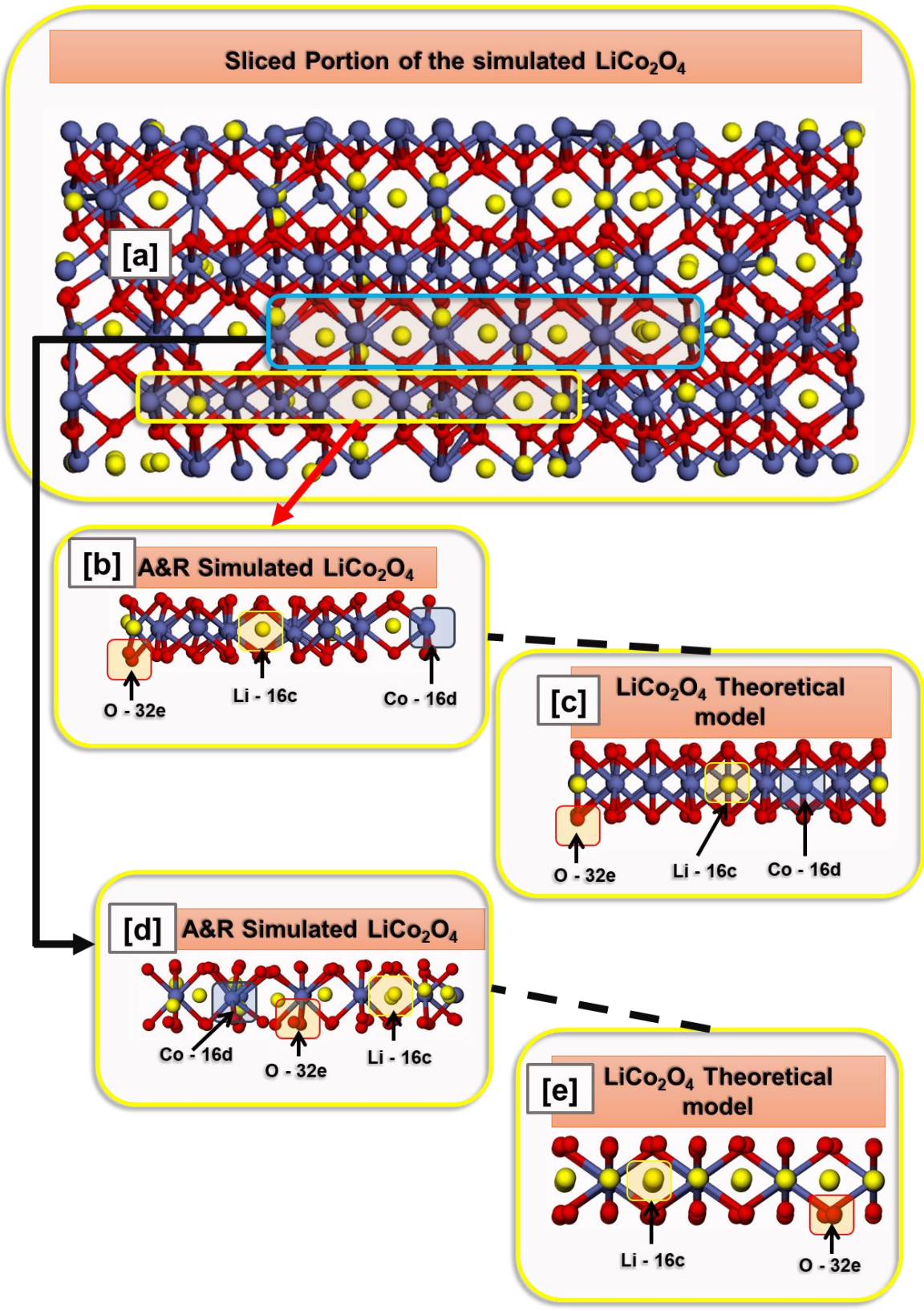

Figure 4.7: (a) Illustration of the layer view of $LiCo_2O_4$ spinel observed from a sliced portion of the A&R-simulated $LiCo_2O_4$ spinel nanosphere. The A&R simulated models are compared to their respective theoretical models.

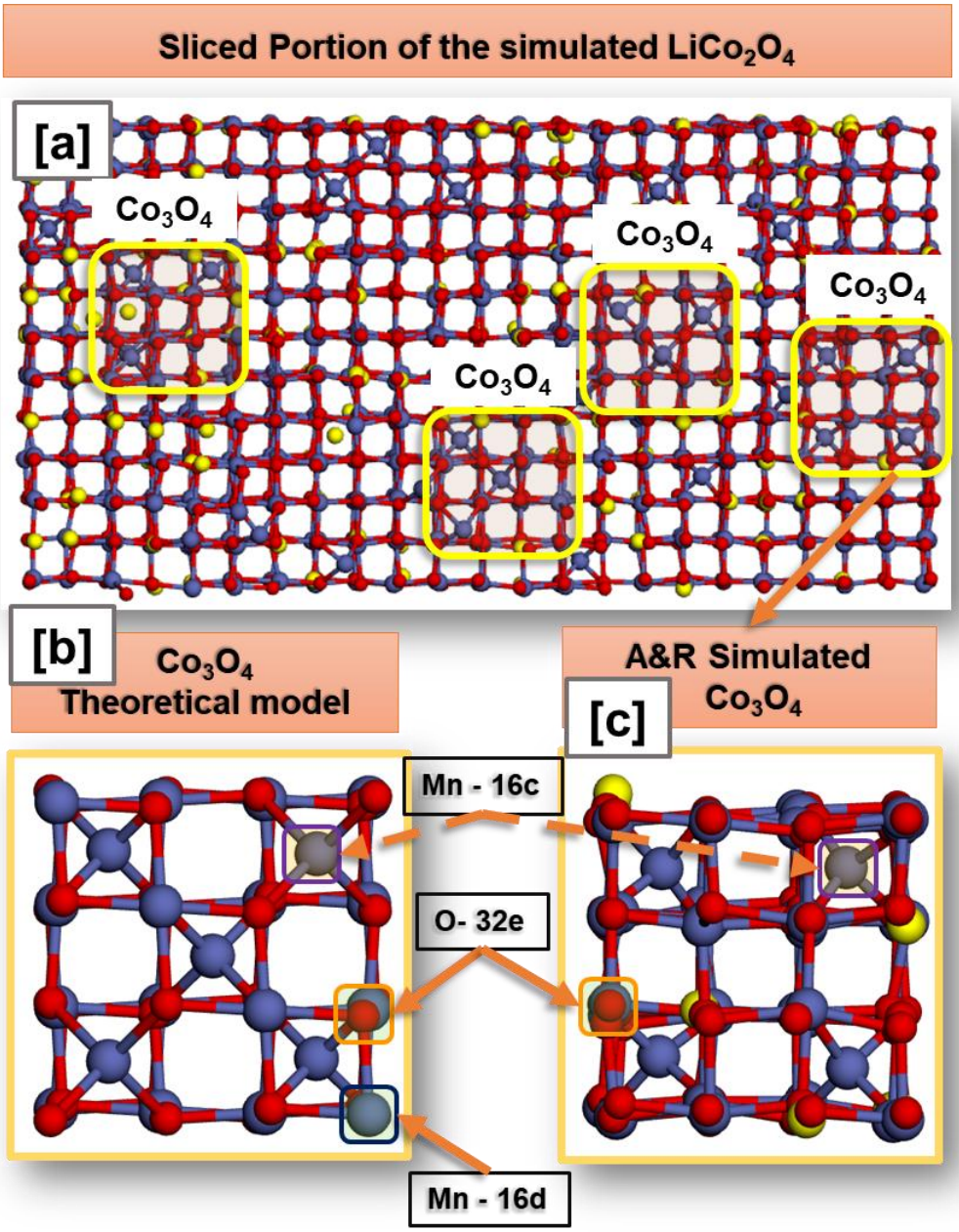

Figure 4.8: (a) A portion of the recrystallized $LiCo_2O_4$ showing the presence of the (a) Co_3O_4 high temperature impurity phase occurring during synthesis. The simulated Co_3O_4 phase is compared to the (c) Co_3O_4 theoretical model.

4.3.2.2 Characterization Through X-ray Diffraction Patterns.

The recrystallized $LiCo_2O_4$ spinel structure was further characterized through XRD patterns, as illustrated in Figure 4.9 (a). The XRD pattern can be indexed to the cubic symmetry of the space group of Fd-3m. All the major spinel diffraction peaks from the diffraction planes (111), (311), (222), (400), (331), (511), and (440) are observed in the diffraction pattern. The successful recrystallization of the spinel structure is also

confirmed by the well-resolved diffraction peaks. The XRD pattern of the A&R-simulated spinel structure is validated by the XRD pattern of $LiCo_2O_4$ spinel from literature shown in Figure 4.9 (b) [224]. The XRD pattern also shows the presence of the Co_3O_4 impurity phase, characterized by the diffraction peak from the (220) plane. The presence of this phase is validated by the XRD pattern of Co_3O_4 from experiment shown in Figure 4.9 (c) [226]. Furthermore, XRD peak splitting at (111), (311), (400), and (331) reflections can be attributed to the co-existence of the Li_2CoO_3 and Co_3O_4 impurity phases in the structure with the $LiCo_2O_4$ at high temperatures.

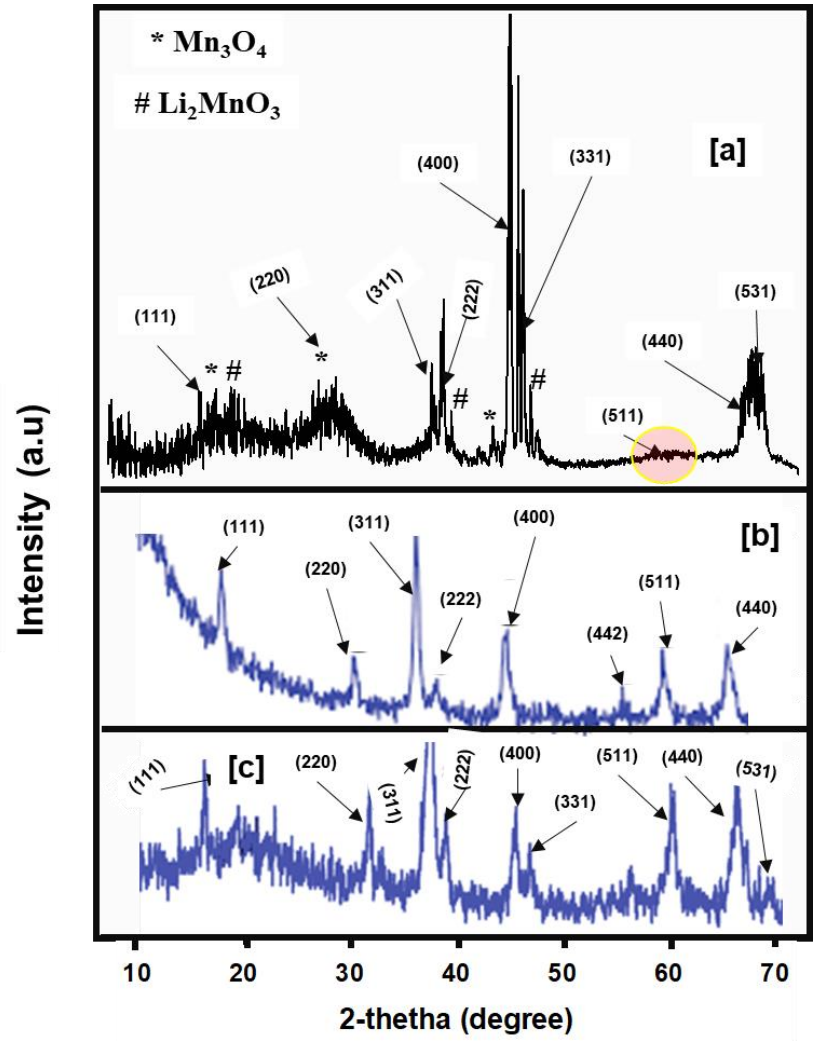

Figure 4.9: XRD pattern of an 8.01 nm A&R-simulated $LiCo_2O_4$ spinel structure compared to the XRD patterns of (b) $LiCo_2O_4$ [224] and (c) Co_3O_4 from experiments [226].

4.4 Simulated synthesis of $LiNi_2O_4$ spinel

4.3.1 Simulated Amorphization $LiNi_2O_4$ spinel

In this section, the simulated amorphization of $LiNi_2O_4$ spinel structure under the microcanonical ensemble (NVE) is discussed. The final amorphized $LiNi_2O_4$ spinel structure is demonstrated in Figure 4.10 (b). The 28007-atom $LiNi_2O_4$ spinel nanosphere illustrated in Figure 4.10 (a) was heated in a step-by-step manner up to a temperature of 1900 K. The structure was found to be totally amorphous at this temperature. A small portion has been sliced from the amorphous $LiNi_2O_4$ structure in Figure 4.10 (b) to illustrate the arrangement of atoms in the structure as illustrated in Figure 10 (c). The random positioning of atoms in the structure can be clearly observed in the diagram. Furthermore, the amorphous state of the $LiNi_2O_4$ spinel structure was also examined through the RDF graph in Figure 4.11. The bonding of Ni and O in the amorphous $LiNi_2O_4$ spinel structure is shown by the first neighbour distance illustrated in the RDF graph in Figure 4.11 around the separation distance of ~1.91 Å. The second neighbour distance is observed at ~4.25 Å. The RDF peaks are very broad, indicating a lack of long-range atomic arrangement. Moreover, the third neighbour distance is noted at around 6.57 Å, with a much lower probability than the second neighbour distance. Furthermore, the fourth neighbour distance is widely spread and can be observed at the atomic separation of ~ 9.09 Å.

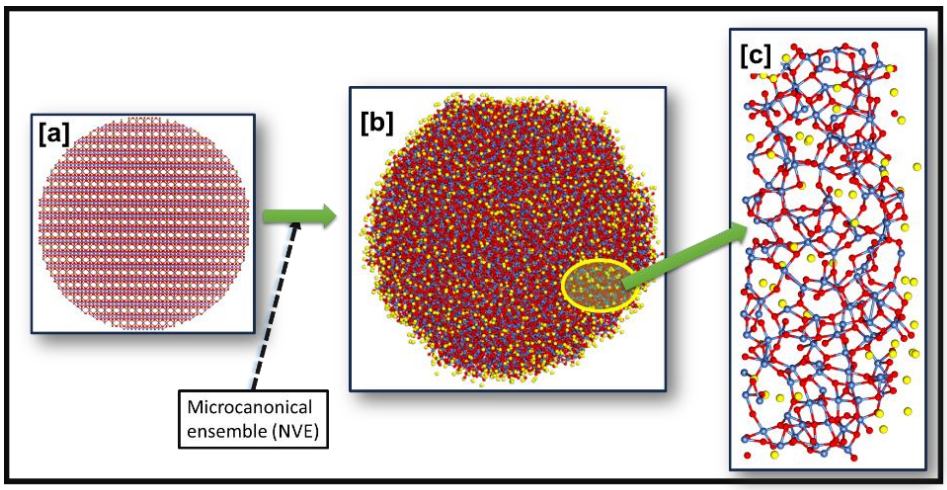

Figure 4.10: (a) A crystalline $LiNi_2O_4$ nanosphere amorphized at 1900 K to form (b) a $LiNi_2O_4$ amorphous structure. (c) An extracted portion of the $LiNi_2O_4$ amorphous structure.

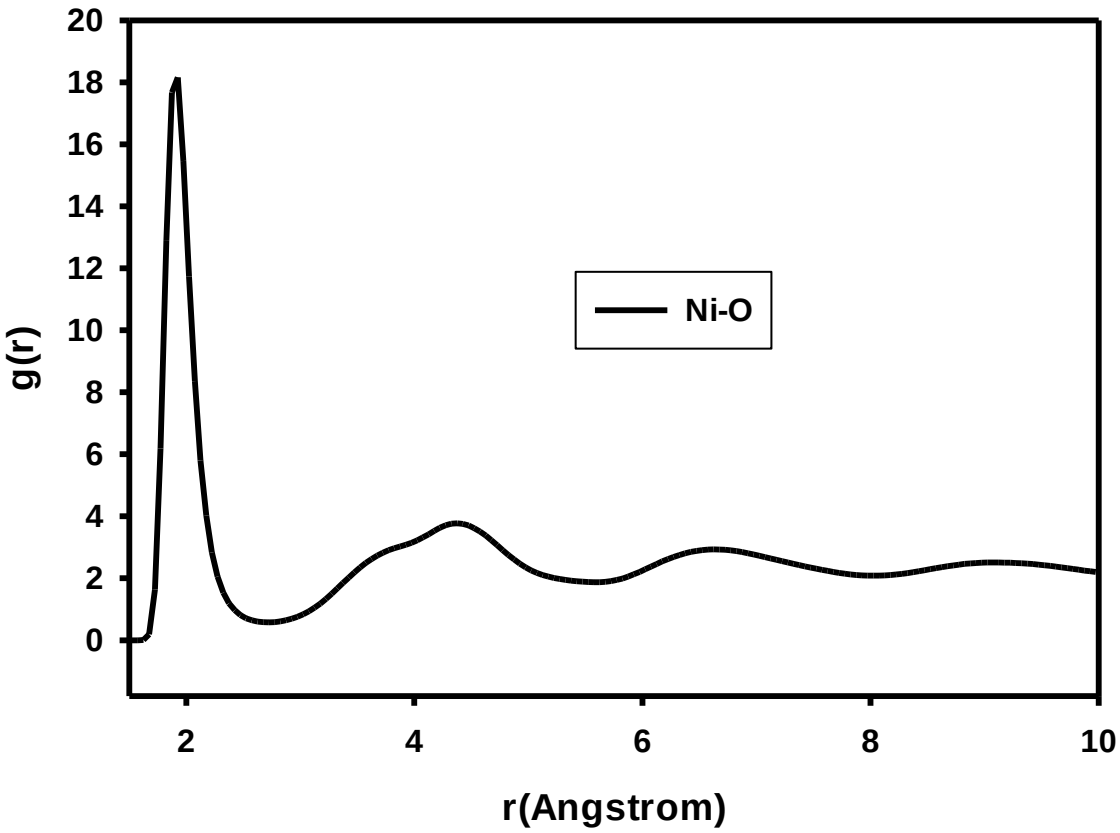

Figure 4.11: RDF graph of the Ni-O interaction in $LiNi_2O_4$ spinel showing the amorphous state of this material.

4.3.2 Simulated Recrystallization of $LiNi_2O_4$

4.3.2.1 Structural characterization of $LiNi_2O_4$ spinel

In this segment, the characterization of $LiNi_2O_4$ spinel through atomic-level snapshots is discussed. Figure 4.12 (a) shows the successful recrystallization of the $LiNi_2O_4$ spinel structure, as evidenced by the clear arrangement of atoms in line patterns. Lines of oxygen atoms are observed in the figure, which are between a mixed layer of lithium and nickel atoms. The line patterns indicate that atoms in the A&R-simulated $LiNi_2O_4$ spinel structure are in an ordered atomic arrangement. Grain 1 and grain 2 in the structure images show the different orientations of atoms in the structure. It shows that the $LiNi_2O_4$ spinel structure recrystallized into a polycrystalline material. The successful recrystallization is also confirmed by the RDF graph of the Ni-O interaction in figure 4.13. The RDF peaks that follow the peak denoting the first neigbhour interaction are sharp, which suggests the presence of long-range atomic ordering in

the figure. Moreover, the bond distance of the Ni-O interaction was found to be ~1.91 Å.

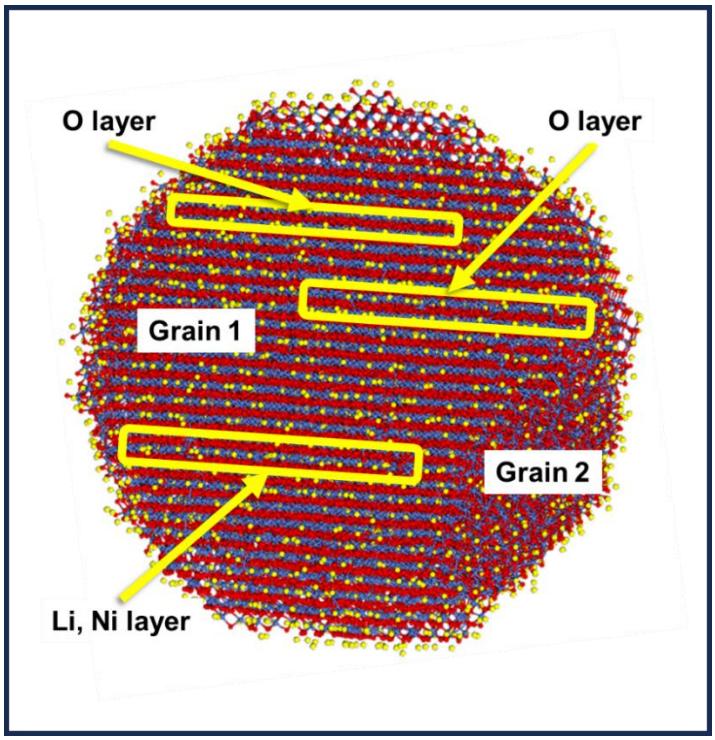

Figure 4.12: Recrystallized $LiNi_2O_4$ showing atoms arranged in line patterns.

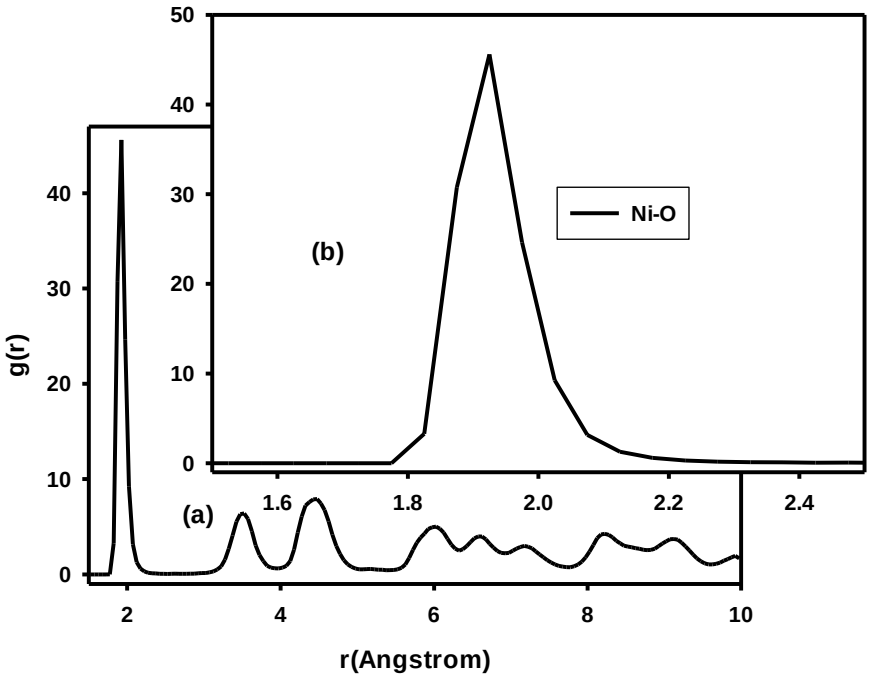

Figure 4.13: (a)RDF graph of the Ni-O interaction in $LiNi_2O_4$ showing successful recrystallization of this material. An inset, showing the Ni-O first neighbour RDF peak.

The 8.01 nm $LiNi_2O_4$ spinel recrystallized into a polycrystalline structure, introducing essential structural features such as grain boundaries and point defects, which are also noted in materials synthesized in experiments. Figure 4.14 (b) shows four different orientations of atoms in the material. This stems from the formation of small nuclei at different locations in the material during recrystallization. The nuclei form at the most stable sites in the structure, which results in the formation of a polycrystalline material. The interface of the four grains is called a grain boundary, which is significantly observed in nanomaterials from experiments [227, 228, 229]. As such, our results will be comparable to what is also observed in experiments. Figure 4.14 (c), (d), and (e) illustrate the interface of two grains and the difference in the orientation of atoms in the two grains.

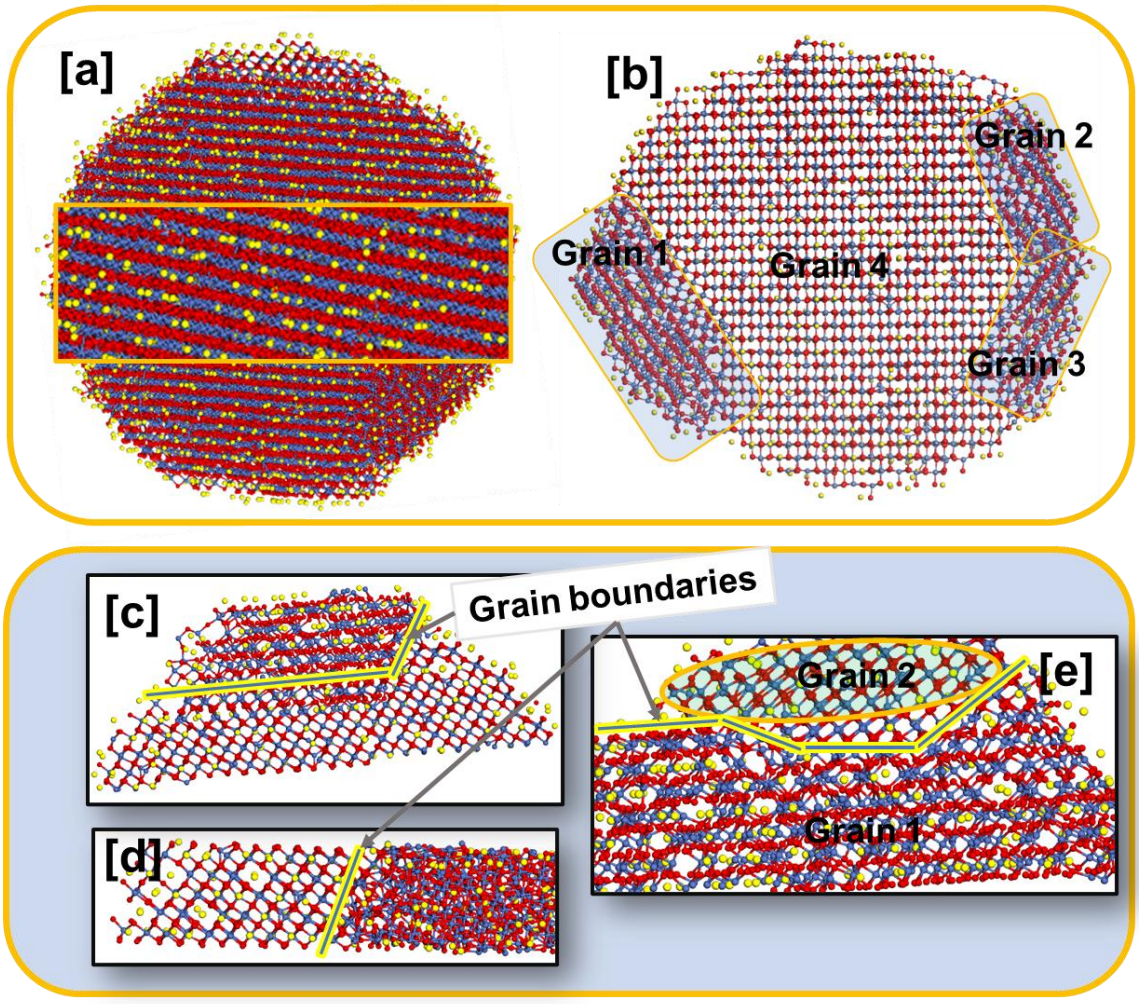

Figure 4.14: Illustration of the successful recrystallization of (a) $LiNi_2O_4$ spinel. The ~8.01 nm $LiNi_2O_4$ spinel structure recrystallized into a polycrystalline nanosphere is illustrated by (b), (c), (d), and (e).

The recrystallized $LiNi_2O_4$ spinel structure was further characterized through atomic-level snapshots. A few layers of atoms of the recrystallized $LiNi_2O_4$ spinel have been extracted to examine the spinel phases that formed during recrystallization, in figure 4.15 (a). In Figure 4.15 (a), a $LiNi_2O_4$ spinel phase magnified and illustrated in figure 4.15 (b) is noted. The conventional unit cell view of $LiNi_2O_4$ illustrates the position of lithium atoms in the 16c octahedral sites. Moreover, manganese and oxygen atoms are situated at the 16d and 32e sites, respectively. The A&R simulated spinel phase is validated with a theoretical model of the conventional unit cell view shown in figure 4.15 (c). Moreover, the presence of the Ni_3O_4 impurity phase that forms during a high-temperature synthesis has also been captured. Figure 4.16 (b) shows the A&R-simulated Ni_3O_4 phase, which is compared to a theoretical Ni_3O_4 model illustrated in Figure 4.16 (c). Moreover, some of the Ni atoms are occupying the 8a tetrahedral sites.

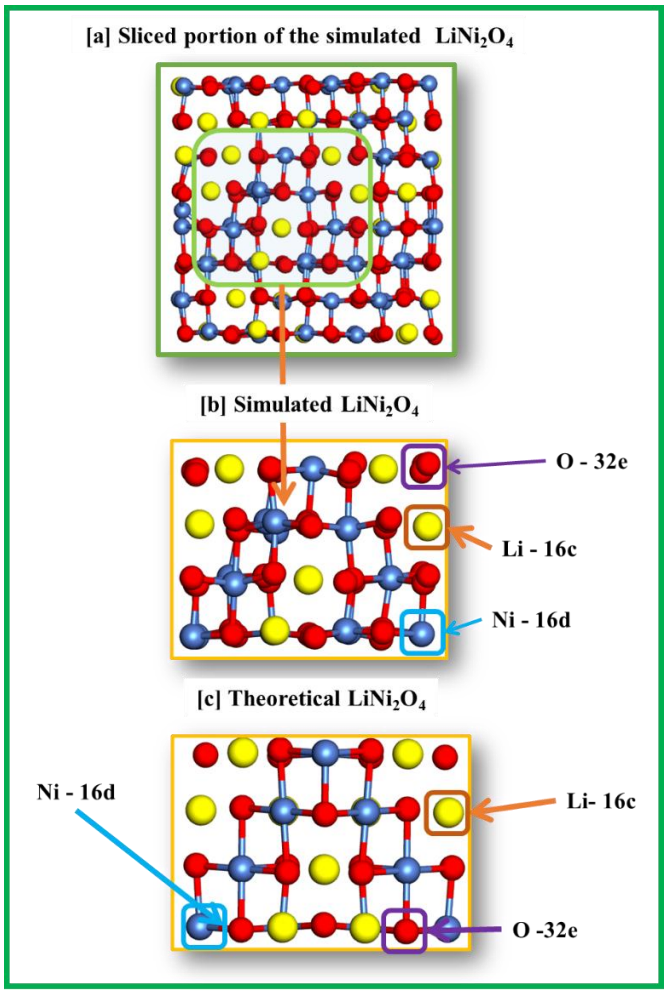

Figure 4.15: The conventional unit cell view of the (b) A&R-simulated $LiNi_2O_4$ spinel view compared to (c) a theoretical model.

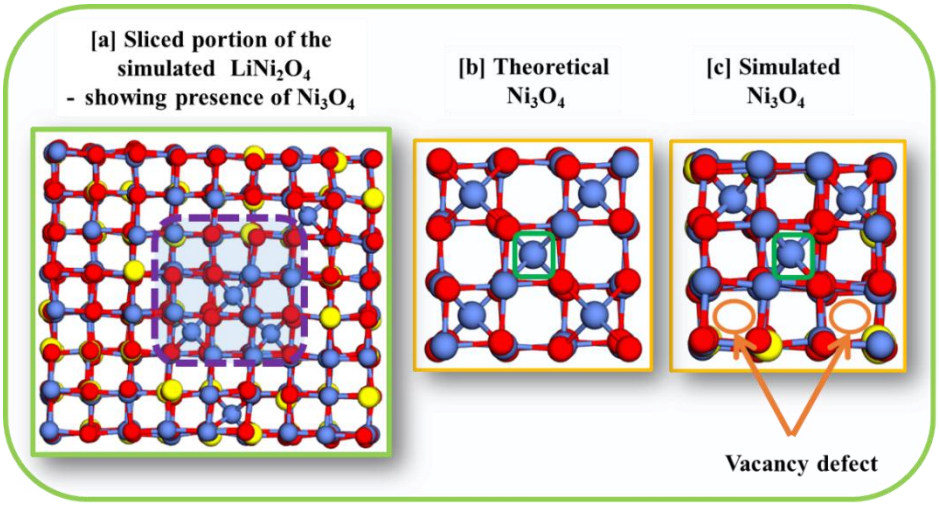

Figure 4.16: The (b) Ni_3O_4 impurity phase emerging at high temperatures in the recrystallized $LiNi_2O_4$ spinel structure viewed against (c) a theoretical Ni_3O_4 spinel phase.

4.3.2.2 Characterization of $LiNi_2O_4$ spinel through XRD patterns

The recrystallized $LiNi_2O_4$ spinel structure was further characterized with XRD patterns to deduce the recrystallization and the spinel phases that formed after synthesis. The XRD pattern of the 8.01 nm $LiNi_2O_4$ spinel structure generated through the simulated A&R technique is illustrated in figure 4.17 (a). The XRD peaks that characterized the $LiNi_2O_4$ spinel phase can be noted in the XRD pattern. The $LiNi_2O_4$ characteristic peaks are observed at ~20.35° (111), 38.8° (311), 38.91° (222), 45.30° (400), 45.70° (331), 65.30° (440), and 66.15° (531) 2θ degrees. As such, the XRD pattern can be indexed to a spinel structure of cubic symmetry with a space group of Fd-3m. These diffraction peaks are also noted in the XRD pattern of $LiNi_2O_4$ determined by Thomas and co-workers [116]. Moreover, the XRD diffraction peak observed at ~29.45° 2θ degrees is linked to the Ni_3O_4 spinel impurity peak. This phase results from the occupation of the 8a tetrahedral sites by the transition element (Ni) in a spinel structure at elevated temperatures. Moreover, the small, less intense XRD peaks attributed to the Li_2NiO_3 high-temperature impurity phase are also observed. The peaks form around the (111), (400), (331), and (531) reflections. The formation of these impurity phases was confirmed by XRD patterns of Mn_3O_4 and Li_2MnO_3 due to the lack of well-resolved XRD peaks of Ni_3O_4 and Li_2NiO_3 [230, 231].

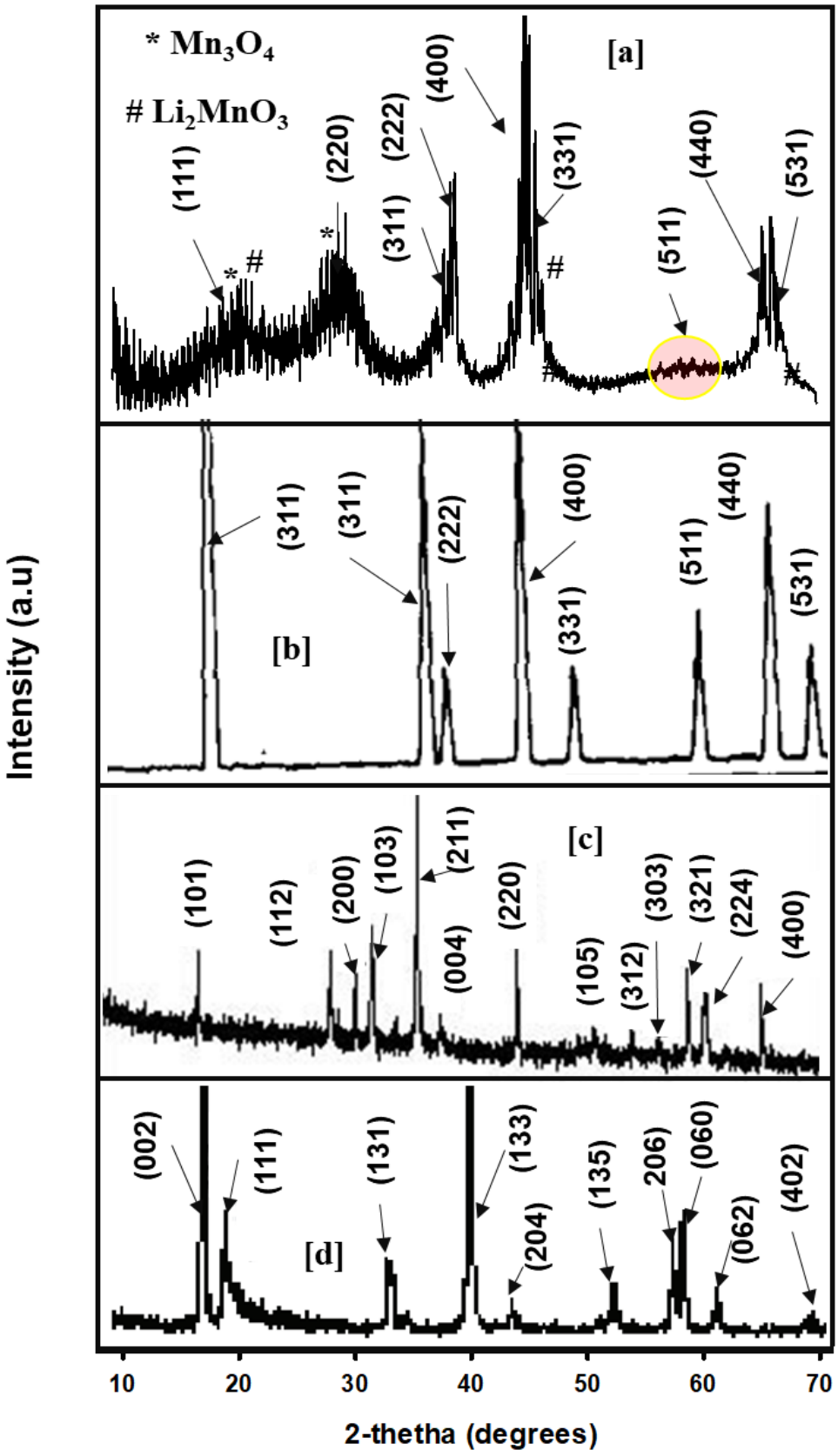

Figure 4.17: The Ni_3O_4 impurity phase emerges at high temperatures in the recrystallized $LiNi_2O_4$ spinel structure.

4.5 Discussion

The reported poor capacity retention of $LiMn_2O_4$ can be improved by substituting a small percentage (1 %) of manganese with Co and/or Ni [76, 77, 78]. However, little is known about the impact of this substitution on the microstructure and the migration of Li^+ in the structure. Hence, the interatomic potentials for the Co-Co, Co-Li, Co-O, Ni-Ni, Ni-Li, and Ni-O interactions developed in Chapter 3 were employed to generate LiM_2O_4 (M=Co, Ni) nanostructures with the simulated synthesis technique [71]. The simulated synthesis technique facilitated the formation of microstructural features such as vacancy point defects, grain boundaries, etc., which significantly affect electrochemical performance. Moreover, the A&R-simulated structures are comparable to experimental materials. The microstructure of $LiNi_2O_4$ was elucidated to guide the doping of $LiMn_2O_4$ with Co and/or Ni and to also serve as a test of the Buckingham interatomic potentials derived in this work.

The first step of the simulated amorphization and recrystallization technique is the simulated amorphization. An 8.01 nm $LiCo_2O_4$ crystalline spinel structure was successfully recrystallized, as confirmed by the structure images and RDF graph of the Co-O interaction. The Co-O interactions make up the Co_2O_4 framework, in which Li atoms are intercalated. The structure images show random arrangement in the structure, which suggests that the material is in an amorphous state. This is confirmed by the broad RDF peaks that follow the first neighbour distance peak. The subsequent step of the A&R-simulated technique is simulated recrystallization. As such, the amorphous $LiCo_2O_4$ spinel structure was recrystallized. The Li, Co, and O atoms were observed in lattice sites on the atomic-level structure images, which shows that the structure recrystallized successfully. The successful recrystallization was also confirmed by the sharp RDF peaks of the Co-O interaction.

Structural characterization was performed through atomic structure snapshots and XRD patterns. The A&R-simulated spinel phases showed that Li atoms occupy the 16c octahedral sites, Co atoms are situated at the 16d octahedral sites, and O atoms occupy the 32e sites. The occupation of the 16c by Li atoms can be attributed to the occupation of the 8a tetrahedral sites by Co atoms. The cooperative displacement of Li 8a into 16c octahedral sites by the transition metal was also noted in literature [224,

225]. Furthermore, the occupation of the 8a tetrahedral sites is due to the formation of the Co_3O_4 impurity phase, which coexists with $LiCo_2O_4$ at high temperatures.

In addition, the A&R simulated structure was also characterized by XRD patterns. The dominance of the $LiCo_2O_4$ spinel phase was confirmed by sharp and intense RDF peaks, which were validated with XRD patterns calculated in experiments [224]. The $LiCo_2O_4$ spinel phase was found to co-exist with the Co_3O_4 and Li_2CoO_3 impurity phases due to high-temperature synthesis. Therefore, a high-temperature synthesis technique that does not mitigate the formation of the Co_3O_4 phase may exhibit poor electrochemical performance. Since the occupation of the 8a tetrahedral sites by the transition metal in a spinel system hinders the transport of Li^+ ions in the structure. Moreover, the Co-O bond length was found to be ~1.92 Å, which was comparable to the value determined by Jalem et al. that ranges from ~1.88-1.92 Å [222]. The Co-O bond length calculated in this study is less than the Mn-O bond length of ~1.923 Å observed in experiments [232]. Therefore, a stronger Co-O bond than the Mn-O bond is expected in a Co-doped $LiMn_2O_4$ spinel. Since a shorted bond length means higher electron affinity, which is also directly proportional to bond strength.

The $LiNi_2O_4$ spinel structure was also synthesized with the simulated A&R technique. The successful amorphization of $LiNi_2O_4$ was also affirmed by the broad RDF peaks of the Ni-O interactions and the random atomic arrangement observed in the atomic structure images. Consequently, the amorphous structure was recrystallized. The recrystallized structure was then characterized through atomic structure snapshots and XRD patterns. The A&R-simulated spinel structure compares well with the theoretical spinel structure. The structure images show Mn atoms in the 16d octahedral sites, O atoms in the 32e sites, and Li atoms at the 16c octahedral sites. Moreover, XRD patterns were also employed to characterize the A&R-simulated spinel structure. The XRD pattern of the simulated structure is in good agreement with the XRD pattern obtained by Thomas and co-workers [116]. The simulated XRD pattern reveals that the $LiNi_2O_4$ spinel phase also exists side by side with the Ni_3O_4 and Li_2NiO_3 impurity phases. The Ni_3O_4 impurity phase can be linked to the occupation of the 16c sites by Li atoms and the occupation of the 8a tetrahedral sites by Ni atoms. Ni_3O_4 has a negative impact on electrochemical performance, particularly for Li^+ ion transport. Li_2NiO_3 can improve the capacity of the spinel structure since it has been reported to form a composite structure with spinel systems [233, 234]. A layered-spinel

composite structure is reported to exhibit synergistic effects, which results in high power and high energy density. Furthermore, the Ni-O bond (~1.91 Å) distance was also found to be smaller than the Mn-O bond (~1.923 Å) distance determined in experiments [232]. Therefore, the capacity retention of $LiMn_2O_4$ can be improved by the introduction of Ni in the structure. Since a decrease in bond distance implies an increase in bond strength.

The derived Buckingham interatomic potentials were able to perform the simulated synthesis of $LiCO_2O_4$ and $LiNi_2O_4$. The simulated structures compare well with experiments [116, 224]. Moreover, microstructural features such as grain boundaries were simulated with the derived potentials. The observed formation of the M_3O_4 and Li_2MO_3 (M=Co, Ni) impurity phases in experiments was captured with the derived potentials [233, 234].

CHAPTER 5

Simulated Synthesis of Transition Metal (Ni, Co) Doped $LiMn_2O_4$ Spinel Nanospheres.

In this chapter, we examine the effect of replacing a small amount of manganese with Co or Ni on the microstructure and transport properties of the $LiMn_2O_4$ spinel structure. Microstructural changes and transport properties such as diffusion affect the performance of Li-ion batteries. The introduction of Co and Ni in $LiMn_2O_4$ for stabilizing the $LiMn_2O_4$ spinel structure to improve its cyclic performance can affect its microstructure and the diffusion of Li^+ ions in the material. Hence, we utilize large-scale atomistic simulations to monitor the impact of Co and Ni in the $LiMn_2O_4$ spinel on its microstructure. Furthermore, the effect of replacing a small amount of manganese with Co and/or Ni on the conductivity of the material will also be investigated. The incorporation of Co and/or Ni in the $LiMn_2O_4$ spinel structure was found to stabilize the MO_6 (M = Mn, Co, and Ni) octahedra. This has been attributed to the fact that Co and Ni have a smaller ionic radius than Mn [215, 216]. Moreover, Co and Ni have comparable ionization energies to that of Mn. Therefore, the 3+ and 4+ charge states are equally accessible in M (M=Mn, Co, and Ni). The results will shed light on the most effective dopants and the improvements that can be realized through cation doping. The chapter is motivated by the lack of information on the effect of Co- and Ni-doping on $LiMn_2O_4$ spinel at the microscale. Moreover, the work is also a test of the Buckingham interatomic potentials developed in Chapter 3, particularly for the Co-Mn, Co-Ni, and Mn-Ni interactions.

5.1 Method

The simulated synthesis technique [71] has been employed to generate Co- and Ni-doped $LiMn_2O_4$ spinel nanostructures. The technique can generate simulated models that are structurally comparable to materials synthesized in experiments. Therefore, valuable insights can be drawn from models generated by the A&R simulated synthesis technique. The DL_POLY code, which is a molecular dynamics simulation program, was used in this work to generate the doped $LiMn_2O_4$ spinel structures. A conventional spinel unit cell consisting of 56 atoms (8 Li, 32 O, and 16 Mn) was cleaved into a nanospherical structure. The $LiMn_2O_4$ nanospherical structure was then

heated under the microcanonical ensemble in a systematic manner until it became amorphous. In a microcanonical ensemble, the particles possess the same energy and are confined to a non-changing volume. A small amount (1%) of manganese is then replaced from the $LiMn_2O_4$ amorphous structure with the dopants (Co and/or Ni). The doping is followed by the simulated recrystallization, which is performed under the canonical ensemble, wherein the temperature of the system is kept constant. Moreover, the volume and the number of particles are also kept constant in the system. The occupation of lattice sites by the dopants in the recrystallized Co- and/or Ni-doped $LiMn_2O_4$ spinel structure is governed by the underlying forcefields and the spontaneous recrystallization process. Moreover, the recrystallized structures are further systematically cooled to a temperature of 5 K to reduce atomic vibrations for characterization. Figure 5.1 summarizes the procedure schematically.

The calibration of temperature was performed by the Nose-Hoover thermostat. Furthermore, the simulated amorphization and recrystallization were performed for a timer per step of 1e-16 s and 3e-15 s, respectively. Moreover, in both processes, the structures were equilibrated for 50 000 steps, and the Ewald summation method was also employed, which considered atoms within an atomic distance of 10 Å. The generated nanostructures will be examined with atomic-level snapshots, RDF graphs, and XRD patterns. The phases emerging during synthesis will be characterized with XRD graphs and atomic-level structure images. A plot of diffusion coefficients at various temperatures will be utilized to investigate the migration of lithium atoms in the structure.

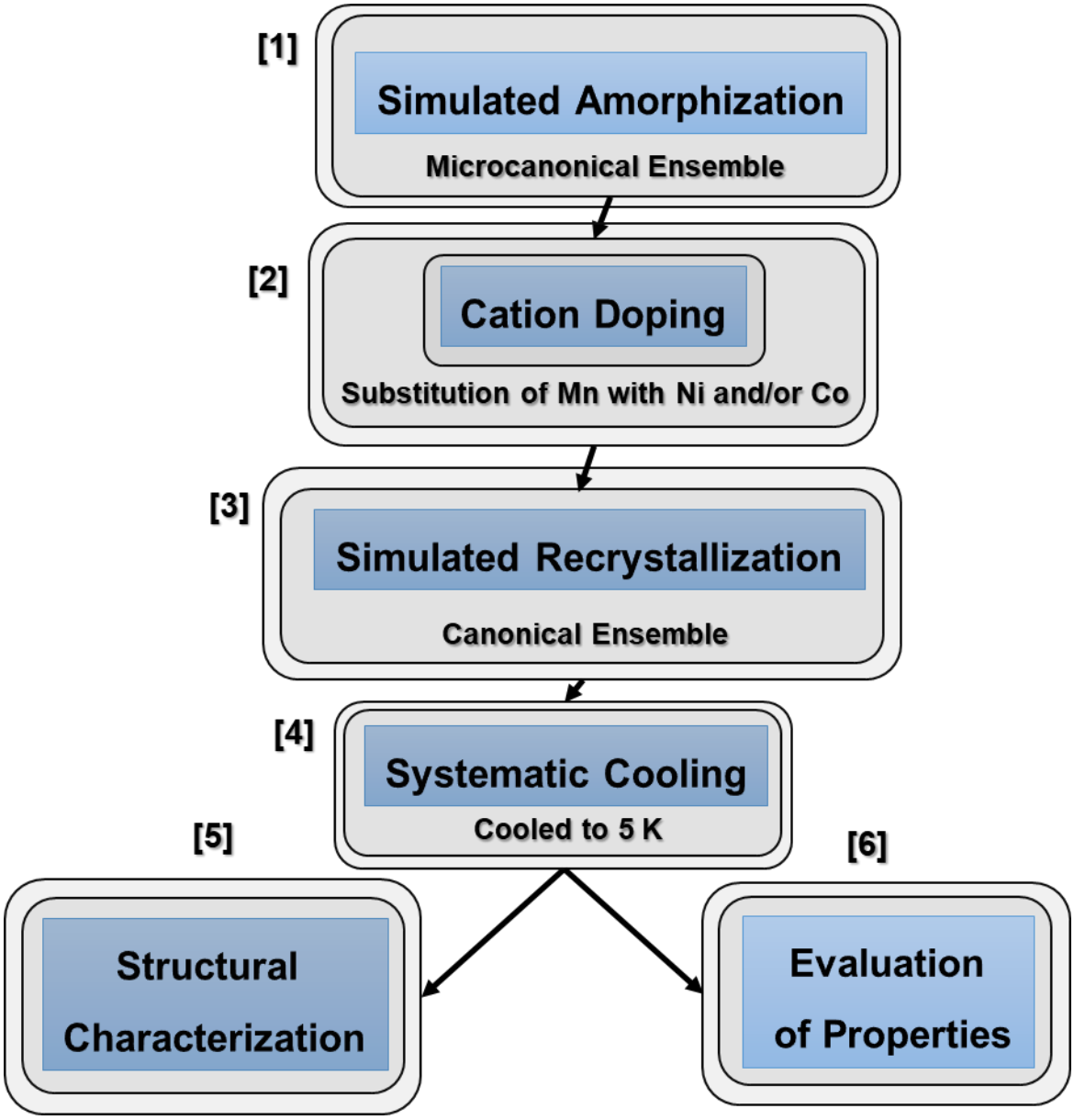

Figure 5.1: Schematic illustration of the workflow employed in this chapter.

5.2 Simulated amorphization of $LiMn_2O_4$ spinel nanosphere

The replacement of a small percentage of manganese atoms in $LiMn_2O_4$ spinel with Co and/or Ni is performed on an amorphous structure. The Co- and/or Ni-doped amorphous $LiMn_2O_4$ spinel structure is then allowed to recrystallize. A 28007-atom $LiMn_2O_4$ crystalline nanosphere optimized with the METADISE program was systematically heated to a temperature of 1800 K [221], where it was found to be amorphous. The $LiMn_2O_4$ spinel structure was examined with the Materials Studio atomic structure visualization programs, and it was found to be disordered at this temperature (1800 K), as illustrated in figure 5.2. Figure 5.2 shows no definitive atomic

ordering, which shows that the structure is amorphous. Moreover, the structure was evaluated with RDF of the Mn-O interaction, which details the distribution of oxygen and manganese atoms in the structure. The first neighbor distance is observed at a separation distance of ~1.910 Å in the RDF graph shown in figure 5.3. The first RDF peak of the Mn-O interaction is responsible for the short-range atomic arrangement and is a characteristic of the bond between Mn and O in the $LiMn_2O_4$ amorphous structure. The RDF peaks that follow the first neighbor distance are broad, which indicates the minimal existence of long-range atomic arrangements in the structure. From this, it can be deduced that $LiMn_2O_4$ spinel at a temperature of 1800 K is in an amorphous state.

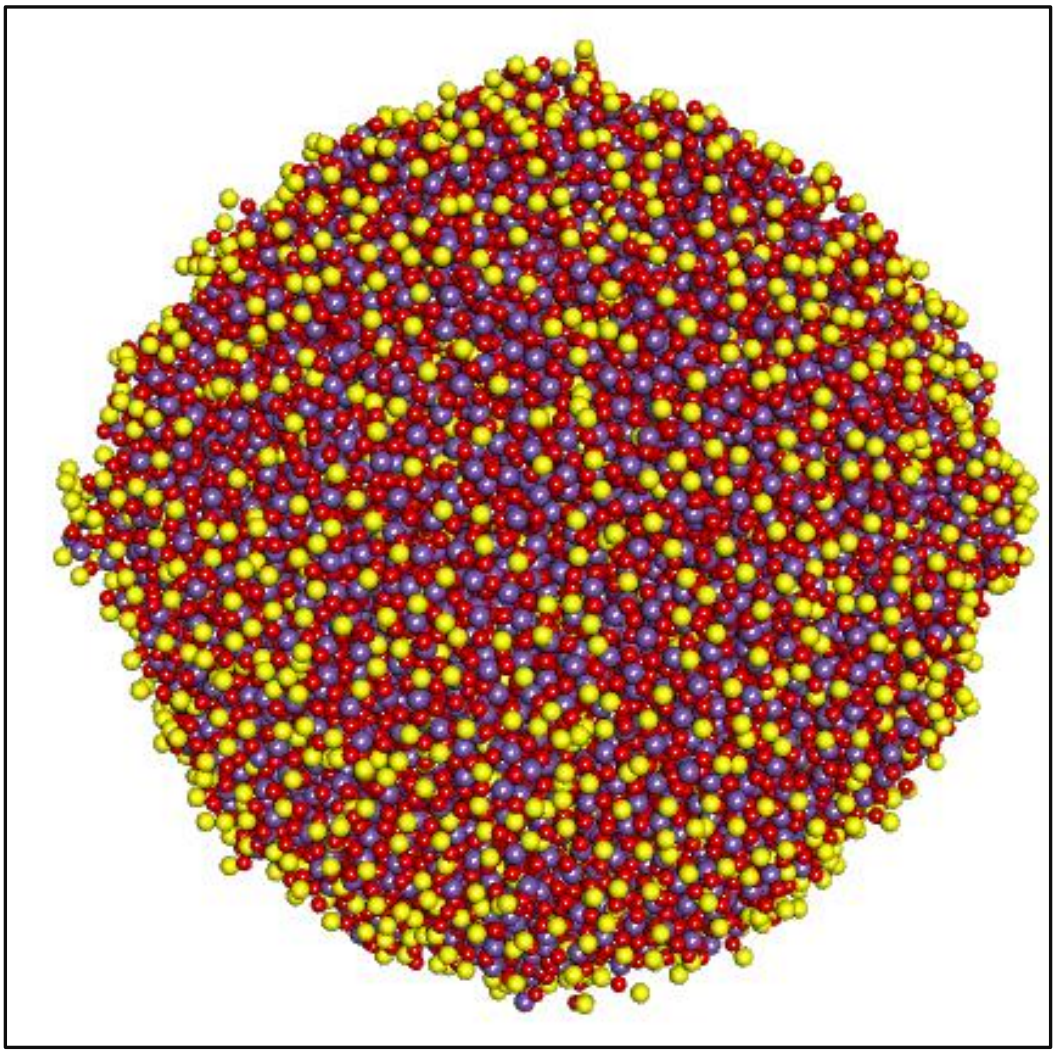

Figure 5.2: Atomic snapshot of an 8.01 nm amorphous $LiMn_2O_4$ spinel at a temperature of 1800 K, illustrating the random arrangement of atoms in the structure.

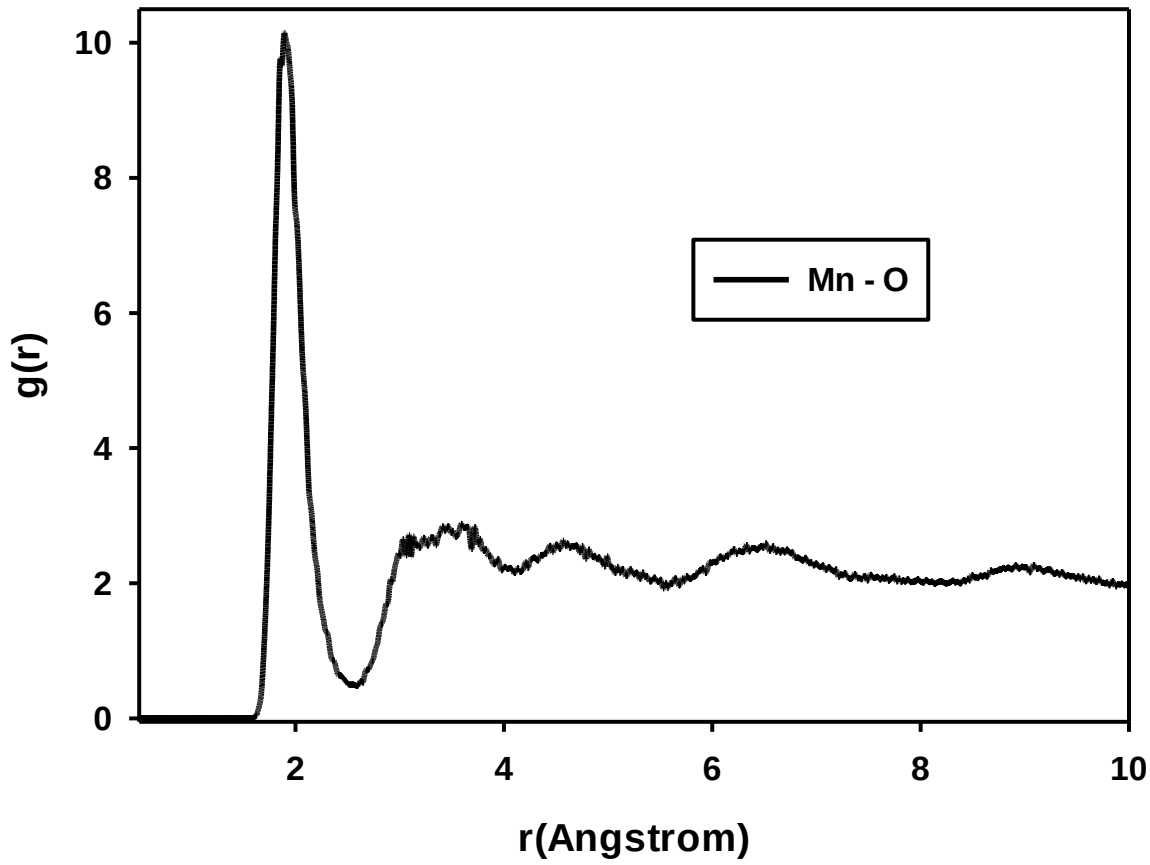

Figure 5.3: RDF of the Mn-O interaction in $LiMn_2O_4$ spinel at 1800 K, illustrating the amorphous state of this structure.

5.3 Doping of amorphous $LiMn_2O_4$ with Co and/or Ni.

The amorphous $LiMn_2O_4$ spinel structure illustrated in figure 5.2 was then doped with Co and/or Ni. The structure contains 8002 manganese (Mn) atoms, where 1% (80) of these atoms are replaced with Co and/or Ni atoms during the doping process. The resulting stoichiometry of the Co- and/or Ni-doped amorphous structure is $LiMn_{1.98}M_{0.02}O_4$ (M=Co, Ni). The Co- and/or Ni-dopants are uniformly distributed throughout the amorphous structure. Figure 5.4 shows a mechanism used to dope $LiMn_2O_4$ with Co and/or Ni on the manganese sites. The first dopant substitutes a random manganese atom, and the second dopant replaces a manganese atom that is furthest from the dopant (Co/Ni) that is already present in the structure, as illustrated in figure 5.4. Furthermore, the third dopant also substitutes a manganese atom that is most distant from the dopants that are currently in the structure. This procedure is followed until the total number of Co and/or Ni atoms that have been substituted into

the amorphous $LiMn_2O_4$ spinel is equivalent to 80. This approach guarantees even distribution of the dopant (Co and/or Ni) in the $LiMn_2O_4$ spinel.

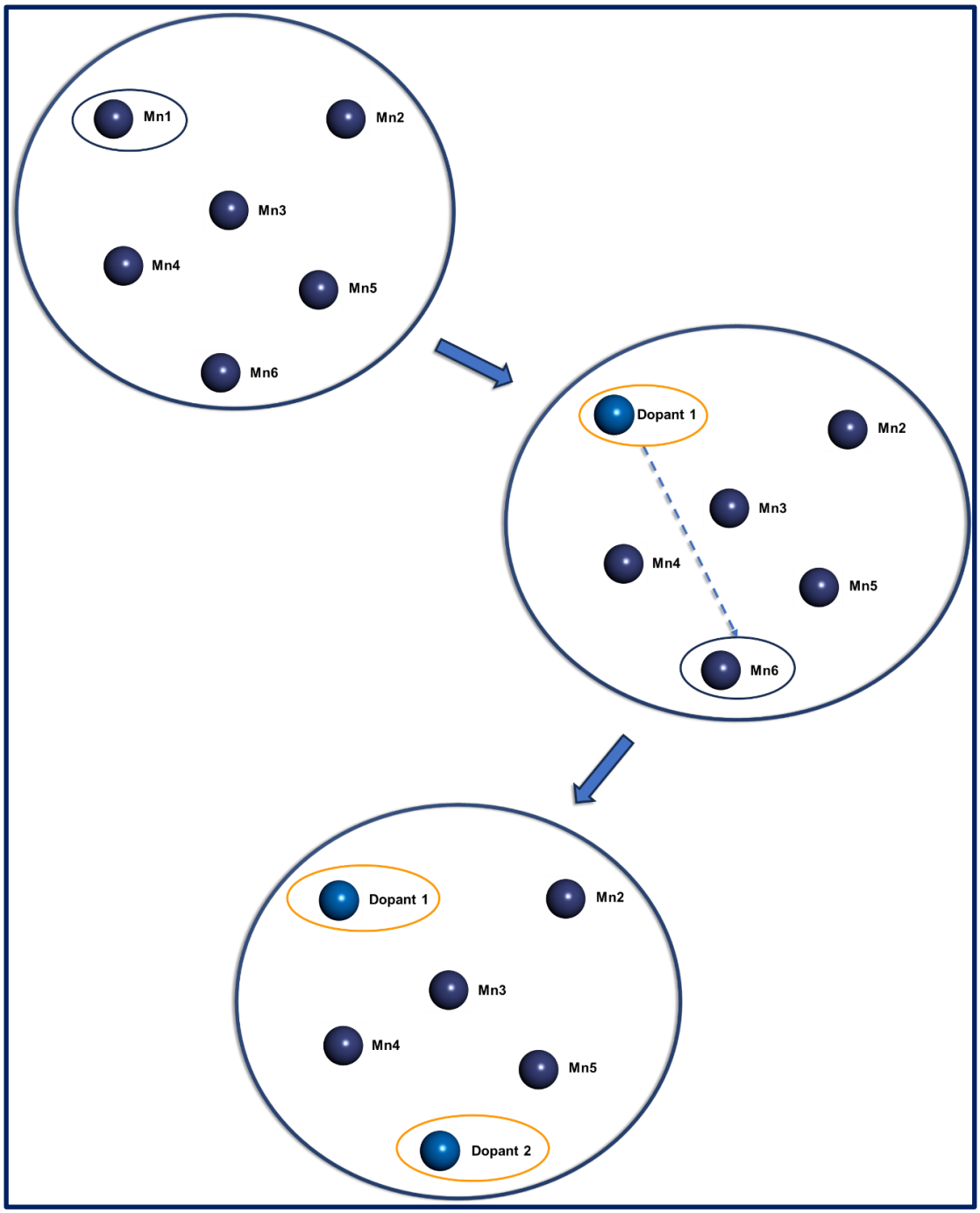

Figure 5.4: The mechanism employed for the doping of the amorphous $LiMn_2O_4$ spinel structure with Co. The next manganese atom to be replaced is one that occupies a lattice position that is furthest from all the cobalt (Co) atoms in the structure.

Figure 5.5 shows a Co-doped amorphous $LiMn_2O_4$ spinel structure, demonstrating the widely dispersed Co dopant in the structure. The widespread distribution of Co atoms in the structure is captured by the RDF graph of the Co-Co interaction depicted in figure 5.6. The first RDF peak is observed at a separation distance of ~3.24 Å, which shows that the Co atoms are at least 3.24 Å apart in the structure. The second RDF peak is noted at a separation distance of ~3.56 Å, which reveals that there is a greater chance for a given Co reference atom to find other Co atoms at this distance. The sharp RDF peaks indicate that this is the same ordering for every Co atom in the structure, and as such, the doping was homogeneous. Figure 5.7 shows the structure images of amorphous $LiMn_2O_4$ spinel doped with Ni. The Ni atoms are universally distributed in the amorphous structure, as evidenced by the sharp RDF peaks of the Ni-Ni interaction depicted in figure 5.8. The sharp RDF peaks located at the separation distances of ~3.24 Å and ~3.56 Å show that the Ni atoms in the structure have the same local environment, which indicates that Ni atoms were homogeneously distributed in the structure.

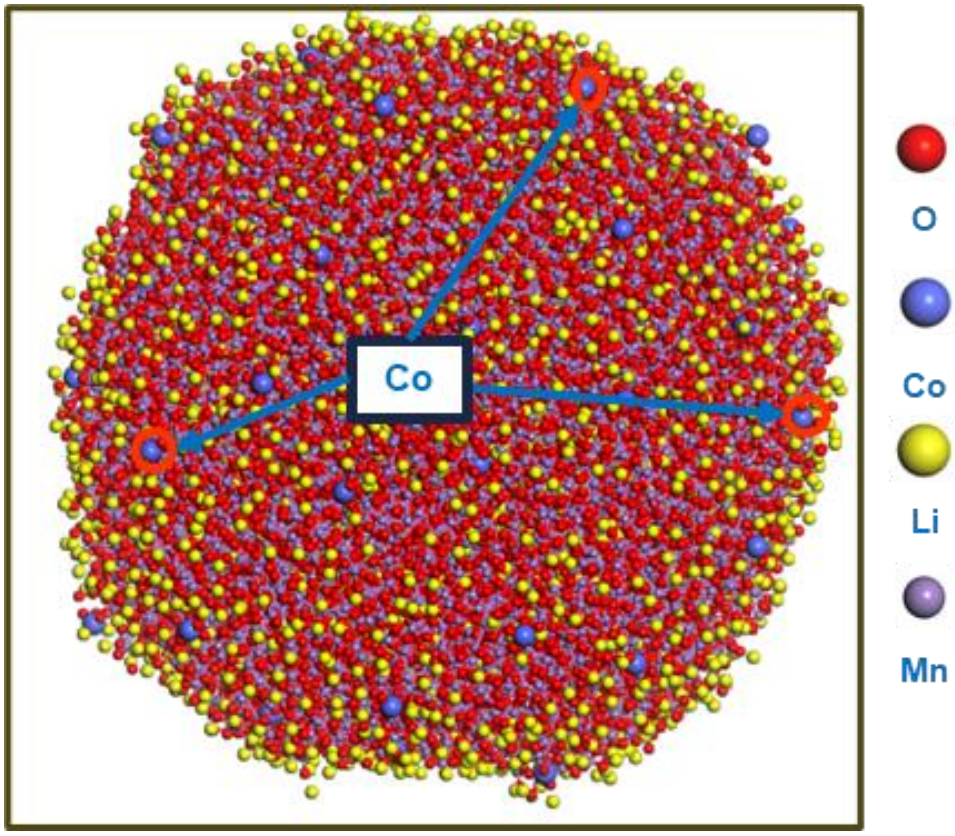

Figure 5.5: Structure image of Co-doped $LiMn_2O_4$ spinel ($LiMn_{1.98}Co_{0.2}O_4$) showing the distribution of Co in the structure.

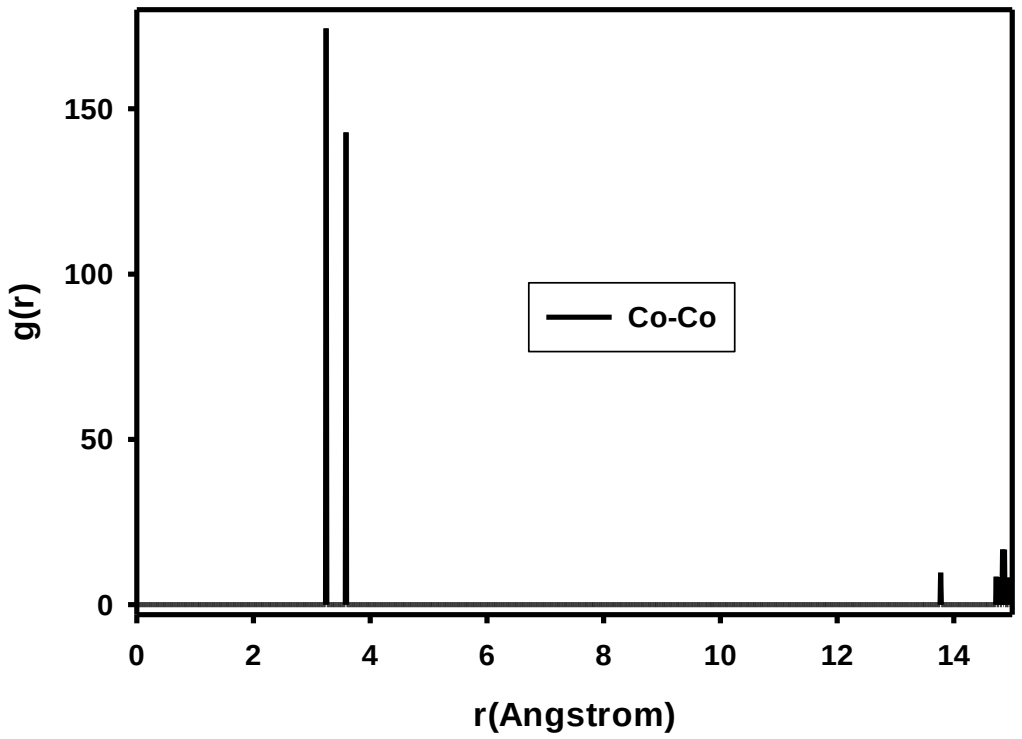

Figure 5.6: RDF graph of the Co-Co interaction in the amorphous $LiMn_{1.98}Co_{0.2}O_4$, indicating a homogeneous distribution of Co atoms in the structure.

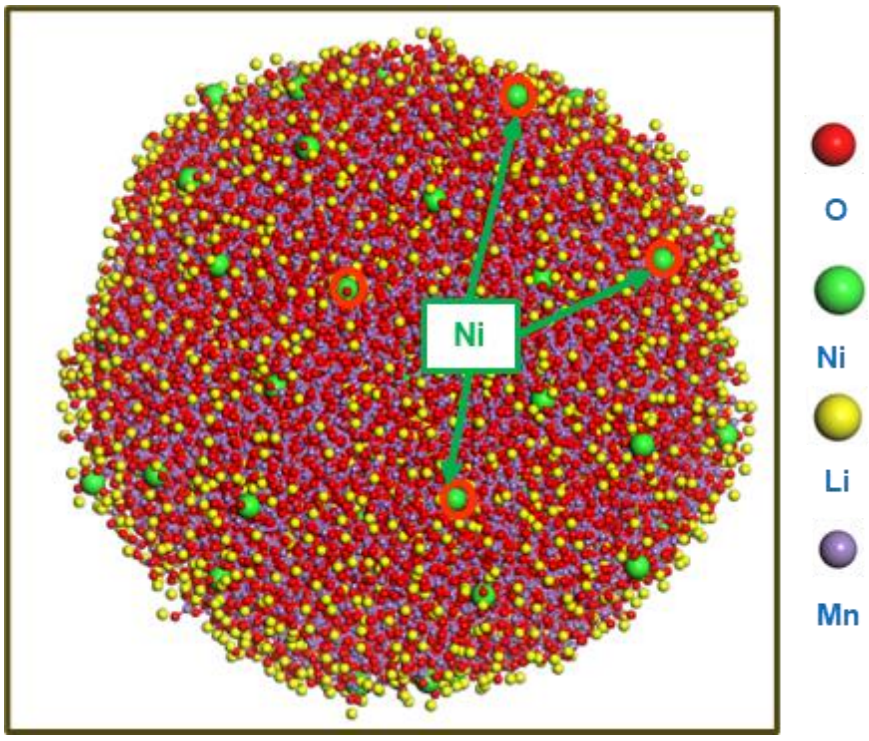

Figure 5.7: An atomic image of amorphous $LiMn_{1.98}Ni_{0.2}O_4$ illustrates the distribution of Ni atoms in the structure.

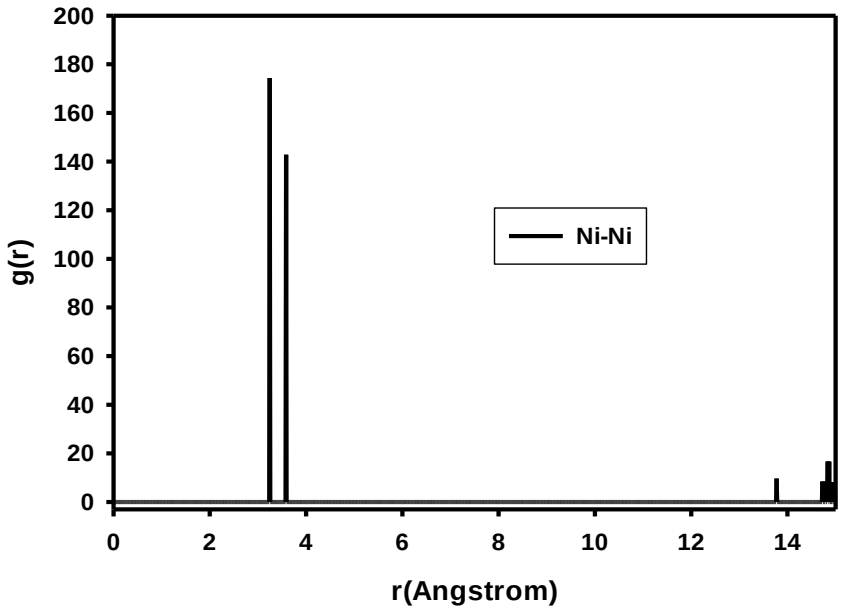

Figure 5.8: Illustration of the allocation of Ni atoms in the amorphous $LiMn_{1.98}Ni_{0.2}O_4$ spinel structure.

Figure 5.9 illustrates the substitution of 1% (80 Mn atoms) manganese with cobalt (40 Co atoms) and nickel (40 Ni atoms) atoms in the amorphous $LiMn_2O_4$ spinel structure. The atomic snapshots captured from the Materials Studio structure visualization program show a widespread distribution of Co and Ni atoms in the structure. Furthermore, the sharp RDF peaks of the Co-Co, Ni-Ni, and Ni-Co interactions in the structure illustrated in figures 5.10, 5.11, and 5.12 demonstrate the uniform distribution of the dopants. The Co atoms were substituted after the substitution of 0.5% of manganese atoms with Ni. Hence, we observe the first RDF peak of the Co-Co interaction at the separation distance of ~3.56 Å and of the Ni-Ni interaction at ~12.55 Å, as illustrated in figures 5.10 and 5.11. Figure 5.10 only shows a single RDF peak between the separation distances of 0 and 15 Å, since only 40 Co atoms were substituted in the structure, which is less than the 80 Co and 80 Ni atoms substituted in $LiMn_{1.98}Co_{0.02}O_4$ and $LiMn_{1.98}Ni_{0.02}O_4$, respectively. Figure 5.12 captures the arrangement of Co atoms regarding Ni atoms in the $LiMn_{1.98}Co_{0.01}Ni_{0.01}O_4$ amorphous spinel structure. The first RDF peak is found at a separation distance of ~3.12 Å, thus the Ni atoms are at least 3.12 Å apart from the Co atoms in the structure. Moreover, the sharp RDF peaks show that this is the same ordering for every Co and Ni atom in the structure. The homogeneous distribution of Co and Ni in the amorphous $LiMn_2O_4$ spinel ensures an even distribution of the effect of doping in the structure.

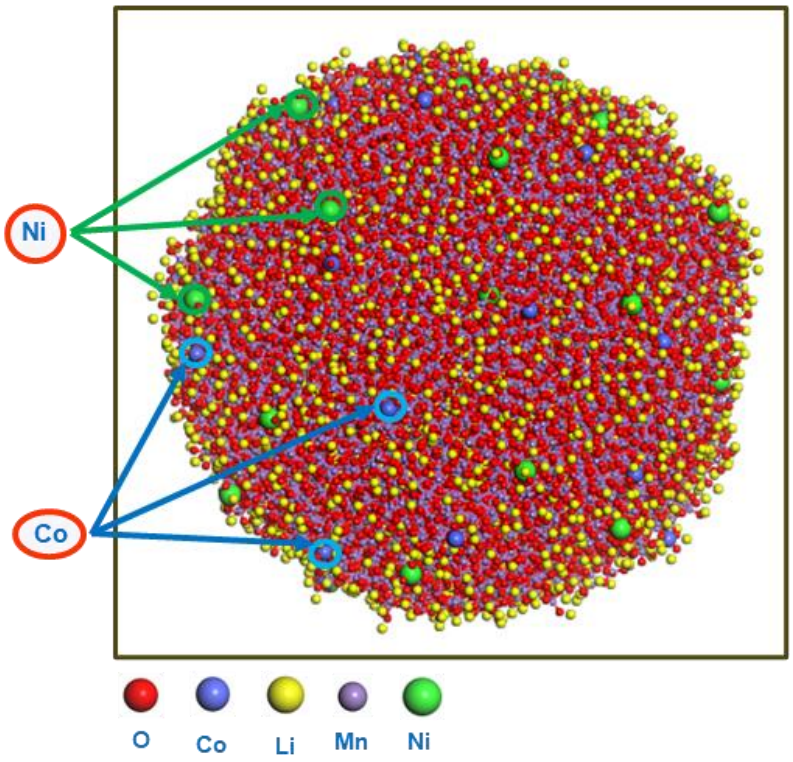

Figure 5.9: Illustration of the sparse distribution of Co and Ni in the $LiMn_2O_4$ spinel nanosphere.

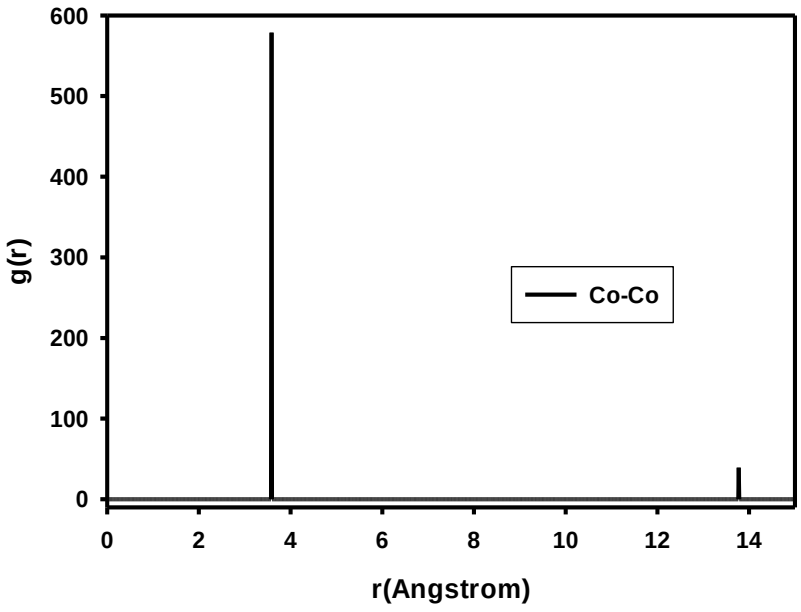

Figure 5.10: RDF graph of the Co-Co interaction in the $LiMn_{1.98}Co_{0.2}O_4$ spinel, showing a uniform distribution of Co atoms in the structure.

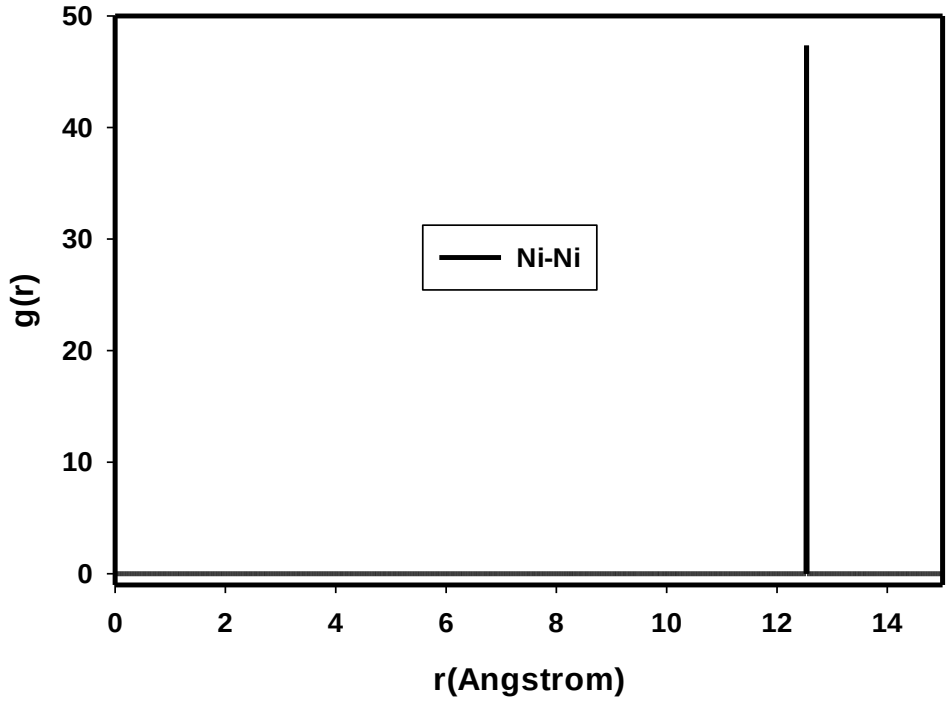

Figure 5.11: RDF of the Ni-Ni interaction illustrating the homogeneous distribution of Ni atoms in the amorphous $LiMn_2O_4$ spinel structure.

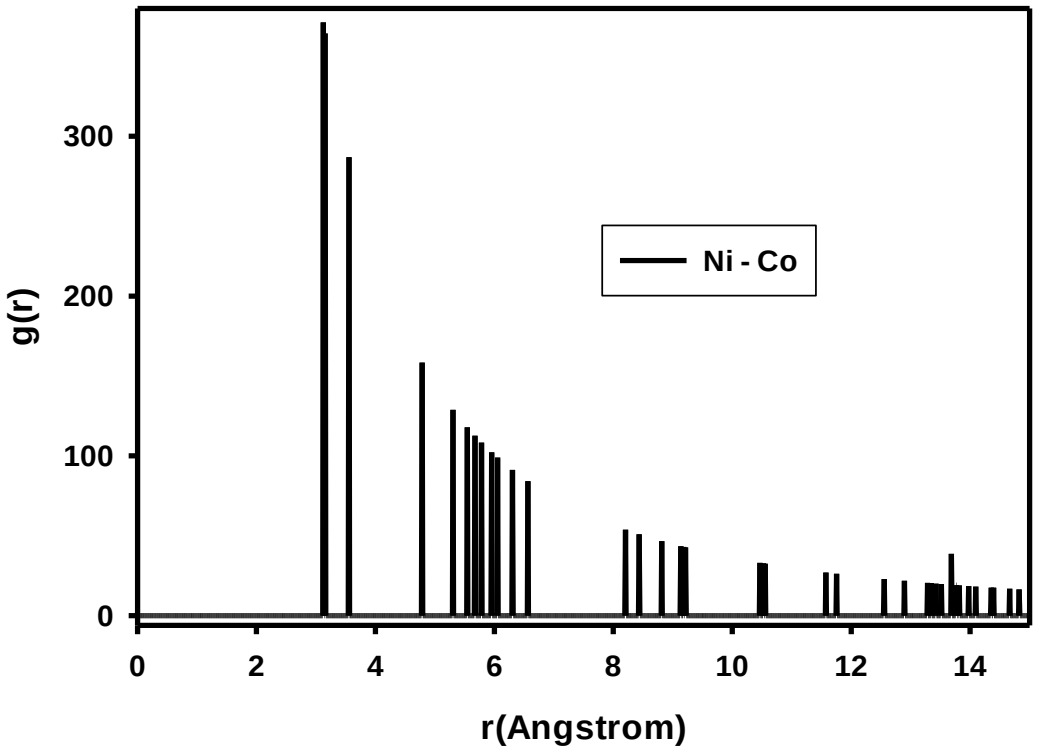

Figure 5.12: (a) RDF of the Ni-Co interactions in the amorphous $LiMn_{1.98}Ni_{0.2}O_4$ spinel structure.

5.4 Simulated recrystallization of the Co- and/or Ni-doped $LiMn_2O_4$

5.4.1 Characterization of $LiMn_{1.98}Co_{0.02}O_4$

The section details the recrystallization of the Co-doped $LiMn_2O_4$ amorphous structure depicted in figure 5.5. The $LiMn_{1.98}Co_{0.02}O_4$ spinel structure was recrystallized at a temperature of 1900 K and cooled to a temperature of 5 K. The structure is cooled to a temperature of 5 K for structural characterization and analysis. The cooled structure is depicted in figure 5.13, which shows that it has recrystallized successfully as captured by the atomic-level structure images. Lithium (Li) atoms are represented by the yellow spheres, manganese (Mn) atoms by the purple spheres, cobalt (Co) atoms by the blue spheres, and oxygen (O) atoms by the red spheres. In figure 5.13 the atoms are arranged in line patterns, which reveals that the structure recrystallized successfully. Moreover, a line of oxygen atoms (red) can be noted from in figure 5.13, which is between a mixed line of manganese (purple), cobalt (blue), and lithium (yellow) atoms.

Furthermore, the crystallinity of the recrystallized $LiMn_{1.98}Co_{0.02}O_4$ structure is deduced from the RDF graph of the M-O (M = Mn and Co) interaction depicted in figures 5.14 (a) and (b). The first neighbour distance of the Mn-O interaction is observed at the atomic separation distance of ~1.915 Å, which is comparable to a value of ~1.923 Å by Kwon and colleagues [232]. The first RDF peak of the Co-O interaction depicting its bond length is found at ~1.895 Å. The bond length of the Co-O interaction was also calculated in a study by Wolverton et al. and was found to be ~1.910 Å, which is not far from the value calculated in the current work [235]. Furthermore, the RDF peaks in figure 5.14, located at ~3.51 Å and ~4.45 Å for the Mn-O interaction and at ~3.4 Å and ~4.5 Å for the Co-O interaction, are well pronounced, which evidences the successful recrystallization of the $LiMn_{1.98}Co_{0.02}O_4$ structure.

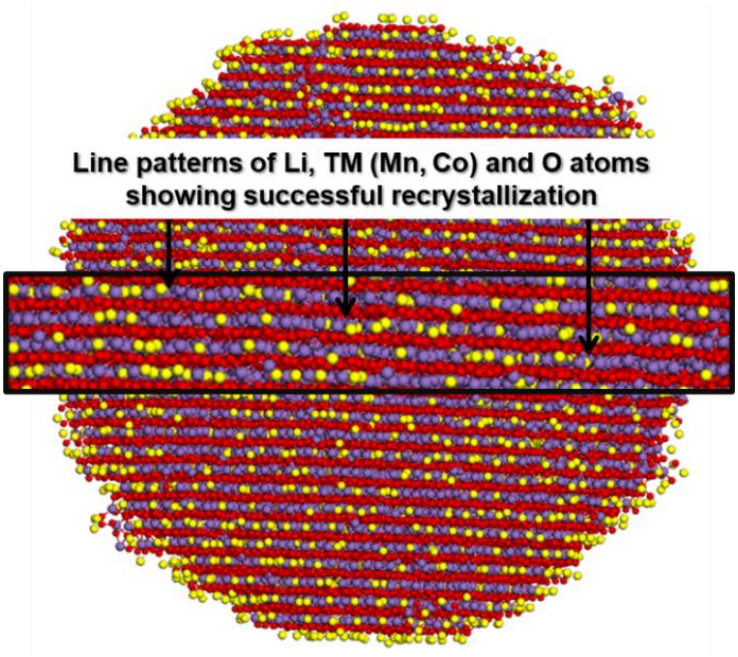

Figure 5.13: Atomic structure image of $LiMn_{1.98}Co_{0.02}O_4$ recrystallized at a temperature of 1900 K and cooled to a temperature of 5 K. The image illustrates the atoms arranged in a line pattern.

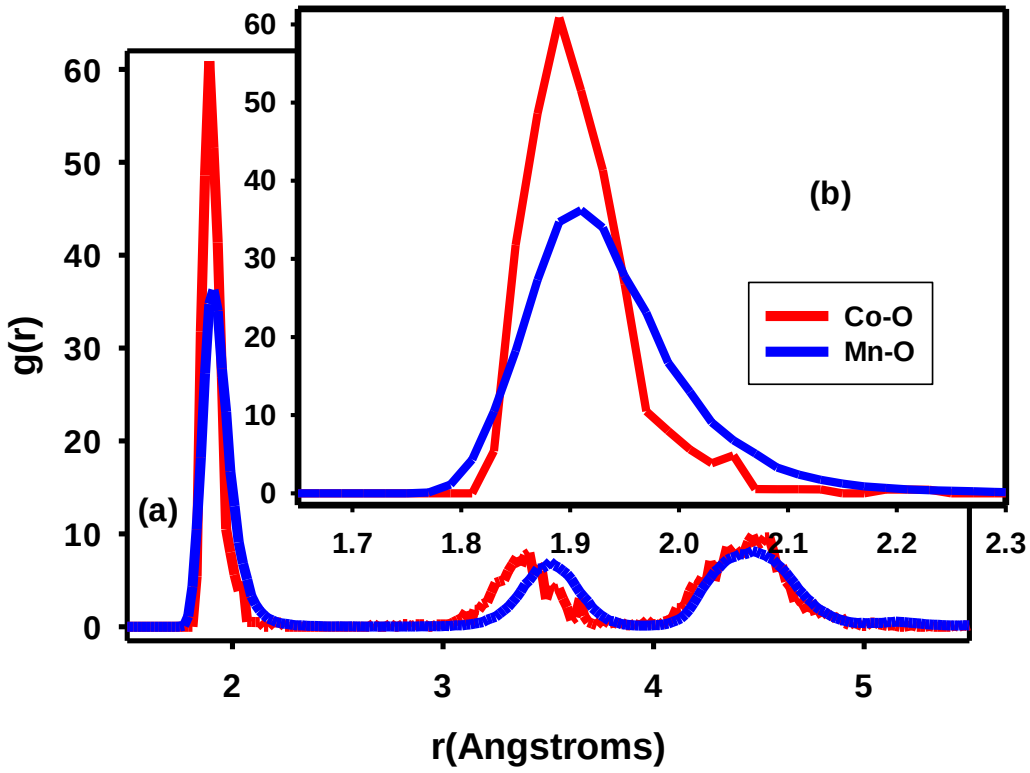

Figure 5.14: (a) RDF of the Co-O and Mn-O interactions illustrating the uniform distribution of Co and Ni atoms in the amorphous $LiMn_2O_4$ spinel structure. (b) An inset showing the magnified first RDF peak.

Figure 5.15 shows the atomic-level structural characterization of the Co-doped $LiMn_2O_4$ spinel ($LiMn_{1.98}Co_{0.02}O_4$). A few layers of Li, Mn, Co, and O atoms have been extracted from the $LiMn_{1.98}Co_{0.02}O_4$ nanostructure in figure 5.15 (a) are illustrated in figure 5.15 (b). The extracted layers show the presence of the spinel phase in a conventional unit cell view, magnified in figure 5.15 (c). The cations are largely occupying the octahedral sites, as illustrated in figure 5.15 (c). Li atoms can be seen on the 16c octahedral sites, and manganese atoms in the 16d octahedral sites. The oxygen atoms are situated at the 32e sites in a close-packed arrangement. The A&R simulated spinel phase is compared to the theoretical spinel phase shown in figure 5.5 (d). Furthermore, the MO_6 (M=Co, Mn) octahedron has also been extracted from the structure for investigation of the Co-O and Mn-O bond lengths. The MnO_6 octahedron has a longer bond between the transition metal and oxygen than the CoO_6 octahedron. The Mn-O octahedron in figure 5.15 (e) has a mean bond length of ~1.929 Å, and the average bond distance of the Co-O octahedron is ~1.904 Å. A bond length of ~1.939 Å is shown for the Mn-O interaction, which is near the Co-O interaction with a bond length of ~1.894 Å. Therefore, the presence of Co provides more leeway for the diffusion of nearby Li ions due to the shorter Co-O bond when compared to the Mn-O bond. Figure 5.16 shows two adjacent MnO_6 and CoO_6 octahedrons extracted from the A&R-simulated $LiMn_{1.98}Co_{0.02}O_4$ spinel structure. The longest Mn-O bond length in the MnO_6 octahedron is ~2.154 Å, while the longest Co-O bond length in the CoO_6 octahedron is ~1.938 Å. Hence, a Jahn-Teller effect in a Co-O environment may have a lesser structural disruption when compared to a Jahn-Teller effect in a Mn-O environment. Moreover, Mn atoms are observed in the octahedral sites, which evidences the formation of the high-temperature impurity phase Mn_3O_4 in $LiMn_2O_4$ spinel structures [236].

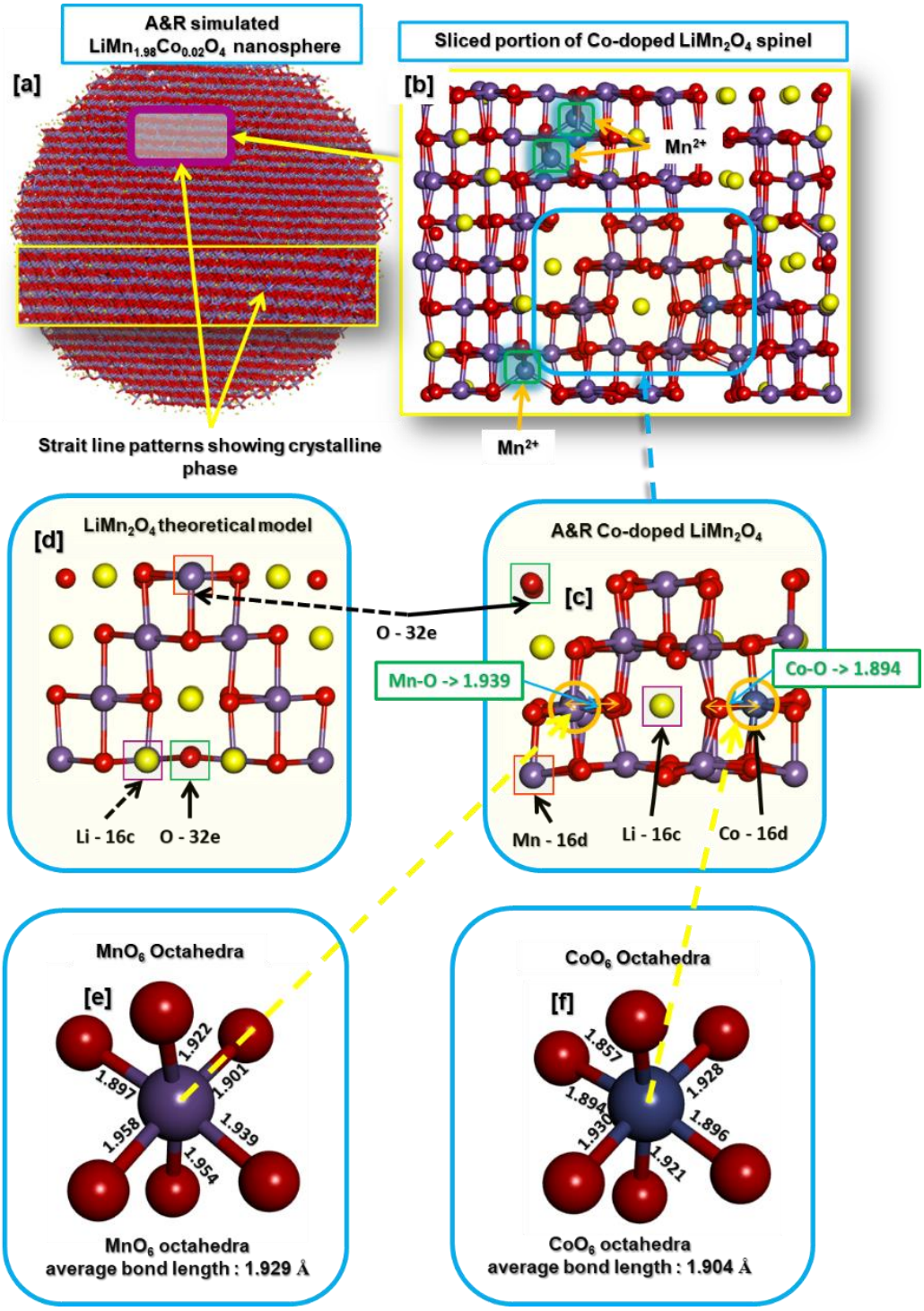

Figure 5.15: The formed LiM_2O_4 (M=Mn, Co) spinel phase in the recrystallized $LiMn_{1.98}Co_{0.02}O_4$ nanosphere. (a) $LiMn_{1.98}Co_{0.02}O_4$ nanosphere. (b) A portion of the LM_2O_4 (M=Mn, Co) spinel nanosphere. (c) A&R simulated LiM_2O_4 (M=Mn, Co) spinel structure validated with a (d) theoretical spinel model. (e) Average bond length of a MnO_6 octahedron compared to the average bond length of a (f) CoO_6 octahedron in the A&R simulated spinel structure.

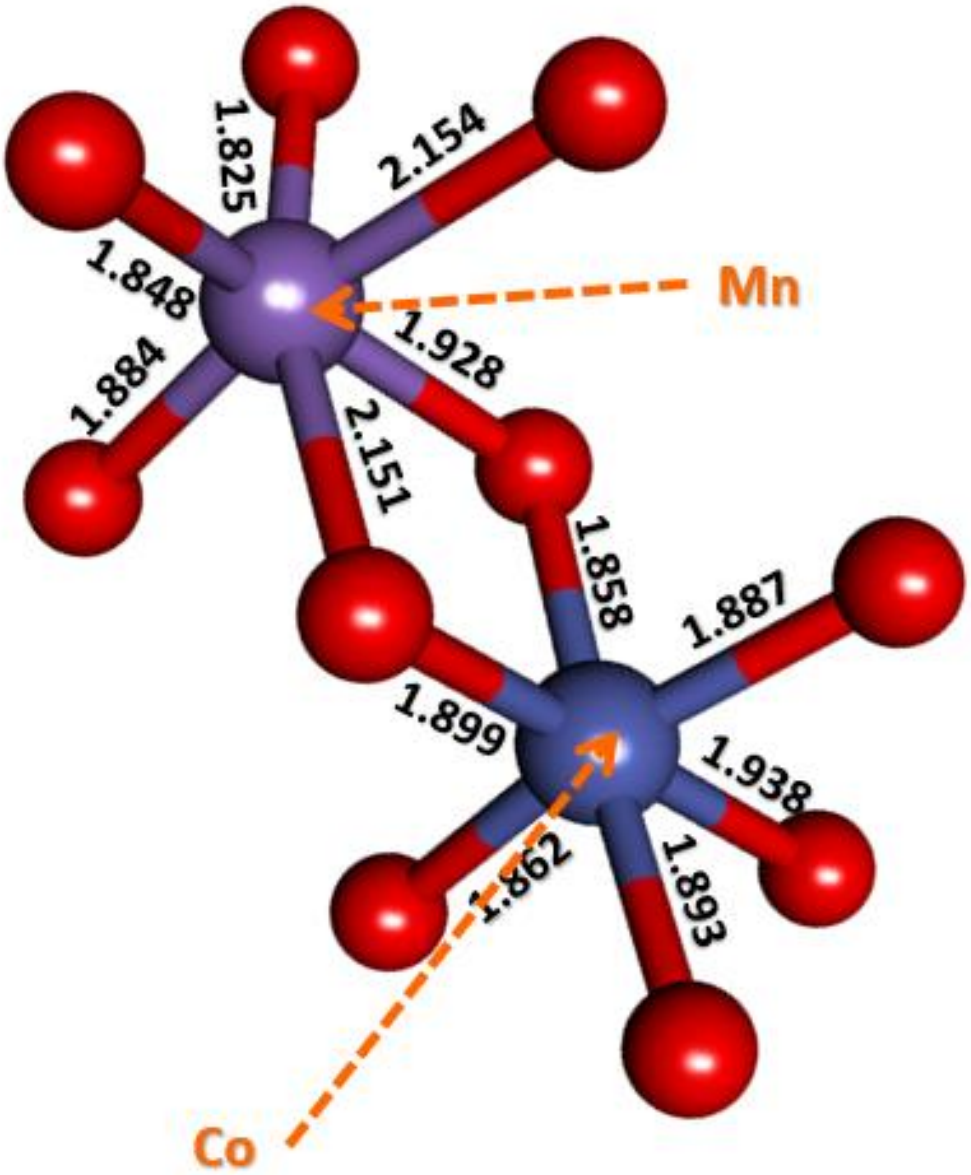

Figure 5.16: The MO_6 (M=Mn, Co) octahedron shows the bond length between M and O in the structure.

Figure 5.17 (a) shows layers of atoms extracted from the A&R-simulated $LiMn_{1.98}Co_{0.02}O_4$ spinel structure for further examination of the Co environment. The magnified Co environments are shown in figures 5.17 (b), (c), and (d), showing two views of the enlarged areas. A Co atom is surrounded by six oxygen atoms, which are at an angle of 90° from it, forming an octahedral coordination. The magnified Co environments in figures 5.17 (a), (b), and (c) show no presence of Li atoms in the intermediate Li vacancies near Co atoms. The absence of Li ions could suggest that Co atoms have a valence state of 4+ in the structure. Since, in the absence of Li atoms around Co atoms, the Co atoms will have to lose 4 electrons to oxygen. Furthermore, Mn atoms are observed in the tetrahedral sites generally occupied by lithium atoms in the $LiMn_2O_4$ spinel structure adjacent to Co atoms. The Mn atoms in the tetrahedral sites are linked to the formation of the Mn_3O_4 high-temperature impurity phase, wherein Mn atoms have a valence state of 2^+ [236].

Figure 5.18 shows the local environment of the Li-Mn and Li-Co interactions through RDF plots. The first RDF peak of the Li-Mn interaction is observed at the atomic separation distance of ~2.825 Å. Xu and co-workers found the bond length of the Li-Mn interaction to range between 2.850 and 3.20 Å, which is not far off from the value calculated in this study [237]. A small RDF peak illustrating the local bond environment of the Li-Co interaction is observed around the atomic separation of ~3.075 Å. The probability of finding atoms at this atomic separation is ~1.11 a.u. This suggests that it is unlikely to find Li atoms close to Co atoms. Moreover, the probabilities of the RDF peaks of the Li-Co interaction that follow the first neighbour peaks are comparable to the RDF peaks of the Li-Mn interaction. The second neighbour RDF peak of the Li-Mn interaction has a probability of ~2.01 a.u, and the second neighbour distance peak for the Li-Co interaction has a probability of ~1.71 a.u. Moreover, figure 5.19 illustrates the average number of Li atoms around Co and Mn atoms in the atomic separation range between 0-3.5 Å and 3.5-70 Å. In the separation range between 0-35 Å, the average number of Li atoms around Co atoms is 0.24, and around Mn atoms, it is found to be 2.77. However, between interatomic distances of 3.5 Å and 7.0 Å, the average number of Li atoms around Co atoms is 13.73, and around Mn atoms it is found to be 13.78. This is in line with the structure images shown in figure 5.17 and the RDF plots in figure 5.18.

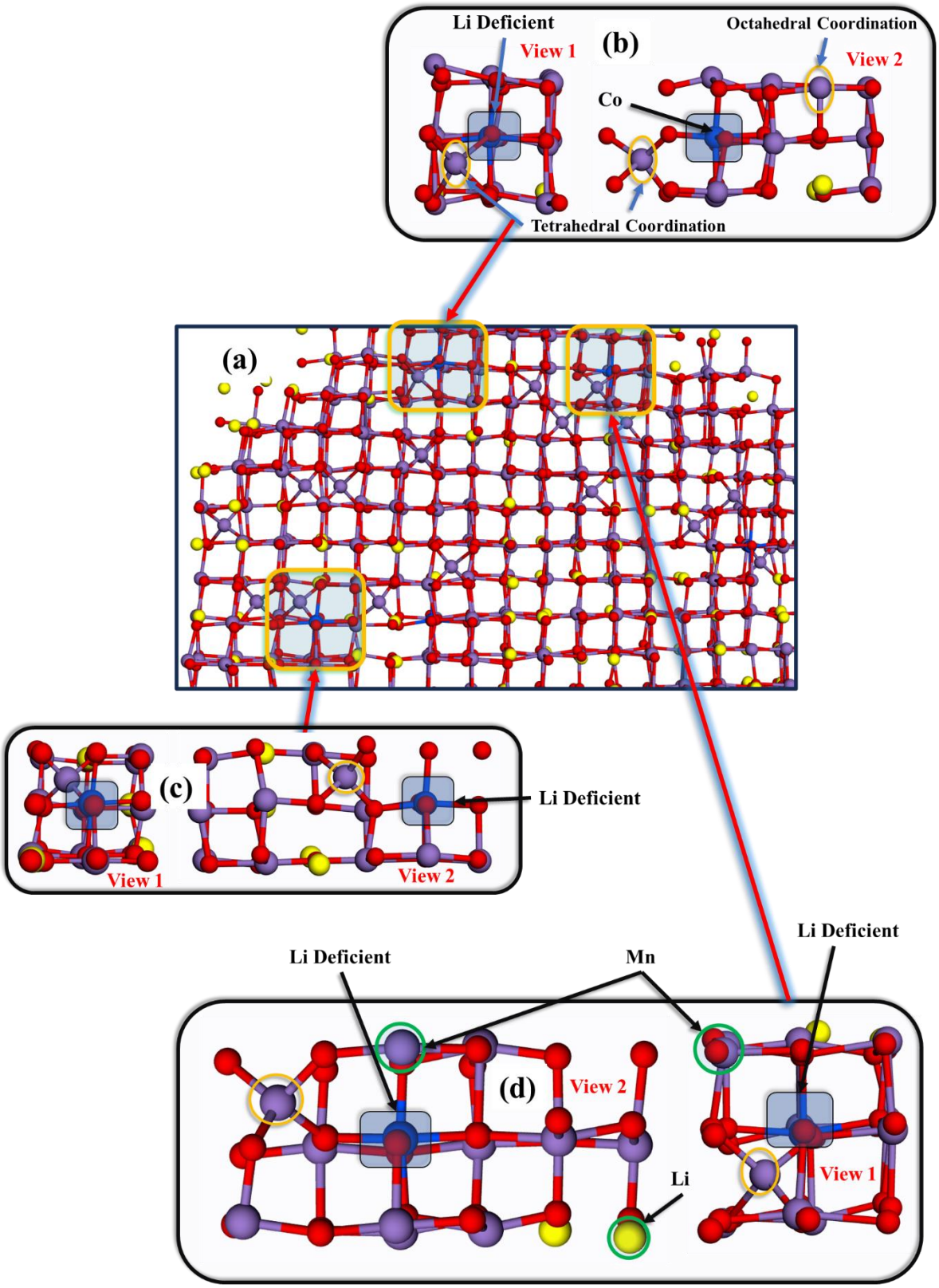

Figure 5.17: A&R-simulated $LiMn_{1.98}Co_{0.02}O_4$ showing the Co environment in the structure.

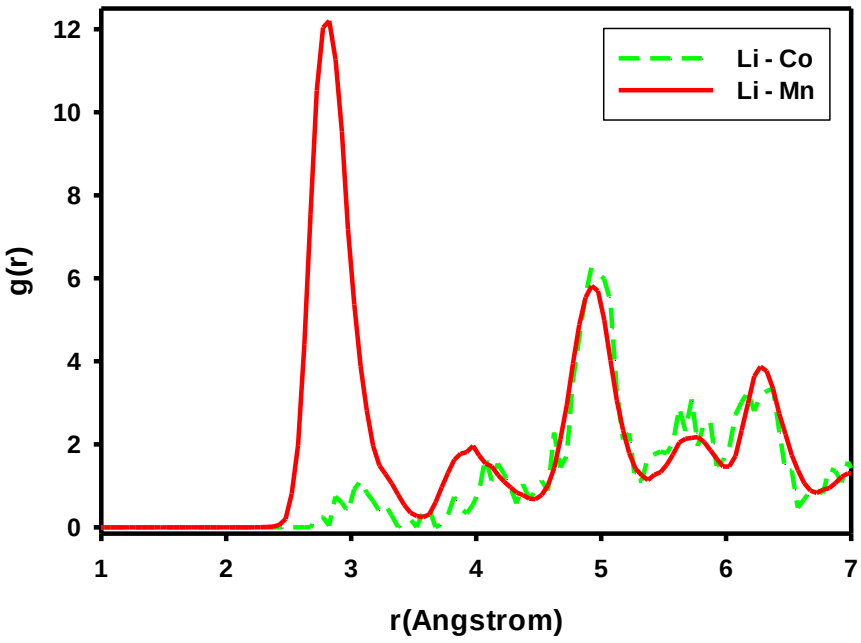

Figure 5.18: The RDF plot of the Li-Mn and Li-Co interactions in the Co-doped Li-Mn-O spinel structure ($LiMn_{1.98}Co_{0.02}O_4$).

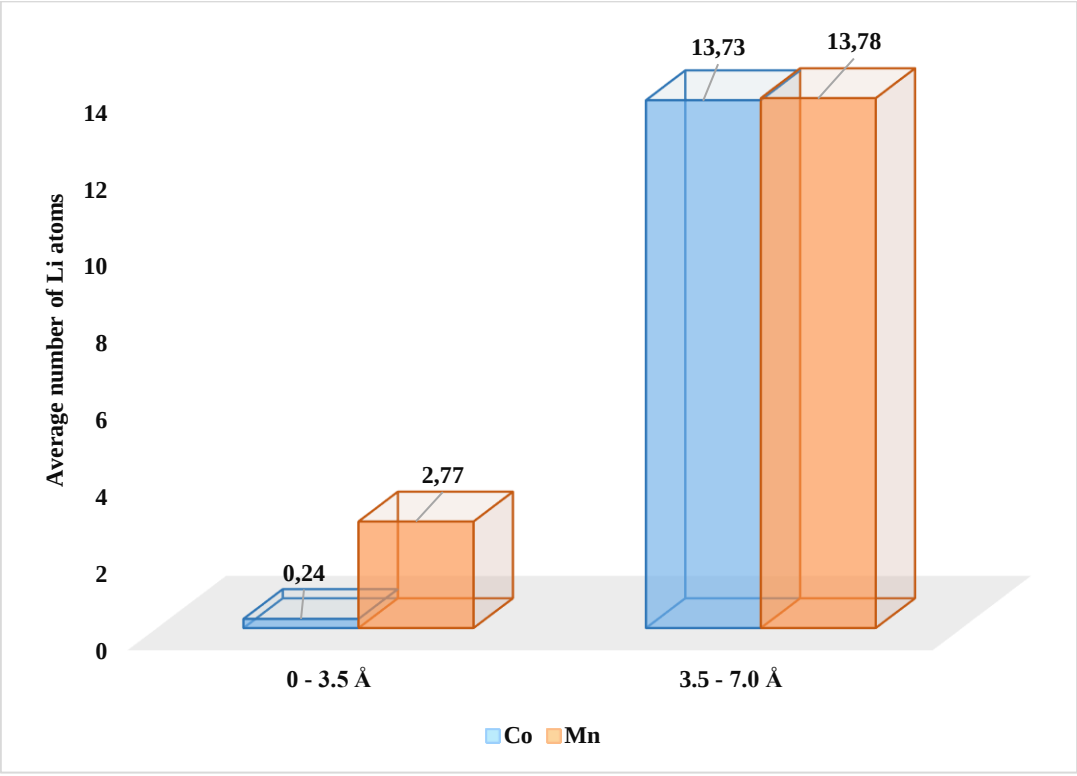

Figure 5.19: Average number of Li atoms around Co and Mn atoms in the atomic separation range of 0-3.5 Å and 3.5-7.0 Å.

Figure 5.20 illustrates the migration of Mn atoms into the tetrahedral sites at high temperatures. The Mn atoms at the tetrahedral sites form the Mn_3O_4 impurity phase,

which is stable at high temperatures. The Mn_3O_4 phase was found to form at a temperature of 600 K, wherein several Mn atoms occupy the 8a tetrahedral sites, lowering the average valence of the $LiMn_2O_4$ spinel structure [225, 238]. Lithium ions hop from the 8a tetrahedral sites into adjacent 8a sites through the 16c octahedral sites. Thus, the occupation of the tetrahedral sites by Mn atoms can disturb the movement of lithium atoms in the structure [237]. In the figure (5.20), only Mn atoms are observed in the 8a tetrahedral sites, which are generally occupied by Li atoms. Figure 5.21 shows the number of CoO_4 and MnO_4 tetrahedral coordinations in the $LiMn_{1.98}Co_{0.02}O_4$ spinel structure. The number of Co atoms occupying tetrahedral lattice positions in the A&R-simulated spinel structure is zero, while the number of Mn atoms occupying the tetrahedral positions is 535.

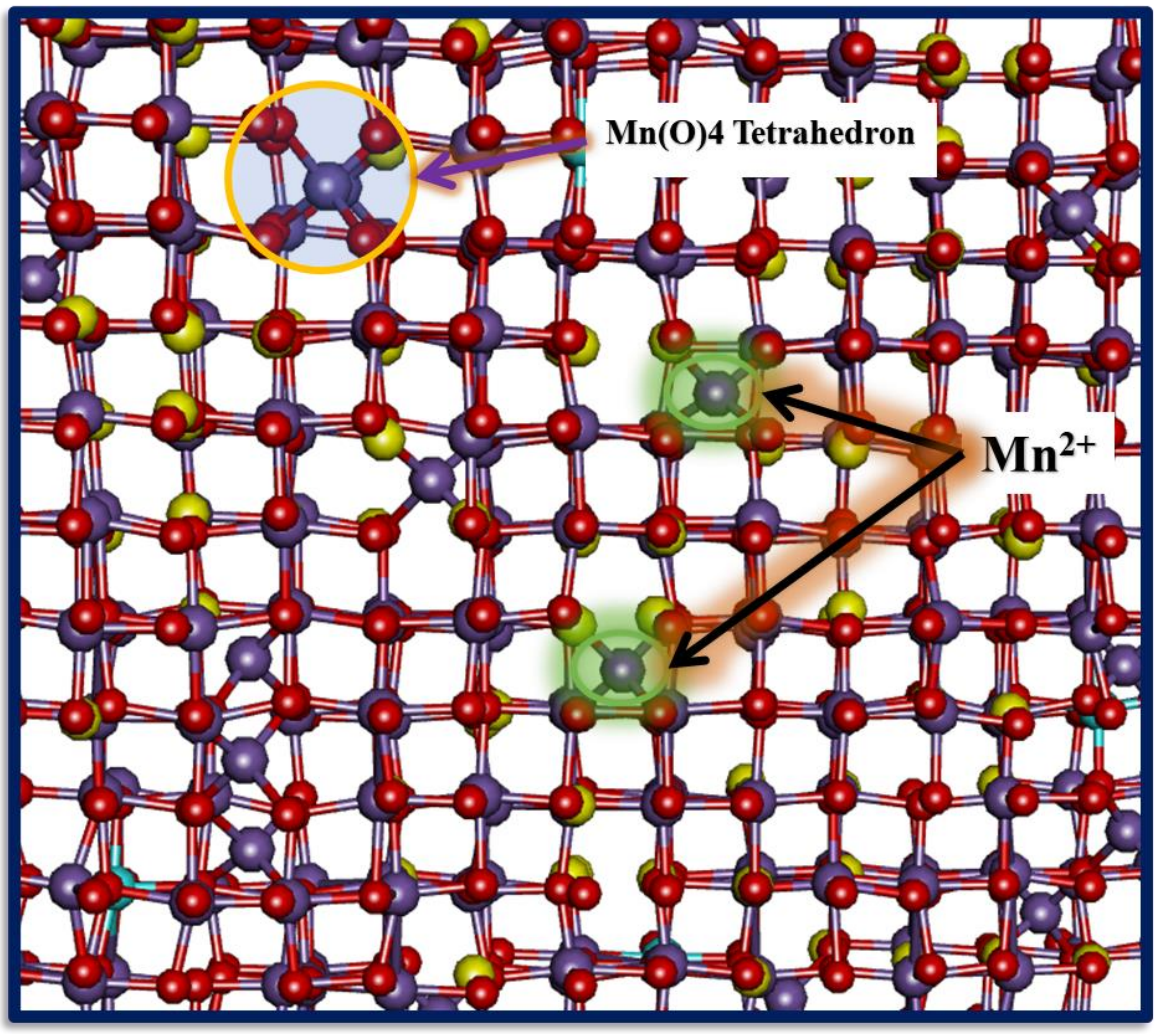

Figure 5.20: Atomic-structure image showing the migration of Mn atoms into the tetrahedral sites.

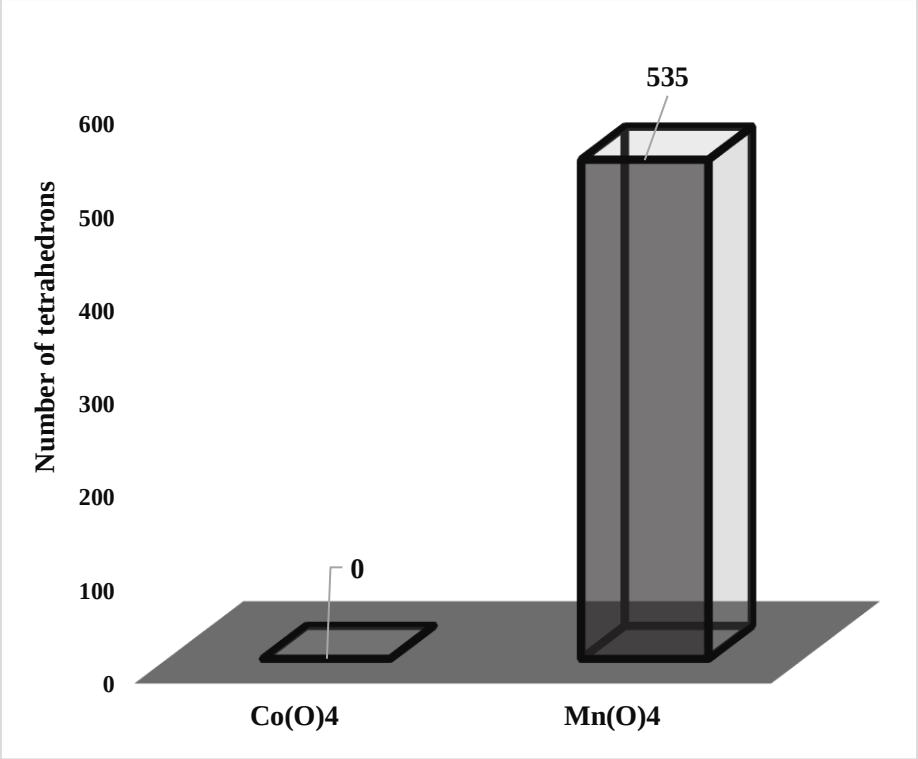

Figure 5.21: Number of CoO_4 and MnO_4 tetrahedral coordination in the A&R simulated $LiMn_{1.98}C_{0.02}O_4$ spinel structure.

The structure of the $LiMn_{1.98}Co_{0.2}O_4$ nanosphere was further characterized with the XRD pattern shown in figure 5.22 (a). The XRD pattern of the A&R-simulated spinel structure can be indexed to a cubic symmetry with a space group of Fd-3m. All the major spinel diffraction peaks demonstrate diffraction at the (111), (311), (222), (400), (331), (511), (440), and (531) planes. The XRD peaks are also observed in the XRD pattern of spinel structure from experiments shown in figure 5.22 (b) [239]. Moreover, the high-temperature Mn_3O_4 spinel impurity phase is also observed in the A&R-simulated $LiMn_{1.98}Co_{0.02}O_4$ spinel structure, as signified by the (220) reflection in the XRD pattern [225, 238]. The XRD pattern of the Co-doped Li-Mn-O spinel structure also shows the presence of the Li_2MnO_3 impurity phase. In addition, the co-existence of these phases is evidenced by the splitting of the (311), (400), (311), and (531) diffraction peaks. The impurity phases are further confirmed by the XRD patterns of the Mn_3O_4 and Li_2MnO_3 structures determined in experiments [230, 231]. The major spinel peaks {(400), (331), (440), and (531)} are sharp and more intense, revealing the successful recrystallization and dominance of the cubic spinel phase. Moreover, the substitution of manganese with cobalt does not destabilize the cubic spinel structure.

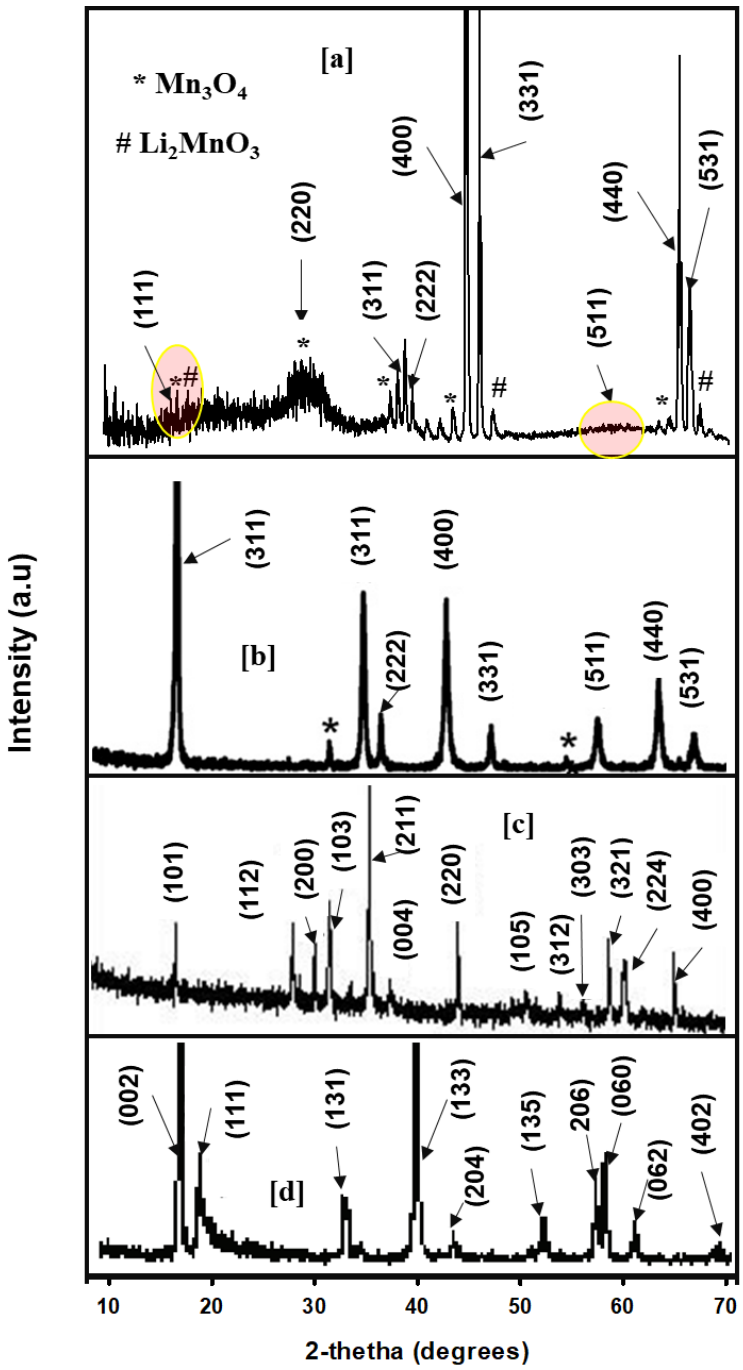

Figure 5.22: XRD pattern of the 8.01 nm $LiMn_{1.98}Co_{0.02}O_4$ spinel structure simulated with the A&R technique compared to the experimental XRD pattern of the (b) $LiMn_2O_4$ [239], (c) Mn_3O_4 [230], and (d) Li_2MnO_3 [231] structures.

5.4.2 Characterization of $LiMn_{1.98}Ni_{0.02}O_4$

The amorphous $LiMn_2O_4$ spinel structure doped with Ni was also recrystallized at a temperature of 1900 K and cooled to a temperature of 5 K. The structure image in figure 5.23 shows Li, Mn, Ni, and O atoms organized in patterns of lines. Layers of

oxygen atoms in between a mixed layer of Li, Mn, and Ni can be noted on the atomic-structure image. This suggests that the $LiMn_{1.98}Ni_{0.02}O_4$ spinel nanosphere recrystallized successfully. Figure 5.24 illustrates the distribution of Mn and Ni atoms around O atoms in the atomic separation range between 0 and 10 Å. RDF peaks are observed at defined atomic separation distances, showing that atoms in the $LiMn_{1.98}Ni_{0.02}O_4$ spinel structure are occupying defined lattice positions. Thus, the RDF graphs also indicate that the $LiMn_{1.98}Ni_{0.02}O_4$ spinel structure recrystallized successfully at a temperature of 1900 K. The first RDF peak for the Mn-O interaction is also observed at the atomic-separation distance of ~1.912 Å, which is close to the value of ~1.915 Å found in the $LiMn_{1.98}Co_{0.02}O_4$ spinel structure in figure 5.13. The bond length between Ni and O deduced from the first peak of the Ni-O interaction in figure 5.24 is ~1.885 Å.

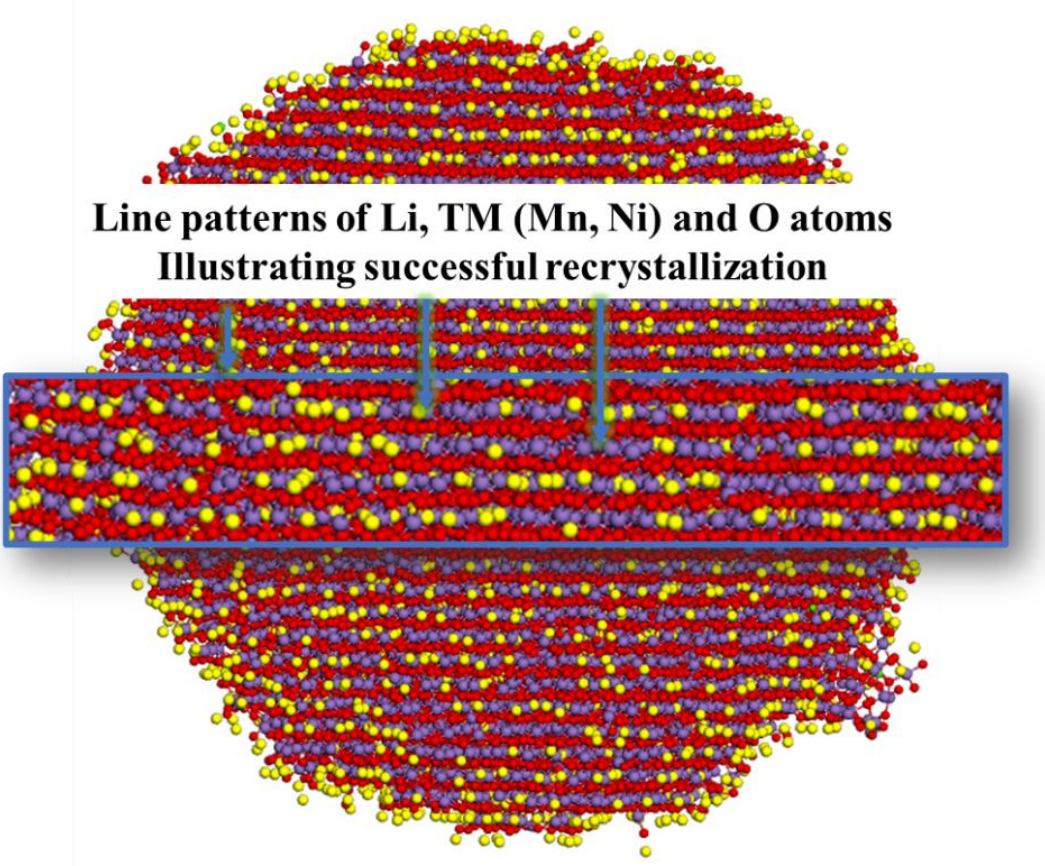

Figure 5.23: Atomic-structure image of A&R-simulated $LiMn_{1.98}Ni_{0.02}O_4$ spinel structure recrystallized at a temperature of 1900 K and systematically cooled to a temperature of 5 K. The atomic-line patterns show successful recrystallization.

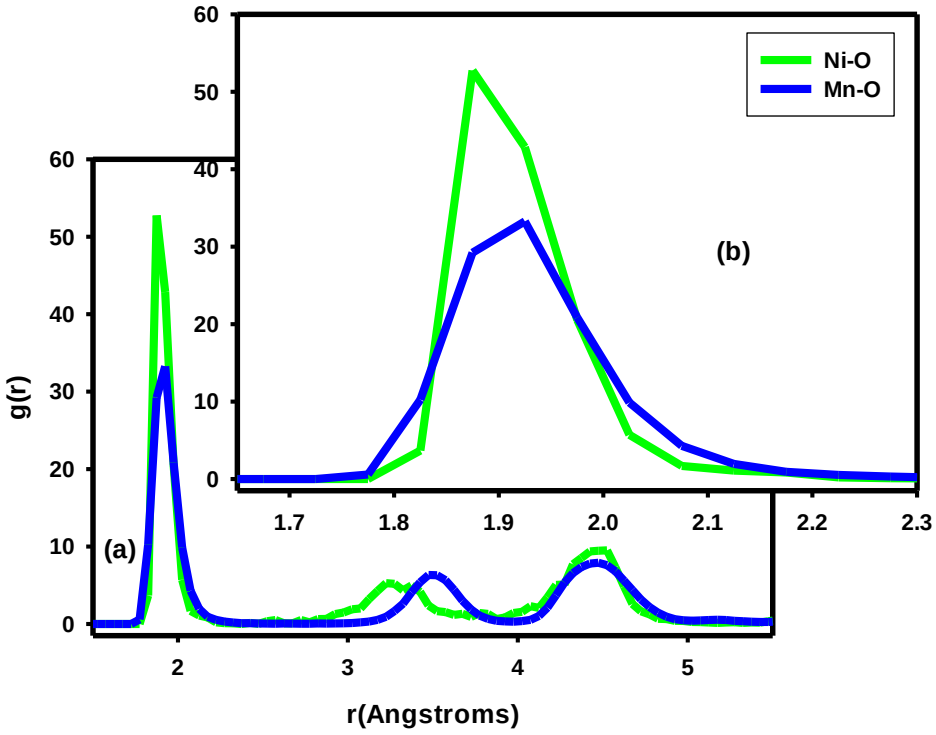

Figure 5.24: (a) RDF graph of the Ni-O (green) and Mn-O (blue) interactions in the recrystallized $LiMn_{1.98}Ni_{0.2}O_4$ spinel nanosphere. (b) an inset of the first RDF peak denoting the first neighbour distance.

The $LiMn_{1.98}Ni_{0.02}O_4$ spinel structure is characterized in figure 5.25. The LiM_2O_4 (M=Mn, Ni) spinel phases that formed during synthesis in the material are illustrated in figure 5.25. The LiM_2O_4 (M=Mn, Ni) spinel phases are shown in a conventional unit cell view, which gives a clear view of the atoms in their respective lattice sites. Figure 5.25 (c) shows the A&R-simulated Ni-doped Li-Mn-O spinel phase captured from a few layers of the structure extracted from the nanosphere in figure 5.25 (a). The A&R-simulated spinel phase is compared to a theoretical Li-Mn-O spinel phase. Therefore, Li atoms are occupying the 16c octahedral sites, Mn atoms are in the 16d tetrahedral sites, and O atoms are observed in the 32e sites. Furthermore, the atomic snapshots show that during recrystallization, Ni (dopant) atoms occupy the 16d lattice sites, which are generally occupied by manganese in this spinel. Furthermore, the bond between the transition metal and oxygen was also monitored on the MO_6 (M=Mn, Ni) octahedrons in figure 5.26, extracted from the recrystallized $LiMn_{1.98}Ni_{0.02}O_4$ spinel structure. The Mn-O bond length ranges from 1.860-2.112 Å, while the Ni-O bond lengths range from 1.837-1.940 Å. The longest TM-O bond is observed in the MnO_6 octahedra, and the shortest TM-O bond is noted on the NiO_6 octahedra.

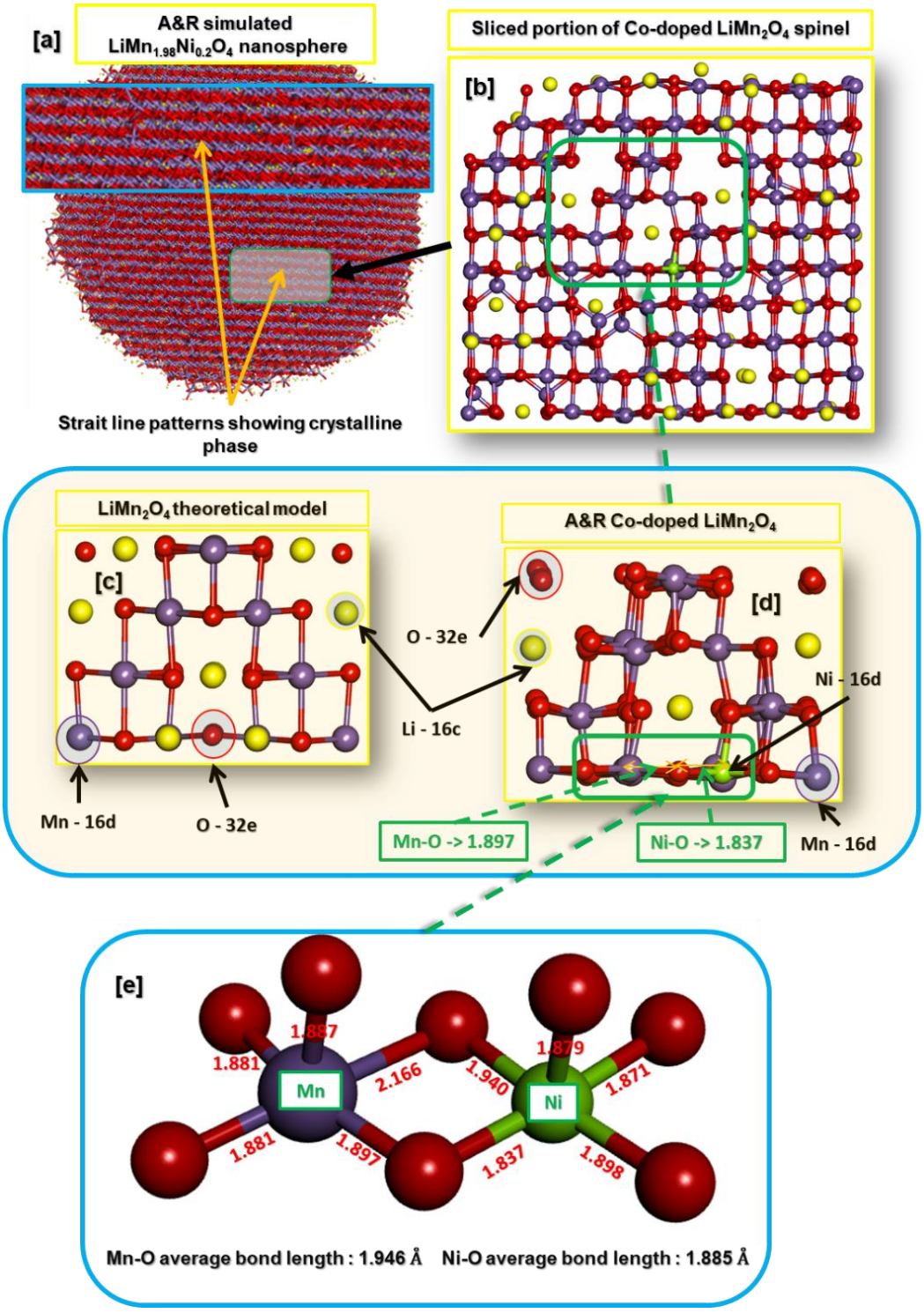

Figure 5.25: Illustration of the structure characterization of the recrystallized (a) $LiMn_{1.98}Ni_{0.2}O_4$ spinel nanosphere. (b) A portion of atoms extracted from the $LiMn_{1.98}Ni_{0.2}O_4$ nanosphere. (c) A theoretical model compared to the A&R-simulated LiM_2O_4 (M=Mn, Co) spinel phase.

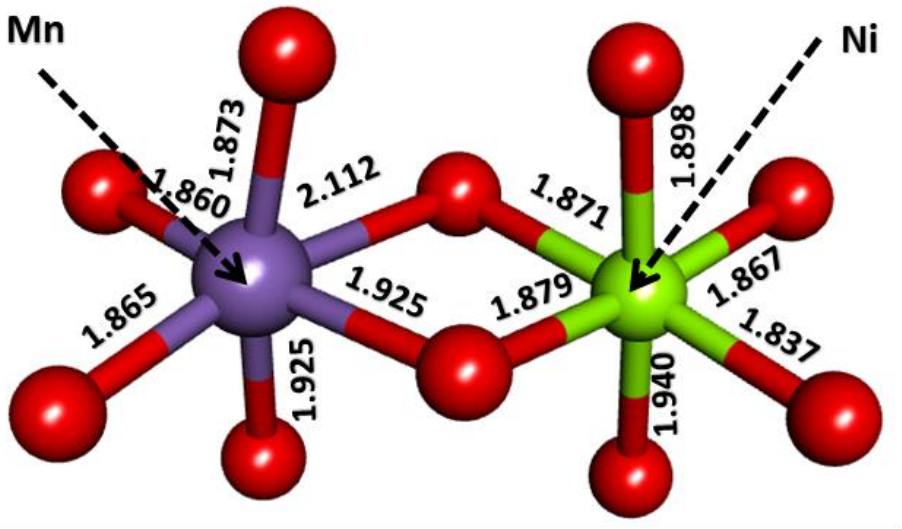

Figure 5.26: The transition metal (TM) and oxygen octahedron in Ni-doped Li-Mn-O ($LiMn_{1.98}Ni_{0.02}O_4$) spinel.

The formation of the M_3O_4 (M=Mn, Ni) phase was also examined in the $LiMn_{1.98}Ni_{0.02}O_4$ spinel structure. Figure 5.27 demonstrates a portion of the $LiMn_{1.98}Ni_{0.02}O_4$ spinel structure depicting Mn atoms occupying the 8a tetrahedral sites. The occupation of the 8a tetrahedral sites with Mn is associated with the formation of the Mn_3O_4 spinel phase at high temperatures [236]. Moreover, Ni atoms are only observed in the 16d octahedral sites, which suggests that the Ni_3O_4 phase does not form for the current concentration of Ni in the doped structure. Furthermore, in figures 5.27 (b), (c), and (d), the first neighbour interaction of Ni and Li is not observed. This was further examined through the RDF plot of the Li-Mn and Li-Ni interactions in figure 5.28. The first neighbour distance of the Li-Mn interaction is found at the atomic separation of ~2.820 Å, which is comparable to a value of ~2.825 Å observed in the $LiMn_{1.98}Co_{0.02}O_4$ spinel structure. However, the first neighbour distance for the Li-Ni interaction is noted at the atomic separation distance of ~4.202 Å. Therefore, Li atoms are ~4.202 Å far from Ni atoms in the structure. This suggests that Ni^{4+} could be more stable than Ni^{3+} at elevated temperatures. The findings were further corroborated by the calculation of the average number of Li atoms around Mn and Ni atoms. Figure 5.29 shows zero Li atoms around Ni atoms in the atomic separation range between 0-3.5 Å and 2.75 Li

atoms around Mn atoms in this range. In the range between 3.5 and 7.0 Å, the average number of Li atoms is found to be 13.65 and 13.81 for Ni and Mn, respectively. Figures 5.30 and 5.31 demonstrate the number of NiO4 octahedrons in the structure. The calculated number of NiO4 octahedrons was found to be zero, which is in line with the atomic-structure images shown in figure 5.30. The images only show Mn atoms in the tetrahedral sites, which are associated with the Mn_3O_4 phase.

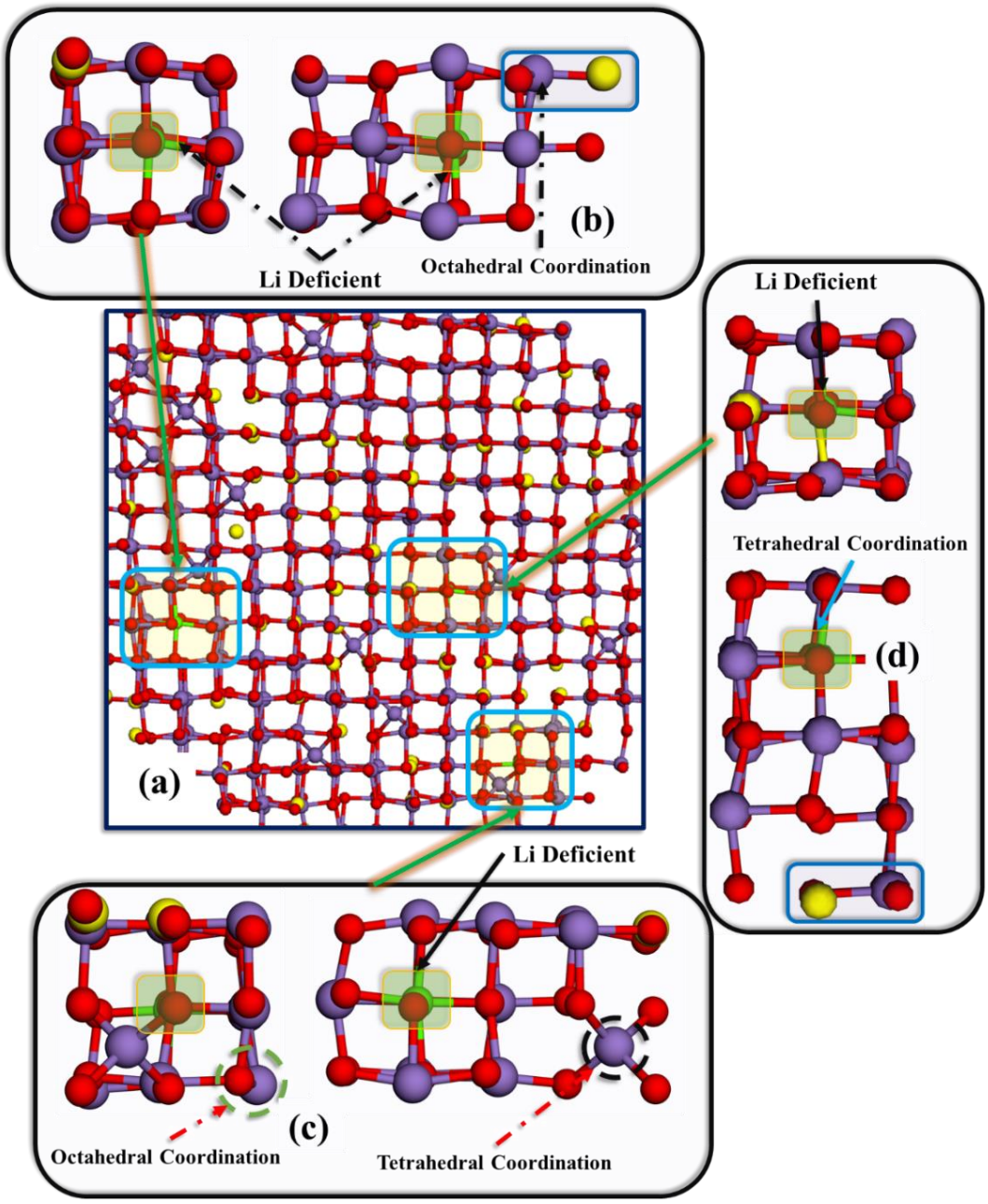

Figure 5.27: Illustration of the M_3O_4 (M=Mn, Ni) phase that formed during the simulated synthesis in the $LiMn_{1.98}Ni_{0.02}O_4$ structure.

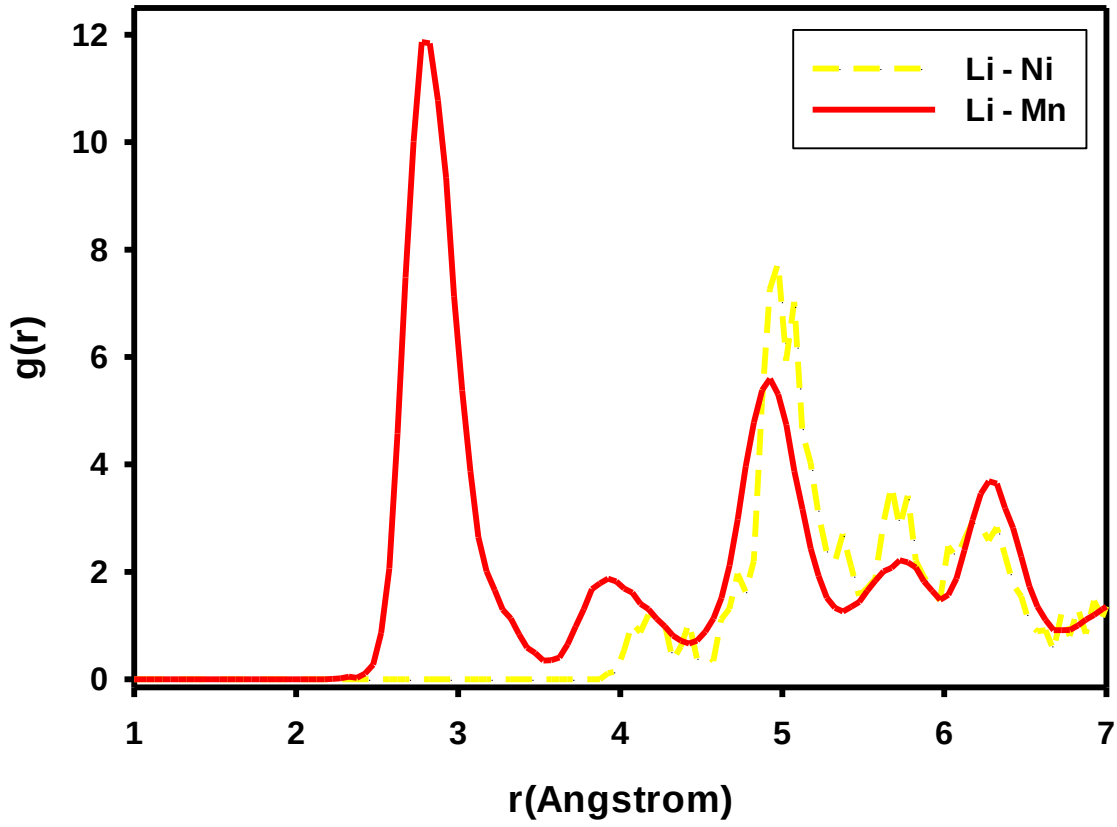

Figure 5.28: RDF plot for the Li-Ni and Li-Mn interactions in the $LiMn_{1.98}Ni_{0.02}O_4$ spinel structure showing the Li-Ni local environment.

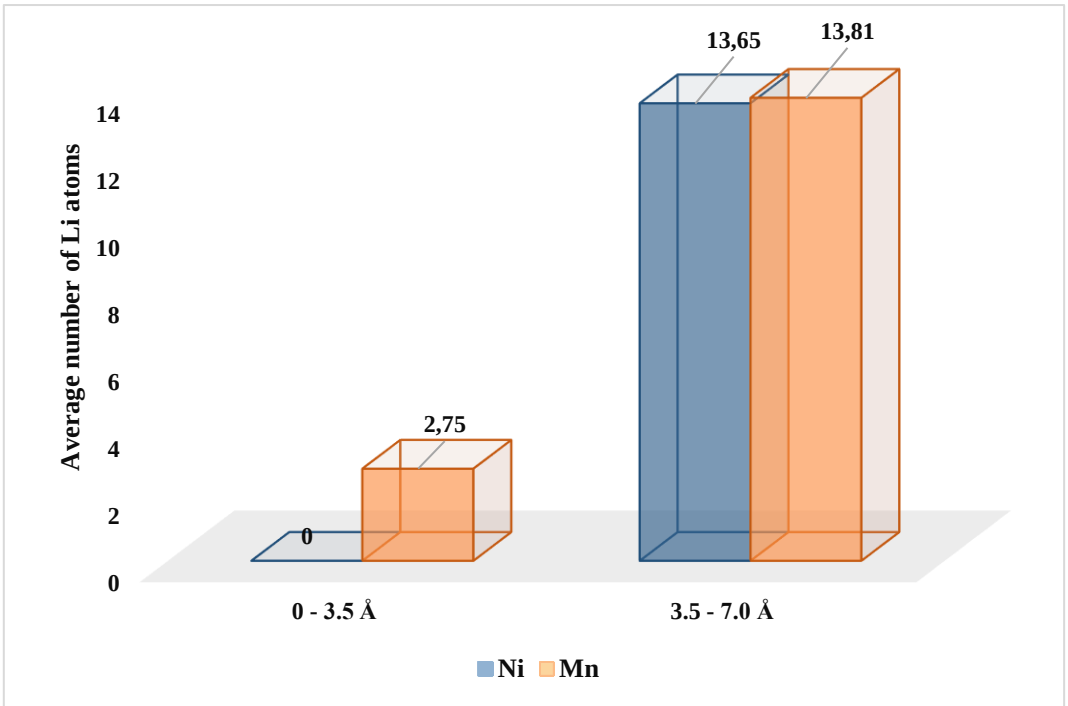

Figure 5.29: The average number of Ni and Mn atoms around Li atoms in the atomic-separation range between 0-3.5 and 3.5-7.0 Å.

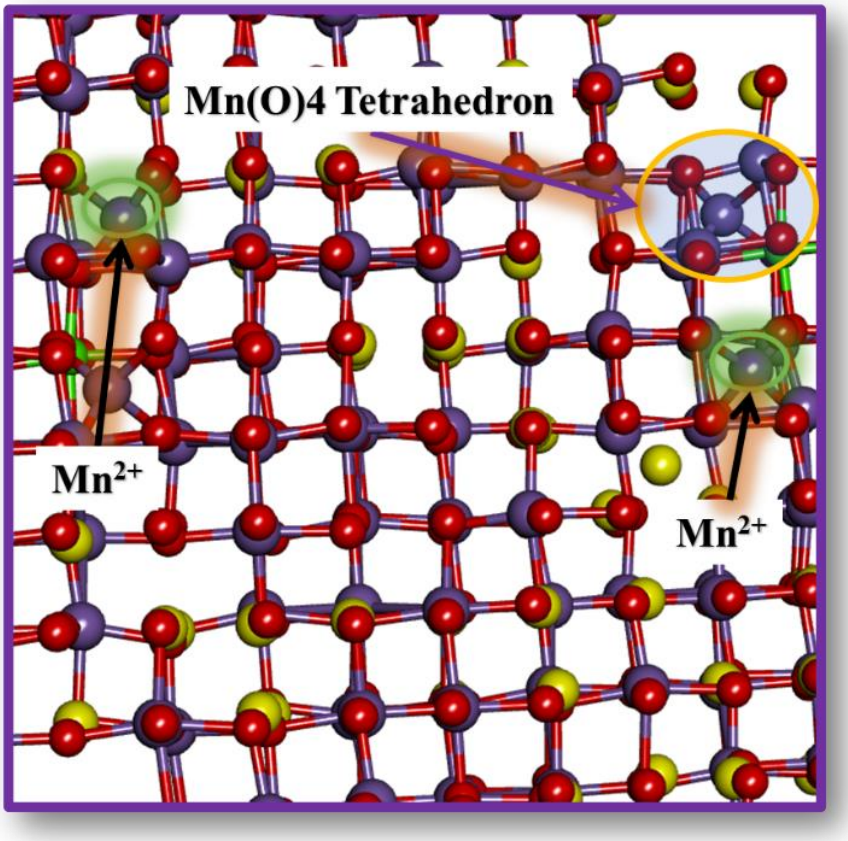

Figure 5.30: Atomic-level structure image showing the occupation of the tetrahedral sites that form MO_4 (M=Mn, Ni) tetrahedrons.

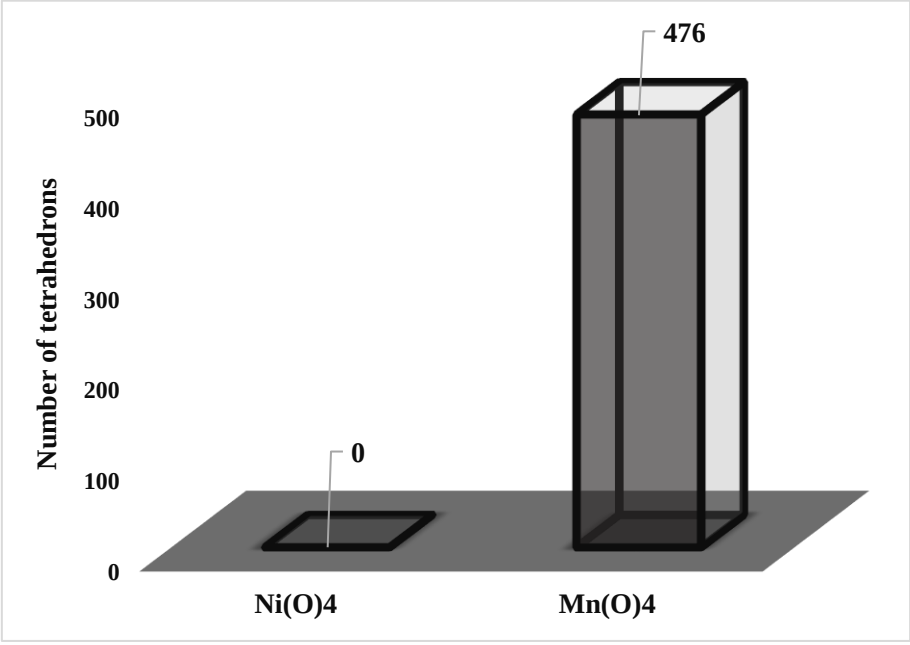

Figure 5.31 The total number of NiO4 and MnO4 tetrahedrons in the $LiMn_{1.98}Ni_{0.02}O_4$ spinel structure.

The 8.01 nm $LiMn_{1.98}Ni_{0.02}O_4$ spinel structure was further characterized with the XRD pattern shown in figure 5.32 (a). The XRD pattern was calculated in the range 2θ= 10-70° with a step size of 0.01. The XRD pattern was indexed to a spinel structure with the Fd-3m space group. All the major spinel diffraction peaks (111), (311), (222), (400), (331), (511), (440), and (531) are observed in the XRD pattern. The observed reflections are comparable to the XRD patterns illustrated in figure 5.32 (b), determined by Tian et al. [239]. Several small impurity phases are observed in the XRD pattern of the A&R-simulated structure. The (311) XRD peak splits into two XRD peaks representing the Mn_3O_4 impurity phase and a cubic $LiMn_{1.98}Co_{0.02}O_4$ spinel. Furthermore, the (222), (400), (331), and (531) XRD peaks split due to the formation of the layered Li_2MnO_3 structure with a space group of c2/2m. Moreover, the Li_2MnO_3 XRD reflections are small and less intense, which suggests that the concentration of the layered phase is lower in the A&R-simulated spinel structure. The Mn_3O_4 and Li_2MnO_3 impurity phases are validated by the XRD patterns illustrated in figures 5.32 (c) and (d) [230, 231]. The cubic spinel phase is the dominant phase in the A&R-simulated structure ($LiMn_{1.98}Ni_{0.02}O_4$), as all the major spinel XRD peaks are sharp and intense.

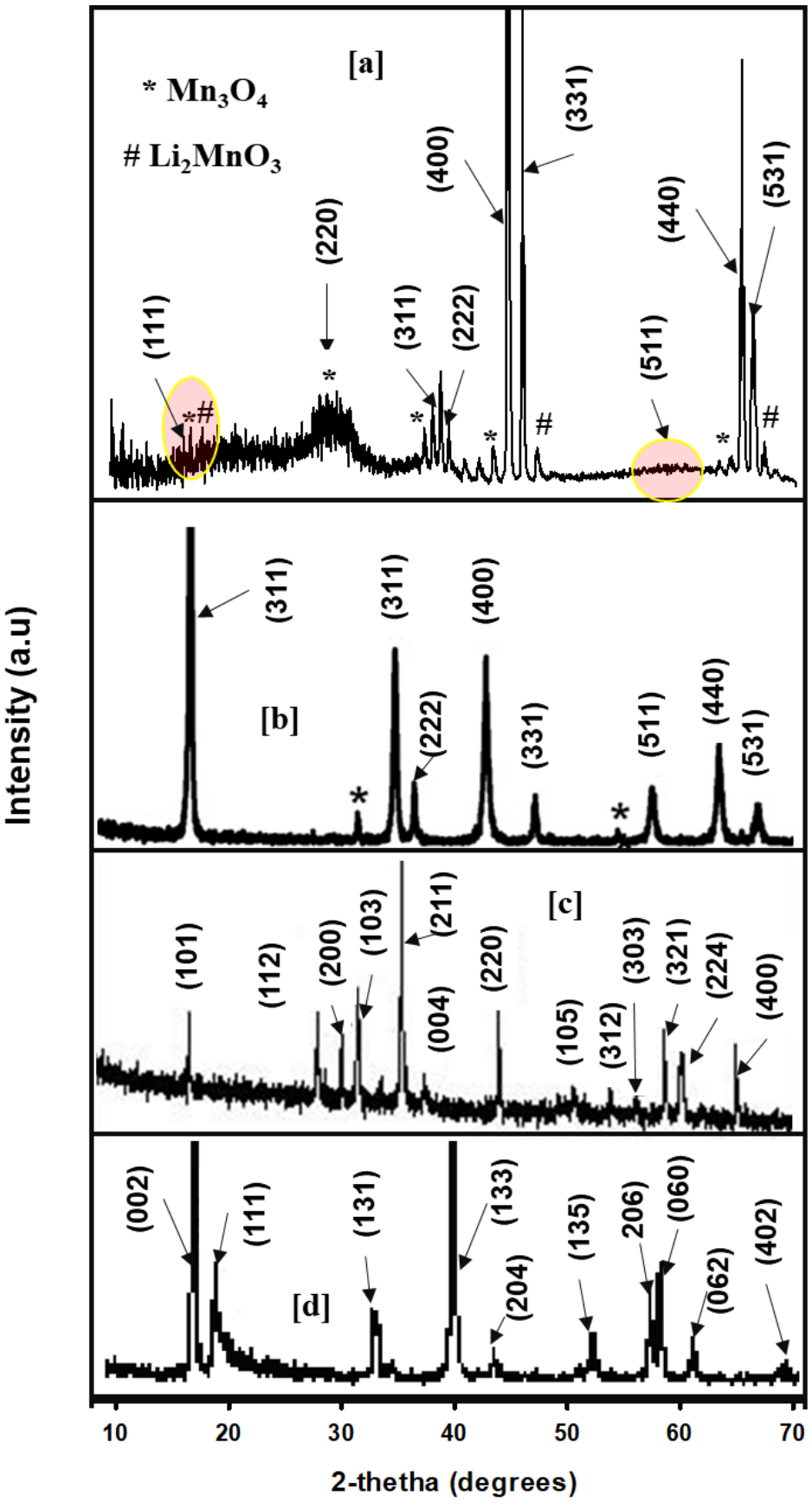

Figure 5.32 The A&R-simulated XRD pattern is compared to the XRD patterns of $LiMn_2O_4$ spinel [239], Mn_3O_4 [230] and Li_2MnO_3 from experiments [231].

5.4.3 Characterization of $LiMn_{1.98}Co_{0.01}Ni_{0.01}O_4$

The amorphous $LiMn_2O_4$ spinel double-doped with Co and Ni was also recrystallized. The final cooled structure is shown in Figure 5.33. The Li, Mn, Co, Ni, and O atoms can be noted forming a line pattern of atoms, as demonstrated by the arrows. The line pattern of atoms indicates the successful recrystallization of the $LiMn_{1.98}Co_{0.01}Ni_{0.01}O_4$ spinel structure. Furthermore, the crystallinity and successful recrystallization of the Co- and Ni-doped Li-Mn-O spinel structure were confirmed with the RDF graph shown in figure 5.34. The Mn-O bond distance is found to be ~1.917 Å, as denoted by the first RDF peak in the figure. The calculated Mn-O bond length is comparable to the value of ~1.923 Å found in experiments [232]. Furthermore, the Co-O bond length is found to be ~1.896 Å, which is not far from the value obtained by Wolverton and co-workers [235]. The bond length of the Ni-O interaction is also examined and found to be ~1.887 Å, which is in line with the findings of [116]. The presence of long-range atomic ordering in the structure is also confirmed by the resolved RDF peaks representing the second and third nearest neighbour distances.

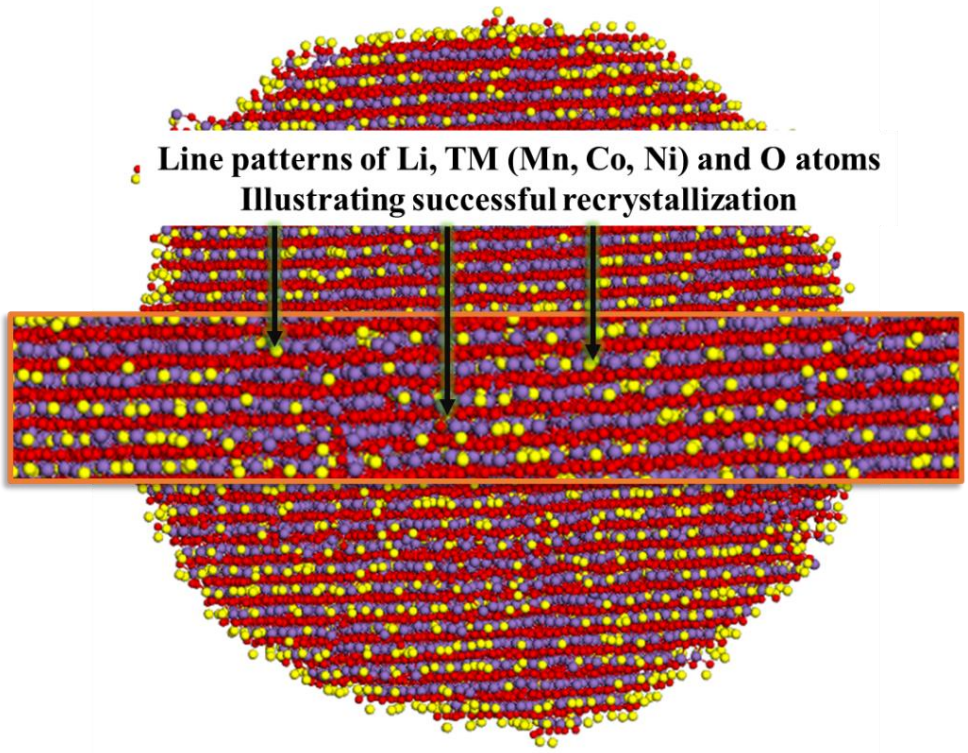

Figure 5.33: The 8.01 nm $LiMn_{1.98}Co_{0.01}Ni_{0.01}O_4$ spinel structure recrystallized at a temperature of 1900 K and cooled to a temperature of 5 K.

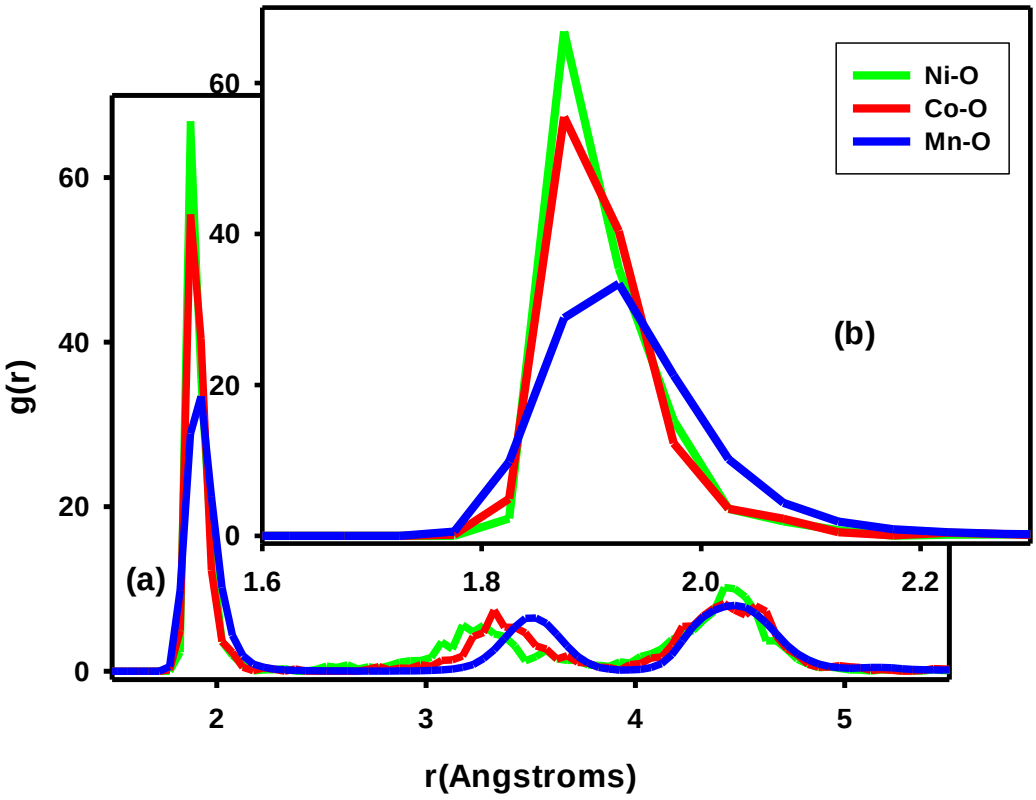

Figure 5.34: RDF graphs of the Ni-O (green), Co-O (red), and Mn-O (blue) in the double-doped spinel structure ($LiMn_{1.98}Co_{0.01}Ni_{0.01}O_4$).

The $LiMn_{1.98}Co_{0.01}Ni_{0.01}O_4$ nanosphere was also further characterized at the atomic level, as shown in figure 5.35. Several layers of the nanosphere have been removed from the structure for investigation of the spinel phase that formed during recrystallization. The atomic-level structure images show the presence of a spinel phase magnified and depicted in Figure 5.35 (d), which is comparable to a theoretical $LiMn_2O_4$ spinel model. Li atoms are observed in the 16c octahedral sites, and the transition metals (Mn and Ni) are noted at the 16d tetrahedral sites. Furthermore, oxygen atoms occupy the 32e sites, as shown in the figure. Figure 5.37 captures the first-neighbour environment of the Li-Mn interaction in the Co and Ni double-doped Li-Mn-O spinel structure. Moreover, the value is comparable to a value of ~2.826 Å found in the $LiMn_{1.98}Co_{0.02}O_4$ and $LiMn_{1.98}Ni_{0.02}O_4$ A&R-simulated spinel structures. This is also consistent with the findings of Xu B. and Meng S. [237]. A small RDF peak of the Li-Co interaction is observed around the atomic separation of ~2.825 Å, which indicates that a small number of lithium atoms are around Co atoms at this atomic separation distance. Furthermore, the Li-Co interaction shows zero probability of finding Li atoms around Ni atoms in the atomic separation near ~2.825 Å. The RDF

plot is in line with the atomic-structure images shown in figure 5.36, showing a deficiency of Li atoms around Co and Ni atoms. Figure 5.38 demonstrates the average number of Li atoms around Mn and Co atoms in the structure. At atomic separation distances between 0 and 3.5 Å, no Li atoms are found around Ni atoms, and 0.20 Li atoms are found near Co atoms. Furthermore, every Mn atom is near 2.78 Li atoms in the atomic separation range between 0 and 3.5 Å. Figure 5.39 demonstrates the occupation of the tetrahedral sites by transition metals (TMs) for the formation of the TM_3O_4 phase. Numerous Mn atoms are noted on the 8a tetrahedral sites, suggesting the formation of the Mn_3O_4 high-temperature impurity phase. The Co and Ni dopants are also observed in the atomic-level structure images, occupying the 16d octahedral sites. Figure 5.40 shows the calculated number of NiO4, CoO4, and MnO4 tetrahedrons in the double-doped Li-Mn-O spinel structure. The total number of CoO4 and NiO4 is zero, and the number of CoO4 octahedrons is 502.

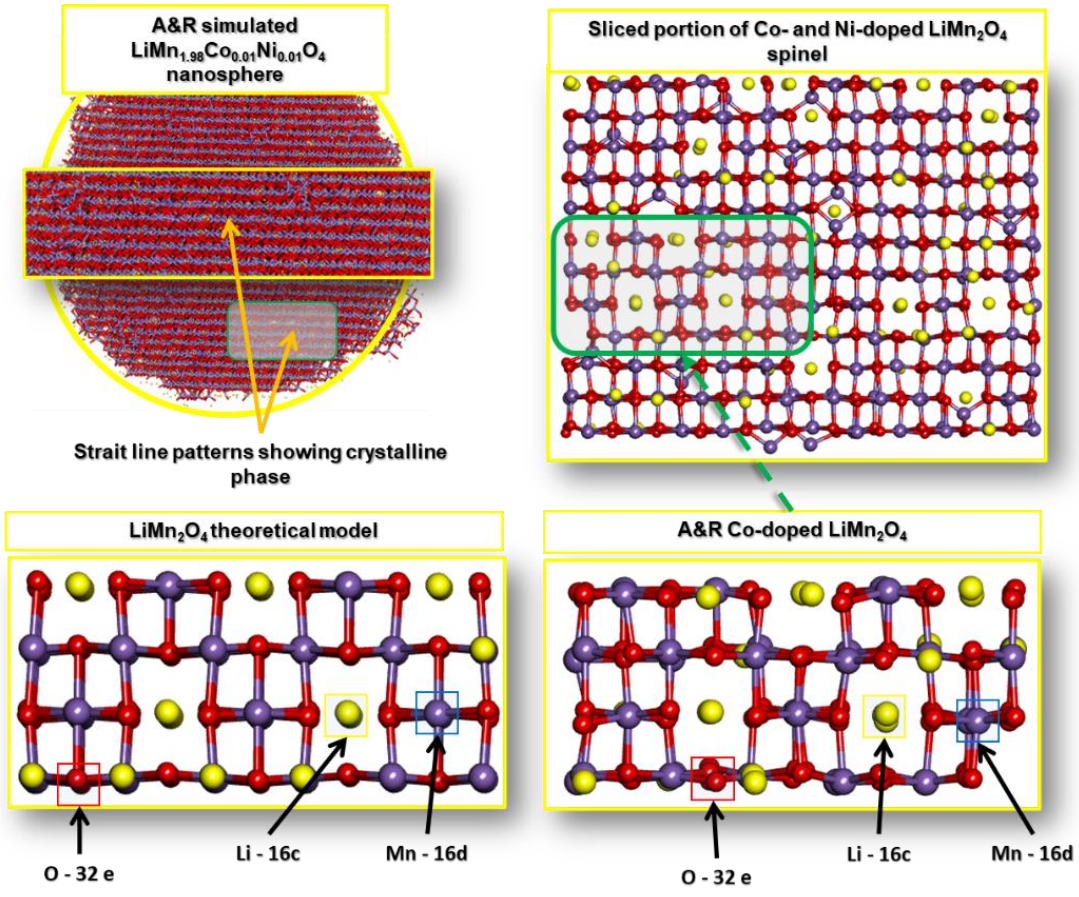

Figure 5.35: RDF graphs of the Ni-O (blue), Co-O (green), and Mn-O (red) in Co- and Ni-doped $LiMn_2O_4$ spinel.

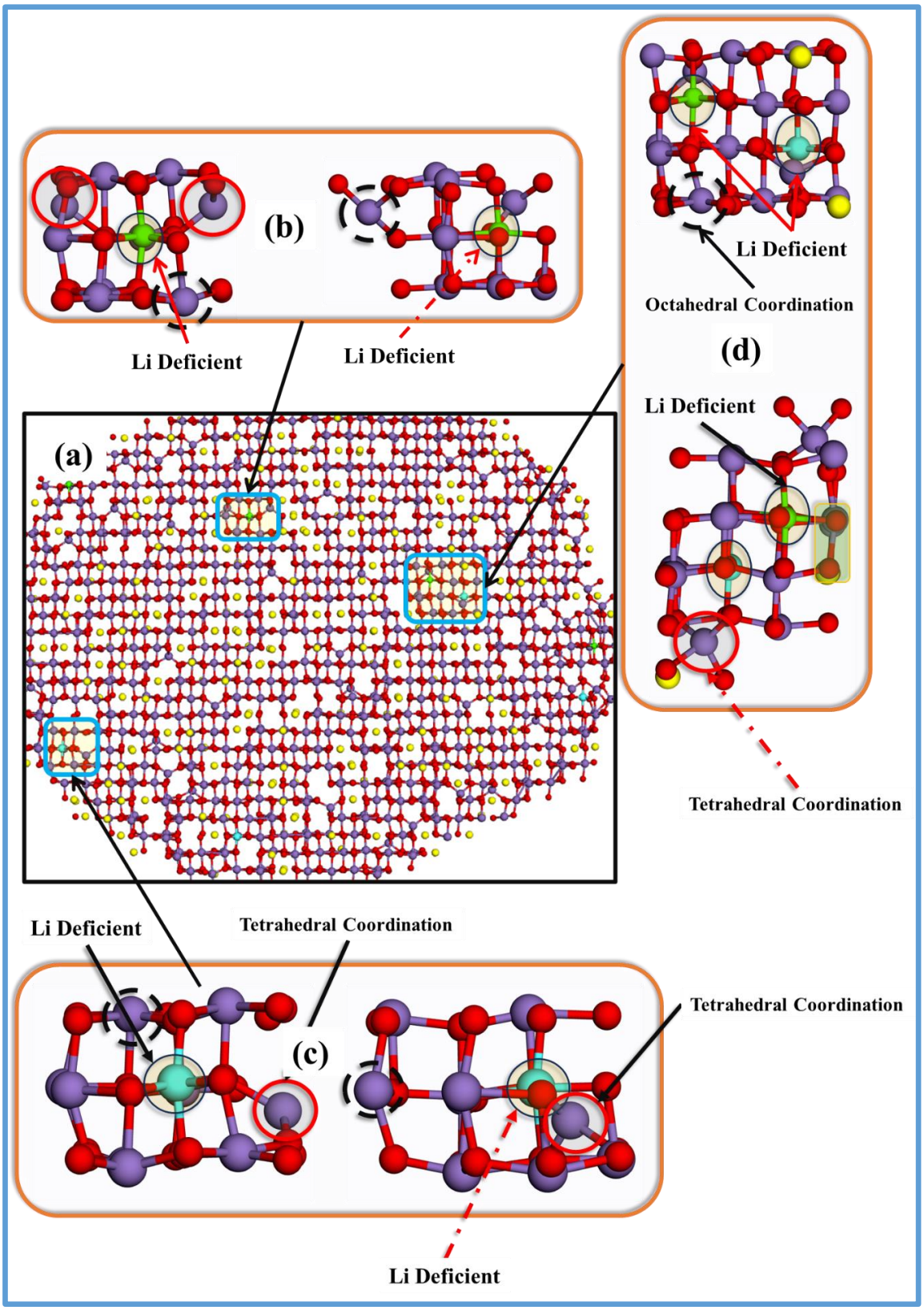

Figure 5.36: Atomic-structure images of a portion of the A&R-simulated $LiMn_{1.98}Co_{0.01}Ni_{0.01}O_4$ spinel structure illustrating the deficiency of Li atoms around Co and Ni atoms.

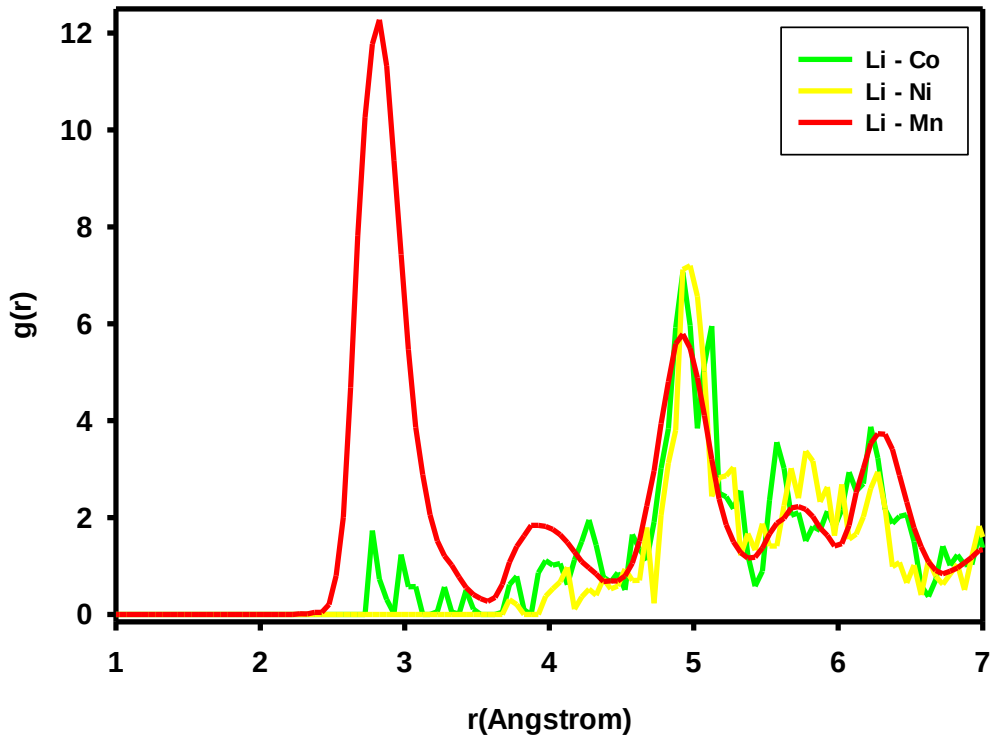

Figure 5.37: RDF graphs of the Ni-O (green), Co-O (red), and Mn-O (blue) in the double-doped spinel structure ($LiMn_{1.98}Co_{0.01}Ni_{0.01}O_4$).

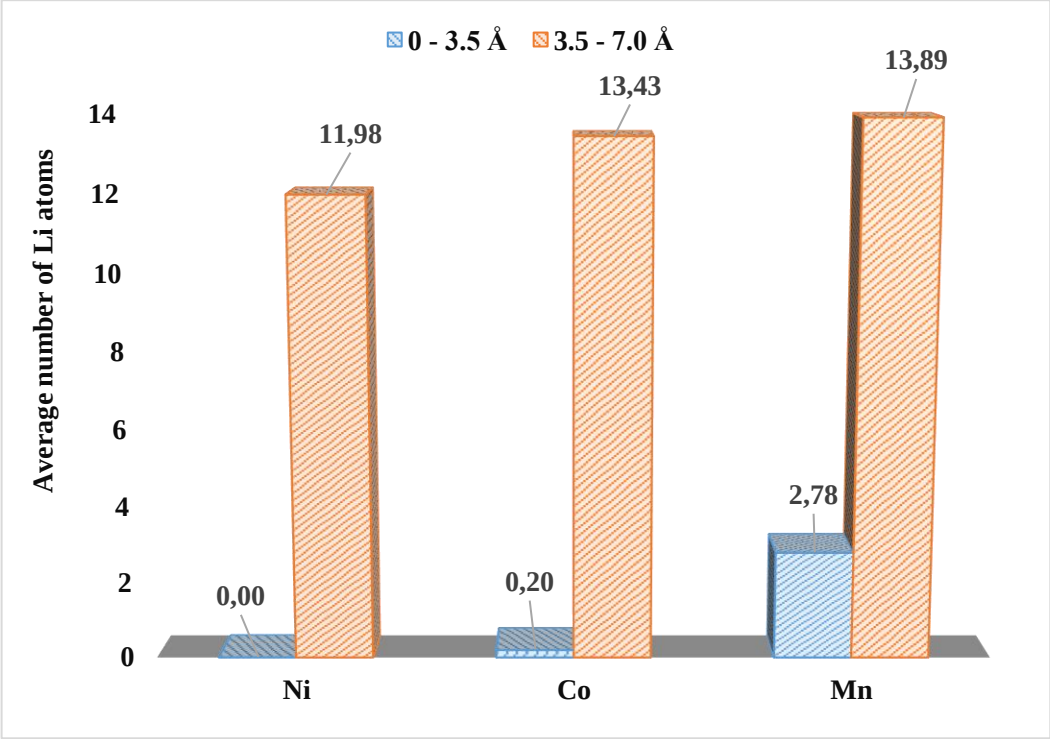

Figure 5.38: The average number of Li atoms around Mn, Ni, and Co atoms in the A&R-simulated $LiMn_{1.98}Co_{0.01}Ni_{0.01}O_4$ spinel structure.

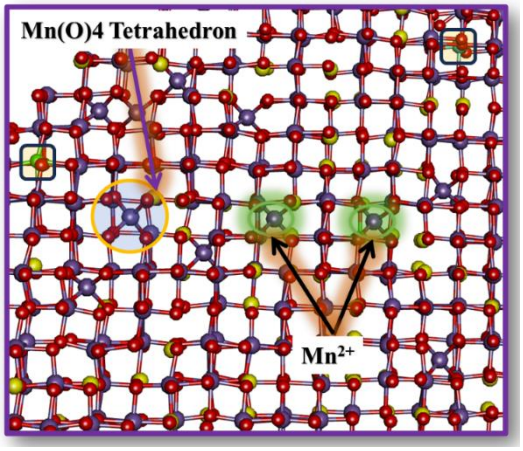

Figure 5.39: Atomic-level structure images illustrating the occupation of the 8a tetrahedral sites by transition metal elements.

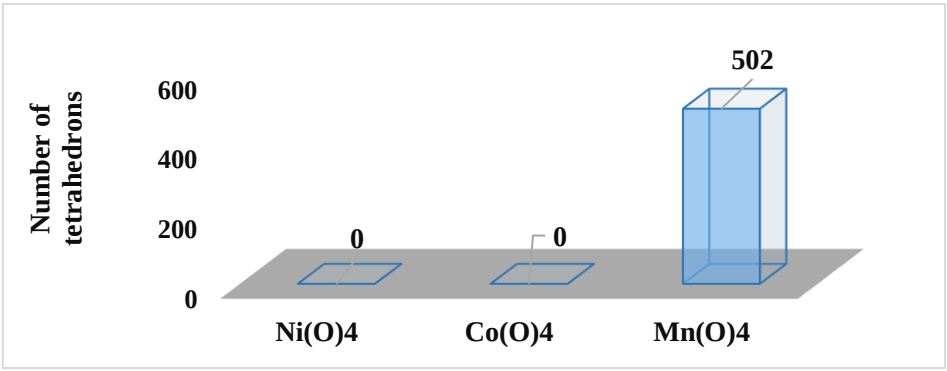

Figure 5.40: The number of NiO4, CoO4, and MnO4 octahedrons in the $LiMn_{1.98}Co_{0.01}Ni_{0.01}O_4$ spinel structure.

The structural characterization of $LiMn_{1.98}Co_{0.01}Ni_{0.01}O_4$ was further carried out through XRD patterns, as illustrated in figure 5.41. The (111), (311), (222), (400), (331), (511), (440), and (531) XRD diffraction peaks that characterize the cubic spinel structure are observed in the pattern shown in figure 5.41 (a). Moreover, the XRD pattern can be indexed to a cubic spinel of the space group Fd-3m. The simulated XRD pattern compares well to the XRD pattern shown in figure 5.41 (b) from experiments [239]. Furthermore, the presence of the Mn_3O_4 and Li_2MnO_3 impurity phases is indicated by the splitting of the spinel characteristic peaks. This is further confirmed by the XRD pattern shown in figures 5.41 (c) and (d) [230, 231]. The major spinel peaks are well pronounced and intense, which suggests that the spinel phase is dominant in the structure.

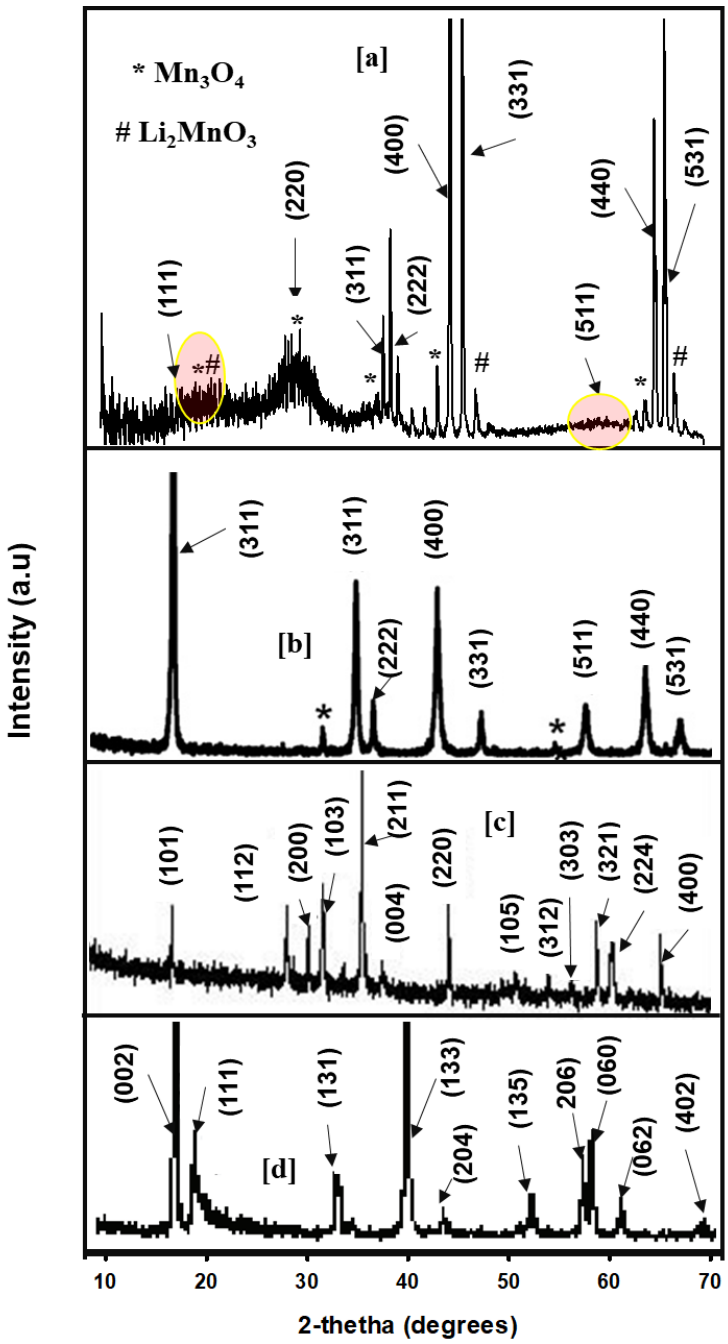

Figure 5.41: XRD pattern of $LiMn_{1.98}Co_{0.1}Ni_{0.1}O_4$, which is compared to the XRD pattern of $LiMn_2O_4$ synthesized in experiments [239]. The (c) Mn_3O_4 [230] and (d) Li_2MnO_3 [231] XRD patterns confirm the presence of these impurity phases in the A&R-simulated structure.

5.5 The effect of substituting Co and/or Ni in $LiMn_2O_4$ spinel

5.5.1 Li transport in the Co- and/or Ni-doped Li-Mn-O spinel nanostructures

The movement of lithium atoms in the Co- and/or Ni-doped Li-Mn-O spinel nanostructures is captured by the mean square displacement (MSD) plot in figure 5.42. The mobility of Li atoms in the structure was monitored for 1400 ps at a temperature of 400 K. This was sufficient to capture the effect of Co and/or Ni in the $LiMn_2O_4$ spinel structure. The Co-doped $LiMn_{1.98}Co_{0.02}O_4$ spinel structure has the lowest activity of lithium atoms in the structure. The introduction of Ni in the $LiMn_2O_4$ structure seems to improve the mobility of Li atoms more than the introduction of Co in the structure. Since in about 1400 ps, Li^+ covers distances of ~0.92, 0.98, and 1.28 Å in $LiMn_{1.98}Co_{0.02}O_4$, $LiMn_{1.98}Co_{0.01}Ni_{0.01}O_4$, and $LiMn_{1.98}Ni_{0.02}O_4$, respectively. Moreover, the movement of lithium atoms in the double-doped spinel structure is greater than in the $LiMn_{1.98}Co_{0.02}O_4$ nanostructure but lower than in the $LiMn_{1.98}Ni_{0.02}O_4$ nanostructure. Figure 5.43 shows the diffusion coefficient of Li in $LiMn_{1.98}Co_{0.02}O_4$, $LiMn_{1.98}Co_{0.01}Ni_{0.01}O_4$, and $LiMn_{1.98}Ni_{0.02}O_4$ in the temperature range (a) 100-400 K and 100-800 K. In the range of 100-400 K, the single-doped $LiMn_{1.98}Ni_{0.02}O_4$ spinel structure shows superior Li^+ diffusion, and the double-doped $LiMn_{1.98}Co_{0.01}Ni_{0.01}O_4$ structure shows inferior Li^+ diffusion. However, in the range 100-800 K, Li diffusion in the double-doped spinel structure improves as compared to $LiMn_{1.98}Ni_{0.02}O_4$ and $LiMn_{1.98}Co_{0.02}O_4$. At 300 K, the diffusion coefficients of $LiMn_{1.98}Co_{0.02}O_4$, $LiMn_{1.98}Co_{0.01}Ni_{0.01}O_4$, and $LiMn_{1.98}Ni_{0.02}O_4$ are 0.61 x 10^{-12} m^2/s, 0.73 x 10^{-12} m^2/s, and 1.6 x 10^{-12} m^2/s, respectively. The ionic conductivity of Li^+ in the doped structures was also calculated, as shown in figure 5.44. The conductivity of Li in $LiMn_{1.98}Ni_{0.02}O_4$ was found to be superior, and in the $LiMn_{1.98}Co_{0.02}O_4$ structure, it was found to be inferior. At 400 K, the ionic conductivity of Li^+ is found to be 0.23 x 10^{-6} S cm^{-1}, 0.36 x 10^{-6} S cm^{-1}, and 0.94 x 10^{-6} S cm^{-1} The ionic conductivity of Li^+ calculated by Xie and co-workers was found to be ~5.25 x 10^{-7} S cm^{-1} at room temperature, which is comparable to values found in this work [240].

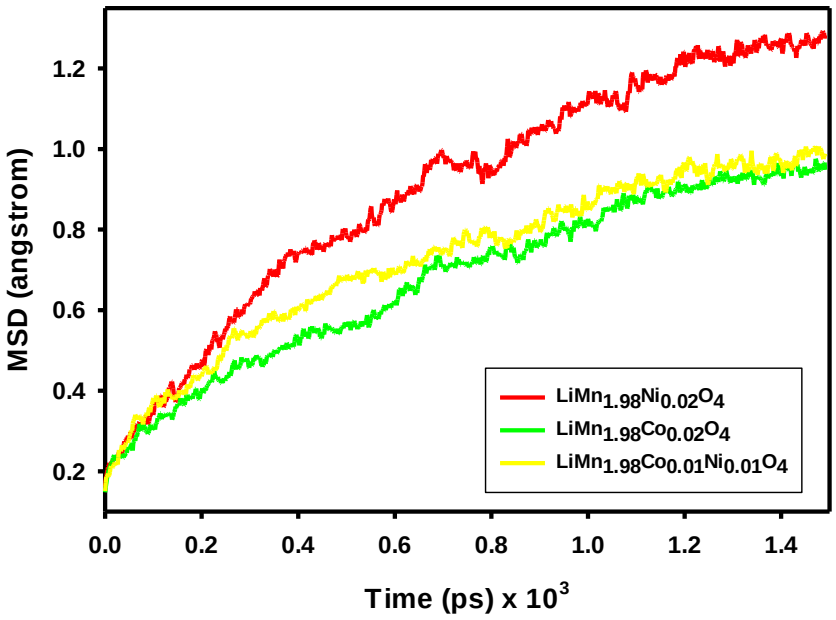

Figure 5.42: MSD plot of Li in $LiMn_{1.98}Ni_{0.02}O_4$, $LiMn_{1.98}Co_{0.02}O_4$, and $LiMn_{1.98}Co_{0.01}Ni_{0.01}O_4$.

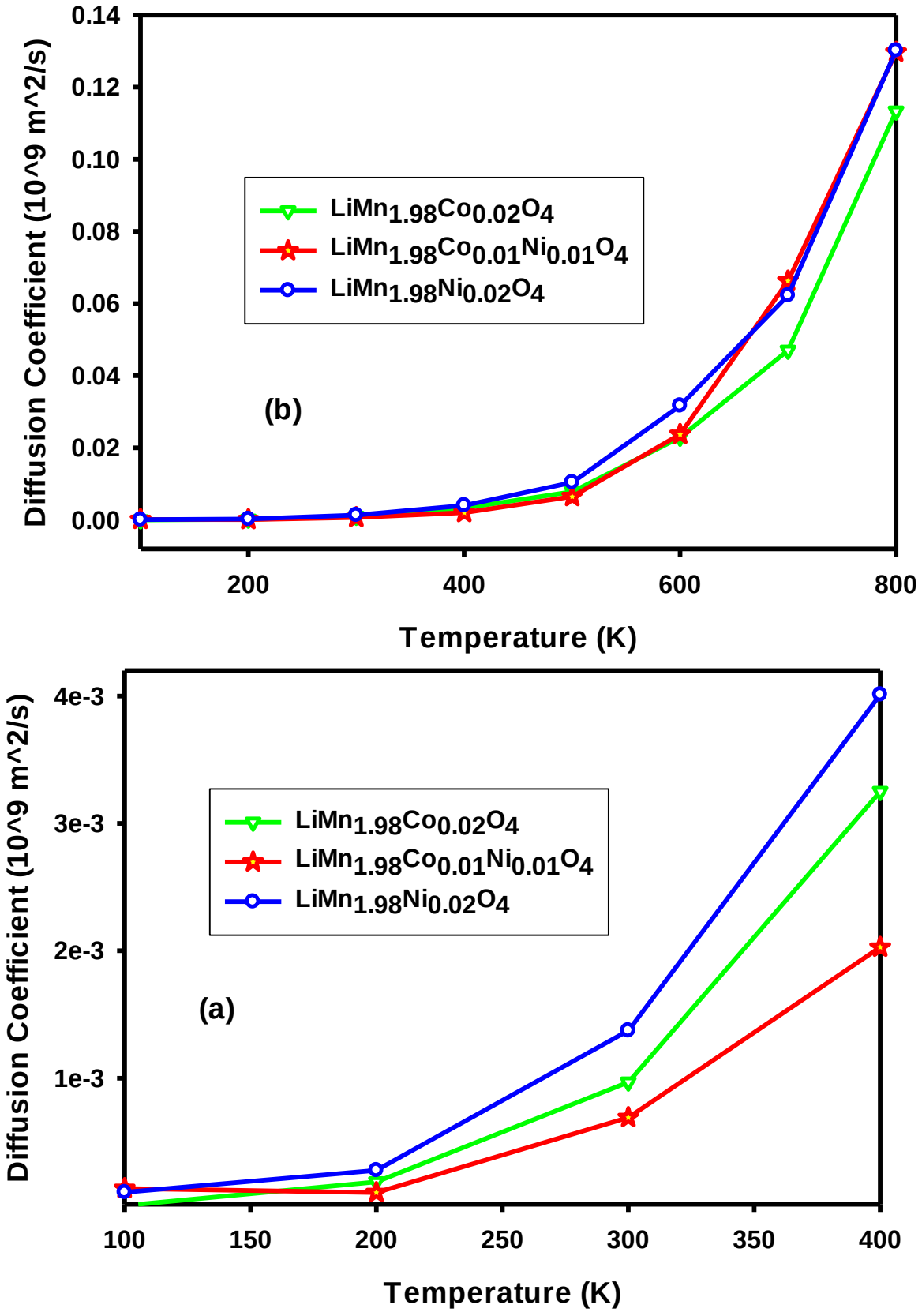

Figure 5.43: The rate of Li^+ diffusion in $LiMn_{1.98}Ni_{0.02}O_4$, $LiMn_{1.98}Co_{0.02}O_4$, and $LiMn_{1.98}Co_{0.01}Ni_{0.01}O_4$.

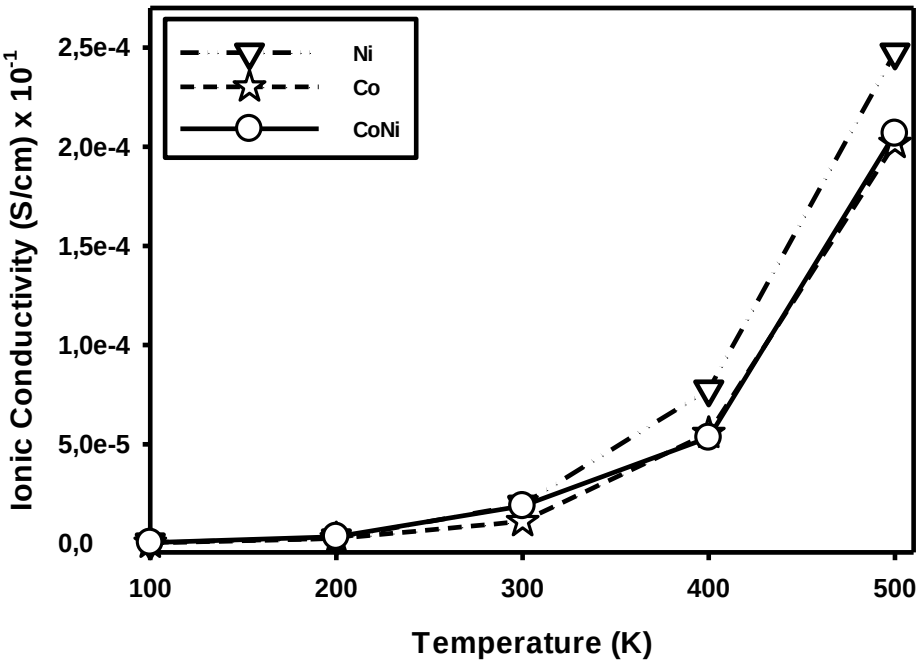

Figure 5.44: Li^+ conductivity in $LiMn_{1.98}Ni_{0.02}O_4$, $LiMn_{1.98}Co_{0.02}O_4$, and $LiMn_{1.98}Co_{0.01}Ni_{0.01}O_4$.

5.6 Discussion

The chapter details the impact of doping $LiMn_2O_4$ spinel with Co and/or Ni on its microstructure and the transport of Li^+ ions in the structure to improve its rate performance and stabilize its structure. The microstructure and transport properties affect the rate capabilities and the overall performance of a Li-ion battery utilizing $LiMn_2O_4$ as cathode material. Moreover, the introduction of Co- and/or Ni- in the structure could impact the microstructure and microstructural properties such as diffusion. The substitution seeks to reduce the number of Mn^{3+} ions in the structure by substituting cations with a comparable ionic radius to that of Mn^{3+} (0.645 Å). The ionic radius of Ni^{3+} is ~0.53 Å and of Co^{3+} is ~0.55 Å, which makes them suitable candidates for partial substitution of Mn with Co^{3+} and/or Ni^{3+} [146, 147]. Moreover, the investigation of the effect of doping of $LiMn_2O_4$ with Co and/or Ni serves as a test for the developed Buckingham potentials for the Co-Co, Co-O, Co-Li, Ni-Ni, Ni-O, Ni-Li, Co-Mn, Ni-Mn, and Ni-Co interactions in chapter 3. The development of the potentials is motivated by the lack of accurate interatomic potentials for the interactions that arise from doping $LiMn_2O_4$ with Co and Ni.

The Co- and/or Ni-doped Li-Mn-O spinel structures are prepared with the molecular dynamics code, DLPOLY [220], using the A&R simulated synthesis (simulated amorphization and recrystallization) technique [71]. The successful amorphization and recrystallization of the doped spinel structure are confirmed with RDF graphs, atomic-level structure images, and XRD graphs. The dopants (Co and Ni) were introduced successfully in the amorphous $LiMn_2O_4$ spinel structure and were confirmed by the sharp RDF peaks at defined lattice positions in figures 5.6, 5.8, 5.10, 5.11, and 5.12. The bond length of the Mn-O interaction is ~1.915 Å, ~1.912 Å, and ~1.917 Å in $LiMn_{1.98}Co_{0.02}O_4$, $LiMn_{1.98}Ni_{0.02}O_4$, and $LiMn_{1.98}Co_{0.01}Ni_{0.01}O_4$, respectively. Kwon et al. found the value of Mn-O bond length to be ~1.923 Å, which is comparable to the values determined in this work [232]. Moreover, XRD patterns (figures 5.22, 5.32, and 5.41) showed the presence of all the major spinel characteristic peaks {(111), (311), (222), (400), (331), (511), (440), and (531)} and were compared to the XRD pattern of $LiMn_2O_4$ determined in experiments [239]. The A&R simulated synthesis technique is a high-temperature process. Therefore, the Li_2MnO_3 and Mn_3O_4 impurity phases were observed in the material, which is consistent with literature [230, 231].

The atomic-level structural characterization of the $LiMn_{1.98}Co_{0.02}O_4$ spinel structure showed a good comparison between the A&R-simulated spinel phase and theoretical spinel models. The Co dopant is observed in the 16d octahedral sites, which shows that the $LiMn_2O_4$ spinel structure was doped successfully. Furthermore, a CoO_6 octahedron was compared to a MnO_6 octahedron. The CoO_6 octahedron has the shortest transition metal (TM)-oxygen (O) bond length, and the MnO_6 octahedron has the longest TM-O bond length. Moreover, the average Co-O bond length was found to be ~1.895 Å, which is smaller than the Mn-O average bond length of ~1.915 Å. This suggests that Co could be replacing the Mn^{3+} ion with an ionic radius of 0.645 Å, which is shorter than the ionic radius of 0.545 Å and 0.530 Å for Co^{3+} and Co^{4+}, respectively [241]. The reduction in TM-O average bond length implies that the TMO_6 octahedral framework can be improved. This is consistent with literature [242]. Moreover, the atomic-structure images in figures 5.17 and 5.20 show the occupation of the 8a tetrahedral sites by Mn atoms in the $LiMn_{1.98}Co_{0.02}O_4$ spinel structure. The occupation of the 8a tetrahedral sites by Mn atoms suggests the formation of the high-temperature Mn_3O_4 spinel phase, with Mn^{2+} in the 8a tetrahedral sites, as also observed in literature [236]. The Mn atoms in the tetrahedral sites block the diffusion of Li, as the 8a-16c-8a

diffusion route is disturbed. Furthermore, Co atoms are only observed in the 16d octahedral sites. Therefore, at this concentration of Co ($LiMn_{1.98}Co_{0.02}O_4$), the doping does not disturb the migration of lithium ions in the structure [243]. The structure images are coherent with the calculated number of CoO_4 and MnO_6 octahedrons in figure 5.21, which shows that the number of MnO_6 octahedrons in the simulated structure is 535, while the number of CoO_6 octahedrons is zero. Moreover, figures 5.17, 5.18, and 5.19 show that there's a deficiency of Li atoms around Co atoms. This could suggest that Mn^{4+} is more stable than Mn^{3+} at high temperatures, as the simulated amorphization and recrystallization are high-temperature processes. Moreover, this could further suggest that the overall valence of Mn in the Co-doped spinel structure is lowered, which favours Jahn-Teller distortion.

The Ni dopants were also substituted successfully in the $LiMn_2O_4$ structure, as shown by the atomic-structure images in figure 5.25. The A&R simulated spinel phase showing the Ni atoms in the 16d octahedral sites in figure 5.25 (d) compares well with the theoretical model in figure 5.25 (c). Moreover, figure 5.25 (e) demonstrates bonding in the MnO_6 and NiO_6 octahedrons extracted from the A&R simulated structure $LiMn_{1.98}Ni_{0.02}O_4$. The Ni-O bond distances range from 1.837 to 1.940 Å, and the Mn-O bond distances start from 1.881 to 2.166 Å. Moreover, the average Ni-O bond distance is ~1.885 Å, and the mean bond length of the Mn-O interaction is ~1.912 Å. Therefore, the NiO_6 octahedron is expected to have a higher electron affinity than the MnO_6 octahedron. Hence, the reported Jahn-Teller distortion can be restrained with the introduction of Ni in the $LiMn_2O_4$ spinel structure [244, 245]. Figures 5.27, 5.28, and 5.29 illustrate the lack of Li atoms around Ni atoms in the atomic separation between 0 and 3.5 Å. This also suggests that Ni^{4+} could be the most stable when compared to Ni^{3+} at high temperatures. If this is the case, a decrease in the valence state of Mn is expected, which is unfavourable to the stability of the MnO_6 framework. The occupation of the tetrahedral sites by Mn atoms is also observed in the Ni-doped $LiMn_2O_4$ spinel structure, as illustrated in figures 5.30 and 5.31. The Ni atoms are only occupying the 16d octahedral sites in the structure. This is in line with the findings of Wei and colleagues [83]. It was suggested that in an under-doped Ni-doped spinel structure, the migration of Ni atoms into the 8a tetrahedral sites is not observed.

The $LiMn_2O_4$ spinel structure was also double-doped with Co and Ni. The nanomaterial is shown in figures 5.33 and 5.35. The average bond lengths of the Co-O and Ni-O

interactions were found to be ~1.896 Å and ~1.887 Å, respectively. The bond distance of ~1.917 Å of the Mn-O interaction is longer than the bond distance of the two interactions. The Ni-O interaction has the shortest average bond length in the structure. Therefore, the structural stability of the $LiMn_2O_4$ could be enhanced with Ni. This is consistent with the findings in literature that the Mn-O interaction has a lower bond energy when compared to the bond energies of Co-O and Ni-O [148, 112]. Thus, the partial substitution of Mn with both Mn and Ni will strengthen the TMO_6 framework and, therefore, improve the rate performance of the material. Moreover, figures 5.36, 5.37, and 5.38 also show that there's a deficiency of Li atoms around Ni and Co atoms. This could be linked to the valence of Ni and Co at high temperatures and at low concentrations of Ni and Co. Furthermore, figures 5.39 and 5.40 show that only Mn atoms are occupying the 8a tetrahedral sites. Therefore, at low concentrations, the introduction of Co and Ni does not interrupt the mobility of Li atoms in the structure.

The transport of Li atoms in the doped spinel structures was also investigated, and the results are shown in figures 5.42, 5.43, and 5.44. The substitution of Ni into the $LiMn_2O_4$ spinel structure was found to influence the movement of Li atoms more positively than Co in the structure. This is deduced from the high MSD plot of the $LiMn_{1.98}Ni_{0.02}O_4$ in figure 5.42. Moreover, the substitution of a small amount of Co with Ni seems to improve the mobility of Li atoms in the structure. Since $LiMn_{1.98}Co_{0.01}Ni_{0.01}O_4$ shows higher Li mobility than $LiMn_{1.98}Co_{0.02}O_4$. Figure 5.43 also captures the movement of Li atoms through the rate of diffusion in the temperature range 100-800 K. The substitution of Ni also seems to influence the movement of Li atoms positively in the structure. Moreover, figure 5.44 captures the conduction of Li^+ in the doped spinel structures. The calculated ionic conductivity of Li^+ in the doped structures is comparable to the value of ~5.25×10^{-7} S cm^{-1} determined in experiments [240]. It can be noted from the graph of ionic conductivity vs. temperature that the introduction of Ni in the structure also improves the conductivity of Li^+ in the structure. This suggests that the strong NiO_6 octahedral framework provides a clear Li migration pathway due to the shortened bond distances.

The derived Buckingham interatomic potentials in chapter 3 were successfully utilized to study the microstructure and transport properties of the Co- and/or Ni-doped Li-Mn-O spinel structures. Furthermore, the A&R simulated spinel structures were found to be in good agreement with materials synthesized in experiments [232, 230, 231].

CHAPTER 6

Simulated Synthesis and Properties Analysis of $LiNi_2O_4$ Spinel Nanoporous Structure

In chapter 5, it has been shown that the introduction of Ni in $LiMn_2O_4$ can improve the mobility and conductivity of Li^+. This was attributed to the shortened M-O (Mn=Mn, Ni) average bonding distance, and it has sparked significant interest in $LiNi_2O_4$ spinel nanoporous materials. Particularly their transport properties as a function of pore diameter. Consequently, the work will further guide the nanostructuring of Ni-doped $LiMn_2O_4$ spinel cathode materials. Nanostructured electrode materials have ignited significant research interest as one of the solutions to improve the performance of Li-ion batteries [246, 247]. The strain incurred during the insertion and extraction of lithium ions can be mitigated in nanostructured materials, such as nanoporous [248, 249]. The Jahn-Teller distortion report in LiM_2O_4 (M=Co, Ni, and Mn) spinel structures can be suppressed in nanostructured materials such as nanoporous. The pore in nanoporous materials can withstand the structural disruption caused by Jahn-Teller active M ions. Moreover, nanoporous materials offer faster diffusion kinetics due to the high surface area over volume ratio [250, 251, 252]. This provides a significant electrolyte and electrode interface, which ensures high rate-capability, high charge and discharge capacity, and thus improves the life cycle of a lithium-ion battery. Microstructural properties such as diffusion and ionic conductivity depend on the pore size and particle size. Ionic conductivity and diffusion affect the rate performance of Li-ion batteries, which is crucial for large-scale applications such as electric vehicles.

In this chapter, we explore the relationship between the pore size of $LiNi_2O_4$ spinel nanostructures and the simulated A&R technique [71]. The work will provide insights on the doping of $LiMn_2O_4$ spinel with Ni, which is a promising positive electrode material for LIBs. Moreover, the chapter also serves as a test for the Buckingham interatomic potentials developed in chapter 3. The development of the Buckingham interatomic potentials in chapter 3 is motivated by the lack of interatomic potentials for the interactions that result from doping $LiMn_2O_4$ spinel with Ni and/or Co. Therefore, $LiNi_2O_4$ nanoporous spinel structures with pore diameters of 1.5 nm, 2.1 nm, and 3 nm will be generated. Atomic-level structure images, RDF graphs, and X-ray diffraction patterns were utilized to explore the generated $LiNi_2O_4$ spinel nanoporous structures.

Furthermore, the volume and the surface area of the $LiNi_2O_4$ nanoporous structures will be linked to the Li^+ transport properties.

6.1 Method

The $LiNi_2O_4$ nanoporous structures are generated using the DLPOLY code, which is based on classical mechanics [220]. A $LiNi_2O_4$ spinel structure optimized with the METADISE program is successfully optimized at a temperature of 1800 K [221]. Subsequently, the amorphous structure is then used to generate a nanoporous amorphous structure under the isothermal-isobaric ensemble. The isothermal-isobaric ensemble allows for variation of volume of the system, which yields a nanoporous morphology. Consequently, the structure that yielded the appropriate volume by measure of the nanoporous pore size is retrieved. Furthermore, the amorphous nanoporous $LiNi_2O_4$ spinel structure is recrystallized with the canonical ensemble. Moreover, the employed technique ensures that the generated $LiNi_2O_4$ nanoporous structures contain structural features that are comparable to those observed in experiments [71]. The Nose-Hoover thermostat was employed for all stages of generating the nanoporous structures.

6.2 Generation of $LiNi_2O_4$ nanoporous spinel structures.

6.2.1 Amorphous $LiNi_2O_4$ nanoporous spinel structures.

Figure 6.1 (a) shows a 28001-atom $LiNi_2O_4$ crystalline nanosphere, which is amorphized at a temperature of ~1800 K under the microcanonical ensemble. The amorphized $LiNi_2O_4$ nanospherical structure is shown in Figure 6.1 (b). Figures 6.1 (d), (c), and (e) illustrate the generated amorphous $LiNi_2O_4$ nanoporous structures with pore diameters of 0.21 nm, 0.30 nm, and 0.15 nm, respectively. The random arrangement of atoms in the structure can be observed from the atomic-level structure image captured from the Materials Studio visualization program. In addition, the organization of atoms in the structure was also investigated through RDF graphs illustrated in Figure 6.2. The RDF peaks of the spinel structure are broad, which indicates a lack of atomic ordering. In addition, after the first RDF peak located at ~1.88 Å, which denotes the first neighbour distance, the probability of finding atoms is greater than zero at any atomic separation. This suggests that the structure is amorphous and that atoms are rarely in an organized arrangement. Moreover, the

structure in figure 6.1 (b) is simulated under the NPT ensemble to generate nanomaterials that, when aggregated, will form different pore sizes or cavities. Figures 6.1 (c), (d), and (e) show the resulting structures collected at different simulation sizes. The structures in figures 6.1 (c), (d), and (e) were collected in simulation cells of sizes 75 x 75 x 75 $Å^3$, 69 x 69 x 69 $Å^3$, and 67 x 67 x 67 $Å^3$, respectively. Moreover, their pore or cavity diameter was found to be 0.30 nm, 0.21 nm, and 0.15 nm, respectively. The structures are then recrystallized under the canonical ensemble at a temperature of 1900 K, and the results are shown in section 6.3.3. The RDF graphs in figure 6.3 confirm their amorphous state after compression under the NPT ensemble. This is deduced from their broad RDF peaks after the RDF peak of the first neighbour interaction.

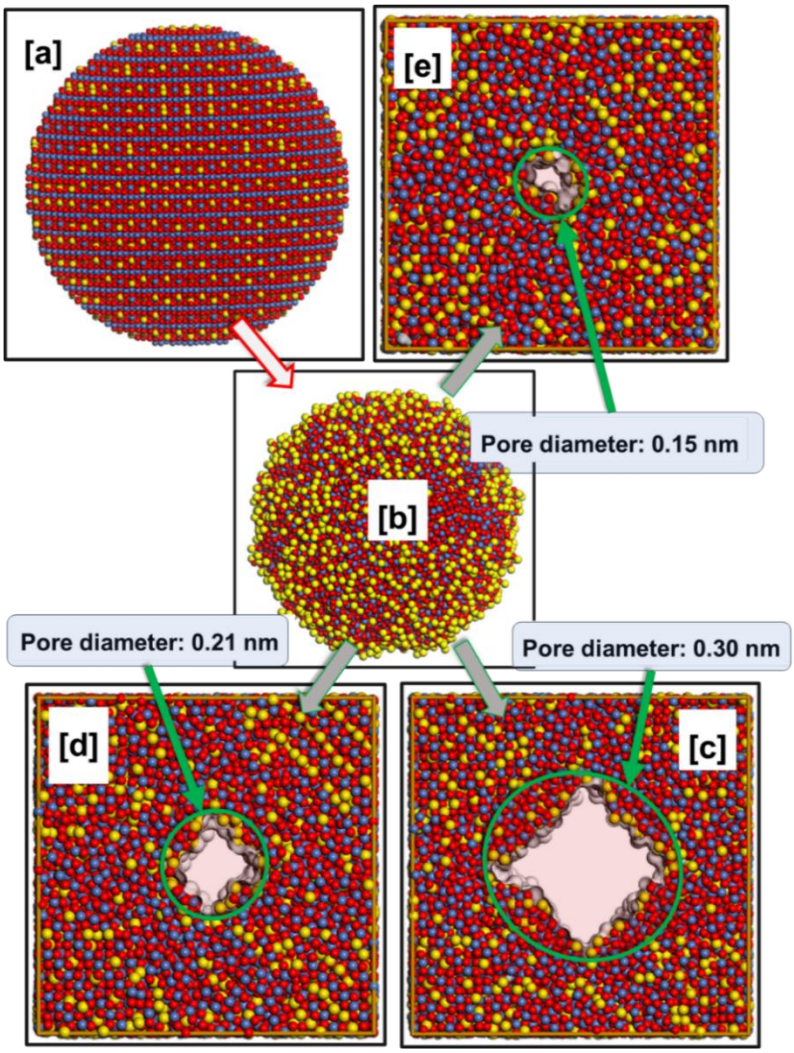

Figure 6.1: $LiNi_2O_4$ nanoporous structures with different pore sizes generated from an amorphous $LiNi_2O_4$ nanosphere under the NPT ensemble.

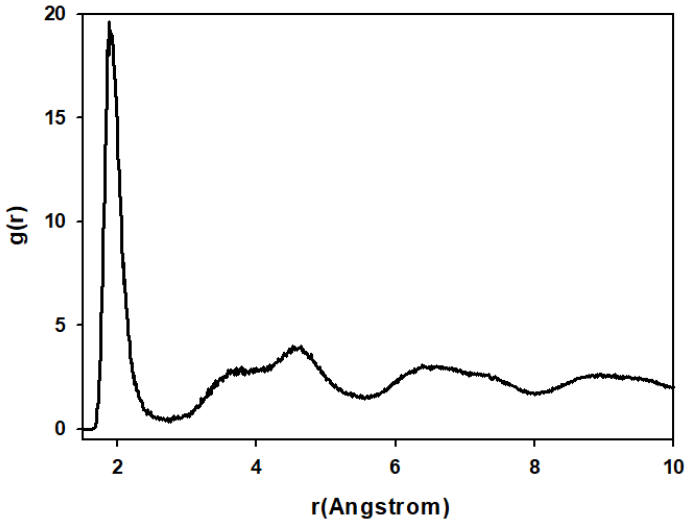

Figure 6.2: RDF graph of an amorphous $LiNi_2O_4$ spinel nanosphere used to generate nanoporous structures of different pore sizes.

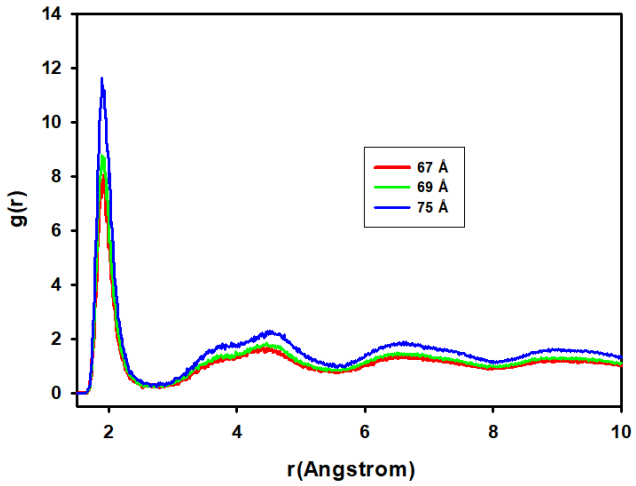

Figure 6.3: RDF graphs of $LiNi_2O_4$ amorphous nanoporous spinel structures of box size 67 Å (red), 69 Å (green), and 75 Å (blue).

6.2.2 Aggregated 2D $LiNi_2O_4$ nanoporous structures.

Figures 6.4, 6.5, and 6.5 illustrate the aggregation of $LiNi_2O_4$ primary particles to form secondary particles with nanoporous morphology. The formed nanoporous structures show different pore sizes, which are a function of the simulation cell. A bigger simulation cell was found to yield a bigger cavity (pore) compared to a smaller simulation cell. The particles in figure 6.4 form a smaller cavity when compared to the particles in figure 6.5. Therefore, the electrode material in figure 6.5 has greater surface contact with the electrolyte than the electrode material in figure 6.4.

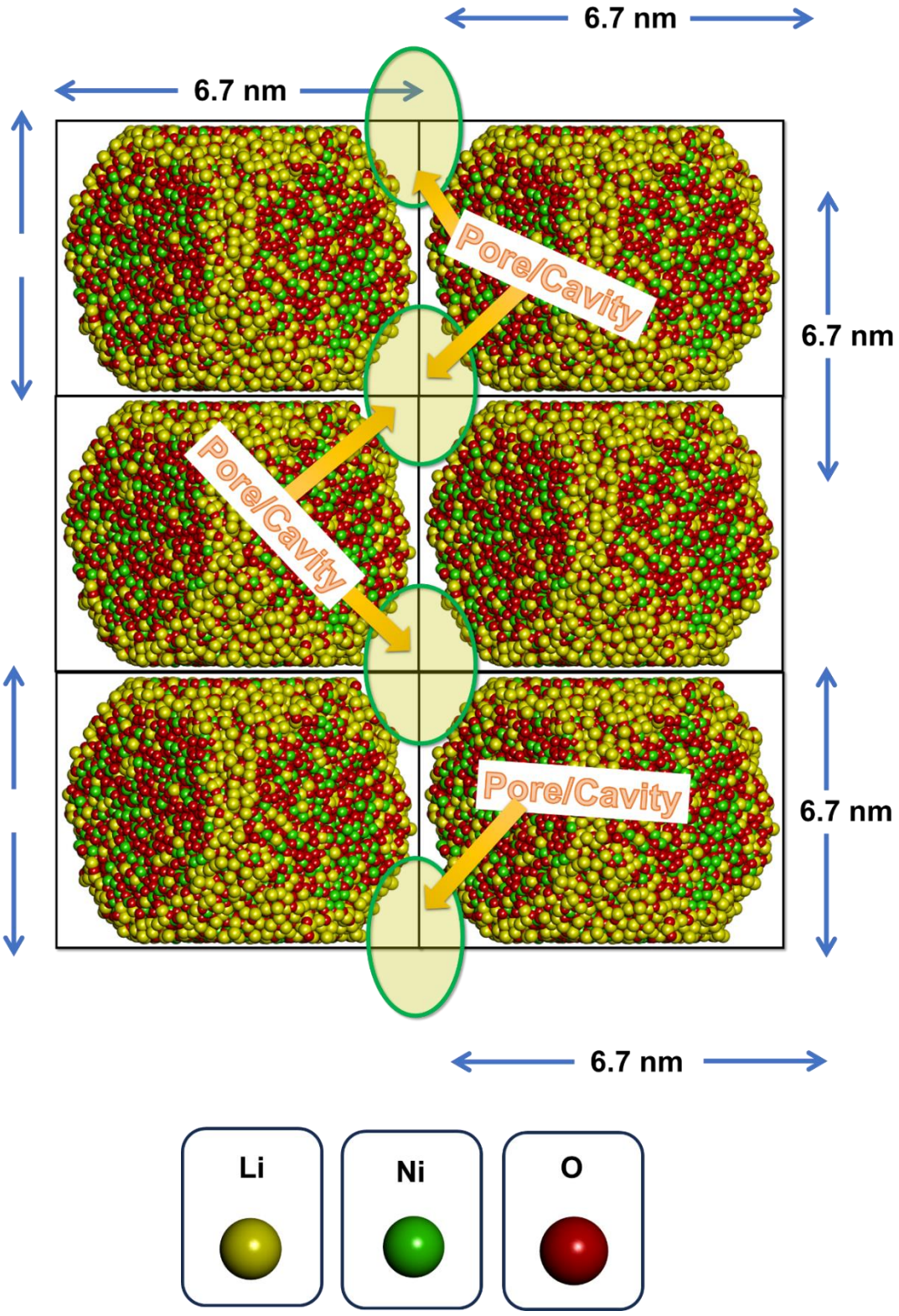

Figure 6.4: A 2D aggregation of $LiNi_2O_4$ simulated particles in a simulation cell of 67 x 67 x 67 A^3, forming a nanoporous morphology.

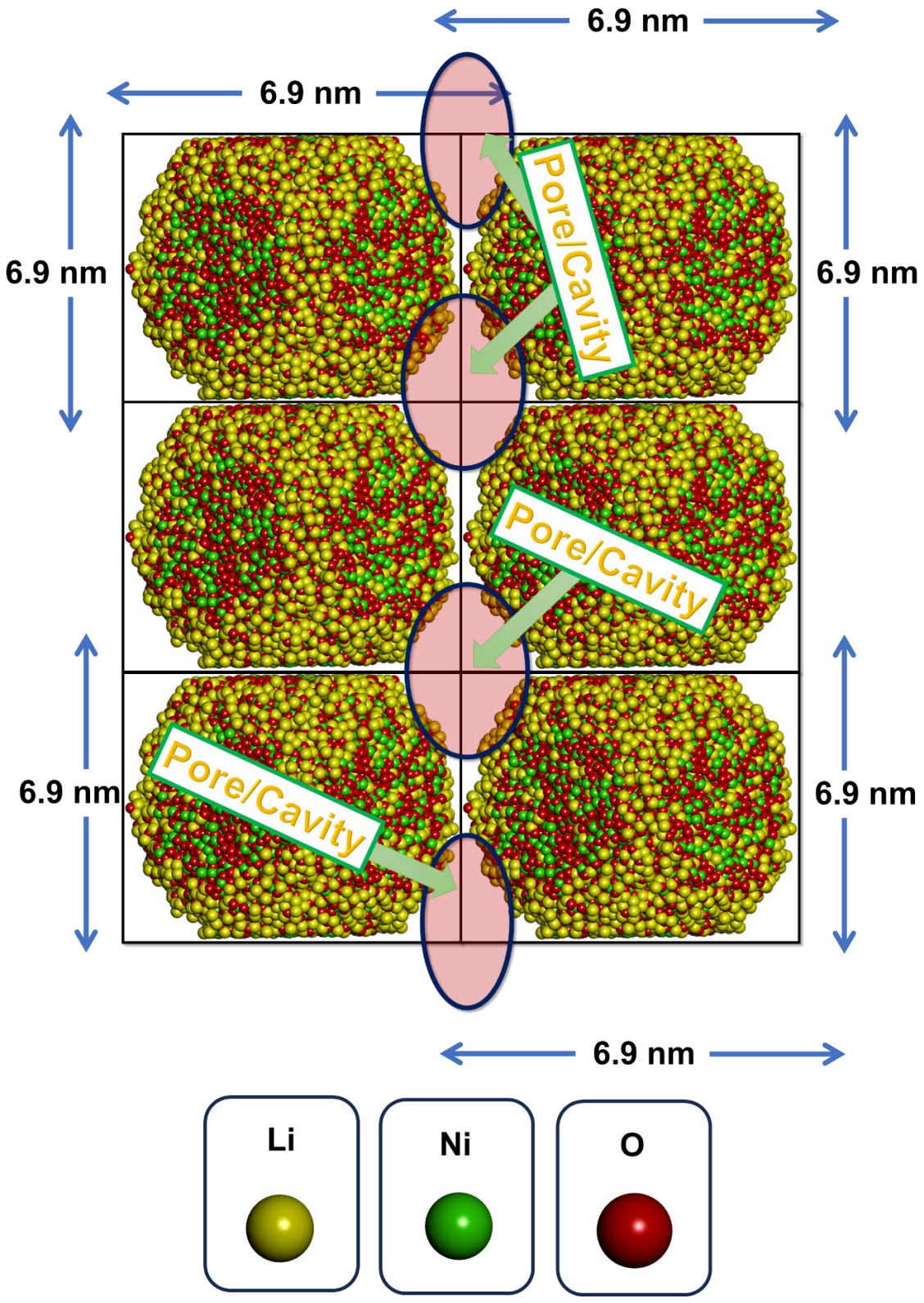

Figure 6.5: A 2D aggregation of $LiNi_2O_4$ simulated particles in a simulation cell of 69 x 69 x 69 A^3, forming a nanoporous morphology.

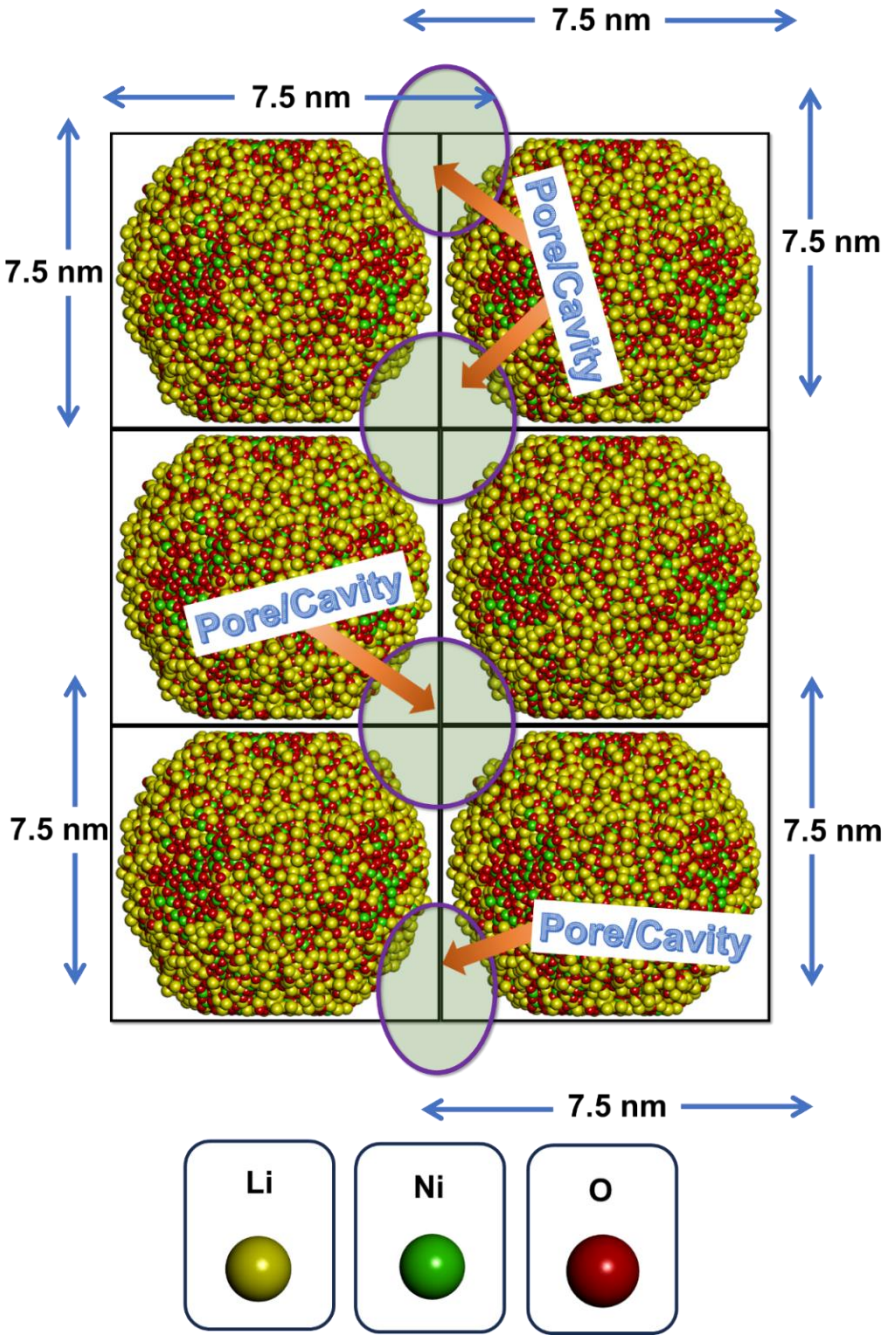

Figure 6.6: A 2D aggregation of $LiNi_2O_4$ simulated particles in a simulation cell of 75 x 75 x 75 A^3, forming a nanoporous morphology.

6.2.3 Recrystallization of $LiNi_2O_4$ nanoporous spinel structures.

The $LiNi_2O_4$ amorphous nanoporous structures were further recrystallized at a temperature of 1800 K under the canonical ensemble. The recrystallized structures were cooled to a temperature of 5 K and are illustrated in figure 6.7. The $LiNi_2O_4$ particles are viewed in a way that shows the pore that was going to form if the particle

was used to form a nanoporous structure. The surface of the particles is turned into the center of the structure, while the center of the structure is turned into its surface. This yields nanoporous material with a pore size that is equivalent to what is obtained if the particle is arranged in a 2D array with other similar particles, as shown in figures 6.4, 6.5, and 6.6.

Figure 6.7 (a) shows the recrystallized structure with a pore diameter of 0.15 nm, formed in a simulation cell of 67 x 67 x 67 A^3. Atoms arranged in a line pattern are noted in the figure, which shows that the structure recrystallized successfully. layers of oxygen atoms are observed in between the layers of lithium and oxygen atoms. The patterns are also observed in the theoretical spinel and the A&R simulated spinel structures in chapter 4 and 5. The same patterns are also noted in the recrystallized $LiNi_2O_4$ particles generated in the simulation cells of 69 x 69 x 69 A^3 and 75 x 75 x 75 A^3 dimensions in figure 6.7 (b) and (c), respectively. Moreover, the structures have pore sizes of 0.21 and 0.30 nm, respectively. The pore size of the structures remained the same after recrystallization.

Figure 6.8 (a) shows the XRD pattern of $LiNi_2O_4$ structure with a pore diameter of 0.15 nm, which compares well to an XRD pattern of $LiNi_2O_4$ spinel calculated by Thomas et al. [116]. The A&R-simulated nanoporous structure can be indexed to a cubic spinel with a space group of Fd-3m. The XRD peaks of the simulated 0.15 nm pore diameter structure are sharp and intense, which suggests that there is a high-ordered atomic arrangement in the structure. Moreover, all the major spinel peaks {(111), (311), (222), (400), (331), (511), (440), and (531)} are observed in the XRD pattern and are comparable to the reference XRD pattern in figure 6.8 (b) [116]. A small, broad peak is observed around 2θ=~30°, which is a characteristic of the Ni_3O_4 spinel phase. Furthermore, the splitting of the (311) and (511) XRD peaks is also observed, which again shows the presence of the Ni_3O_4 impurity phase. However, the XRD peaks that denote the Ni_3O_4 phase are less intense and broad, which suggests that the quantity of this phase is less in the nanomaterial. Moreover, the Ni_3O_4 phase is confirmed by the XRD patterns of Mn_3O_4 illustrated in figure 6.8 (c) [230]. The XRD patterns of Mn_3O_4 and Li_2MnO_3 are used due to the lack of clear reference XRD patterns from literature. Since the XRD patterns of Ni_3O_4 and Mn_3O_4, as well as those of Li_2NiO_3 and Li_2MnO_3, are similar. Therefore, their XRD patterns are the same. The splitting of the (111), (222), (331), and (531) signifies the presence of the Li_2NiO_3 phase, as confirmed

by the XRD pattern of Li_2MnO_3 in figure 6.8 (d) [231]. However, the peaks are also small and broad, which suggests that Li_2NiO_3 is present in small quantities. The XRD patterns of the $LiNi_2O_4$ nanoporous spinel structures with pore sizes of 0.21 and 0.30 nm shown in figures 6.9 and 6.10, respectively, can be indexed to a cubic spinel structure. The XRD patterns are comparable to the reference XRD patterns of $LiNi_2O_4$ in figures 6.9 (b) and 6.10 (b), respectively. However, the XRD pattern of the 0.15 nm nanoporous structures shows less intense and broad XRD peaks that characterize the Li_2MnO_4 and Ni_3O_4 impurity phases. Conversely, the XRD pattern of the 0.3 nm structure shows the splitting of the (111), (222), (331), and 531 peaks, showing that the structure contains the Ni_3O_4 and Li_2MnO_3 impurity phases.

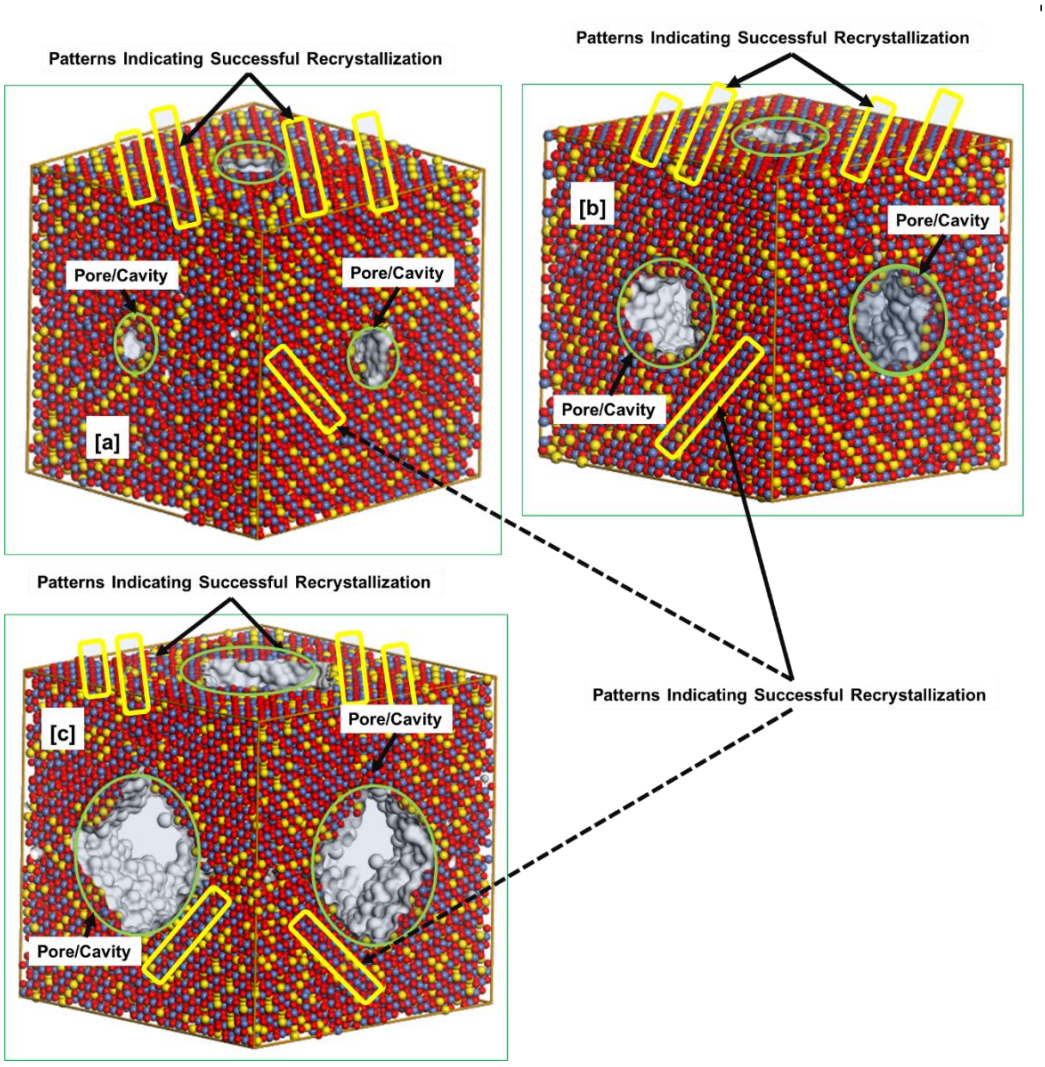

Figure 6.7: The recrystallized and cooled $LiNi_2O_4$ nanoporous structures with a pore diameter of (a) 0.15, (b) 0.21, and (c) 0.30 nm.

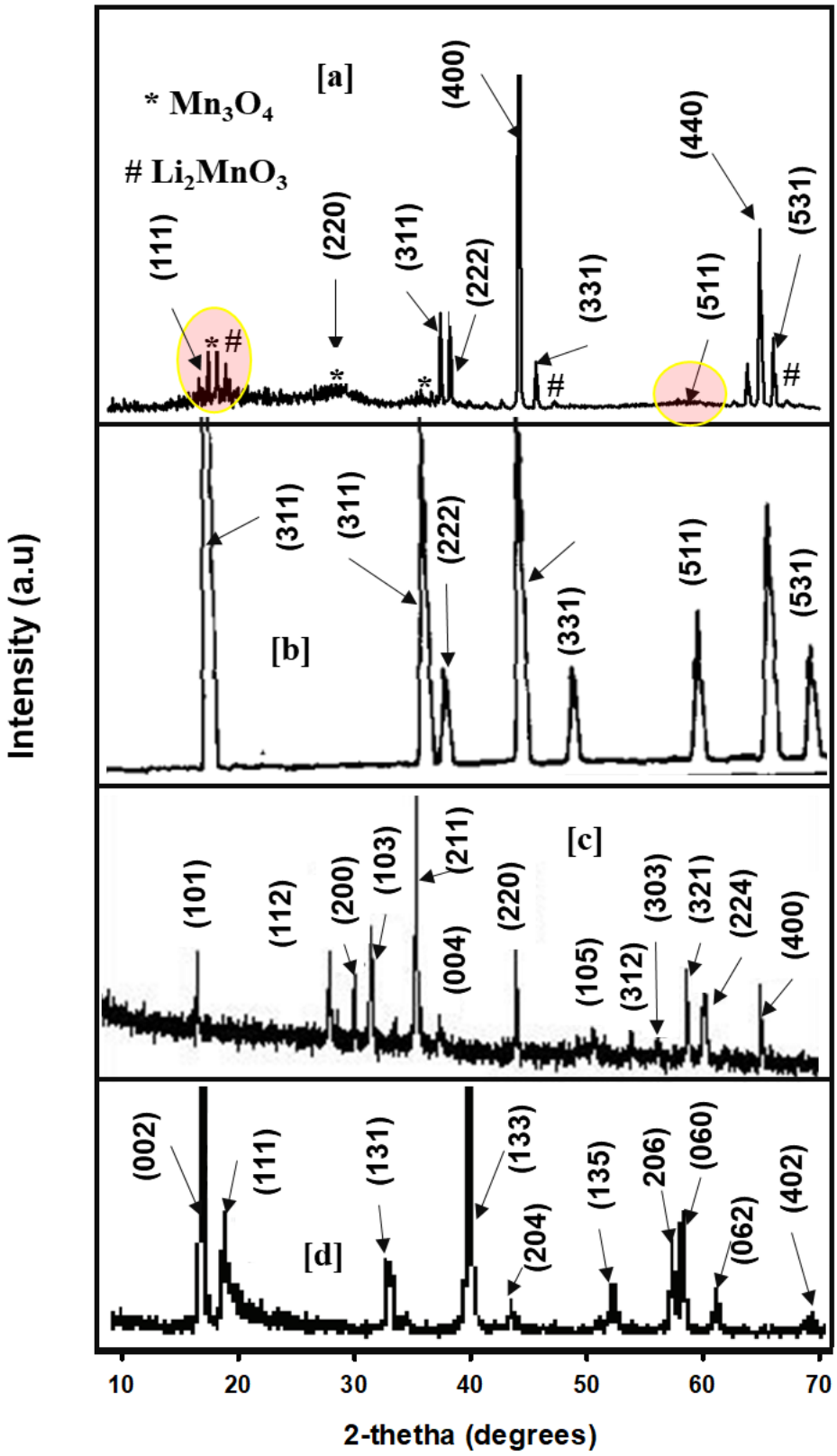

Figure 6.8: (a) XRD pattern of the $LiNi_2O_4$ porous structure with a pore diameter of 0.15 nm compared to the XRD patterns of (b) $LiNi_2O_4$ [116], (c) Mn_3O_4 [230], and (d) Li_2MnO_3 [231].

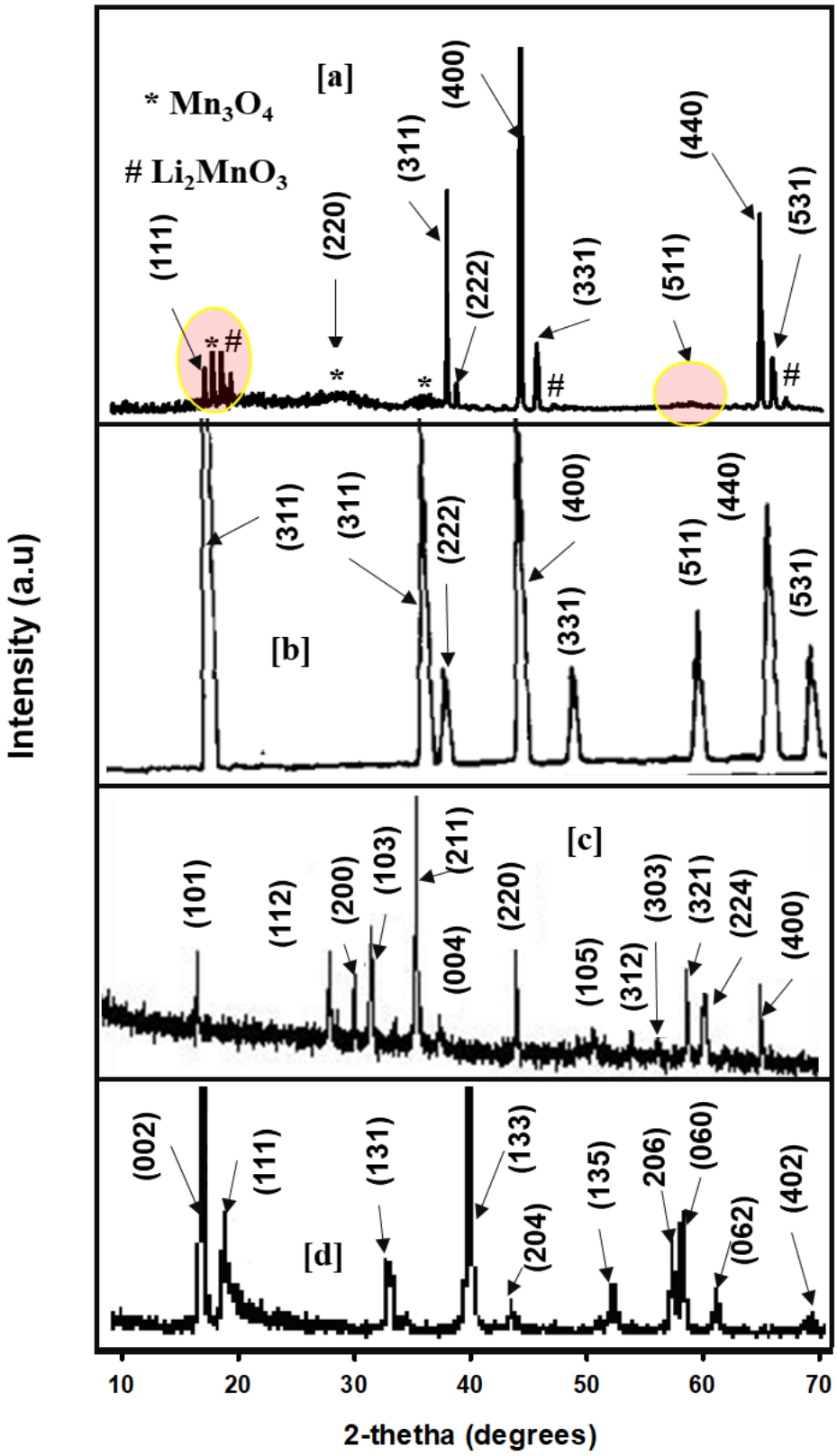

Figure 6.9: (a) XRD pattern of the $LiNi_2O_4$ porous structure with a pore diameter of 0.21 nm compared to the XRD patterns of (b) $LiNi_2O_4$ [116], (c) Mn_3O_4 [230], and (d) Li_2MnO_3 [231].

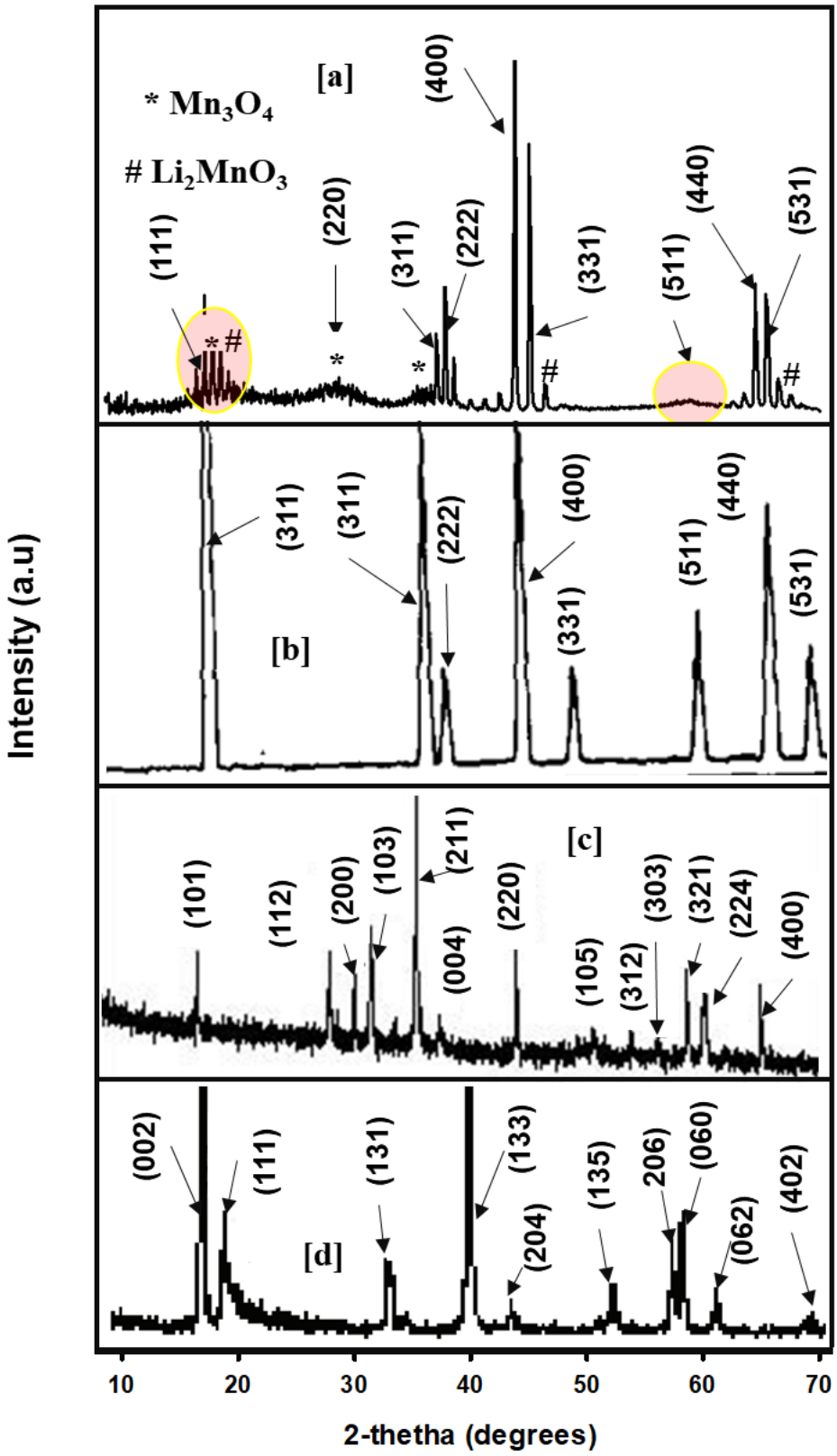

Figure 6.10: (a) XRD pattern of the $LiNi_2O_4$ porous structure with a pore diameter of 0.30 nm compared to the XRD patterns of (b) $LiNi_2O_4$ [116], (c) Mn_3O_4 [230], and (d) Li_2MnO_3 [231].

6.3 Volume and surface area of $LiNi_2O_4$ nanoporous (0.15, 0.21, and 0.30 nm).

In this section, the volume of the $LiNi_2O_4$ porous structures is calculated and related to their respective pore sizes. Figure 6.11 demonstrates the calculated volume that is occupied by atoms in the nanoporous structures. The $LiNi_2O_4$ nanoporous material with a pore diameter of 0.15 nm has the lowest occupied volume, and the structure with a pore diameter of 0.3 nm has the largest volume that is occupied by atoms. Moreover, the structure with a larger unit cell dimension provides enough space for atoms to occupy. Furthermore, the occupied volume was combined with an unoccupied volume to give the total volume of the nanoporous materials, as illustrated in figure 6.12. Moreover, the structure generated from a larger simulation cell is found to also have a larger total cell volume. Figure 6.13 shows the surface area of the $LiNi_2O_4$ nanoporous structures (0.15, 0.21, and 0.3 nm). The surface areas of the nanoporous structures with a pore diameter of ~0.15 and 0.21 nm were found to be 12047.75 and 15504.17 $Å^2$, respectively. However, the surface area of the nanoporous structure with a pore diameter of 0.30 nm is 22158.57 $Å^2$. Therefore, the surface area increases as the pore or cavity size increases.

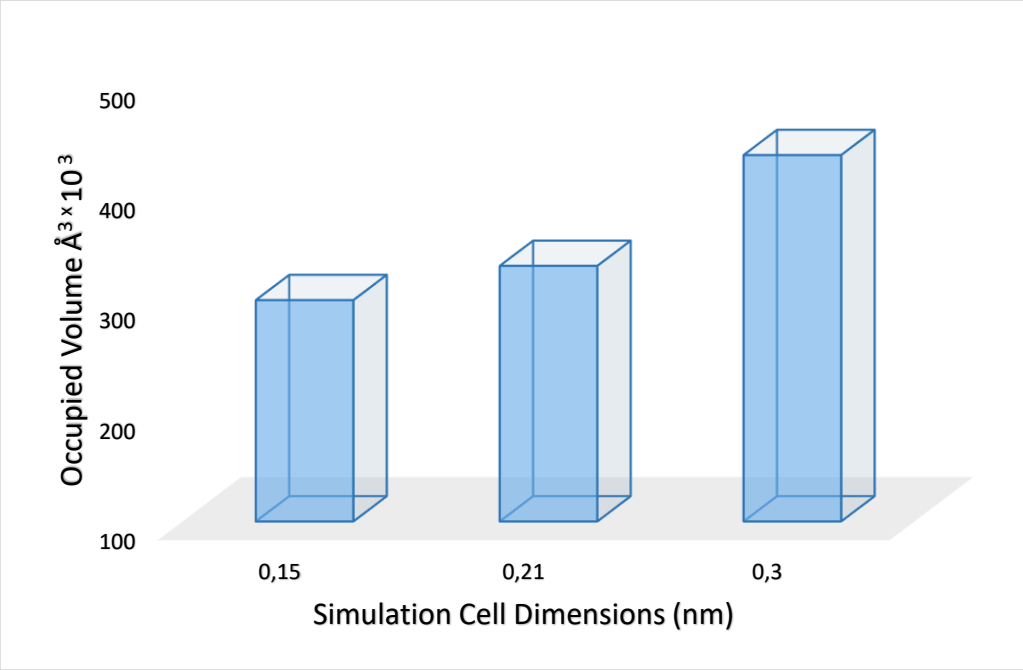

Figure 6.11: Investigation of volume as a function of box size of the three $LiNi_2O_4$ nanoporous spinel structures (0.15, 0.21, and 0.30 nm).

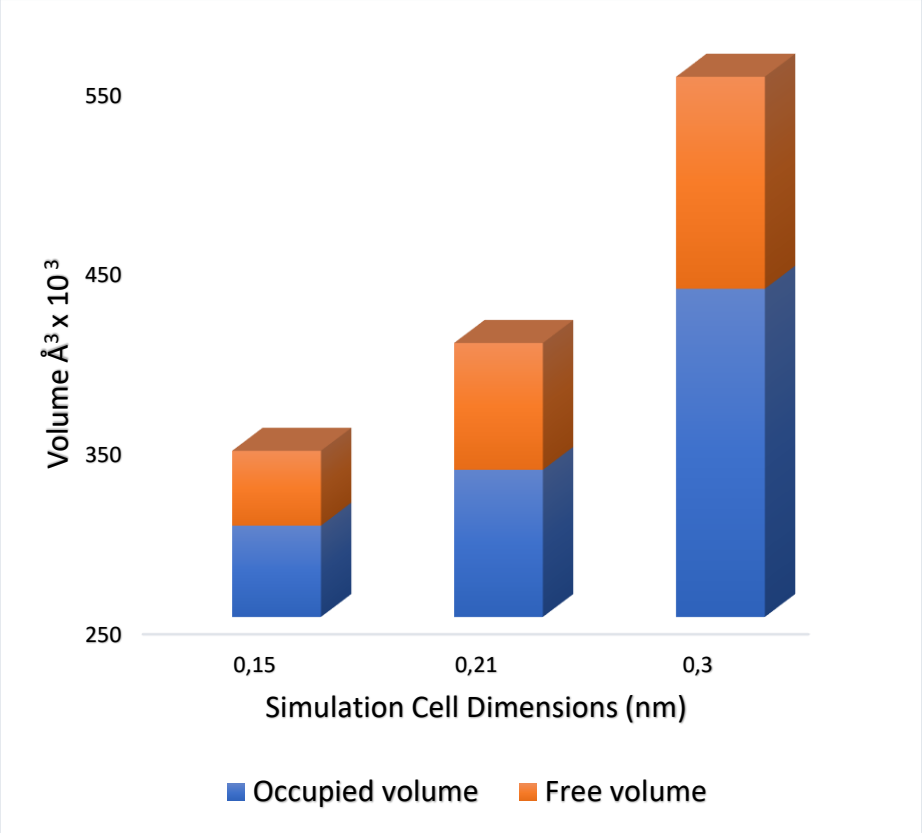

Figure 6.12: The sum of the occupied volume and free volume of the $LiNi_2O_4$ nanoporous spinel structures with pore diameters of 0.15, 0.21, and 0.30 nm.

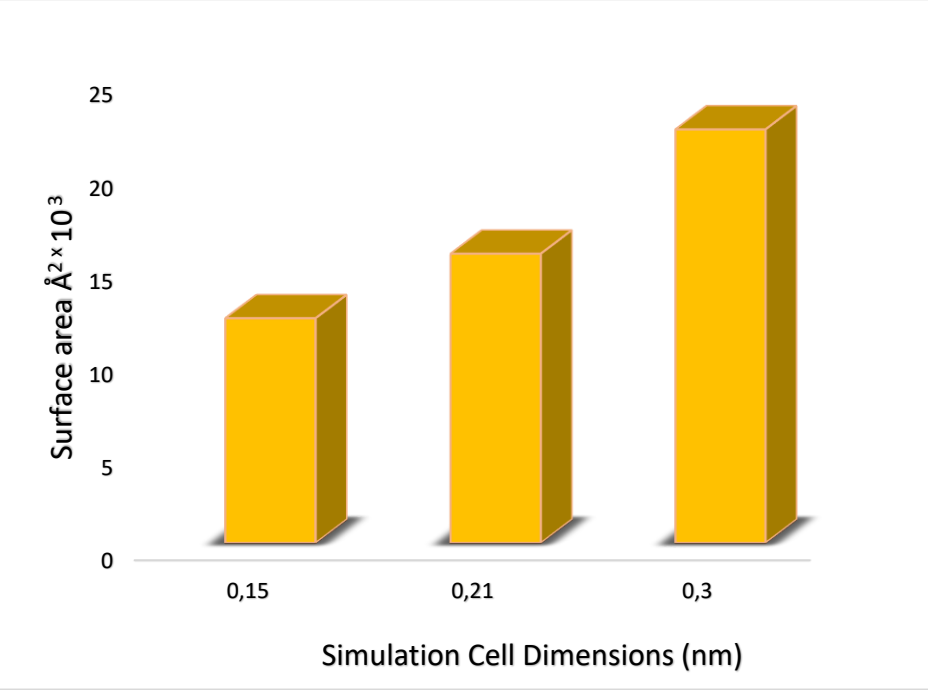

Figure 6.13: The surface area of the $LiNi_2O_4$ nanoporous structure with pore diameters of 0.15, 0.21, and 0.30 nm

6.4 Impact of pore size on the migration of lithium ions

Figure 6.14 illustrates the mobility of Li^+ ions in the $LiNi_2O_4$ nanoporous structures (0.15, 0.21, and 0.30 nm), monitored for 1400 ps at a temperature of 300 K. The MSD of the 0.15 nm (pore diameter = 0.15) $LiNi_2O_4$ structure is almost plateauing when compared to the MSD of the 0.21 nm (pore diameter = 0.21 nm) $LiNi_2O_4$ structure. The MSD of the 0.21 nm shows fluctuating increases as time increases. However, the MSD of the plot of the 0.30 nm structure is parallel to the y-axis for the maximum accumulated distance of 1.2 Å. Figure 6.15 captures the mobility of the nanoporous material with a pore diameter of 0.30 nm measured with the MSD approach for distances between 0 and 30. The movement of Li^+ between 0 and 1400 ps in the 0.15 and 0.21 nm structures does not exceed ~0.7 and ~1.3 Å, respectively. However, in the 0.30 nm structure, Li^+ ions cover an accumulated maximum distance of ~29 Å within 1400 ps. In addition, its MSD plot shows almost linear behaviour, and it has not fully converged for the simulation time (1400 ps). Figure 6.16 demonstrates the change in the motion of Li^+ ions in the structures with increasing temperature. In all the structures (0.15, 0.21, and 0.30 nm), the motion of Li^+ ions increases when the temperature increases, but the increase is far greater in the 0.30 nm structure as compared to the other structures.

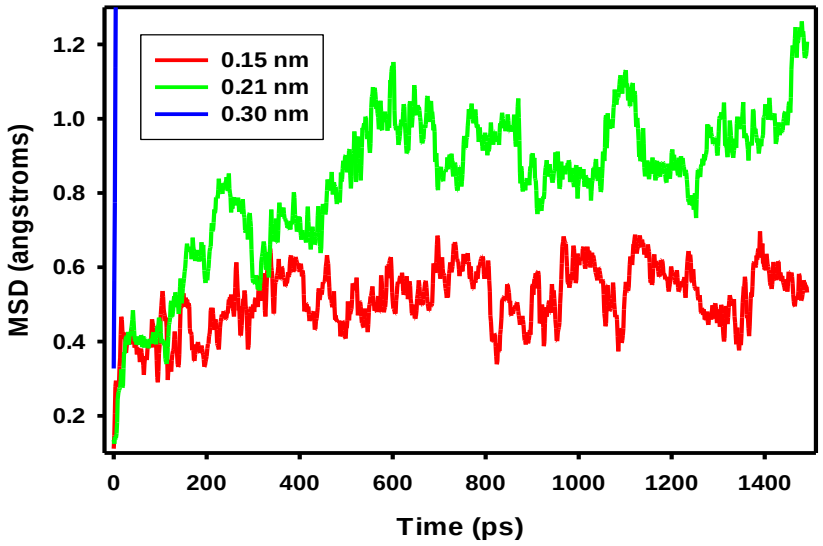

Figure 6.14: Mean Squared Displacement of Li in $LiNi_2O_4$ particles with a pore diameter of (a) 0.15 nm, (b) 0.21 nm, and (c) 0.30 nm at a temperature of 300 K for distances between 0-1.2 Å.

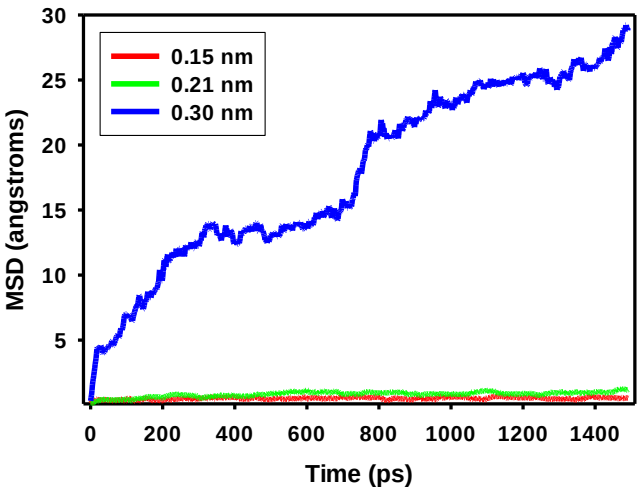

Figure 6.15: Mean Squared Displacement of Li in $LiNi_2O_4$ particles with a pore diameter of (a) 0.15 nm, (b) 0.21 nm, and (c) 0.30 nm at a temperature of 300 K for distances between 0 and 30 Å.

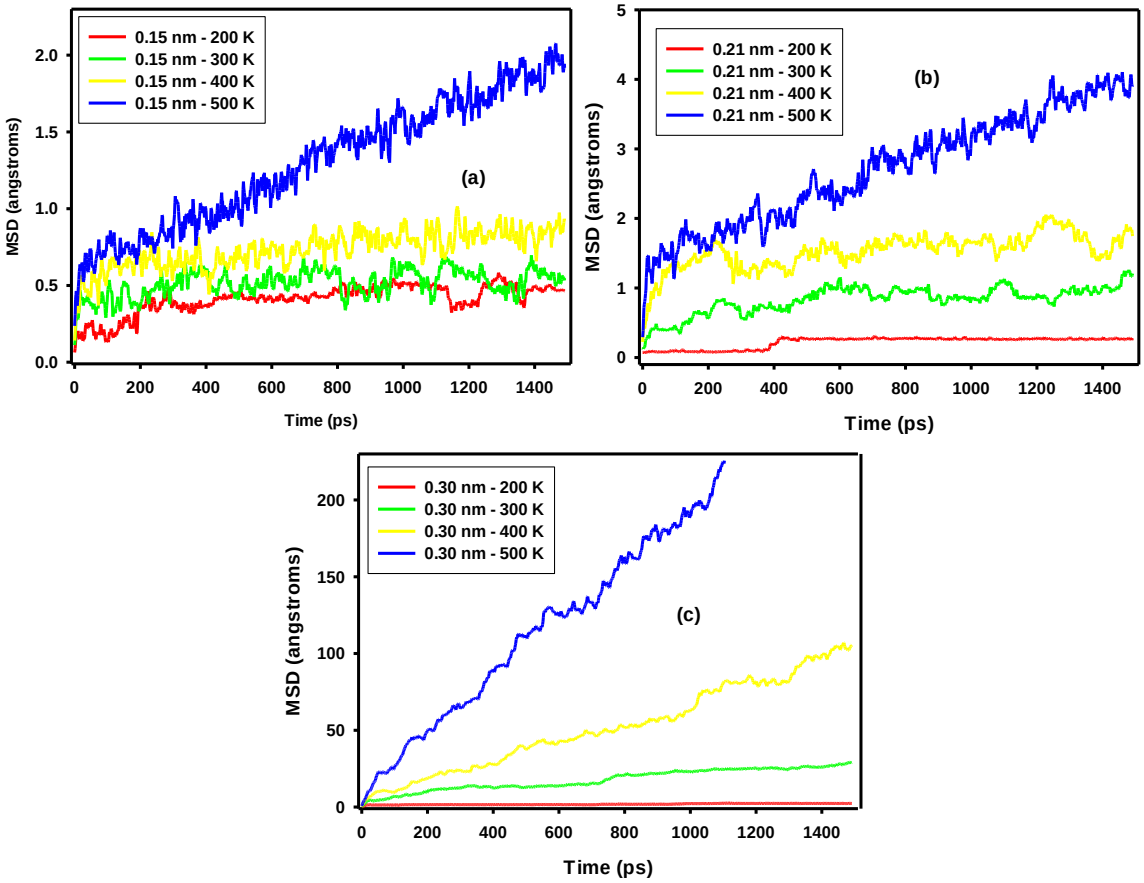

Figure 6.16: Mean Squared Displacement of Li in $LiNi_2O_4$ particles with a pore diameter of (a) 0.15 nm, (b) 0.21 nm, and (c) 0.30 nm.

The motion of Li^+ ions in the nanoporous structures was further investigated through a plot of the diffusion coefficients against temperature. In figure 6.17 (a), it can be noted that the 0.21 nm structure has the highest rate of diffusion as compared to the 0.15 nm structure. At 300 K, we observed a jump in the value of the diffusion coefficient for the 0.21 nm structure. This is because of the smaller simulation period during which the rate of diffusion was calculated. The diffusion coefficient of 0.15 nm nanoporous structure is 0.0067 x 10^{-9} m^2/s, and that of the 0.21 nm nanoporous structure is 0.0070 x 10^{-9} m^2/s at a temperature of 500 K. At a temperature of 500 K, the diffusion coefficient of the 0.30 nm nanoporous structure is 1.4 x 10^{-8} m^2/s, as shown in figure 6.17 (b). The same trend is observed at temperatures between 100 and 800 K. The diffusion of the 0.30 nm structure is far greater than the diffusion of the 0.15 and 0.21 nm, as shown in figures 6.17 (a) and (b). The diffusion coefficients of the nanoporous structures (0.15, 0.21, and 0.31 nm) are also captured in figure 18 at temperatures between 100 and 800 K.

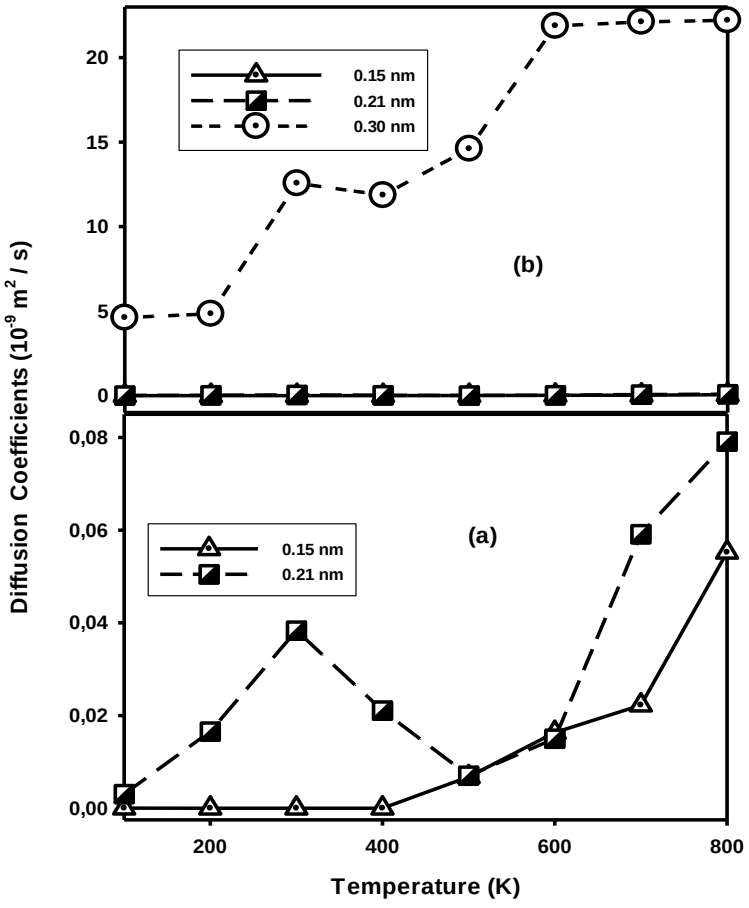

Figure 6.17: The rate of Li diffusion in $LiNi_2O_4$ particles with a pore diameter of (a) 0.15 nm, (b) 0.21 nm, and (c) 0.30 nm in one plot.

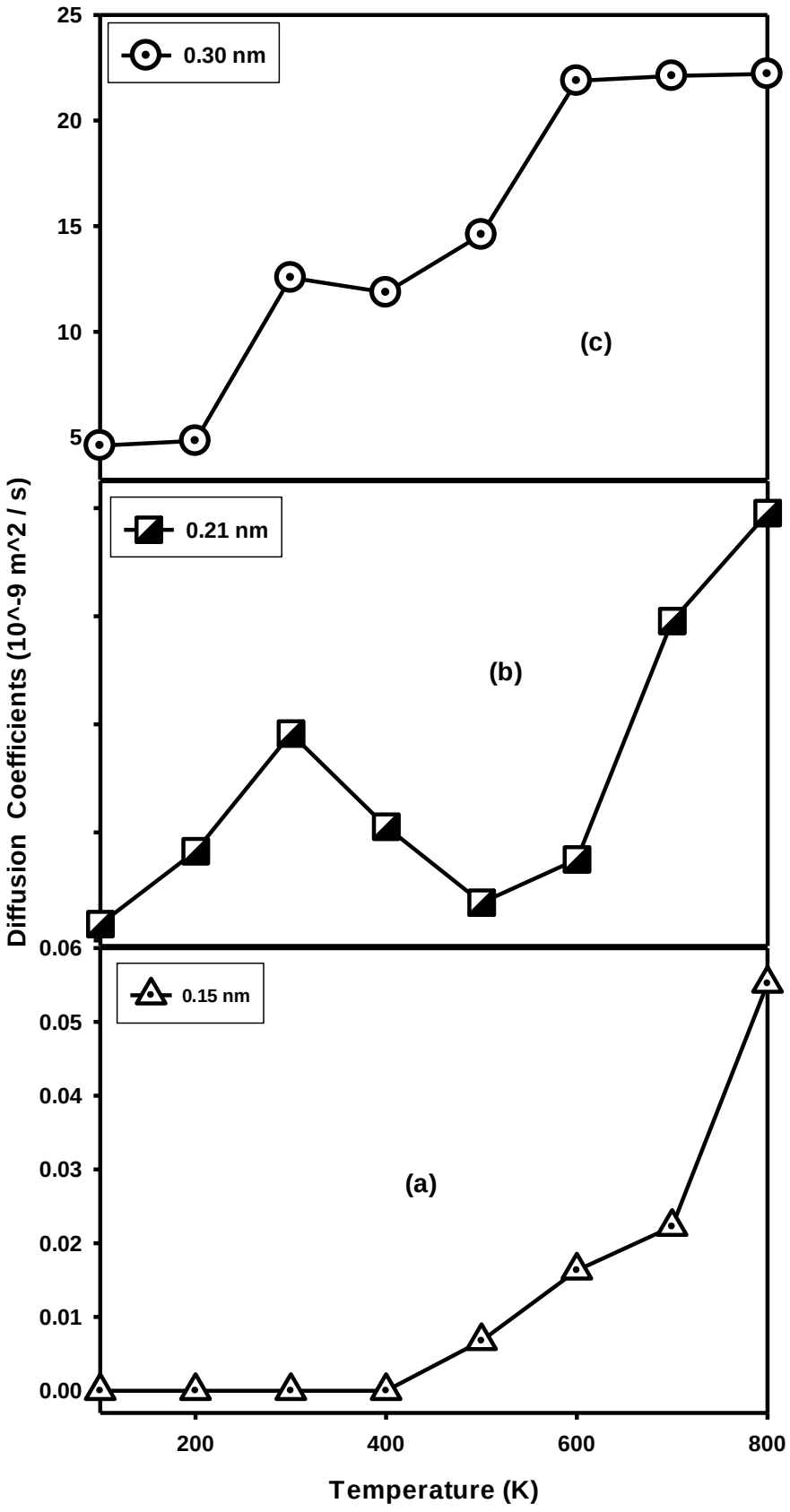

Figure 6.18: The rate of Li diffusion in $LiNi_2O_4$ particles with a pore diameter of (a) 0.15 nm, (b) 0.21 nm, and (c) 0.30 nm.

Figures 6.19 and 6.20 capture the conductivity of lithium ions in the nanoporous structures (0.15, 0.21, and 0.30 nm). At 300 K, the conductivity of Li^+ is 2.34 x 10^{-8}, 7.86 x 10^{-8}, and 1.5 x 10^{-7} S/cm for the 0.15, 0.21, and 0.30 nm, respectively. The nanoporous structure with a pore diameter of 0.3 nm shows superior Li^+ ionic conductivity at a temperature of 300 K, which is not comparable to Li^+ conductivity in the 0.15 and 0.21 nm structures with increasing temperature. The ionic conductivity of Li^+ in the nanoporous structures with pore diameters of 0.15 and 0.21 nm is comparable from a temperature of 200 K to 400 K, but the 0.21 nm exhibits higher Li^+ ionic conductivity. The Li^+ ionic conductivity increases with the increase in temperature in all the nanoporous structures (0.15, 0.21, and 0.30 nm), as illustrated in figure 6.20.

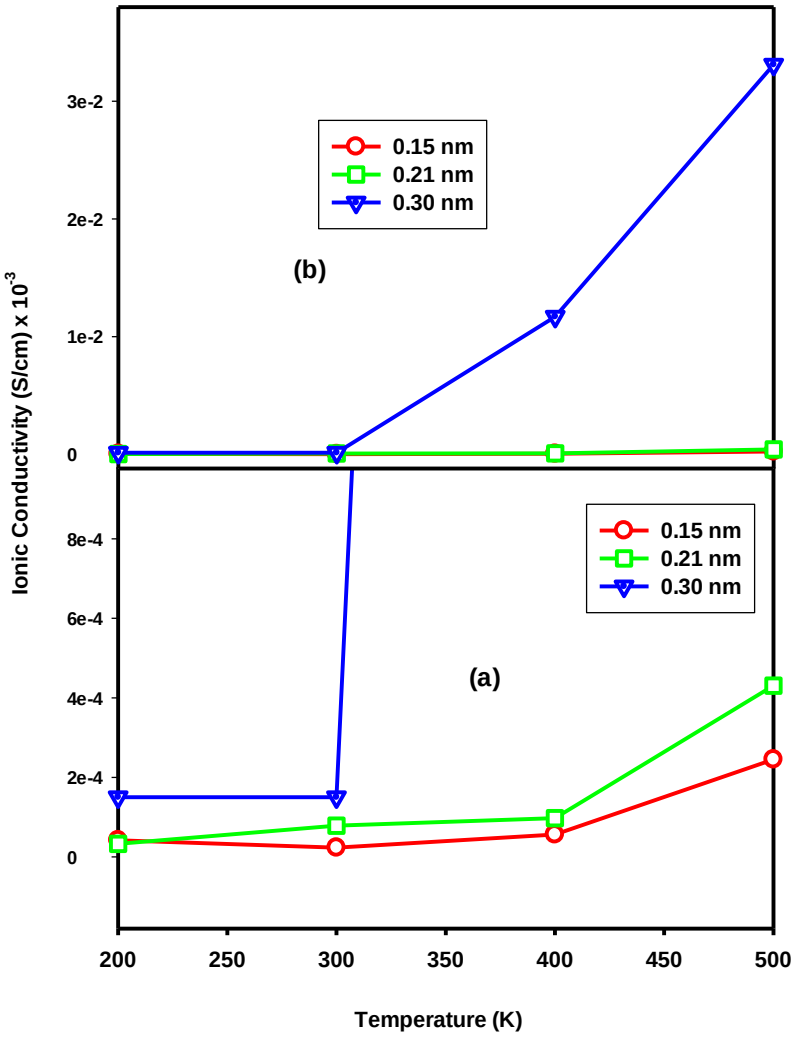

Figure 6.19: Comparison of the Li^+ ionic conductivity in $LiNi_2O_4$ nanoporous structures with a pore diameter of (a) 0.15 nm, (b) 0.21 nm, and (c) 0.30 nm.

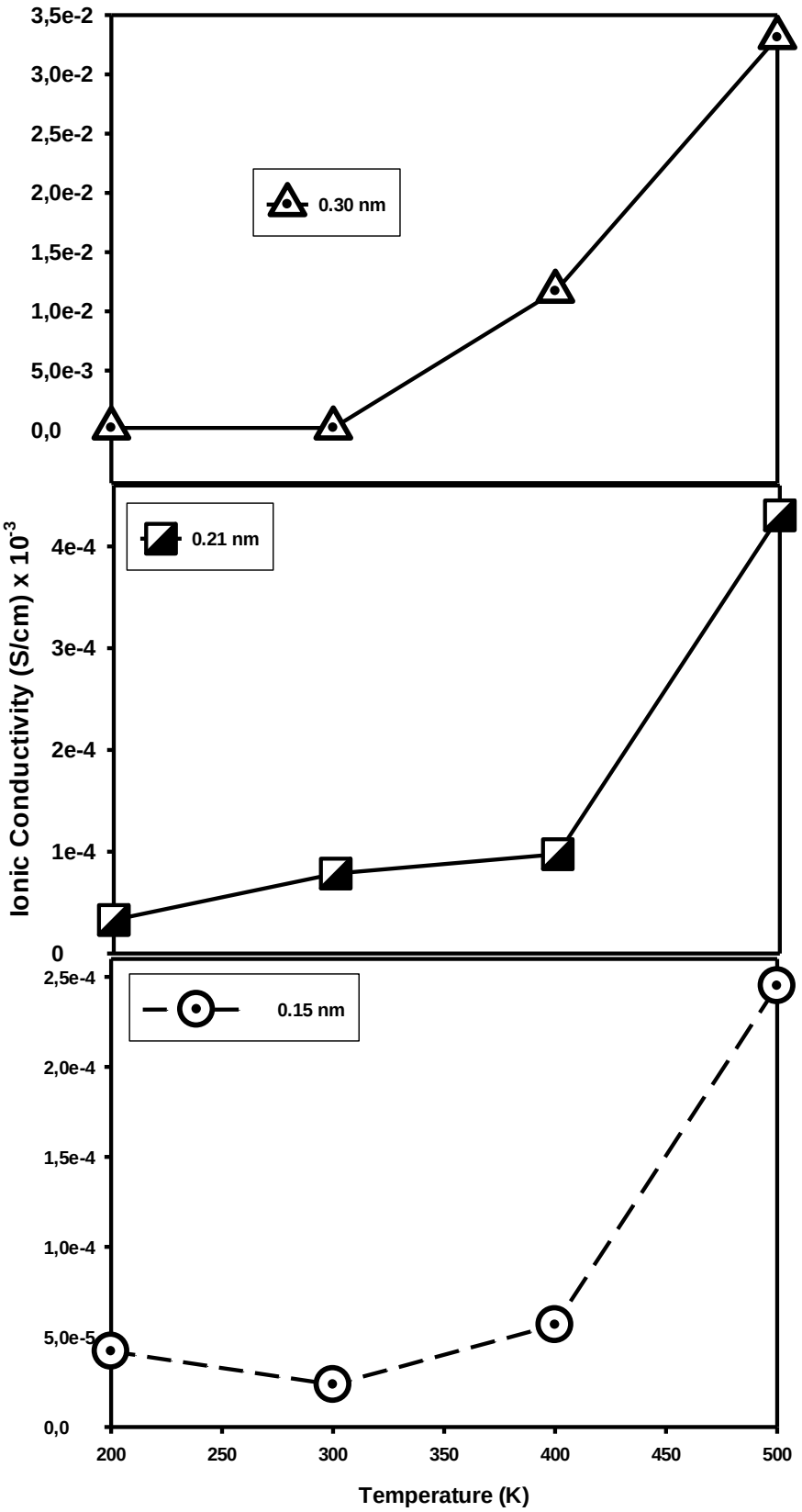

Figure 6.20: Demonstration of the Li^+ ionic conductivity in $LiNi_2O_4$ particles with a pore diameter of (a) 0.15 nm, (b) 0.21 nm, and (c) 0.30 nm.

6.5 Discussion

The development of nanostructured cathode materials for enhancing the performance of Li-ion batteries for large-scale applications such as electric vehicles and the storage of the intermittent energy garnered from renewable energy sources has incited great interest in the science community [253, 254]. The high-rate capabilities of battery materials can be improved by the development of nanostructured materials. Moreover, the disruptive strains induced by the insertion and/or extraction of lithium ions can be mitigated in nanostructured materials with nanoporous morphology. Furthermore, nanoporous materials demonstrate superior performance (high capacity retention and fast charge and discharge rates) as compared to their bulk counterparts. Nanostructured cathode materials with nanoporous morphology offer a larger contact area between the electrolyte and the cathode material than bulk cathode materials [255, 249, 256]. High-rate capabilities are crucial for large-scale applications.

The investigation of the transport of Li^+ in Co- and Ni-doped $LiMn_2O_4$ spinel in chapter 5 revealed that the mobility and conductivity of Li^+ can be enhanced with the introduction of Ni in the material. It has ignited research interest in $LiNi_2O_4$ spinel nanostructures for future lithium-ion batteries. Hence, in this chapter, the relationship between the pore size and the transport properties of Li^+ ions in $LiNi_2O_4$ nanoporous structures is explored. The investigation is motivated by the lack of information on the properties of nanoporous materials and how they relate to electrochemical performance. Moreover, the study also serves as a test for the Buckingham interatomic potentials of the Ni-Ni, Ni-Li, and Ni-O interactions derived in chapter 3. $LiNi_2O_4$ nanoporous structures with different pore sizes were generated successfully in different simulation cell sizes under the NPT ensemble. The variation of the cell volume facilitated the generation of $LiNi_2O_4$ spinel nanoporous structures with varying pore sizes.

The generated $LiNi_2O_4$ nanoporous structures with pore diameters of 0.15, 0.21, and 0.30 nm recrystallized successfully, as confirmed by atomic-structure images and XRD patterns from experiments [116, 230, 231]. Moreover, the formation of the Ni_3O_4 and Li_2MnO_3 high-temperature impurity phases was found to be irrelevant to increasing pore size. Since the concentration of the impurity phases was lower in the $LiNi_2O_4$ nanoporous structure with a pore diameter of 0.21 nm than in the structures with pore

diameters of 0.15 and 0.30 nm. As evinced by the less intense XRD peaks associated with the Ni_3O_4 and Li_2MnO_3 impurity phases illustrated in figures 6.8, 6.9, and 6.10. The volume occupied by atoms in the three nanoporous structures (0.15, 0.21, and 0.30 nm) was explored. The structure generated in a simulation cell of 75 x 75 x 75 $Å^3$ (0.30 nm) has the largest occupied volume (432.39 $Å^3$) as compared to the structures generated in simulation cells of 69 x 69 x 69 (331.81 $Å^3$) and 67 x 67 x 67 $Å^3$ (300.77 $Å^3$). The larger volume facilitates the formation of a larger cavity, and thus, increasing the box size also increases the pore size. In a smaller simulation cell, the atoms occupy most of the available space, which results in minimal space for the development of a larger pore.

Moreover, the structure with a pore diameter of 0.30 nm was also found to possess a larger surface area (22.16 $Å^2$) as compared to the structures with pore diameters of 0.21 (15.50 $Å^2$) and 0.15 nm (12.05 $Å^2$). The larger surface area will provide a wide interface between the electrolyte and the nanoporous material. Moreover, a large surface area also provides more redox-active sites, which will facilitate high-rate capabilities. Furthermore, the active redox sites (oxidation and reduction sites) ensure that all the energy that is stored in the cathode material is retrieved. As such, the power density of the battery is increased, which is a significant requirement for large-scale applications. In addition, a larger surface area mitigates the stress induced by the charge and discharge processes. Therefore, the structural integrity of the material can be retained during cycling by designing and developing nanoporous material with a larger cavity and surface area [257, 258]. Moreover, in experiments, a nanoporous material with mesopores of less than 200 nm retained 90% of its capacity over 100 cycles [259], which is in good agreement with the findings in this study.

The pore size of the $LiNi_2O_4$ nanoporous spinel structures was also related to the transport properties of Li^+ in the nanostructures. The analysis of the MSD plot of the nanoporous structures revealed that the mobility of Li^+ ions increases with increasing pore size. In 1400 ps, lithium ions covered accumulated distance of ~29.0 Å, ~1.2 Å, and ~0.6 Å in 0.30, 0.21, and 0.15 nm, respectively. As such, the pore size has a significant influence on the transport of Li^+ ions in the material. This is due to the larger surface area, which contains an increased number of oxidation and reduction locations. Furthermore, the calculated Li^+ ionic conductivity also shows a similar trend, which also suggests that by increasing the pore size of a nanoporous material, the

conductivity of Li^+ ions can be enhanced. At a temperature of 300 K, the Li^+ ionic conductivity for the 0.15, 0.21, and 0.30 nm structures was found to be ~2.34 x 10^{-8}, ~7.86 x 10^{-8}, and ~1.50 x 10^{-7} S/cm, respectively. However, there isn't much information in literature to compare for $LiNi_2O_4$ spinel structures. Lian C. and co-workers observed an increase in conductivity with increasing pore size, until a pore width of 0.6 nm (~2.5 x 10-4 S/cm) for porous carbon electrodes [260]. Moreover, smaller pore sizes were found to cause a significant reduction in ionic conductivity.

CHAPTER 7

Conclusion and Recommendations

7.1 Conclusion

The cathode material is currently a bottleneck to the performance of lithium-ion batteries (LIBs) due to its high cost and deteriorating cycle performance. LIBs are currently the leading secondary batteries, and as such, researchers are actively looking for replacements for the current commercial cathode material [261, 262]. To better the performance of LIBs to meet exponential technological advancements, to fully support electric vehicles, and to efficiently harness the intermittent energy from renewables. The $LiMn_2O_4$ spinel has been put forward as a promising replacement for $LiCoO_2$, which suffers from poor cycle performance and is expensive [263, 264, 57]. $LiMn_2O_4$ spinel offers high-rate capability due to its three-dimensional structure, which allows facile insertion and extraction of lithium ions in the structure. Furthermore, $LiMn_2O_4$ spinel is cost-effective due to the availability of manganese, particularly in South Africa. However, its performance also falls short after extended charge and discharge cycles. The performance deterioration is exacerbated at elevated temperatures and discharge voltages. The performance attenuation has been linked to the degradation of Mn^{3+} in the structure due to Jahn-Teller distortion and the disproportionation reaction of manganese [265, 266]. Several DFT studies have shown that cation-doping can improve the performance of $LiMn_2O_4$ by reducing the amount of Mn^{3+} and strengthening the structure [76, 77, 78]. However, there is insufficient information on the impact of cation doping on the microstructure and transport properties of $LiMn_2O_4$, which significantly affect electrochemical performance. Especially the doping of $LiMn_2O_4$ spinel with Co and Ni at the microscale due to the lack of accurate interatomic potentials.

Initially, a method inspired by a machine learning approach was employed to develop interatomic potentials for the interactions that arise from doping $LiMn_2O_4$ spinel Co and Ni (Ni-Ni, Ni-Li, Ni-O, Co-Co, Co-Li, Co-O, Co-Ni, Co-Mn, Ni-Mn, Ni-Ni, Ni-Li, and Ni-O). The Buckingham interatomic potentials were determined successfully from structure information calculated with DFT (lattice parameters, cell volume, elastic constants, and bulk modulus). The final derived interatomic potentials also embody

high-level interatomic interaction details extracted from DFT potential energy surfaces through a machine learning inspired approach. The determined potentials reproduced the fitted structure properties (lattice parameters, cell volume, elastic constants, and bulk modulus) to acceptable percentage differences of less than 7.1% for all the interactions. Furthermore, the derived Buckingham interatomic potentials for the Co-Co, Co-Li, Co-O, Ni-Ni, Ni-Li, and Ni-O interactions were used to describe atomic interactions in $LiCo_2O_4$ and $LiNi_2O_4$ with MD simulations. The potentials were able to reproduce the high-temperature behaviour of the spinel structures in line with the reported thermodynamic properties, such as the melting point. The melting points of $LiNi_2O_4$ and $LiCo_2O_4$ were found to be ~1800 K and ~1900 K, respectively. The same trend is also observed in the melting points of Ni and Co, which are ~1726.15 K [218] and 1831 K [217], respectively. Therefore, the potentials are fitting for the high-temperature technique, simulated amorphization and recrystallizations, and monitoring the performance of Co- and Ni-doped spinel systems [71].

The microstructure of $LiNi_2O_4$ and $LiCo_2O_4$ was also explored to provide the information that will guide the doping of $LiMn_2O_4$ with Co and Ni and to further test the derived potentials captured in chapter 3. The successfully simulated synthesis was confirmed by atomic-level structure images, RDF graphs, and XRD patterns. The average bond length of the Co-O (~1.920 Å) interaction was found to be less than the average bond length of Mn-O (~1.923) calculated by Kwon et al. [232]. Therefore, the structural stability of $LiMn_2O_4$ can be improved with the partial substitution of Mn with Co. Thackery and co-workers also suggested that the substitution could improve the structural stability of $LiMn_2O_4$ [242]. Moreover, XRD patterns and atomic structure images showed that the dominant phase in the simulated structure is $LiCo_2O_4$ spinel, which co-exists with a small concentration of the Co_3O_4 high-temperature impurity phase. The potentials were able to capture this high-temperature behaviour that occurs during the synthesis of spinel materials, which is also noted in experiments [224, 225].

The successfully simulated synthesis of $LiNi_2O_4$ was also inspected with atomic-level structure images and XRD patterns. The $LiNi_2O_4$ phase was found to be the dominant phase. Moreover, it compared well with a theoretical $LiNi_2O_4$ phase, showing Li in the 16c octahedral sites, Ni in the 16d octahedral sites, and O occupying the 32e sites. The XRD pattern of the A&R-simulated $LiNi_2O_4$ spinel showed the presence of its

major characteristic peaks {(111), (311), (222), (400), (331), (511), (440), and (531)} corroborated by the XRD pattern from experiments [116]. The Ni_3O_4 and Li_2NiO_3 impurity phases occurring during high-temperature synthesis are also observed in the XRD patterns. The Ni_3O_4 phase is evidenced by the splitting of the (111), (311) and (511) and the presence of the (200) reflection. The Li_2NiO_3 is revealed by the splitting of the (111), (222), (331), and (531) XRD peaks. The foreign XRD peaks in the XRD reflection of the cubic spinel structure are broad, which suggests that the concentration of these impurity phases is very low in the structure. The Ni_3O_4 phase results in the occupation of the tetrahedral sites, which interrupts the conductivity of Li^+ ions in the structure. Li_2NiO_3 is known to form a composite structure with superior specific capacity [233, 234]. Furthermore, the Ni-O average bond length was found to be less than the average bond length of Mn-O (~1.923 Å) calculated in experiments [232]. As such, the Ni-O (~1.91 Å) interaction is expected to be stronger than the Mn-O (~1.923 Å) interaction [232].

The synthesis of pristine $LiCo_2O_4$ and $LiNi_2O_4$ was followed by the synthesis of partially Co-doped $LiMn_2O_4$ spinel to probe how the substitution affects its microstructure. Moreover, the microstructural changes are compared to the electrochemical performance of the material. Atomic snapshots and XRD patterns revealed that the dominant phase is the cubic spinel phase. The dominance of the cubic phase of space group Fd-3m is evidenced by the sharp and intense XRD peaks confirmed by the XRD pattern of Tian et al. [239]. However, the XRD patterns also reveal that the doped spinel phase is co-existing with the Mn_3O_4 and Li_2MnO_3 high-temperature impurity phases. The Mn_3O_4 phase can only be linked with Mn atoms since Co atoms are only observed in the 16d octahedral sites.

The Mn in tetrahedral sites is known to be in the 2+ charge state, and it has been extensively reported to be soluble in organic electrolytes, resulting in a loss of capacity during cycling [267]. Moreover, the total number of MnO_4 tetrahedrons was found to be 535 and that of CoO_4 tetrahedrons to be zero. Therefore, Co does not disturb the transportation of Li^+ ions in the 8a tetrahedral sites. Analysis of the average number of Li atoms around Mn and Co shows that 0.24 atoms are found around Co and 2.77 are found around Mn atoms. Suggesting that Co^{4+} may be substituting Mn, which implies that the total valence of Mn in the structure is raised when the spinel structure is doped with Co at high temperatures. In addition, the Mn-O (~1.915 Å) interaction

was found to have a longer average bond length than the Co-O (~1.895 Å) interaction. Hence, the CoO_6 framework is expected to be stronger than the MnO_6 framework since bond strength increases with decreasing bond length.

Since the ionic radius of Ni is ~0.53 Å and the results of pristine $LiNi_2O_4$ showed that the Ni-O bond length is shorter than the Mn-O bond distance, $LiMn_2O_4$ was also doped with Ni. From the atomic-level structure images, the cubic spinel phase with a space group of Fd-3m was found to compare well to a theoretical spinel. Moreover, the XRD pattern of the A&R-simulated spinel structure can be indexed to a cubic symmetric structure with a space group of Fd-3m, which is in line with the XRD pattern from experiments. The dominant phase was also found to be the Fd-3m cubic spinel phase, as evidenced by the sharp and intense XRD peaks that characterize the phase {(111), (311), (222), (400), (331), (511), (440), and (531)}. Therefore, the spinel phase was synthesized successfully with the simulated synthesis technique. The Fd-3m cubic spinel phase is also found to exist along with the Mn_3O_4 and Li_2MnO_3 impurity phases, which were also observed in literature [268]. The Mn_3O_4 phase may deteriorate the specific capacity and cycling performance of $LiMn_2O_4$ spinel due to the Mn^{2+} ions occupying the 8a tetrahedral sites.

Furthermore, Mn^{2+} ions were also found to be soluble in organic electrolytes, which subsequently causes capacity fading [267]. While the Li_2MnO_3 phase can exhibit a synergistic effect with the dominant cubic spinel phase, resulting in an increase in specific capacity. Moreover, a total of 476 MnO_4 tetrahedrons were found, which implies that 476 Mn atoms are occupying the 8a tetrahedral sites in the structure. Consequently, the total number of NiO_4 tetrahedrons in the structure was found to be zero. Therefore, at low Ni concentrations (≤ 0.02), Ni atoms don't occupy the 8a tetrahedral sites, which are linked to the lowering of the Mn valence that influences the increase of the disruptive Mn^{3+} ions. Moreover, a deficiency of Li atoms around Ni atoms in the atomic separation distance between 0 and 3.5 was noted. However, 2.75 Li atoms are observed around Mn atoms on average. This could suggest that the most thermodynamically stable dopant at high temperatures could be the Ni^{4+} ion, which will result in a lowering of the Mn valence. The lowering of the average Mn valence will facilitate the disruption of the spinel lattice structure. Moreover, the Ni-O (~1.887 Å) bond distance is also found to be lower than the Mn-O (~1.917 Å) bond distance. Therefore, a stronger NiO_6 framework than the MnO_6 framework is expected. This will

increase the overall stability of the spinel phase and consequently enhance the cycle performance of the material.

Finally, $LiMn_2O_4$ was doped with both Ni and Co to monitor the impact of double-doping on the microstructure of this material. XRD patterns and atomic-level structure images confirmed the successful synthesis of this material with the simulated synthesis technique [71]. Theoretical atomic snapshots and XRD patterns from experiments confirmed the cubic Fd-3m spinel phase [239]. Therefore, the introduction of both Co and Ni in the $LiMn_2O_4$ spinel structure did not compromise its lattice structure. Additionally, the Mn_3O_4 and Li_2MnO_3 impurity phases are also observed in the double-doped spinel structure verified by XRD patterns from experiments [230, 231]. However, examinations of the average CoO_4, NiO_4, and MnO_4 tetrahedrons reveal that Co and Ni atoms are only occupying the 16d octahedral sites in the double-doped spinel structure. The Mn_3O_4 phase is linked to Mn atoms in the structure. Therefore, at low concentrations of Ni and Co, the doping of $LiMn_2O_4$ spinel does not contribute to the disruption of Li^+ transport, which leads to poor capacity retention. In addition, the average number of Li atoms around Ni, Co, and Mn in the atomic separation distance between 0 and 3.5 Å was found to be 0.00, 0.20, and 2.78, respectively. This aligned with observations in $LiMn_{1.98}Co_{0.02}O_4$ and $LiMn_{1.98}Ni_{0.02}O_4$ that, at high temperatures, the Co and Ni dopants may be more stable in their 4+ valence states. However, a small number of Co atoms are in the vicinity of Li^+ ions in the structure, deduced from the average value of 0.20 of Li atoms around Co atoms. Moreover, the bond distances of the Mn-O, Ni-O, and Co-O interactions were also inspected. The Ni-O interaction has the shortest bond length of ~1.885 Å, and for the Co-O interaction, the bond distance was found to be ~1.895 Å. The Mn-O interaction has the longest bond distance of ~1.905 Å. Therefore, the NiO_6 octahedra is expected to be more stable than the CoO_6 and MnO_6 octahedra, and the MnO_6 octahedra is expected to be the least stable.

The impact of the partial substitution of 1% Mn with Co and/or Ni on the transport of Li^+ ions was also explored, as it affects rate performance and capacity retention. Analysis of ionic conductivity, MSD, and the rate of diffusion in the doped structures suggested that Ni has a more positive influence on the migration of Li^+ in the structure as compared to Co. Li^+ covered distances of ~1.28 Å in $LiMn_{1.98}Ni_{0.02}O_4$, which is greater than the ~0.92 in $LiMn_{1.98}Co_{0.02}O_4$. Moreover, the diffusion coefficient of lithium

ions in $LiMn_{1.98}Ni_{0.02}O_4$ at 300 K was found to be 1.6 x 10^{-12} m^2/s, which is higher than 0.61 x 10^{-12} m^2/s observed in $LiMn_{1.98}Co_{0.02}O_4$. The same trend is also noted on the ionic conductivity, in $LiMn_{1.98}Ni_{0.02}O_4$ at 300 K, a value of 0.94 x 10^{-6} S cm^{-1} is observed, while a value of 0.23 x 10^{-6} S cm^{-1} was found in $LiMn_{1.98}Co_{0.02}O_4$. This can be attributed to the shorter Ni-O bond length, which provides leeway for the migration of Li^+. Moreover, ionic conduction in the $LiMn_2O_4$ spinel structure is linked to the Mn^{3+} polaron. If the Li deficiency around Ni atoms implies that there's an increase in the number of Mn^{3+} in the structure due to charge neutrality, as such, the superior conductivity could be linked to the concentration of Mn^{3+} in the structure. Since a small number of Li atoms are observed around Co atoms, as shown in figures 5.18 and 5.37, this implies that Co lowers the average valence of Mn a bit less than Ni.

The influence of pore size on transport properties and surface area of $LiNi_2O_4$ porous materials was also investigated. The exploration of the nanoporous structure is incited by the alluring transport properties of Ni observed in the Co- and Ni-doped Li-Mn-O spinel structures studied in this work. This will also provide guidance for improving the performance of $LiNi_2O_4$ and other spinel systems through nanostructuring. $LiNi_2O_4$ nanoporous structures were successfully generated with pore/cavities of diameters of 0.15, 0.21, and 0.30 nm. The sharp XRD peaks and line patterns of atoms in the structure images confirmed the successful recrystallization of the nanoparticles with porous morphology. XRD patterns also showed the presence of the Ni_3O_4 and Li_2MnO_3 impurity phases. However, they are not prevalent in the 0.21 nm nanoporous structure. Therefore, they are not linked with the increase in pore size but to the simulated synthesis conditions. The structure with a pore diameter of 0.30 nm showed a high surface area (22.16 $Å^2$) compared to the 0.21 (15.50 $Å^2$) and 0.15 nm (12.05 $Å^2$) nanoporous structures. This can be attributed to the higher pore diameter of the 0.3 nm structure as compared to the 0.15 and 0.21 nm structures. From the ionic conductivity analysis, it was found that the 0.30 nm structure exhibits superior ionic conductivity. The conductivity of Li^+ in the 0.15, 0.21, and 0.30 nm nanoporous structures was found to be ~2.34 x 10^{-8}, ~7.86 x 10^{-8}, and ~1.50 x 10^{-7} S/cm, respectively. This was also in good agreement with the MSD and diffusion coefficient results. The superior transport properties can be linked to the larger surface area and active redox sites in the material as compared to the 0.15 and 0.21 nm structures. However, the movement of Li^+ ions increases rapidly with increasing temperature in

the 0.30 nm structure. Therefore, the 0.30 nm may be less stable at high temperatures, causing side reactions with the electrolyte that can degrade the electrolyte or cause an explosion. As such, the pore size should be carefully controlled as it is directly proportional to the surface area of the 2D nanomaterial, and a large surface area may affect battery performance negatively.

The Buckingham interatomic potentials derived in this work have been utilized to explore the impact of partially doping Li-Mn-O spinel with Co and/or Ni on the microstructure and transport properties of this spinel. Our findings suggest that Li-Mn-O spinel can be successfully doped with Co and Ni. However, doping of Li-Mn-O spinel with Co and Ni at high temperatures could increase the concentration of the disruptive Mn^{3+} ion. It was also noted that the overall stability of the $LiMn_2O_4$ spinel structure can be improved with the introduction of Co and/or Ni in the structure. In addition, the substituted Co and Ni dopants don't disrupt the transport of Li^+ ions in the structure by occupying the 8a tetrahedral sites at a lower concentration (≤ 0.02) of the dopants. Additionally, the rate-performance of $LiMn_2O_4$ spinel can be improved by the introduction of Ni in the structure. Moreover, nanoporous $LiNi_2O_4$ with a larger pore diameter results in a higher surface area and high-rate capabilities. As such, nanoporous materials can be very crucial in the design of high-power and high-energy dense cathode materials for large-scale applications.

7.2 Recommendations

Future work involves:

i. An investigation of the discharge process of Co- and Ni-doped $LiMn_2O_4$ spinel with the variation of the dopant (Co and Ni) concentration will be monitored to see how it impacts the microstructure and Li^+ transport. The increase in the concentration of Co and Ni in the structure could cause them to occupy the 8a tetrahedral sites. Therefore, a suitable concentration of Co and Ni in the doped $LiMn_2O_4$ spinel structure will be investigated.
ii. The charge states of Co, Ni, and Mn in $LiMn_2O_4$ will be explored with nuclear magnetic resonance (NMR) spectroscopy to give a clear understanding of the average Mn valence, which affects the capacity retention of this material.
iii. Furthermore, future work also includes an investigation of the stability of the Co- and Ni-doped $LiMn_2O_4$.

iv. The $LiMn_2O_4$ spinel was found to co-exist in a high-power and high-energy density composite structure with layered structures. As such, a program that quantifies the concentration of the layered-spinel composite structure will also be developed in future. The concentrations will be related to the material's operating voltages during cycling performance.

v. Operating voltages of Co- and/or Ni-doped $LiMn_2O_4$ spinel and Li-Mn-O layered-spinel composite structures will also be explored, as they also affect the total energy density of a lithium-ion battery.

References

[1] Xu C. Q., Tian Y. W., Zhai Y. C. and Liu L. Y., "Influence of Y^{3+} doping on structure and electrochemical property of the $LiMn_2O_4$," *Materials Chemistry and Physics,* vol. 98, pp. 532-538, 2006.

[2] Ledwaba R. S., Womack J. C., Skylaris C. K. and Ngoepe P. E., "Intercalation voltages for spinel $Li_xMn_2O_4$ ($0 \leq x \leq 2$) cathode materials: Calibration of calculations with the ONETEP linear-scaling DFT code," *Materials Today Communications,* vol. 27, pp. 102380-102380, 2021.

[3] Hou Z., Zhang X., Dong M., Xiong Y., Zhang Z., Ao H., Liu M., Zhu Y. and Qian Y., "A large format aqueous rechargeable $LiMn_2O_4$/Zn battery with high energy density and long cycle life," *Science China Materials,* vol. 64, pp. 783-788, 2021.

[4] Lesel B. K., Cook J. B., Yan Y., Lin T. C. and Tolbert S. H., "Using nanoscale domain size to control charge storage kinetics in pseudocapacitive nanoporous $LiMn_2O_4$ powders," *ACS Energy Letters,* vol. 2, pp. 2293-2298, 2017.

[5] Kebede M. A., Palaniyandy N., Koao L. F., Ezema F. I. and Mhlongo M. R., "Current Status and Trends in Spinel Cathode Materials for Lithium-Ion Battery," *In Electrode Materials for Energy Storage and Conversion,* pp. 35-46, 2021.

[6] Rada E., Lima E., Ruiz F. and Moreno S., "Small hollow nanostructures as a new morphology to improve stability of $LiMn_2O_4$ cathodes in Li-ion batteries," *Nanotechnology,* vol. 32, pp. 435403-435403, 2021.

[7] Singh V., Chakraborty T. and Tripathy S. K., "A review of low grade manganese ore upgradation processes.," *Mineral Processing and Extractive Metallurgy Review.,* vol. 41, pp. 417-438, 2020.

[8] Tsikos H., Beukes N. J., Moore J. M. and Harris C., "Deposition, diagenesis, and secondary enrichment of metals in the paleoproterozoic hotazel iron formation, Kalahari manganese field, South Africa.," *Economic Geology.,* vol. 98, pp. 1449-1462, 2003.

[9] Manthiram A, "A reflection on lithium-ion battery cathode chemistry," *Nature Communications,* vol. 11, pp. 1-9, 2020.

[10] Liu D., Ouyang C., Shu J., Jiang J., Wang Z. and Chen L, "Theoretical study of cation doping effect on the electronic conductivity of $Li_4Ti_5O_{12}$," *Physica Status Solidi,* vol. 243, pp. 1835-1841, 2006.

[11] Schipper F., Dixit M., Kovacheva D., Talianker M., Haik O., Grinblat J., Erickson E. M., Ghanty C., Major D. T., Markovsky B. and Aurbach D, "Stabilizing nickel-rich layered cathode materials by a high-charge cation doping strategy: zirconium-doped $LiNi_{0.6}Co_{0.2}Mn_{0.2}O_2$," *Journal of Materials Chemistry A,* vol. 4, pp. 16073-16084, 2016.

[12] Zhang Y., Alarco J. A., Nerkar J. Y., Best A. S., Snook G. A., Talbot P. C. and Cowie B. C., "Observation of preferential cation doping on the surface of $LiFePO_4$ particles and its effect on properties," *ACS Applied Energy Materials,* vol. 3, pp. 9158-9167, 2020.

[13] Ma Y., Shang R., Liu Y., Lake R., Ozkan M. and Ozkan C. S, "Enabling fast-charging capability for all-solid-state lithium-ion batteries," *Journal of Power Sources,* vol. 559, pp. 232647-232647, 2023.

[14] Kucur G., Tur M. R., Bayindir R., Shahinzadeh H. and Gharehpetian G. B., "A Review of Emerging Cutting-Edge Energy Storage Technologies for Smart Grids Purposes," *In 2022 9th Iranian Conference on Renewable Energy & Distributed Generation (ICREDG),* vol. 1, pp. 1-11, 2022.

[15] Lai X., Chen Q., Tang X., Zhou Y., Gao F., Guo Y., Bhagat R. and Zheng Y., "Critical review of life cycle assessment of lithium-ion batteries for electric vehicles: A lifespan perspective," *Etransportation,* vol. 1, pp. 100169-100169, 2022.

[16] Blomgren G. E, "The development and future of lithium ion batteries," *Journal of The Electrochemical Society,* vol. 164, pp. A5019-A5019, 2016.

[17] Manthiram A., " An outlook on lithium ion battery technology," *ACS central science,* vol. 3, pp. 1063-1069, 2017.

[18] Scrosati B., Hassoun J. and Sun Y. K., "Lithium-ion batteries. A look into the future," *Energy & Environmental Science,* vol. 4, pp. 3287-3295, 2011.

[19] Xie J. and Lu Y. C., "A retrospective on lithium-ion batteries," *Nature Communications,* vol. 11, pp. 1-4, 2020.

[20] Yoshio M., Brodd R. J. and Kozawa A, "Lithium-ion batteries," *New York: Springer,* vol. 1, pp. 2-3, 2009.

[21] Wakihara M., "Recent developments in lithium ion batteries," *Materials Science and Engineering: R: Reports,* vol. 33, pp. 109-134, 2001.

[22] Means, G, "FAVPNG," November 2021. [Online]. Available: https://favpng.com/png_view/black-friday-poster-gadget-electronics-handheld-devices-schematic-electrical-engineering-png/9bKmDWH2. [Accessed May 2020].

[23] Diaz, M. A, "FAVPNG," September 2017. [Online]. Available: https://favpng.com/png_view/ride-electric-vehicles-2018-buick-encore-preferred-general-motors-car-automatic-transmission-png/wuHFuPm6.

[24] Ali, S, "FAVPNG," April 2017. [Online]. Available: https://favpng.com/png_view/vector-green-energy-energy-power-station-wind-power-png/nNqcFhCW.

[25] Zou H., Gratz E., Apelian D. and Wang Y., "A novel method to recycle mixed cathode materials for lithium ion batteries," *Green Chemistry,* vol. 15, pp. 1183-1191, 2013.

[26] Xu B., Qian D., Wang Z. and Meng Y. S, "Recent progress in cathode materials research for advanced lithium ion batteries," *Materials Science and Engineering: R: Reports,* vol. 73, pp. 51-65, 2012.

[27] Wang J., He X., Paillard E., Laszczynski N., Li J. and Passerini S., "Lithium-and Manganese-Rich Oxide Cathode Materials for High-Energy Lithium Ion Batteries," *Advanced Energy Materials,* vol. 6, pp. 1600906-1600906, 2016.

[28] Beukes N. J., Swindell E. P. and Wabo H., "Manganese deposits of Africa.," *Episodes Journal of International Geoscience,* vol. 39, pp. 285-317, 2016.

[29] Chetty D. and Gutzmer J., "REE redistribution during hydrothermal alteration of ores of the Kalahari manganese deposit," *Ore Geology Reviews,* vol. 47, pp. 126-135, 2012.

[30] Tsikos H. and Moore J. M., "Petrography and geochemistry of the Paleoproterozoic Hotazel Iron-Formation, Kalahari manganese field, South Africa; implications for Precambrian manganese metallogenesis," *Economic Geology,* vol. 92, pp. 87-97, 1997.

[31] Zhang W. J., "Structure and performance of $LiFePO_4$ cathode materials: A review," *Journal of Power Sources,* vol. 196, pp. 2962-2970, 2011.

[32] Zhang Y. and Wang C. Y., "Cycle-life characterization of automotive lithium-ion batteries with $LiNiO_2$ cathode," *Journal of the Electrochemical Society,* vol. 156, pp. A527-A527, 2009.

[33] Takahashi Y., Tode S., Kinoshita A., Fujimoto H., Nakane I. and Fujitani S., "Development of lithium-ion batteries with a $LiCoO_2$ cathode toward high capacity by elevating charging potential," *Journal of the Electrochemical Society,* vol. 155, pp. A537-A537, 2008.

[34] Zhu X., Meng F., Zhang Q., Xue L., Zhu H., Lan S., Liu Q., Zhao J., Zhuang Y., Guo Q. and Liu B., "$LiMnO_2$ cathode stabilized by interfacial orbital ordering for sustainable lithium-ion batteries," *Nature Sustainability,* vol. 4, pp. 392-401, 2021.

[35] Wang H. Q., Lai F. Y., Li Y., Zhang X. H., Huang Y. G., Hu S. J. and Li Q. Y., "Excellent stability of spinel $LiMn_2O_4$-based cathode materials for lithium-ion batteries," *Electrochimica Acta,* vol. 177, pp. 290-297, 2015.

[36] Winter M., Barnett B. and Xu K., "Before Li ion batteries," *Chemical Reviews,* vol. 118, pp. 11433-11456, 2018.

[37] Reddy M. V., Mauger A., Julien C. M., Paolella A. and Zaghib K, " Brief history of early lithium-battery development," *Materials,* vol. 13, pp. 1884-1884, 2020.

[38] Liu W., Oh P., Liu X., Lee M. J., Cho W., Chae S., Kim Y. and Cho J., " Nickel-rich layered lithium transition-metal oxide for high-energy lithium-ion batteries," *Angewandte Chemie International Edition,* vol. 54, pp. 4440-4457, 2015.

[39] He P., Yu H. and Zhou H., "Layered lithium transition metal oxide cathodes towards high energy lithium-ion batteries," *Journal of Materials Chemistry,* vol. 22, pp. 3680-3695, 2012.

[40] Zhang J. and Yu A., "Nanostructured transition metal oxides as advanced anodes for lithium-ion batteries.," *Science Bulletin,* vol. 60, pp. 823-838, 2015.

[41] Arai H., Okada S., Sakurai Y. and Yamaki J. I., "Reversibility of LiNiO2 cathode," *Solid State Ionics,* vol. 95, pp. 275-282, 1997.

[42] Bai N., Qi Y., Sun Z., Guo D., Chen G. and Wang A., "Effect of Mg and Al cosubstitution on the structure and electrochemical performance of a Co-free $LiNiO_2$ cathode material," *Journal of Materials Science: Materials in Electronics,* vol. 33, pp. 18533-18543, 2022.

[43] Pan R., Jo E., Cui Z. and Manthiram A., "Degradation Pathways of Cobalt-Free LiNiO2 Cathode in Lithium Batteries," *Advanced Functional Materials,* vol. 33, pp. 2211461-2211461, 2023.

[44] Cho J., Kim Y. J. and Park B., "Novel $LiCoO_2$ cathode material with Al_2O_3 coating for a Li ion cell," *Chemistry of Materials,* vol. 12, pp. 3788-3791, 2000.

[45] Kong W., Zhou D., Zhang Q., Wong D., An K., Schulz C., Zhang N., Zhang J. and Liu X., "Adjusting the Redox Coupling Effect via Li/Co Anti-Site Defect for Stable High-Voltage $LiCoO_2$ Cathode," *Advanced Functional Materials,* vol. 33, pp. 2211033-2211033, 2023.

[46] Zhang S., Wang J., Tao X., Yan X., Du Y., Seifert, H. J. and Lei T., "Understanding the different effects of 4d-transition metals on the performance of Li-rich cathode Li_2MnO_3 by first-principles," *Physical Chemistry Chemical Physics,* vol. 25, pp. 2282-2293, 2023.

[47] Rana J., Stan M., Kloepsch R., Li J., Schumacher G., Welter E., Zizak I., Banhart J. and Winter M., "Structural changes in Li_2MnO_3 cathode material for Li-Ion batteries.," *Advanced Energy Materials,* vol. 4, pp. 1300998-1300998, 2014.

[48] Mogashoa T., Ledwaba R. S. and Ngoepe P. E., "Analysing the implications of charging on nanostructured Li_2MnO_3 cathode materials for lithium-ion battery performance," *Materials,* vol. 15, pp. 5687-5687, 2022.

[49] Sun Y., Zan L. and Zhang Y., "Enhanced electrochemical performances of Li_2MnO_3 cathode materials via adjusting oxygen vacancies content for lithium-ion batteries," *Applied Surface Science,* vol. 483, pp. 270-277, 2019.

[50] Radzi Z. I., Arifin K. H., Kufian M. Z., Balakrishnan V., Raihan S. R. S., Abd Rahim N. and Subramaniam R., "Review of spinel $LiMn_2O_4$ cathode materials under high cut-off voltage in lithium-ion batteries: Challenges and strategies," *Journal of Electroanalytical Chemistry,* vol. 1, pp. 116623-116623, 2022.

[51] Whittingham M. S, " Lithium batteries and cathode materials," *Chemical Reviews,* vol. 104, pp. 4271-4302, 2004.

[52] Kang K., Meng Y. S., Breger J., Grey C. P. and Ceder G., "Electrodes with high power and high capacity for rechargeable lithium batteries," *Science,* vol. 311, pp. 977-980, 2006.

[53] Yi T. F., Hao C. L., Yue C. B., Zhu R. S. and Shu J., " A literature review and test: structure and physicochemical properties of spinel $LiMn_2O_4$ synthesized by different temperatures for lithium ion battery.," *Synthetic Metals,* vol. 159, pp. 1255-1260, 2009.

[54] Gao Y. and Dahn J. R., "Synthesis and Characterization of $Li_{1+x}Mn_{2-x}O_4$ for Li-Ion Battery Applications," *Journal of the Electrochemical Society,* vol. 143, pp. 100-100, 1996.

[55] Thackeray M. M., Johnson P. J., De Picciotto L. A., Bruce P. G. and Goodenough J. B., "Electrochemical extraction of lithium from $LiMn_2O_4$," *Materials Research Bulletin,* vol. 19, pp. 179-187, 1984.

[56] Thackeray M. M. and Amine K., "$LiMn_2O_4$ spinel and substituted cathodes," *Nature Energy,* vol. 6, pp. 566-566, 2021.

[57] Radzi Z. I., Arifin K. H., Kufian M. Z., Balakrishnan V., Raihan S. R. S., Abd Rahim N. and Subramaniam R., "Review of spinel $LiMn_2O_4$ cathode materials under high cut-off voltage in lithium-ion batteries: Challenges and strategies," *Journal of Electroanalytical Chemistry,* vol. 1, pp. 116623-116623, 2022.

[58] Liu G. Y., Guo J. M., Zhang L. L., Wang B. S. and He Y., "A contrastive study on $LiMn_2O_4$ prepared by solution combustion synthesis using nitrate or acetate salts as raw materials," *In Applied Mechanics and Materials,* vol. 142, pp. 205-208, 2012.

[59] Yang G., Wang L., Wang J. and Yan W., "Tailoring the morphology of one-dimensional hollow $LiMn_2O_4$ nanostructures by single-spinneret electrospinning," *Materials Letters,* vol. 177, pp. 13-16, 2016.

[60] Wei C., Shen J., Zhang J., Zhang H. and Zhu C., "Effects of ball milling on the crystal face of spinel $LiMn_2O_4$," *RSC advances,* vol. 4, pp. 44525-44528, 2014.

[61] Liu H., Wu Y. P., Rahm E., Holze R. and Wu H. Q., "Cathode materials for lithium ion batteries prepared by sol-gel methods," *Journal of Solid State Electrochemistry,* vol. 8, pp. 450-466, 2004.

[62] Park Y. J., Kim J. G., Kim M. K., Chung H. T. and Kim H. G., "Preparation of $LiMn_2O_4$ thin films by a sol–gel method," *Solid State Ionics,* vol. 130, pp. 203-214, 2000.

[63] Sun Y. K., Oh I. H. and Kim K. Y., "Synthesis of spinel $LiMn_2O_4$ by the sol-gel method for a cathode-active material in lithium secondary batteries," *Industrial & engineering chemistry research,* vol. 36, pp. 4839-4846, 1997.

[64] Shandilya M., Rai R. and Singh J., "Hydrothermal technology for smart materials," *Advances in Applied Ceramics,* vol. 115, pp. 354-376, 2016.

[65] Chan H. W., Duh J. G. and Sheen S. R, "$LiMn_2O_4$ cathode doped with excess lithium and synthesized by co-precipitation for Li-ion batteries," *Journal of Power Sources,* vol. 115, pp. 110-118, 2003.

[66] Ebin B., Lindbergh G. and Gürmen S., "Preparation and electrochemical properties of nanocrystalline $LiB_xMn_{2-x}O_4$ cathode particles for Li-ion batteries by ultrasonic spray pyrolysis method," *Journal of Alloys and Compounds,* vol. 620, pp. 399-406, 2015.

[67] Matsuda K. and Taniguchi I., "Relationship between the electrochemical and particle properties of $LiMn_2O_4$ prepared by ultrasonic spray pyrolysis," *Journal of Power Sources,* vol. 132, pp. 156-160, 2004.

[68] Angelopoulou P., Paloukis F., Słowik G., Wójcik G. and Avgouropoulos G., "Combustion-synthesized $Li_xMn_2O_4$-based spinel nanorods as cathode materials for lithium-ion batteries," *Chemical Engineering Journal,* vol. 311, pp. 191-202, 2017.

[69] Kalyani P., Kalaiselvi N. and Muniyandi N., "A new solution combustion route to synthesize $LiCoO_2$ and $LiMn_2O_4$," *Journal of Power Sources,* vol. 111, pp. 232-238, 2002.

[70] Du K. and Zhang H., "Preparation and performance of spinel $LiMn_2O_4$ by a citrate route with combustion," *Journal of Alloys and Compounds,* vol. 352, pp. 250-254, 2003.

[71] Sayle D. C. and Johnston R. L., "Evolutionary techniques in atomistic simulation: thin films and nanoparticles," *Current Opinion in Solid State and Materials Science,* vol. 7, pp. 3-12, 2003.

[72] Lee S. and Park S. S, "Atomistic simulation study of mixed-metal oxide ($LiNi_{1/3}Co_{1/3}Mn_{1/3}O_2$) cathode material for lithium ion battery," *The Journal of Physical Chemistry C,* vol. 116, pp. 6484-6489, 2012.

[73] Sayle D. C., Feng X., Ding Y., Wang Z. L. and Sayle T. X., ""Simulating synthesis": ceria nanosphere self-assembly into nanorods and framework architectures," *Journal of the American Chemical Society,* vol. 129, pp. 7924-7935, 2007.

[74] Maphanga R. R., Sayle D. C., Sayle T. X. and Ngoepe P. E., " Amorphization and recrystallization study of lithium insertion into manganese dioxide," *Physical Chemistry Chemical Physics,* vol. 13, pp. 1307-1313, 2011.

[75] Ledwaba R. S., Sayle D. C. and Ngoepe P. E., "Atomistic Simulation and Characterization of Spinel $Li_{1+x}Mn_2O_4$ ($0 \leq x \leq 1$) Nanoparticles," *ACS Applied Energy Materials,* vol. 3, pp. 1429-1438, 2020.

[76] Xu W., Zheng Y., Cheng Y., Qi R., Peng H., Lin H. and Huang R., "Understanding the effect of Al doping on the electrochemical performance improvement of the $LiMn_2O_4$ cathode material," *ACS Applied Materials & Interfaces,* vol. 13, pp. 45446-45454, 2021.

[77] Amaral F. A., Bocchi N., Brocenschi R. F., Biaggio S. R. and Rocha-Filho R. C., "Structural and electrochemical properties of the doped spinels $Li_{1.05}M_{0.02}Mn_{1.98}O_{3.98}N_{0.02}$ (M= Ga^{3+}, Al^{3+}, or Co^{3+}; N= S^{2-} or F^{-}) for use as cathode material in lithium batteries," *Journal of Power Sources,* vol. 195, pp. 3293-3299, 2010.

[78] Wu H. M., Tu J. P., Chen X. T., Li Y., Zhao X. B. and Cao G. S., "Effects of Ni-ion doping on electrochemical characteristics of spinel $LiMn_2O_4$ powders prepared by a spray-drying method," *Journal of Solid State Electrochemistry,* vol. 11, pp. 173-176, 2007.

[79] Luo Q. and Manthiram A., "Effect of Low-Temperature Fluorine Doping on the Properties of Spinel $LiMn_{2-2y}Li_yM_yO_{4-\eta}F_\eta$ (M= Fe, Co, and Zn) Cathodes," *Journal of The Electrochemical Society,* vol. 156, pp. A84-A84, 2008.

[80] Bach S., Henry M., Baffier N. and Livage J., "Sol-gel synthesis of manganese oxides," *Journal of Solid State Chemistry,* vol. 88, pp. 325-333, 1990.

[81] Hayashi, N., Ikuta, H. and Wakihara, M., "Cathode of $LiMg_yMn_{2-y}O4$ and $LiMg_yMn_{2-y}O_{4-\delta}$ Spinel Phases for Lithium Secondary Batteries," *Journal of the Electrochemical Society,* vol. 146, pp. 1351-1351, 1999.

[82] Liu R. S. and Shen C. H., "Structural and electrochemical study of cobalt doped $LiMn_2O_4$ spinels," *Solid State Ionics,* vol. 157, pp. 95-100, 2003.

[83] Wei Y. J., Yan L. Y., Wang C. Z., Xu X. G., Wu F. and Chen G., "Effects of Ni doping on [MnO6] octahedron in $LiMn_2O_4$," *The Journal of Physical Chemistry B,* vol. 108, pp. 18547-18551, 2004.

[84] Zhang X., Lan X., Feng Y., Wang X., Kong S., Xu Z., Ma Z., Gong W., Yao Y. and Li Q., "Boosting Li-Ion Storage Capability of Self-Standing Ni-Doped $LiMn_2O_4$ Nanowall Arrays as Superior Cathodes for High-Performance Flexible Aqueous Rechargeable Li-Ions Batteries," *Advanced Materials Interfaces,* vol. 1, pp. 2202035-2202035, 2022.

[85] Liu R. S. and Shen C. H., "Structural and electrochemical study of cobalt doped $LiMn_2O_4$ spinels," *Solid State Ionics,* vol. 157, pp. 95-100, 2003.

[86] Schipper F., Dixit M., Kovacheva D., Talianker M., Haik O., Grinblat J., Erickson E. M., Ghanty C., Major D. T., Markovsky B. and Aurbach D., "Stabilizing nickel-rich layered cathode materials by a high-charge cation doping strategy: zirconium-doped $LiNi_{0.6}Co_{0.2}Mn_{0.2}O_2$," *Journal of Materials Chemistry A,* vol. 4, pp. 16073-16084, 2016.

[87] Bellitto C., Bauer E. M., Righini G., Green M. A., Branford W. R., Antonini A. and Pasquali M, "The effect of doping $LiMn_2O_4$ spinel on its use as a cathode in Li-ion batteries: neutron diffraction and electrochemical studies," *Journal of Physics and Chemistry of Solids,* vol. 65, pp. 29-37, 2004.

[88] Capsoni D., Bini M., Chiodelli G., Mustarelli P., Massarotti V., Azzoni C. B., Mozzati M. C. and Linati L., "Inhibition of Jahn - Teller Cooperative Distortion in

$LiMn_2O_4$ Spinel by Ga^{3+} Doping," *The Journal of Physical Chemistry B,* vol. 106, pp. 7432-7438, 2002.

[89] Yamada A. and Tanaka M., "Jahn-Teller structural phase transition around 280K in $LiMn_2O_4$," *Materials Research Bulletin,* vol. 30, pp. 715-721, 1995.

[90] Manthiram A., "Materials challenges and opportunities of lithium ion batteries," *The Journal of Physical Chemistry Letters,* vol. 2, pp. 176-184, 2011.

[91] Manthiram A. V. M. A., Murugan A. V., Sarkar A. and Muraliganth T., "Nanostructured electrode materials for electrochemical energy storage and conversion," *Energy & Environmental Science,* vol. 1, pp. 621-638, 2008.

[92] Liu R., Duay J. and Lee S. B., "Heterogeneous nanostructured electrode materials for electrochemical energy storage," *Chemical Communications,* vol. 47, pp. 1384-1404, 2011.

[93] Kim M. G. and Cho J, "Reversible and high-capacity nanostructured electrode materials for Li-ion batteries," *Advanced Functional Materials,* vol. 19, pp. 1497-1514, 2009.

[94] Sun Y. K., Chen Z., Noh H. J., Lee D. J., Jung H. G., Ren Y., Wang S., Yoon C. S., Myung S. T. and Amine K, "Nanostructured high-energy cathode materials for advanced lithium batteries," *Nature Material,* vol. 11, pp. 942-947, 2012.

[95] Kim S. B., Kim S. J., Kim C. H., Kim W. S. and Park K. W., "Nanostructure cathode materials prepared by high-energy ball milling method," *Materials Letters,* vol. 65, pp. 3313-3316, 2011.

[96] Zhang Y., Shin H. C., Dong J. and Liu M, "Nanostructured $LiMn_2O_4$ prepared by a glycine-nitrate process for lithium-ion batteries," *Solid State Ionics,* vol. 17, pp. 25-31, 2004.

[97] Pederson R., Kalita B. and Burke K., "Machine learning and density functional theory," *Nature Reviews Physics,* vol. 4, pp. 357-358, 2022.

[98] Hernández E., Gillan M. J. and Goringe C. M., "Linear-scaling density-functional-theory technique: The density-matrix approach," *Physical Review B,* vol. 53, pp. 7147-7147, 1996.

[99] Ercolessi F. and Adams J. B., "Interatomic potentials from first-principles calculations: the force-matching method.," *Europhysics Letters,* vol. 26, pp. 583-583, 1994.

[100] Cohen A. J., Mori-Sánchez P. and Yang W, "Insights into current limitations of density functional theory.," *Science,* vol. 321, pp. 792-794, 2008.

[101] Cai Z. L., Sendt K. and Reimers J. R., "Failure of density-functional theory and time-dependent density-functional theory for large extended π systems," *The Journal of Chemical Physics,* vol. 117, pp. 5543-5549, 2002.

[102] McCammon J. A., Gelin B. R. and Karplus M., "Dynamics of folded proteins," *Nature,* vol. 267, pp. 585-590, 1997.

[103] Alder B. J. and Wainwright T. E., "Phase transition for a hard sphere system," *The Journal of chemical physics,* vol. 27, pp. 1208-1209, 1957.

[104] Alder B. J. and Wainwright T. E., "Studies in molecular dynamics. I. General method," *The Journal of Chemical Physics,* vol. 31, pp. 459-466, 1959.

[105] Harrison R. L., " Introduction to monte carlo simulation. In AIP conference proceedings," *American Institute of Physics,* vol. 1, pp. 17-21, 2010.

[106] Raychaudhuri S., "December. Introduction to monte carlo simulation," *Winter Simulation Conference,* vol. 1, pp. 91-100, 2008.

[107] Chen H. Y. and Tsou N. T., "The analysis of thermal-induced phase transformation and microstructural evolution in Ni-Ti based shape memory alloys by molecular dynamics," *Computer Modeling in Engineering & Sciences,* vol. 120, pp. 319-332, 2019.

[108] Lyu G. J., Qiao J. C., Yao Y., Wang Y. J., Morthomas J., Fusco C. and Rodney D., " Microstructural effects on the dynamical relaxation of glasses and glass

composites: A molecular dynamics study," *Acta Materialia,* vol. 220, pp. 117293-117293, 2021.

[109] Hou Z., Tian Z., Liu R., Dong K. and Yu A., "Formation mechanism of bulk nanocrystalline aluminium with multiply twinned grains by liquid quenching: A molecular dynamics simulation study," *Computational Materials Science,* vol. 99, pp. 256-261, 2015.

[110] O'connor D. J. and Biersack J. P., "Comparison of theoretical and empirical interatomic potentials," *Nuclear Instruments and Methods in Physics Research Section B: Beam Interactions with Materials and Atoms,* vol. 15, pp. 14-19, 1986.

[111] Deringer V. L., Caro M. A. and Csányi G., "Machine learning interatomic potentials as emerging tools for materials science," *Advanced Materials,* vol. 31, pp. 1902765-1902765, 2019.

[112] Wei Y., Nam K. W., Kim K. B. and Chen G., "Spectroscopic studies of the structural properties of Ni substituted spinel $LiMn_2O_4$," *Solid State Ionics,* vol. 177, pp. 29-35, 2006.

[113] Yu Z. M. and Zhao L. C, "Structure and electrochemical properties of $LiMn_2O_4$," *Transactions of Nonferrous Metals Society of China,* vol. 17, pp. 659-664, 2007.

[114] Wills A. S., Raju N. P. and Greedan J. E, "Low-temperature structure and magnetic properties of the spinel $LiMn_2O_4$: a frustrated antiferromagnet and cathode material," *Chemistry of Materials,* vol. 11, pp. 1510-1518, 1999.

[115] Peña O., Bodenez V., Guizouarn T., Meza E. and Gautier J. L., " Influence of the cation substitution on the magnetic properties of $LiCo_2O_4$ and $Li(Me, Co)_2O_4$ spinels," *Boletín de la Sociedad Española de Cerámica y Vidrio,* vol. 43, pp. 736-739, 2004.

[116] Thomas M. G. S. R., David W. I. F., Goodenough J. B. and Groves P., "Synthesis and structural characterization of the normal spinel $Li[Ni_2]O_4$," *Materials Research Bulletin,* vol. 20, pp. 1137-1146, 1985.

[117] Liu W., Kowal K. and Farrington G. C., "Mechanism of the Electrochemical Insertion of Lithium into $LiMn_2O_4$ Spinels," *Journal of The Electrochemical Society,* vol. 145, pp. 459-459, 1998.

[118] Liu Z., Wang H., Fang L., Lee J. Y. and Gan L. M., "Improving the high-temperature performance of $LiMn_2O_4$ spinel by micro-emulsion coating of $LiCoO_2$," *Journal of Power Sources,* vol. 104, pp. 101-107, 2002.

[119] Chevrier V. L., Ong S. P., Armiento R., Chan M. K. and Ceder G, "Hybrid density functional calculations of redox potentials and formation energies of transition metal compounds," *Physical Review B,* vol. 82, pp. 75122-75122, 2010.

[120] Cho J. and Kim G., "Enhancement of Thermal Stability of $LiCoO_2$ by $LiMn_2O_4$ Coating," *Electrochemical and Solid-State Letters,* vol. 2, pp. 253-253, 1999.

[121] Gabrisch H., Ozawa Y. and Yazami R., "Crystal structure studies of thermally aged $LiCoO_2$ and $LiMn_2O_4$ cathodes," *Electrochimica acta,* vol. 52, pp. 1499-1506, 2006.

[122] Ellis B. L., Lee K. T. and Nazar L. F., "Positive electrode materials for Li-ion and Li-batteries," *Chemistry of Materials,* vol. 22, pp. 691-714, 2010.

[123] Park O. K., Cho Y., Lee S., Yoo H. C., Song H. K. and Cho J., " Who will drive electric vehicles, olivine or spinel?," *Energy & Environmental Science,* vol. 4, pp. 1621-1633, 2011.

[124] Wakihara M., "Recent developments in lithium ion batteries," *Materials Science and Engineering: R: Reports,* vol. 33, pp. 109-134, 2001.

[125] Li J., Daniel C. and Wood D., "Materials processing for lithium-ion batteries," *Journal of Power Sources,* vol. 196, pp. 2452-2460, 2011.

[126] Armand M. and Tarascon J. M., "Building better batteries," *Nature,* vol. 451, pp. 652-657, 2008.

[127] Yang Z., Zhang J., Kintner-Meyer M. C., Lu X., Choi D., Lemmon J. P. and Liu J., "Electrochemical energy storage for green grid," *Chemical Reviews,* vol. 111, pp. 3577-3613, 2011.

[128] Jang D. H., Shin Y. J. and Oh S. M., "Dissolution of spinel oxides and capacity losses in 4 V Li/$Li_xMn_2O_4$ cells," *Journal of the Electrochemical Society,* vol. 143, pp. 2204-2204, 1996.

[129] Xia Y., Zhou Y. and Yoshio M., "Capacity fading on cycling of 4V Li/$LiMn_2O_4$ cells," *Journal of the Electrochemical Society,* vol. 144, pp. 2593-2593, 1997.

[130] Yamada A., "Lattice instability in $Li(Li_xMn_{2-x})O_4$," *Journal of Solid State Chemistry,* vol. 122, pp. 160-165, 1996.

[131] Benedek R, "Role of disproportionation in the dissolution of Mn from lithium manganate spinel," *The Journal of Physical Chemistry C,* vol. 121, pp. 22049-22053, 2017.

[132] Cho J., Kim T. J., Kim Y. J. and Park B., "Complete blocking of Mn^{3+} ion dissolution from a $LiMn_2O_4$ spinel intercalation compound by Co_3O_4 coating," *Chemical Communications,* vol. 12, pp. 1074-1075, 2001.

[133] Wei A., Mu J., He R., Bai X., Li X., Zhang L., Wang Y., Liu Z. and Wang S, "Enhanced Electrochemical Performance of $LiNi_{0.5}Mn_{1.5}O_4$ Composite Cathodes for Lithium-Ion Batteries by Selective Doping of K+/Cl− and K+/F−," *Nanomaterials,* vol. 11, pp. 2323-2323, 2021.

[134] Rodríguez R. A., Montiel M. G., Mohallem N. D. S., Laffita Y. M., Montoro L. A., Santos M. A., Ramírez H. L. and Pérez-Cappe E. L., "The role of defects on the Jahn-teller effect and electrochemical charge storage in nanometric $LiMn_2O_4$ material," *Solid State Ionics,* vol. 369, pp. 115707-115707, 2021.

[135] Sun Y. K., Jeon Y. S. and Leeb H. J., "Overcoming Jahn-Teller Distortion for Spinel Mn Phase," *Electrochemical and Solid State Letters,* vol. 3, pp. 7-7, 1999.

[136] Liu C., Sun J., Tan W. L., Lu J., "Alkali cation doping for improving the structural stability of 2D perovskite in 3D/2D PSCs," *Nano Letters,* vol. 20, pp. 1240-1251, 2020.

[137] ngber T. T., Liebenau D., Biedermann M., Kolek M., Diddens D., Wiemhöfer H. D., Heuer A., Winter M. and Bieker P, "Increasing the Lithium Ion Mobility in Poly (Phosphazene)-Based Solid Polymer Electrolytes through Tailored Cation Doping," *Journal of The Electrochemical Society,* vol. 168, pp. 70559-70559, 2021.

[138] Ferdi C. A., Belaiche M. and Iffer E, "Investigation of Tetravalent Cation Doping with (M= Sn^{4+}, Zr^{4+}, and Ge^{4+}) on the Electrochemical Properties of Monoclinic $Li_3V_2(PO_4)_3$ Using First-Principles Calculations," *Journal of The Electrochemical Society,* vol. 168, pp. 70518-70518, 2021.

[139] Xu W., Li H., Zheng Y., Lei W., Wang Z., Cheng Y., Qi R., Peng H., Lin H., Yue F. and Huang R., "Atomic insights into Ti doping on the stability enhancement of truncated octahedron $LiMn_2O_4$ nanoparticles," *Nanomaterials,* vol. 11, pp. 508-508, 2021.

[140] Michalska M., Ziółkowska D. A., Jasiński J. B., Lee P. H., Ławniczak P., Andrzejewski B., Ostrowski A., Bednarski W., Wu, S. H. and Lin J. Y., "Improved electrochemical performance of $LiMn_2O_4$ cathode material by Ce doping," *Electrochimica Acta,* vol. 276, pp. 37-46, 2018.

[141] Chen Z., Zhang W. and Yang Z., "A review on cathode materials for advanced lithium ion batteries: microstructure designs and performance regulations," *Nanotechnology,* vol. 31, pp. 012001-012001, 2019.

[142] Gale J. D., "A computer program for the symmetry-adapted simulation of solids," *Journal of the Chemical Society, Faraday Transactions,* vol. 93, pp. 629-637, 1997.

[143] Virtanen P., Gommers R., Oliphant T. E., Haberland M., Reddy T., Cournapeau D., Burovski E., Peterson P., Weckesser W., Bright J. and Van Der Walt S. J.,

"SciPy 1.0: fundamental algorithms for scientific computing in Python," *Nature Methods,* vol. 17, pp. 261-272, 2020.

[144] Xu W., Li Q., Sui F., Guo S., Qi R., Yan C., Chen L., Xia S., Guo J., Li Z. and Huang R., "Unveiling the role of Ni doping in the electrochemical performance improvement of the $LiMn_2O_4$ cathodes," *Applied Surface Science,* vol. 624, pp. 157142-157142, 2023.

[145] Hou X., Liu X., Wang H., Zhang X., Zhou J. and Wang M, "Specific countermeasures to intrinsic capacity decline issues and future direction of $LiMn_2O_4$ cathode," *Energy Storage Materials,* vol. 57, pp. 577-606, 2023.

[146] Zhang Z., Li J., Yi T., Sun L., Zhang Y., Hu X., Cui W. and Yang X., "Surface density of synthetically tuned spinel oxides of Co^{3+} and Ni^{3+} with enhanced catalytic activity for methane oxidation," *Chinese Journal of Catalysis,* vol. 39, pp. 1228-1239, 2018.

[147] Mandal S., Rojas R. M., Amarilla J. M., Calle P., Kosova N. V., Anufrienko V. F. and Rojo J. M., "High temperature Co-doped $LiMn_2O_4$-based spinels. Structural, electrical, and electrochemical characterization," *Chemistry of Materials,* vol. 14, pp. 1598-1605, 2002.

[148] Xu W., Guo S., Li Q., Xia S., Cheng F., Sui F., Qi R., Cao Y. and Huang R., "Cobalt doped spinel $LiMn_2O_4$ cathode toward high-rate performance lithium-ion batteries," *Vacuum,* vol. 219, pp. 112724-112724, 2024.

[149] Blum, V., Gehrke R., Hanke F., Havu P., Havu V., Ren X., Reuter K. and Scheffler M., "The Fritz Haber Institute ab initio molecular simulations package (FHI-aims)," 2009. [Online]. Available: http://www.fhi-berlin.mpg.de/aims.

[150] Hansson T., Oostenbrink C. and van Gunsteren W., "Molecular dynamics simulations.," *Current Opinion in Structural Biology.,* vol. 12, pp. 190-196, 2002.

[151] Yang W., "Direct calculation of electron density in density-functional theory.," *Physical Review Letters.,* vol. 66, pp. 1438-1438, 1991.

[152] Parr R. G., "Density functional theory of atoms and molecules.," *In Horizons of Quantum Chemistry.,* vol. 2, pp. 5-15, 1980.

[153] Hohenberg P. and Kohn W., "Inhomogeneous electron gas.," *Physical Review.,* vol. 136, pp. B864-B864, 1964.

[154] Singh D. J. and Nordstrom L., Planewaves, Pseudopotentials, and the LAPW method, vol. 1, Springer Science & Business Media, 2006, pp. 1-132.

[155] Sahni V., Bohnen K. P. and Harbola M. K., "Analysis of the local-density approximation of density-functional theory," *Physical Review A,* vol. 37, pp. 1895-1895, 1988.

[156] Perdew J. P., Burke K. and Ernzerhof M., "Generalized gradient approximation made simple," *Physical Review Letters,* vol. 77, pp. 3865-3865, 1996.

[157] Perdew J. P., Chevary J. A., Vosko S. H., Jackson K. A., Pederson M. R., Singh D. J. and Fiolhais C, "Atoms, molecules, solids, and surfaces: Applications of the generalized gradient approximation for exchange and correlation," *Physical Review B,* vol. 46, pp. 6671-6671, 1992.

[158] Bloch F, "On the quantum mechanics of electrons in crystal lattices," *Zeitschrift Für Physik,* vol. 52, pp. 555-600, 1929.

[159] Bylaska E. J., "Plane-wave DFT methods for chemistry," *In Annual Reports in Computational Chemistry,* vol. 13, pp. 185-228, 2017.

[160] Schwerdtfeger P, "The pseudopotential approximation in electronic structure theory," *ChemPhysChem,* vol. 12, pp. 3143-3155, 2011.

[161] Chadi D. J. and Cohen M. L., "Special points in the Brillouin zone.," *Physical Review B.,* vol. 8, pp. 5747-5747, 1973.

[162] Hamann D. R., Schlüter M. and Chiang C., "Norm-conserving pseudopotentials," *Physical Review Letters,* vol. 43, pp. 1494-1494, 1979.

[163] Kresse G. and Hafner J, "Norm-conserving and ultrasoft pseudopotentials for first-row and transition elements," *Journal of Physics: Condensed Matter,* vol. 6, pp. 8245-8245, 1994.

[164] Brueckner K. A., "Many-body problem for strongly interacting particles. II. Linked cluster expansion," *Physical Review,* vol. 100, pp. 36-36, 1955.

[165] Goldstone J., "Derivation of the Brueckner many-body theory. Proceedings of the Royal Society of London," *Series A. Mathematical and Physical Sciences,* vol. 239, pp. 267-279, 1957.

[166] Kohn W. and Sham L. J., "Self-consistent equations including exchange and correlation effects," *Physical Review,* vol. 140, pp. A1133-A1133, 1965.

[167] Soler J. M., Artacho E., Gale J. D., García A., Junquera J., Ordejón P. and Sánchez-Portal D., "The SIESTA method for ab initio order-N materials simulation," *Journal of Physics: Condensed Matter,* vol. 14, pp. 2745-2745, 2002.

[168] Pérez-Jorda J. and Yang W., "An algorithm for 3D numerical integration that scales linearly with the size of the molecule," *Chemical Physics Letters,* vol. 241, pp. 469-476, 1995.

[169] Guerra C. F., Snijders J. G., te Velde G. T. and Baerends E. J., "Towards an order-N DFT method," *Theoretical Chemistry Accounts,* vol. 99, pp. 391-403, 1998.

[170] Kresse G. and Hafner J., "Ab initio molecular dynamics for liquid metals," *Physical Review B,* vol. 47, pp. 558-558, 1993.

[171] Kresse G. and Furthmüller J., "Efficiency of ab-initio total energy calculations for metals and semiconductors using a plane-wave basis set," *Computational Materials Science,* vol. 6, pp. 15-50, 1996.

[172] Kresse G. and Joubert D., "From ultrasoft pseudopotentials to the projector augmented-wave method," *Physical Review B,* vol. 59, pp. 1758-1758, 1999.

[173] Haile J. M., Johnston I., Mallinckrodt A. J. and McKay S., "Molecular dynamics simulation: elementary methods," *Computers in Physics,* vol. 7, pp. 625-625, 1993.

[174] Perilla J. R., Goh B. C., Cassidy C. K., Liu B., Bernardi R. C., Rudack T., Yu H., Wu Z. and Schulten K, "Molecular dynamics simulations of large macromolecular complexes," *Current opinion in Structural Biology,* vol. 31, pp. 64-74, 2015.

[175] Tosi M. P, "Cohesion of ionic solids in the Born model," *Solid State Physics,* vol. 16, pp. 1-120, 1964.

[176] Wallace W. E., "The Born-Mayer Model for Ionic Solids and the Heats of Formation and Lattice Spacings of Alkali Halide Solid Solutions," *The Journal of Chemical Physics,* vol. 17, pp. 1095-1099, 1949.

[177] Buckingham R. A., "The classical equation of state of gaseous helium, neon and argon," *Proceedings of the Royal Society of London. Series A. Mathematical and Physical Sciences,* vol. 168, pp. 264-283, 1938.

[178] Smith W. and Forester T. R., "A general-purpose parallel molecular dynamics simulation package," *Journal of Molecular Graphics,* vol. 6, pp. 141-141, 1996.

[179] Jones J. E., "On the determination of molecular fields. From the variation of the viscosity of a gas with temperature," *Proceedings of the Royal Society of London,* vol. 106, pp. 441-462, 1924.

[180] Lennard-Jones J. E., "Cohesion," *Proceedings of the Physical Society,* vol. 45, pp. 461-461, 1931.

[181] Gallavotti G., "Statistical Ensembles. In Statistical Mechanics," *Springer, Berlin, Heidelberg,* vol. 1, pp. 57-87, 1999.

[182] Glimm J. and Jaffe A., "Classical Statistical Mechanics. In Quantum Physics," *Springer, New York, NY,* vol. 1, pp. 28-42, 1987.

[183] Sayle D. C. and Watson G. W, "Structural exploration of thin-film oxide interfaces via ‘simulated amorphisation and recrystallisation," *Surface Science,* vol. 473, pp. 97-107, 2001.

[184] Shibiri B., Ledwaba R. S. and Ngoepe P. E, "Discharge induced structural variation of simulated bulk $Li_{1+x}Mn_2O_4$ (0≤ x≤ 1)," *Optical Materials,* vol. 92, pp. 67-70, 2019.

[185] Cao Q., Gunawan O., Copel M., Reuter K. B., Chey S. J., Deline V. R. and Mitzi D. B., "Defects in Cu (In, Ga) Se^2 chalcopyrite semiconductors: a comparative study of material properties, defect states, and photovoltaic performance.," *Advanced Energy Materials.,* vol. 1, pp. 845-853, 2011.

[186] Dominguez J. E., Fu L. and Pan X. Q., "Effect of crystal defects on the electrical properties in epitaxial tin dioxide thin films.," *Applied Physics Letters.,* vol. 81, pp. 5168-5170, 2002.

[187] Burt H. M. and Mitchell A. G., "Crystal defects and dissolution.," *International Journal of Pharmaceutics.,* vol. 9, pp. 137-152, 1981.

[188] Casey W. H., Carr M. J. and Graham R. A., "Crystal defects and the dissolution kinetics of rutile.," *Geochimica et Cosmochimica Acta.,* vol. 52, pp. 1545-1556, 1998.

[189] Sammalkorpi M., Krasheninnikov A., Kuronen A., Nordlund K. and Kaski K, "Mechanical properties of carbon nanotubes with vacancies and related defects," *Physical Review B,* vol. 70, pp. 245416-245416, 2004.

[190] Liu Y., Cao Y., Mao Q., Zhou H., Zhao Y., Jiang W., Liu Y., Wang J. T., You Z. and Zhu Y., "Critical microstructures and defects in heterostructured materials and their effects on mechanical properties," *Acta Materialia,* vol. 189, pp. 129-144, 2020.

[191] Van Swygenhoven H., "Grain boundaries and dislocations.," *Science.,* vol. 296, pp. 66-67, 2002.

[192] Read W. T. and Shockley W., "Dislocation models of crystal grain boundaries.," *Physical Review.,* vol. 78, pp. 275-275, 1950.

[193] Brandon D. G., "The structure of high-angle grain boundaries.," *Acta Metallurgica.,* vol. 14, pp. 1479-1484, 1966.

[194] Gurevich A. and Pashitskii E. A., "Current transport through low-angle grain boundaries in high-temperature superconductors.," *Physical Review B.,* vol. 57, pp. 13878-13878, 1998.

[195] Gendler, I, "Isaac's science blog," February 2017. [Online]. Available: https://isaacscienceblog.com/2017/02/17/grain-boundaries/.

[196] Rashid M. S., Kim C., Ryntz E. F., Saunders F. I., Verma R. and Kim S., "Quick plastic forming of aluminum alloy sheet metal.," *United States Patent US.,* vol. 253, pp. 588-588, 2001.

[197] Krajewski P. E. and Schroth J. G, "Overview of quick plastic forming technology.," *Materials Science Forum.,* vol. 551, pp. 12-12, 2007.

[198] De Rosa C. and Auriemma F., "The deformability of polymers: the role of disordered mesomorphic crystals and stress-induced phase transformations.," *Angewandte Chemie International Edition.,* vol. 51, pp. 1207-1211, 2012.

[199] Kröner E., "The differential geometry of elementary point and line defects in Bravais crystals.," *International Journal of Theoretical Physics.,* vol. 29, pp. 1219-1237, 1990.

[200] Yan Q., Zhou Z., Zhao X. S. and Chua S. J., "Line defects embedded in three-dimensional photonic crystals.," *Advanced Materials.,* vol. 17, pp. 1917-1920, 2005.

[201] Yarnell J. L., Katz M. J., Wenzel R. G. and Koenig S. H., "Structure factor and radial distribution function for liquid argon at 85 K.," *Physical Review A.,* vol. 7, pp. 2130-2130, 1973.

[202] Li F. and Lannin J. S., "Radial distribution function of amorphous carbon.," *Physical Review Letters.,* vol. 65, pp. 1905-1905, 1990.

[203] Giessen B. C. and Gordon G. E., "X-ray diffraction: new high-speed technique based on X-ray spectrography.," *Science.,* vol. 159, pp. 973-975, 1968.

[204] Chatterjee A. K., "X-ray Diffraction.," *Handbook of Analytical Techniques in Concrete Science and Technology.,* vol. 1, pp. 275-332, 2001.

[205] Scherrer P., "Bestimmung der Grosse und inneren Struktur von Kolloidteilchen mittels Rontgenstrahlen," *Nach Ges Wiss Gottingen,* vol. 2, pp. 8-100, 1918.

[206] Kresse G. and Furthmüller J., "Efficient iterative schemes for ab initio total-energy calculations using a plane-wave basis set," *Physical review B,* vol. 54, pp. 11169-11169, 1996.

[207] Blöchl P. E., “Projector augmented-wave method”***,*** *Physical Review,* vol. 50, pp. 17953 - 17953, 1994.

[208] Ravindran P., Fast L., Korzhavyi P. A., Johansson B., Wills J. and Eriksson O., "Density functional theory for calculation of elastic properties of orthorhombic crystals: Application to $TiSi_2$," *Journal of Applied Physics,* vol. 84, pp. 4891-4904, 1998.

[209] Alers G. A. and Neighbours J. R, "Crystal stability and elastic constants," *Journal of Applied Physics,* vol. 28, pp. 1514-1514, 1957.

[210] Jamal M., Asadabadi S. J., Ahmad I. and Aliabad H. R., "Elastic constants of cubic crystals," *Computational Materials Science,* vol. 95, pp. 592-599, 2014.

[211] Lin Y., Yang Y., Ma H., Cui Y. and Mao W. L., "Compressional behavior of bulk and nanorod $LiMn_2O_4$ under nonhydrostatic stress," *The Journal of Physical Chemistry C,* vol. 115, pp. 9844-9849, 2011.

[212] Dang S. O., Modelling Thermodynamic Properties of Intercalation Compounds for Lithium Ion Batteries, Forschungszentrum Jülich GmbH, 2016, pp. 2015-07545.

[213] Huang L. and Wu Y., "Spinel Ni-doped $LiMn_2O_4$ cathode material with high oxygen reduction catalytic performance for low temperature solid ceramic fuel cells," *Ceramics International,* vol. 50, pp. 5150-5159, 2024.

[214] Madhu M., Venkateswara Rao A. and Mutyala S., "La and Ni Co-doping effect in $LiMn_2O_4$ on structural and electrochemical properties for lithium-ion batteries," *Journal of Electronic Materials,* vol. 50, pp. 5141-5149, 2021.

[215] Guohua L., Ikuta H., Uchida T. and Wakihara M., "The Spinel Phases LiM y $Mn_{2-y}O_4$ (M= Co, Cr, Ni) as the Cathode for Rechargeable Lithium Batteries," *Journal of the Electrochemical Society,* vol. 143, pp. 178-178, 1996.

[216] Yu Y., Xiang M., Guo J., Su C., Liu X., Bai H., Bai W. and Duan K.,, "Enhancing high-rate and elevated-temperature properties of Ni-Mg co-doped $LiMn_2O_4$ cathodes for Li-ion batteries," *Journal of Colloid and Interface Science,* vol. 555, pp. 64-71, 2019.

[217] Wang J., He D., Li X., Zhang J., Li Q., Wang Z., Su Y., Tian Y., Yang J. and Peng B, "The melting curve of cobalt under high pressure," *Solid State Communications,* vol. 307, pp. 113805-113805, 2020.

[218] Thellaputta G. R., Chandra P. S. and Rao C. S. P., "Machinability of nickel based superalloys: a review," *Materials Today: Proceedings,* vol. 4, pp. 3712-3721, 2017.

[219] Sayle T. X., Catlow C. R. A., Maphanga R. R., Ngoepe P. E. and Sayle D. C., "Generating MnO_2 nanoparticles using simulated amorphization and recrystallization," *Journal of the American Chemical Society,* vol. 1227, pp. 12828-12837, 2005.

[220] Smith W. and Forester T. R., "DL_POLY_2. 0: A general-purpose parallel molecular dynamics simulation package.," *Journal of Molecular Graphics.,* vol. 14, pp. 136-141, 1996.

[221] Kellerman D. G. and Gorshkov V. S., "Structure, properties, and application of lithium–manganese spinels.," *Russian Journal of Electrochemistry.,* vol. 37, pp. 1227-1227, 2001.

[222] Jalem R., Mochiduki Y., Nobuhara K., Nakayama M. and Nogami M., "Global minimum structure search in Li_xCoO_2 composition using a hybrid evolutionary algorithm," *Physical Chemistry Chemical Physics,* vol. 14, pp. 13095-13100, 2012.

[223] Lin J., Wu J., Fan E., Zhang X., Chen R., Wu F. and Li L., "Environmental and economic assessment of structural repair technologies for spent lithium-ion battery cathode materials," *International Journal of Minerals, Metallurgy and Materials,* vol. 29, pp. 942-952, 2022.

[224] Mouhib Y., Belaiche M., Ferdi C. A., Lacham M. and Elacham A., "New technique for elaboration and characterization of a high voltage spinel $LiCo_2O_4$ cathode and theoretical investigation," *New Journal of Chemistry,* vol. 44, pp. 2538-2546, 2020.

[225] Massarotti V., Capsoni D. and Bini M., "Stability of $LiMn_2O_4$ and new high temperature phases in air, O_2 and N_2," *Solid State Communications,* vol. 122, pp. 317-322, 2002.

[226] Prabaharan D. D. M., Sadaiyandi K., Mahendran M. and Sagadevan S., "Precipitation method and characterization of cobalt oxide nanoparticles," *Applied Physics A,* vol. 123, pp. 1-6, 2017.

[227] Nakajima K., Souza F. L., Freitas A. L., Thron A. and Castro R. H., "Improving thermodynamic stability of nano-$LiMn_2O_4$ for Li-ion battery cathode," *Chemistry of Materials,* vol. 33, pp. 3915-3925, 2021.

[228] Liquan C. and Schoonman J., "Polycrystalline, glassy and thin films of $LiMn_2O_4$," *Solid State Ionics,* vol. 67, pp. 17-23, 1993.

[229] Erichsen T., Pfeiffer B., Roddatis V. and Volkert C. A., "Tracking the diffusion-controlled lithiation reaction of $LiMn_2O_4$ by in situ tem," *ACS Applied Energy Materials,* vol. 3, pp. 5405-5414, 2020.

[230] Wu Z., Yu K., Huang Y., Pan C. and Xie Y., " Facile solution-phase synthesis of γ-Mn_3O_4 hierarchical structures," *Chemistry Central Journal,* vol. 1, pp. 1-9, 2007.

[231] Li S. and Lei D., "Synthesis and electrochemical characterization of nanosized Li_2MnO_3 cathode material for lithium ion batteries," *In AIP Conference Proceedings,* vol. 1, pp. 1-1, 2017.

[232] Kwon O. S., Kim M. S. and Kim K. B., "A study on the effect of lithium insertion-extraction on the local structure of lithium manganese oxides using X-ray absorption spectroscopy," *Journal of Power Sources,* vol. 81, pp. 510-516, 1999.

[233] Cabana, J., Johnson C. S., Yang X. Q., Chung K. Y., Yoon W. S., Kang S. H., Thackeray M. M. and Grey C. P, "Structural complexity of layered-spinel composite electrodes for Li-ion batteries," *Journal of Materials Research,* vol. 25, pp. 1601-1616, 2010.

[234] Park S. H., Kang S. H., Johnson C. S., Amine K. and Thackeray M. M., " Lithium–manganese–nickel-oxide electrodes with integrated layered–spinel structures for lithium batteries," *Electrochemistry Communications,* vol. 9, pp. 262-268, 2007.

[235] Wolverton C. and Zunger A, "Prediction of Li Intercalation and Battery Voltages in Layered vs. Cubic $LixCoO_2$," *Journal of The Electrochemical Society,* vol. 147, p. 2424, 1998.

[236] Peng C., Bai H., Xiang M., Su C., Liu G. and Guo J., "Effect of calcination temperature on the electrochemical properties of spinel $LiMn_2O_4$ prepared by solid-state combustion synthesis," *International Journal of Electrochemical Science,* vol. 9, pp. 1791-1798, 2014.

[237] Xu B. and Meng S., "Factors affecting Li mobility in spinel $LiMn_2O_4$-A first-principles study by GGA and GGA+ U methods.," *Journal of Power Sources,* vol. 195, pp. 4971-4976, 2010.

[238] Wang H., Wang J., Wang H., Wang S., Dong X., Hao W., Lu J. and Lu F., "Study and Property Characterization of $LiMn_2O_4$ Synthesized from Octahedral Mn_3O_4," *Sustainability,* vol. 15, pp. 13858-13858, 2023.

[239] Tian L. and Yuan A., "Electrochemical performance of nanostructured spinel $LiMn_2O_4$ in different aqueous electrolytes," *Journal of Power Sources,* vol. 192, pp. 693-697, 2009.

[240] Xie J., Tanaka T., Imanishi N., Matsumura T., Hirano A., Takeda Y. and Yamamoto O., " Li-ion transport kinetics in LiMn2O4 thin films prepared by radio frequency magnetron sputtering," *Journal of Power Sources,* vol. 180, pp. 576-581, 2008.

[241] Siqueira G. O., Belardi R. M., Almeida P. H., da Silva C. L., Brant M. C., Matencio T. and Domingues R. Z., "Determination of the Mn3+/Mn4+ ratio in $La_{1-x}Sr_xMnO_3$±d powders," *Journal of Alloys and Compounds,* vol. 521, pp. 50-54, 2012.

[242] Gummow R. J., De Kock A. and Thackeray M. M., "Improved capacity retention in rechargeable 4 V lithium/lithium-manganese oxide (spinel) cells," *Solid State Ionics,* vol. 69, pp. 59-67, 1994.

[243] Nieto S., Majumder S. B. and Katiyar R. S., "Improvement of the cycleability of nano-crystalline lithium manganate cathodes by cation co-doping," *Journal of Power Sources,* vol. 136, pp. 88-98, 2004.

[244] Hlungwani D., Ledwaba R. S. and Ngoepe P. E., "irst-Principles Study on the Effect of Lithiation in Spinel $Li_xMn_2O_4$ ($0 \leq x \leq 1$) Structure: Calibration of CASTEP and ONETEP Simulation Codes," *Materials,* vol. 15, pp. 5678-5678, 2022.

[245] Xu W., Guo S., Li Q., Xia S., Cheng F., Sui F., Qi R., Cao Y. and Huang R., "Cobalt doped spinel $LiMn_2O_4$ cathode toward high-rate performance lithium-ion batteries," *Vacuum,* vol. 219, pp. 112724-112724, 2024.

[246] Pitchai R., Thavasi V., Mhaisalkar S. G. and Ramakrishna S., "Nanostructured cathode materials: a key for better performance in Li-ion batteries," *Journal of Materials Chemistry,* vol. 21, pp. 11040-11051, 2011.

[247] Wang Y. and Cao G., "Developments in nanostructured cathode materials for high-performance lithium-ion batteries," *Advanced materials,* vol. 20, pp. 2251-2269, 2008.

[248] Ding H., Li H., Tao Q., Ren J. and He J., "Nanoporous Cathode Material for High-Energy-Density Sodium-Ion Batteries," *ACS Applied Nano Materials,* vol. 7, pp. 243-252, 2023.

[249] Sun Y. K., Oh S. M., Park H. K. and Scrosati B, "Micrometer-Sized, Nanoporous, High-Volumetric-Capacity $LiMn_{0.85}Fe_{0.15}PO_4$ Cathode Material for Rechargeable Lithium-Ion Batteries.," *Advanced Materials,* vol. 23, pp. 5050-5054, 2011.

[250] Shi Y., Zhou X., Zhang J., Bruck A. M., Bond A. C., Marschilok A. C., Takeuchi K. J., Takeuchi E. S. and Yu G., "Nanostructured conductive polymer gels as a general framework material to improve electrochemical performance of cathode materials in Li-ion batteries," *Nano Letters,* vol. 17, pp. 1906-1914, 2017.

[251] Lee M. J., Lee S., Oh P., Kim Y. and Cho J., "High performance $LiMn_2O_4$ cathode materials grown with epitaxial layered nanostructure for Li-ion batteries," *Nano Letters,* vol. 14, pp. 993-999, 2014.

[252] Pitchai R., Thavasi V., Mhaisalkar S. G. and Ramakrishna S., "Pitchai R., Thavasi V., Mhaisalkar S. G. and Ramakrishna S.," *Nanostructured athode materials: a key for better performance in Li-ion batteries,* vol. 21, pp. 11040-11051, 2011.

[253] Pitchai R., Thavasi V., Mhaisalkar S. G. and Ramakrishna S., "Nanostructured cathode materials: a key for better performance in Li-ion batteries.," *Journal of Materials Chemistry,* vol. 21, pp. 11040-11051, 2011.

[254] Myung S. T., Amine K. and Sun Y. K., "Nanostructured cathode materials for rechargeable lithium batteries," *Journal of Power Sources,* vol. 283, pp. 219-236, 2015.

[255] Ding H., Li H., Tao Q., Ren J. and He J., "Nanoporous Cathode Material for High-Energy-Density Sodium-Ion Batteries," *ACS Applied Nano Materials,* vol. 7, pp. 243-252, 2024.

[256] Wang F. X., Xiao S. Y., Gao X. W., Zhu Y. S., Zhang H. P., Wu Y. P. and Holze R., "Nanoporous $LiMn_2O_4$ spinel prepared at low temperature as cathode material for aqueous supercapacitors," *Journal of Power Sources,* vol. 242, pp. 560-565, 2013.

[257] Kim H., Han B., Choo J. and Cho J., "Three-dimensional porous silicon particles for use in high-performance lithium secondary batteries," *Angewandte Chemie,* vol. 120, pp. 10305-10308, 2008.

[258] Yu Y., Gu L., Zhu C., Tsukimoto S., Van Aken P. A. and Maier J., "Reversible storage of lithium in silver-coated three-dimensional macroporous silicon," *Advanced Materials,* vol. 22, pp. 2247-2250, 2010.

[259] Du C., Gao C., Yin G., Chen M. and Wang L., "Facile fabrication of a nanoporous silicon electrode with superior stability for lithium ion batteries," *Energy & Environmental Science,* vol. 4, pp. 1037-1042, 2011.

[260] Lian C., Su H., Li C., Liu H. and Wu J., "Non-negligible roles of pore size distribution on electroosmotic flow in nanoporous materials," *ACS Nano,* vol. 13, pp. 8185-8192, 2019.

[261] Kim T., Song W., Son D. Y., Ono L. K. and Qi Y., "Lithium-ion batteries: outlook on present, future, and hybridized technologies," *Journal of Materials Chemistry A,* vol. 7, pp. 2942-2964, 2019.

[262] Armand M., Axmann P., Bresser D., Copley M., Edström K., Ekberg C., Guyomard D., Lestriez B., Novák P., Petranikova M. and Porcher W., "Lithium-ion batteries–Current state of the art and anticipated developments," *Journal of Power Sources,* vol. 479, pp. 228708-228708, 2020.

[263] Abou-Rjeily J., Bezza I., Laziz N. A., Autret-Lambert C., Sougrati M. T. and Ghamouss F., "High-rate cyclability and stability of $LiMn_2O_4$ cathode materials for lithium-ion batteries from low-cost natural β− MnO_2," *Energy Storage Materials,* vol. 26, pp. 423-432, 2020.

[264] Tang W., Wang X. J., Hou Y. Y., Li L. L., Sun H., Zhu Y. S., Bai Y., Wu Y. P., Zhu K. and Van Ree T., "Nano $LiMn_2O_4$ as cathode material of high rate capability for lithium ion batteries," *Journal of Power Sources,* vol. 198, pp. 308-311, 2012.

[265] Haruna A. B., Barrett D. H., Rodella C. B., Erasmus R. M., Venter A. M., Sentsho Z. N. and Ozoemena K. I., "Microwave irradiation suppresses the Jahn-Teller distortion in Spinel $LiMn_2O_4$ cathode material for lithium-ion batteries.," *Electrochimica Acta,* vol. 426, pp. 140786-140786, 2022.

[266] Chung K. Y., Ryu C. W. and Kim K. B., "Onset mechanism of Jahn-Teller distortion in 4 V $LiMn_2O_4$ and its suppression by $LiM_{0.05}Mn_{1.95}O_4$ (M= Co, Ni) coating," *Journal of the Electrochemical Society,* vol. 152, pp. A791- A791, 2005.

[267] Zhou G., Sun X., Li Q. H., Wang X., Zhang J. N., Yang W., Yu X., Xiao R. and Li H., " Mn ion dissolution mechanism for lithium-ion battery with $LiMn_2O_4$ cathode: in situ ultraviolet–visible spectroscopy and ab initio molecular dynamics simulations.," *The journal of Physical Chemistry Letters,* vol. 11, pp. 3051-3057, 2020.

[268] Grygar T., Bezdička P., Piszora P. and Wolska E., "Electrochemical reactivity of Li-Mn-O and Li-Fe-Mn-O spinels," *Journal of Solid State Electrochemistry,* vol. 5, pp. 487-494, 2001.

[269] Maphanga R. R., Sayle D. C., Sayle T. X. and Ngoepe P. E., "Amorphization and recrystallization study of lithium insertion into manganese dioxide.," *Physical Chemistry Chemical Physics.,* vol. 13, pp. 1307-1313, 2011.

APPENDIX A

PUBLICATIONS AND CONFERENCE PRESENTATIONS

Presentations

1. **Hlungwani D**, Ledwaba R.S and Ngoepe P.E, First-Principles DFT Study on the Effect of Lithiation on the Spinel $Li_xMn_2O_4$ Structure: Calibration of CASTEP and ONETEP Simulation Codes (ORAL), South African Institute of Physics (SAIP) Conference, Potchefstroom, North-West University, 2021.
2. **Hlungwani D**, Ledwaba R.S and Ngoepe P.E, Investigation of Significant Electronic Properties of Spinel $Li_xMn_2O_4$ with the ONETEP (linear-scaling) and CASTEP (cubic-scaling) simulation codes (ORAL), Faculty of Science and Agriculture Research Day, Fusion Boutique Conference, Polokwane, 2021.
3. **Hlungwani D**, Ledwaba R.S and Ngoepe P.E, Density Functional Theory Study of spinel $LiMn_2O_4$: Towards the Order-N DFT method implemented in the ONETEP code (Poster), Centre for High Performance Computing (CHPC) Conference, Virtual Conference, 2021.
4. **Hlungwani D**, Ledwaba R.S and Ngoepe P.E, Machine Learned Buckingham Interatomic Potentials for Co-doped Li-Mn-O spinel (Oral), South African Institute of Physics (SAIP) Conference, Virtual Conference, 2022.
5. **Hlungwani D**, Ledwaba R.S and Ngoepe P.E, Development of Co – O, Co – Co, and Co – Mn Buckingham Interatomic potentials for Li-Mn-Co-O spinel in the General Utility Lattice Program coupled with a machine learning approach (ORAL), Faculty of Science and Agriculture Research Day Conference, Fusion Boutique, Polokwane, 2022.
6. **Hlungwani D**, Ledwaba R.S and Ngoepe P.E, Derivation of accurate Co-Co, Co-O, and Co-Mn Buckingham interatomic potentials for a Co-doped Li-Mn-O spinel (POSTER), Centre for High Performance Computing (CHPC) Conference, CSIR ICC, Pretoria, 2022.
7. **Hlungwani D**, Ledwaba R.S and Ngoepe P.E, Derivation of Buckingham Potential Parameters: Guided by First-Principles Potential Energy Surfaces (Oral), CHEM4ENERGY Conference, Potchefstroom, North-West University, 2023.

8. **Hlungwani D**, Ledwaba R.S and Ngoepe P.E, Derivation of empirical interatomic potentials for interactions that emanate from doping Li-Mn-O spinel with nickel and cobalt (ORAL), South African Institute of Physics (SAIP) Conference, University of Zululand (Richards Bay Campus), Richards Bay, 2023.
9. **Hlungwani D**, Ledwaba R.S and Ngoepe P.E, Large-Scale Modelling of Pristine and Transition Metal Doped Spinel $LiMn_2O_4$ Cathode Materials (ORAL), Faculty of Science and Agriculture Research Day Conference, Fusion Boutique, Polokwane, 2023.
10. **Hlungwani D**, Ledwaba R.S and Ngoepe P.E, Large-Scale Modelling of Pristine and Transition Metal Doped Spinel $LiMn_2O_4$ Cathode Materials (ORAL), The Rapid Product Development Association of South Africa (RAPDASA) Conference, CSIR ICC, Pretoria, 2023.
11. **Hlungwani D**, Ledwaba R.S and Ngoepe P.E, Examining the Microstructure and Properties of Co- and/or Ni-doped Lithium-Manganese-Oxide Spinel Structure (Poster), Centre for High Performance Computing (CHPC) Conference, Skukuza Lodge Hotel, Kruger National Park, 2023.

Publications

1. Hlungwani D, Ledwaba R.S. and Ngoepe P.E, First-Principles Study on the Effect of Lithiation in Spinel $Li_xMn_2O_4$ ($0 \leq x \leq 1$) Structure: Calibration of CASTEP and ONETEP Simulation Codes, Materials
2. Hlungwani D, Ledwaba R.S. and Ngoepe P.E, Simulated Synthesis and atomic-level Structural Characterization of $LiNi_2O_4$, EDP Sciences
3. Hlungwani D, Ledwaba R.S. and Ngoepe P.E, Derivation of empirical interatomic Potentials for Doping Co and Ni into $LiMn_2O_4$ spinel, South African Institute of Physics (SAIP) Conference Proceedings

Awards

1. 3rd Place, Poster Presentation (PhD), Centre for High Performance Computing (CHPC) Conference, 2021
2. 2nd Place, Oral Presentation (PhD), Faculty of Science and Agriculture Research Day Conference, 2022

3. 3rd Place, Oral Presentation (PhD), the Rapid Product Development Association of South Africa (RAPDASA) Conference,2023
4. Best PhD Oral Presentation, South African Institute of Physics Conference (SAIP), 2024